Microplasma synthesis and emergent optoelectronic properties of nanoparticles

Bruno Alessi

BSc., MSc. Physics

Faculty of Computing, Engineering and the Built Environment

Ulster University

Thesis submitted for the degree of Doctor of Philosophy

September 2020

I confirm that the word count of this thesis is less than 100,000 words

This page was intentionally left blank

Contents

Aknowledgements

I would like to thank Prof. Davide Mariotti for his continuous guidance and support throughout these years, without whom none of it would have been possible. In particular, he made me open my eyes on my good and bad qualities as a researcher, always in his unique peer-to-peer way that especially encouraged me to grow, both personally and professionally during this journey. Special thanks to him also because his flexibility in giving me the unique opportunity to divert my research towards the topics which I found more interesting, and the opportunities to travel for conferences and trainings which has fuelled my professional growth and abilities in networking. In this context I would like to acknowledge my second supervisor Prof. Paul Maguire for his precious advices and constructive criticism from which my knowledge and the present work has benefited. I feel like it has been a great privilege for me to work with them during the last years, as their irreverent critical spirit towards scientific matters and attention to detail has often fired up discussions which have been prolific to the mutual advancement in knowledge, and always in a positive way.

I would like to thank all the past and present group members for their friendship and collaboration throughout these years. Special acknowledgements go to Dr. Manuel Macias-Montero which has supported me during the first year of my PhD and has been fundamental to my work even after he left the lab. Also, I would like to thank in particular Dr. Dilli Babu Padmanaban for whom I developed feelings of brotherhood as we grew up together in this journey and he has always been supportive, personally and professionally in the good and in the bad times, despite my occasional ability to be selfish and careless on his behalf.

I would like to also acknowledge members of other research groups including students and professors, the academic and technical staff in NIBEC as they have been always friendly and supportive, and we pleasantly shared daily life in the lab as a close community.

Bruno Alessi

Abstract

Nanoparticles have acquired enormous interest in all application fields of materials science because of the size-dependent material properties, modified in respect to their macroscopic counterparts. These deviations originate from the dominance of surface effects and in the case of 1-10 nanometre particles (i.e. *quantum dots*) from the confinement of electron wavefunctions in constricting potential wells.

To date, existent synthesis methods viable for industrial integration of quantum dots are limited in obtaining control over particle size, composition, and aggregation at reduced costs. Among all the methods, gas-phase non-equilibrium plasma methods have distinguished themselves for the synthesis of nanoparticles which are not embedded in a matrix or agglomerated. Moreover, nanoparticles of materials which are demanding to synthesize with common chemical and physical routes can be obtained.

Recently, microplasmas have acquired attention for unique qualities of interest to nanomaterial synthesis. These plasmas operate at atmospheric pressure and are confined to a sub-millimetre space. Microplasmas are particularly versatile because of the presence of highly reactive species in the discharge and because they permit to tailor key plasma parameters by the design of reactors. These features enable the synthesis of separated quantum dots from different types of precursors and processing of temperature sensitive materials at reduced costs.

However, while there have been many efforts in recent year for the practical development of reactors and the empirical control of plasma synthesis, little attention has been given to their fundamental physics and the relation between plasma physics and the synthesized nanoparticles. The present work is a modelling and experimental effort that is intended to bridge the two aspects by studying the relation between plasma parameters, nanoparticle formation and the resulting material properties of nanoparticles, with a particular emphasis on their optoelectronic properties and the issues related to their integrability in real world applications.

List of publications and presentations

A. Published and accepted journal papers

1. Alessi B., Macias-Montero M, Maddi C., Maguire P., Svrcek V., Mariotti D. - Bridging energy bands to the crystalline and amorphous states of Si QDs - *Faraday Discussions*, 222 - (2020)

2. Mcglynn R., Chakrabarti S., Alessi B., Hussein S.M., Maguire P., - Plasma-induced non-equilibrium electrochemistry synthesis of nanoparticles for solar thermal energy harvesting – *Solar Energy*, 203 - (2020)

3. Bürkle M., Lozac'h M., McDonald C., Macias-Montero M., Alessi B., Mariotti D., Švrček V. - Tuning the Bandgap Character of Quantum-Confined Si–Sn Alloyed Nanocrystals – *Advanced Functional Materials*, 1907210 - (2020)

4. Chakrabarti S., Carolan D., Alessi B., Maguire P., Svrcek V., Mariotti D. - Microplasma-synthesized ultra-small NiO nanocrystals, a ubiquitous hole transport material - *Nanoscale Advances*, 1(12) – (2019)

5. Gasparotto A., Maccato C., Carraro G., Sada C., Štangar U.L., Alessi B., Rocks C., Mariotti D., La Porta A., Altantzis T., Barreca D. - Surface Functionalization of Grown-on-Tip ZnO Nanopyramids: From Fabrication to Light-Triggered Applications - *ACS Applied Materials and Interfaces*, 11(17) – (2019)

6. Barreca D., Gri F., Gasparotto A., Carraro G., Bigiani L., Altantzis T., Žener B., Štangar U.L., Alessi B., Padmanaban D.B., Mariotti D., Maccato C. - Multi-functional MnO2 nanomaterials for photo-activated applications by a plasma-assisted fabrication route – *Nanoscale*, 11(1) – (2019)

B. Presentations at conference

1. Alessi B., Ul Haq A., Padmanaban D.B., Maguire P., Mariotti D. - Ultra-small metallic nanocrystals synthesis from solid wire precursors via an atmospheric pressure microplasma – Oral presentation at *Material Research Society Fall 2018 meeting*, Boston (MA), USA

2. Alessi B., Macias-Montero M., Maguire P., Mariotti D. - Crystallization of Silicon and Diamond in an atmospheric pressure microplasma – Poster presentation at *Plasma Processing Science, Gordon Research Conference 2018*, Smithfield (RI), USA

3. Alessi B., Macias-Montero M., Maguire P., Mariotti D. - Crystallization of Silicon and Diamond in an atmospheric pressure microplasma – Oral presentation at *16th UK Technological Plasma Workshop*, Coventry, UK

4. Alessi B., Macias-Montero M., Maguire P., Mariotti D. - Nanodiamonds Formation from Ferrocene Precursor by Atmospheric Pressure Microplasmas – Oral presentation at *Material Research Society Fall 2017 meeting*, Boston (MA), USA

C. Other professional development activities during the PhD

1. Participation at *International school on low temperature plasma physics 2017*, Bad Honnef, Germany

2. Participation at *Gatan Advanced EELS Workshop JEOL GmbH 2017*, Freising, Germany

3. Participation at *SuperSolar Research Methods PV Workshop 2017*, Bangor, UK

4. Participation at *Kelvin Probe Training KP Technologies 2016*, Wick, UK

List of abbreviations

NP	Nanoparticle	ND	Nanodiamond
NC	Nanocrystal	XRD	X-ray diffractometry
QD	Quantum dot	UPS	Ultraviolet Photoemission Spectroscopy
OES	Optical emission spectroscopy	KP	Kelvin Probe
RF	Radio frequency	EBD	Energy band diagram
APP	Atmospheric pressure plasma	EEDF	Electron energy distribution function
TEM	Trasmission electron microscopy	APS	Air photoemission spectroscopy
HRTEM	High resolution TEM	FE	Field emission
FTIR	Fourier Transform Infrared	CCM	Collision-corrected model
XPS	X-ray photoemission spectroscopy	PMT	Photomultiplier tube
EDX	Energy dispersive x-ray spectroscopy	RMS	Root mean square
SEM	Scanning electron microscopy	FFT	Fast fourier transform
UV-VIS	Ultraviolet-Visible-Near infrared	PL	Photoluminescence
sccm	Standard cubic centimetres / minute	CCD	Charge coupled device
sLm	Standard litre / minute	DOS	Density of states
OML	Orbital motion limited	CVD	Chemical vapour deposition
AC/DC	Alternate/Direct current	PE-CVD	Plasma-enhanced CVD
GND	Ground	SAED	Selected area electron diffraction
FCC	Face centered cubic	SPS	Surface photovoltage spectroscopy
FWHM	Full width at half maximum	ATR	Attenuated total reflection
VBM	Valence band maximum	CBM	Conduction band minimum
CPD	Contact potential difference	UHV	Ultra-high vacuum
MFC	Mass flow controller		

Chapter 1 - Introduction

1.1 Background of the thesis

In the past three decades nanoparticles (NPs) have acquired enormous interest in almost all the application fields of materials science including energy production and storage,[1–7] sensors,[8,9] electronics,[10–12] biotechnology and medicine,[13,14] environmental sciences,[15,16] cosmetics,[17] automotive,[18,19] agriculture[20,21] and many others[22] because of the plethora of material properties which can be modified through the control of their size and surface functionalization. The size-dependent properties of NPs such as the modification of light absorption properties, the reduction of melting point, the different thermal and electrical conductivities originate from the dominance of surface properties over the bulk ones[23] and in the case of smaller particles (i.e. within the quantum regime) from the confinement of the electron wavefunction.[24–27] At the same time, NPs are of interest to fundamental sciences as model systems for studying quantum effects at the mesoscale, a transition region between the purely quantum behaviour of atoms and molecules and the macroscopic particles described by classical physics. In addition, various NPs are naturally produced by many cosmological,[28] geological,[28–30] metereological[31,32] and biological[33,34] processes of which they form an important part of their understanding.

A nanoparticle synthesis method must be affordable and permit a good control over the particles size, composition and aggregation, as these qualities determine the unique benefits of NPs. From the fundamental point of view, it is important to have a reliable synthesis process which can ameliorate the repeatability of experiments. From the industrial point of view, the production costs associated to the synthesis of NPs must be able to compete with established technologies.

Artificial nanoparticles of metals, dielectrics or semiconductors have been created from all kinds of solids, liquids and gases and in different forms, whether homogeneous, doped, alloyed or core-shell structures. Among all the synthesis methods, gas-phase non-equilibrium plasma methods have distinguished themselves for the synthesis of free-standing small particles (1-100 nm),[11,35,36] nanoparticles which are not embedded or agglomerated, of materials which are somewhat inaccessible with common chemical and physical routes. Magnetron sputtering methods, radio frequency-jets, dielectric barrier discharges, hollow cathode discharges and microplasmas are part of this group and have now developed separately for different distinctive features.[37] All these methods though

rely on the non-equilibrium properties of plasmas. The most important ones are the charging of nanoparticles inside the plasmas that prevents their agglomeration at the synthesis stage and the non-equilibrium chemistry pathways that make them able to produce particles of metastable phases, alloys of immiscible elements in the bulk form, non-stoichiometric compounds and other materials which are thermodynamically demanding to synthesize in the bulk form.[38]

Recently, atmospheric pressure microplasmas have acquired attention for the unique aspects of interest for the synthesis of nanomaterials.[39–43] These plasma sources operate at atmospheric pressure and are confined to a sub-millimetre discharge gap at least in one of the dimensions. High electron density and non-Maxwellian electron energy distribution with pronounced high energy electron tail make these discharges particularly reactive and efficient for the dissociation of molecular species.[43–46] At the same time, microplasma are particularly versatile as permit to tailor the gas temperature by the design of the reactor, thus enabling processing of temperature sensitive materials as well as the possibility to use liquids as part of the discharge.[47–49] The most important advantage of microplasmas for the synthesis of nanoparticles is the typical short residence time of particles in the reactors that limits their in-flight growth, culminating in the synthesis of typically 1 nm to 10 nm nanoparticles. However, it is the combination of all the mentioned features which make them unique for the synthesis of very small non-agglomerated nanoparticles of different materials (metals, semiconductors, oxides) from likewise different precursors (solids, liquids, molecular gases).[41]

While there have been many efforts in recent years for the practical development of reactors and the empirical control of plasma synthesis processes, little attention has been given to their fundamental physics and the relation between plasma physics and the synthesized products. This work is a cross-disciplinary modelling and experimental effort that is intended to bridge the two aspects by studying the relation between plasma parameters, nanoparticle formation and the resulting material properties of nanoparticles. Optical emission spectroscopy (OES) is used as the basic diagnostic to characterize the active plasma species involved in the formation of nanoparticles and estimate plasma parameters as electron density, effective electron temperature and gas temperature in combination with theoretical models of the discharge. The conditions for particle formation are assessed through the evolution of OES spectra and a particle heating model which describes the plasma environment in which particles are formed. Finally, the assessment of the structural, optical and electronic properties of synthesized nanoparticles in the form of colloids or films is performed through advanced techniques

of material science. Particular attention is given to building the energy band diagrams of the synthesized nanomaterials, as they are essential for integrating them in real world devices.

1.2 Research objectives

The research objectives of this study were:

- Develop atmospheric pressure microplasma reactor designs for the gas-phase controlled synthesis of small nanoparticles, from different kinds of precursors;
- Estimate the optoelectronic properties of synthesized nanoparticles and their films, with an emphasis on quantum dots and their size-dependent properties of interest to energy applications;
- Study of the plasma parameters through OES and related models applied to understanding the forming conditions of nanoparticles in atmospheric pressure microplasmas;
- Study of the relationship between forming conditions of nanoparticles in microplasma reactors and the resulting optoelectronic properties of synthesized nanoparticles for process control.

1.3 Structure of the thesis

The thesis is organized in the following order:

Chapter 2: A literature review introduces the fundamental plasma physics and the description of physical quantities used throughout the study, the characterization of unique features of microplasmas of interest to nanoparticle synthesis compared to other particle-forming plasmas along with the description of the most common reactor designs used to the purpose.

Chapter 3: Details of OES experimental procedures along with the models used for the estimation of plasma parameters and the details of a particle heating model developed to understand the forming conditions of nanoparticles in collisional plasmas.

Chapter 4: Experimental chapter on the formation of nanodiamonds from a metal-organic precursor, their material characterization and the application of OES and particle heating models to understand their formation.

Chapter 5: Basic description of energy band diagrams (EBD), their importance for applications and the experimental procedures used to derive each parameter along with the application of these to build the EBDs of two case studies in collaboration with external partners.

Chapter 6: Experimental chapter which first reviews a published collaborative study on the synthesis of Si quantum dots (QDs) in different crystalline phases from a gaseous precursor in the form of colloids, the relative material characterization and the understanding of the relation between particle heating at the synthesis stage and their crystalline structure. Then, a related experimental study on the morphological and optoelectronic properties of Si QDs films, their oxidation behaviour and one example of application in a solar cell design developed by collaborators.

Chapter 7: Experimental proof-of-concept chapter on the formation of QDs of bismuth and antimony from a reactor design that uses pure wires of the parent element as solid precursor, together with preliminary results on the characterization of their structure, composition, optoelectronic properties and formation process.

Chapter 8: Concluding remarks about the present study and future perspectives for further improvement of understanding of microplasmas for nanoparticles synthesis, better reactor designs and experimental practice.

1.4 List of contributions to characterization methods

Collaborators performed part of the experimental work in this thesis, it follows a distinction of the contributions to measurements and analysis per experimental chapter for the characterization methods. In the case that both the author and collaborators contributed to the same measurement or analysis, it will be explicitly mentioned in the text. Also, there are some contribution from collaborators that do not relate to characterization methods, in that case their contribution will be explicitly mentioned in the text.

Technique	**Equipment**	**Operation carried by**	**Analysis carried by**
Chapter 4 - Nanodiamonds			
Transmission electron microscopy	JEOL JEM-2100F	Author	Author
X-ray Photoemission Spectroscopy	Kratos Axis Ultra DLD spectrometer	Collaborator	Author
Raman Spectroscopy	Horiba LabRAM 300	Author	Author
Optical Emission Spectroscopy	Ocean Optics HR4000CG	Author	Author
Chapter 6 – Silicon QDs and their films			
Transmission electron microscopy	JEOL JEM-2100F	Author and Collaborator	Author and Collaborator
Fourier transform infrared spectroscopy	Thermo Scientific Nicolet iS5	Collaborator	Author

Ultraviolet Photoemission Spectroscopy	Thermo Scientific ESCALAB 250 Xi	Collaborator	Collaborator
X-ray photoemission spectroscopy	Thermo Scientific ESCALAB 250 Xi	Collaborator	Author and Collaborator
Ultraviolet - Visible spectrophotometry	Perkin-Elmer 650S	Author	Author
Kelvin Probe, Surface Photovoltage, Air photoemission	KP technologies APS04	Author	Author
Scanning electron microscopy and energy-dispersive x-ray spectroscopy	Hitachi SU5000	Author	Author
Optical Emission Spectroscopy	Ocean Optics HR4000CG	Collaborator	Collaborator
Chapter 7 – Wire precursors			
Transmission electron microscopy	JEOL JEM-2100F	Author	Author
X-ray diffractometry	Bruker AXS D8Discover	Author	Author
X-ray photoemission spectroscopy	Thermo Scientific ESCALAB 250 Xi	Collaborator	Author
Ultraviolet - Visible spectrophotometry	Perkin-Elmer 650S	Author	Author
Ultraviolet – Visible Fluorescence spectroscopy	Agilent Cary Eclipse	Author	Author

Scanning electron microscopy and energy-dispersive x-ray spectroscopy	Hitachi SU5000	Author	Author

Table 1.1 – List of contributions to measurements and analysis of data distinguished per characterization and divided per experimental chapter.

References

1. Sargent, E. Colloidal quantum dot solar cells. *Nat. Photonics* **6**, 133–135 (2012).

2. Conibeer, G. *et al.* Silicon nanostructures for third generation photovoltaic solar cells. *Thin Solid Films* **511**–**512**, 654–662 (2006).

3. Green, M. A. & Pillai, S. Harnessing plasmonics for solar cells. *Nat. Photonics* **6**, 130–132 (2012).

4. Lohse, S. E. & Murphy, C. J. Applications of colloidal inorganic nanoparticles: From medicine to energy. *J. Am. Chem. Soc.* **134**, 15607–15620 (2012).

5. de Aberasturi, D. J., Serrano-Montes, A. B. & Liz-Marzán, L. M. Modern Applications of Plasmonic Nanoparticles: From Energy to Health. *Adv. Opt. Mater.* **3**, 602–617 (2015).

6. Mahian, O., Kianifar, A., Kalogirou, S. A., Pop, I. & Wongwises, S. A review of the applications of nanofluids in solar energy. *Int. J. Heat Mass Transf.* **57**, 582–594 (2013).

7. Yang, X. *et al.* Phase Inversion: A Universal Method to Create High-Performance Porous Electrodes for Nanoparticle-Based Energy Storage Devices. *Adv. Funct. Mater.* **26**, 8427–8434 (2016).

8. Khanna, V. K. Nanoparticle-based sensors. *Def. Sci. J.* **58**, 608–616 (2008).

9. Sriram, M., Zong, K., Vivekchand, S. R. C. & Justin Gooding, J. Single nanoparticle plasmonic sensors. *Sensors (Switzerland)* **15**, 25774–25792 (2015).

10. Matsui, I. Nanoparticles for electronic device applications: A brief review. *J. Chem. Eng. Japan* **38**, 535–546 (2005).

11. Kruis, F. E., Fissan, H. & Peled, A. Synthesis of nanoparticles in the gas phase for electronic, optical and magnetic applications—a review. *J. Aerosol Sci.* **29**, 511–535 (1998).

12. Ko, S. H. Low temperature thermal engineering of nanoparticle ink for flexible electronics applications. *Semicond. Sci. Technol.* **31**, (2016).

13. Salata, O. V. Journal of Nanobiotechnology. *J. Nanobiotechnology* **6**, 1–6 (2004).

14. De, M., Ghosh, P. S. & Rotello, V. M. Applications of nanoparticles in biology. *Adv. Mater.* **20**, 4225–4241 (2008).

15. Liu, W. T. Nanoparticles and their biological and environmental applications. *J. Biosci. Bioeng.* **102**, 1–7 (2006).

16. Obare, S. O. & Meyer, G. J. Nanostructured Materials for Environmental Remediation of Organic Contaminants in Water. *J. Environ. Sci. Heal. Part A-Toxic/Hazardous Subst. Environ. Eng.* **39**, 2549–2582 (2004).

17. Wiechers, J. W. & Musee, N. Engineered inorganic nanoparticles and cosmetics: Facts, issues, knowledge gaps and challenges. *J. Biomed. Nanotechnol.* **6**, 408–431 (2010).

18. Presting, H. & König, U. Future nanotechnology developments for automotive applications. *Mater. Sci. Eng. C* **23**, 737–741 (2003).

19. Garcés, J. M., Moll, D. J., Bicerano, J., Fibiger, R. & McLeod, D. G. Polymeric nanocomposites for automotive applications. *Adv. Mater.* **12**, 1835–1839 (2000).

20. Ditta, A., Arshad, M. & Muhammad, I. Nanotechnology and plant sciences: Nanoparticles and their impact on plants. *Nanotechnol. Plant Sci. Nanoparticles Their Impact Plants* 1–303 (2015).

21. Shojaei, T. R. *et al. Applications of Nanotechnology and Carbon Nanoparticles in Agriculture*. *Synthesis, Technology and Applications of Carbon Nanomaterials* (Elsevier Inc., 2019). doi:10.1016/b978-0-12-815757-2.00011-5.

22. Stark, W. J., Stoessel, P. R., Wohlleben, W. & Hafner, A. Industrial applications of nanoparticles. *Chem. Soc. Rev.* **44**, 5793–5805 (2015).

23. Batista, C. A. S., Larson, R. G. & Kotov, N. A. Nonadditivity of nanoparticle interactions. *Science (80-.).* **350**, (2015).

24. Bera, D., Qian, L., Tseng, T. K. & Holloway, P. H. Quantum dots and their multimodal applications: A review. *Materials (Basel).* **3**, 2260–2345 (2010).

25. Pietryga, J. M. *et al.* Spectroscopic and device aspects of nanocrystal quantum dots. *Chem. Rev.* **116**, 10513–10622 (2016).

26. Beard, M. C. Multiple exciton generation in semiconductor quantum dots. *J. Phys.*

Chem. Lett. **2**, 1282–1288 (2011).

27. Wheeler, D. A. & Zhang, J. Z. Exciton dynamics in semiconductor nanocrystals. *Adv. Mater.* **25**, 2878–2896 (2013).

28. Simakov, S. K. Nano- and micron-sized diamond genesis in nature: An overview. *Geosci. Front.* **9**, 1849–1858 (2018).

29. Hough, R. M. *et al.* Naturally occurring gold nanoparticles and nanoplates. *Geology* **36**, 571–574 (2008).

30. Zhmodik, S. M. *et al.* Nanoparticles of noble metals in the supergene zone. *Geol. Ore Depos.* **54**, 141–154 (2012).

31. Rapp, M. *et al.* Observations of positively charged nanoparticles in the nighttime polar mesosphere. *Geophys. Res. Lett.* **32**, 1–4 (2005).

32. Gottselig, N. *et al.* Elemental Composition of Natural Nanoparticles and Fine Colloids in European Forest Stream Waters and Their Role as Phosphorus Carriers. *Global Biogeochem. Cycles* **31**, 1592–1607 (2017).

33. Stanley, S. Biological nanoparticles and their influence on organisms. *Curr. Opin. Biotechnol.* **28**, 69–74 (2014).

34. Singh, P., Kim, Y. J., Zhang, D. & Yang, D. C. Biological Synthesis of Nanoparticles from Plants and Microorganisms. *Trends Biotechnol.* **34**, 588–599 (2016).

35. Vollath, D. Plasma synthesis of nanopowders. *J. Nanoparticle Res.* **10**, 39–57 (2008).

36. Yves Huttel. *Gas-Phase Synthesis of Nanoparticles Edited by Yves Huttel*. (2017).

37. Belmonte, T., Arnoult, G., Henrion, G. & Gries, T. Nanoscience with non-equilibrium plasmas at atmospheric pressure. *J. Phys. D. Appl. Phys.* **44**, (2011).

38. Kortshagen, U. Nonthermal plasma synthesis of semiconductor nanocrystals. *J. Phys. D. Appl. Phys.* **42**, (2009).

39. Mariotti, D. *et al.* Low-Temperature Atmospheric Pressure Plasma Processes for 'Green' Third Generation Photovoltaics. *Plasma Process. Polym.* **13**, 70–90

(2016).

40. Mariotti, D. & Sankaran, R. M. Perspectives on atmospheric-pressure plasmas for nanofabrication. *J. Phys. D. Appl. Phys.* **44**, (2011).

41. Mariotti, D. & Sankaran, R. M. Microplasmas for nanomaterials synthesis. *J. Phys. D. Appl. Phys.* **43**, (2010).

42. Mariotti, D. & Ostrikov, K. Tailoring microplasma nanofabrication: From nanostructures to nanoarchitectures. *J. Phys. D. Appl. Phys.* **42**, (2009).

43. Bruggeman, P. & Brandenburg, R. Atmospheric pressure discharge filaments and microplasmas: Physics, chemistry and diagnostics. *J. Phys. D. Appl. Phys.* **46**, (2013).

44. Bruggeman, P. J., Iza, F. & Brandenburg, R. Foundations of atmospheric pressure non- equilibrium plasmas. *Plasma Sources Sci. Technol* **26**, (2017).

45. Iza, F. *et al.* Microplasmas: Sources, particle kinetics, and biomedical applications. *Plasma Process. Polym.* **5**, 322–344 (2008).

46. Iza, F., Lee, J. K. & Kong, M. G. Electron kinetics in radio-frequency atmospheric-pressure microplasmas. *Phys. Rev. Lett.* **99**, 2–5 (2007).

47. Bruggeman, P. J. *et al.* Plasma-liquid interactions: A review and roadmap. *Plasma Sources Sci. Technol.* **25**, (2016).

48. Bruggeman, P. J. Plasma Technologies II : Development at Atmospheric Pressure and in/with Liquids. *Int. Sch. Low Temp. Plasma Phys. 2017* 1–47 (2017).

49. Velusamy, T. *et al.* Ultra-small CuO nanoparticles with tailored energy-band diagram synthesized by a hybrid plasma-liquid process. *Plasma Process. Polym.* **14**, 1–8 (2017).

Chapter 2 – Literature review

2.1 Plasma Physics Background

2.1.1 Definition of a plasma

Plasmas are ionized gases whose dynamics are dominated by long-range Coulomb forces and as such show some collective behavior to a certain degree. A plasma can be excited with electric fields (e.g.: figure 2.1), heat or chemical reactions and the resulting electrons, ions, atoms and molecules store energy in the form of kinetic energy or excitation of internal degrees of freedom (electronic excitations, vibrational and rotational excited states).

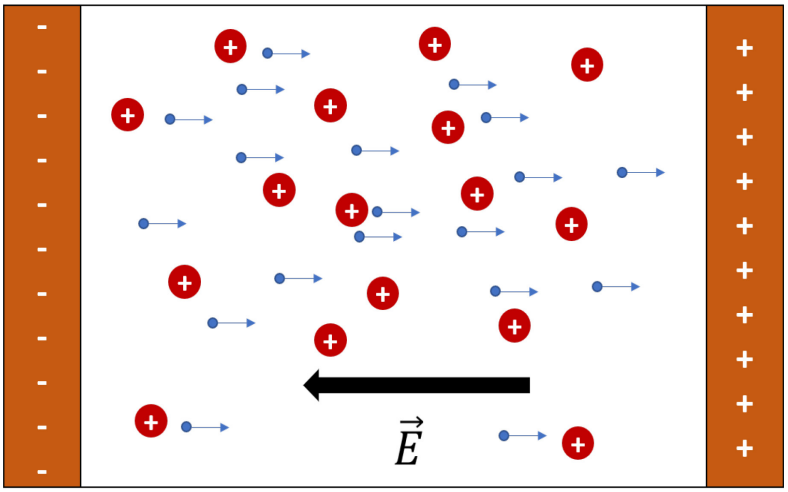

Figure 2.1 - Schematic diagram of a discharge ignited between two parallel plate electrodes, in which the gaseous atoms are ionized. Electrons (blue dots) are lighter in mass (compared to the corresponding ions) and drift because of the applied electric field against a background of almost static positive ions (red disks).

The energy stored in the plasma species can promote different processes in a molecular gas such as the dissociation of molecules or their ionization, the formation of radical species or the heating of particles or else the chemical activation of a surface in contact with the plasma. All these phenomena are of interest to materials science for the treatment of surfaces or for formation of particles and deposition of thin films. Most of the technologically relevant plasmas are also operated in non-equilibrium conditions, where the energy can be channeled into selected species. As such, plasmas are particularly reactive environments that can promote chemical reactions and other physical processes

which are otherwise difficult to achieve with equilibrium methods. The steady state of a plasma is a dynamical equilibrium in which electrons and ions are generated at the same rate as they are lost through recombination events and other loss mechanisms, and the bulk part of the plasma is electrically (quasi-) neutral.

Different types of plasmas are distinguished based on electron and ions temperatures, densities, operational pressure, frequency of applied voltage, and configuration of the electrodes. There is a large variety of plasmas which are of interest to diverse fields (see Figure 2.2),[1,2] from astrophysics to microelectronic industry to medicine and the importance of each configuration for a certain application can be understood from the fundamental physical quantities distinguishing them.

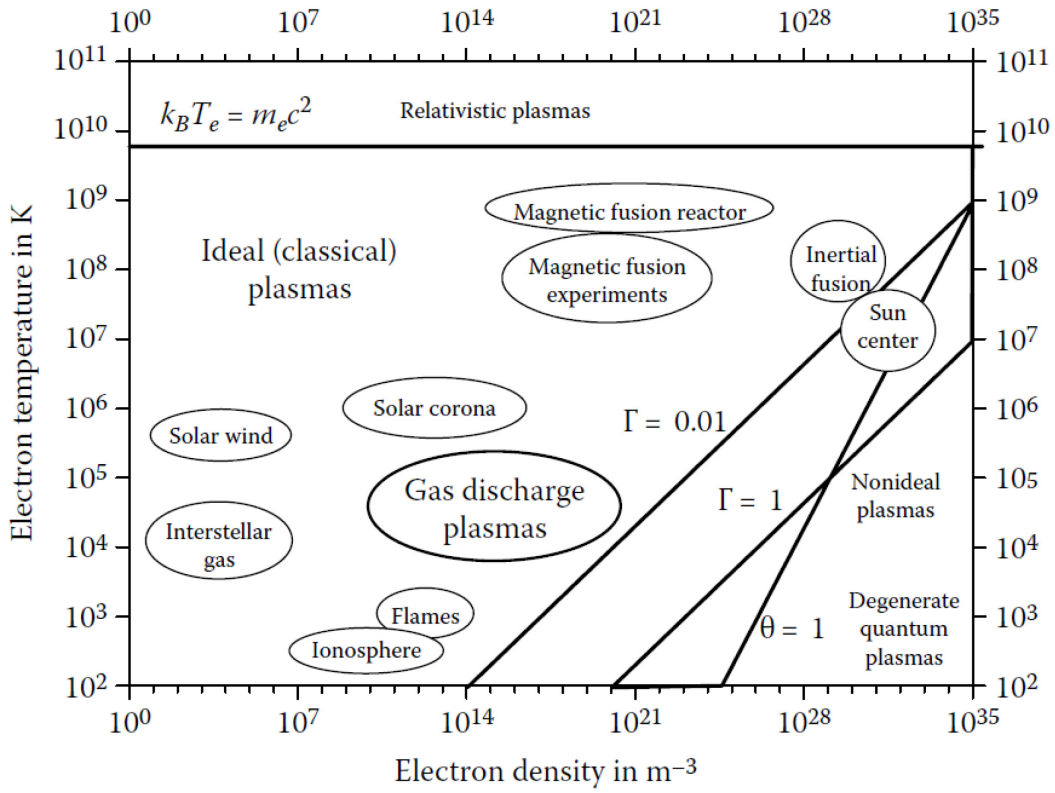

Figure 2.2 - Example diagram showing parameters space for astrophysical and laboratory plasmas, distinguished by different orders of magnitude for electron density and temperature.[2]

2.1.2 Temperatures and energy distribution functions

The way energy is delivered from electrons and ions of a plasma to molecules and materials exposed to the discharge depends on the distribution of energies of each species. At the macroscopic level, this concept is intimately connected to the thermodynamic

definition of temperature: the temperature (T) of a gas in thermal equilibrium with the surroundings is related to the average kinetic energy of a collection of particles undergoing random binary collisions. The particles making up a gas in thermal equilibrium have a certain energy distribution which in the simplest case depends on the distribution of their velocities (kinetic energy). The most probable distribution in equilibrium conditions is called the Maxwellian distribution:

$$f(v) = \left(\frac{m}{2\pi k_B T}\right)^{3/2} e^{\frac{-\frac{1}{2}mv^2}{k_B T}} \qquad \text{Eq. 2.1}$$

where $f(v)dv$ represents the number of particles in a cubic meter with velocity between v and $v+dv$, $1/2mv^2$ is the kinetic energy, m is their mass and k_B is the Boltzmann constant. Averaging over all the distribution of velocities it is found that the average energy of an ideal gas is equal to $\frac{1}{2}(k_B T)$ per degree of freedom.

Obviously this is an ideal case, whereas if particles are charged, an electric field (for example, in one dimension, along the z direction) imposes a drift velocity which shifts the distribution along that direction to higher velocities (Figure 2.3a); also, other mechanisms like heating, ionization loss to the walls are able to depress or enhance the high energy tail of the distribution, i.e. affect the dynamics of species in a certain range of energies (Figure 2.3b).[3]

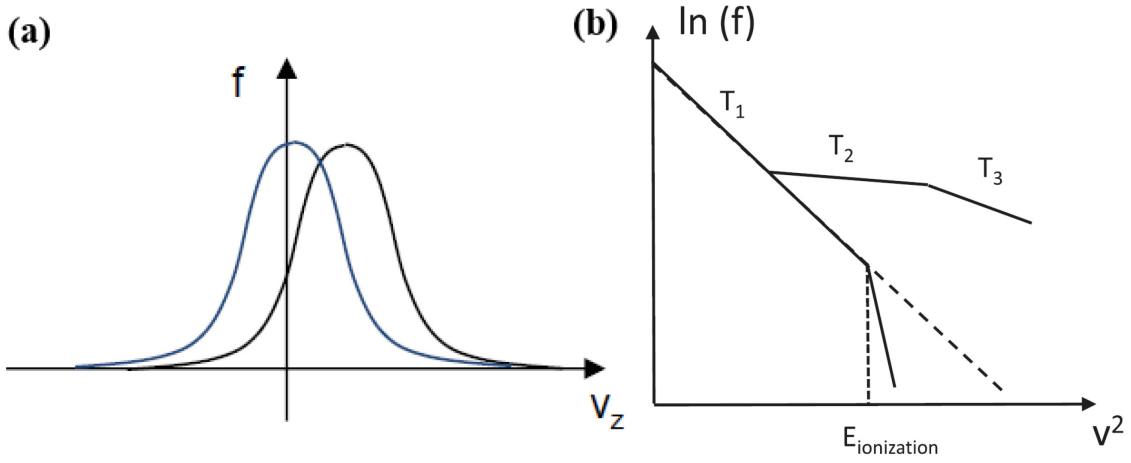

Figure 2.3 - (**a**) 1D Component of Maxwell distribution for a charged species moving along the direction z, unperturbed (blue curve) and when an electric field is applied along the same direction (black curve). (**b**) Deviation of the high energy tail of the Maxwell distribution. In a logarithmic plot against v^2, the distribution function is a straight line with slope proportional to the temperature T_1 (dashed line). A specific heating mechanism may cause a distribution characterized by temperatures T_2 or T_3, while ionization at threshold energy $E_{ionization}$ causes a depletion of electrons at higher energies.[3]

Most of the plasma processes, of interest to materials science, can be described on a first approximation by a two-temperature distribution, for electrons and ions. Collisions among species is the main mechanism that tends to establish equilibrium, exchanging energy between particles and is more efficient whenever the mass of the particles is similar. Given the difference in mass between electrons and ions, the equilibration is generally not efficient, and if there is not any other thermalization mechanism then each electron and ions can be described by a distribution with its own temperature, respectively electron temperature (T_e) and ion temperatiure (T_i). However, ions created by the parent gas atoms have the same masses and if the fraction of ionized atoms (ionization degree) is small, which is the common case for plasmas of interest to materials science, their temperature is the same (gas temperature $T_g \cong T_i$). The pressure at which the plasma is operated affects this non-equilibrium character, in fact at high pressures the frequent collisions with background gas atoms (neutrals) tend to thermalize particle energies and establish thermal equilibrium among them (Figure 2.4).[4]

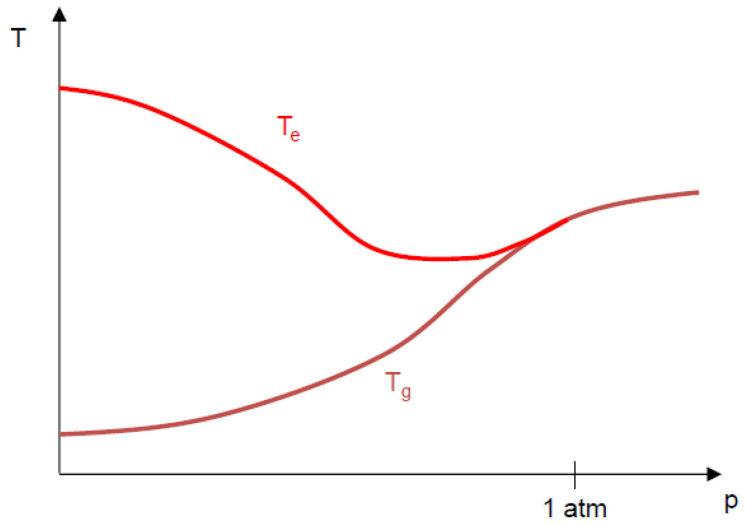

Figure 2.4. Schematic plot of functional dependence of electron temperature (T_e) and gas temperature (T_g) on the pressure of the reactor chamber for a discharge with gap on the order of 1 cm. The two temperatures tend to equalize near atmospheric pressure if there are no other mechanisms that sustains non-equilibrium.

Typically, the temperatures of electrons are in the order of 1 eV to 10 eV and ions one or two orders of magnitude lower. In addition, the energy distribution of electrons has a high energy tail that can span up to 20 eV, which is sufficient to promote further ionization of the gas and the dissociation of molecules interacting with them in the discharge region.[3]

2.1.3 Debye Shielding and sheaths

A major characteristic of plasma is its capability of shielding electric fields. Placing a test charge inside the plasma gives rise to an electrostatic potential Φ_0 and the high diffusivity of electrons makes them able to quickly accumulate or deplete the region around the charge. The space charge created builds an electrostatic field which counteracts the one induced by the test charge, effectively screening the rest of the plasma from it. In this frame, ions can be considered static given their large inertia. The length scale of this screening region is called the Debye Length λ_D and is an important parameter determining the length over which the plasma can be considered electrically *quasi-neutral* and the electric fields, whether external or arising from a local charge concentration, are effectively screened. For a plasma with equal amounts of positive ions and electrons the Debye length reads:

$$\lambda_{\mathrm{D}} = \sqrt{\frac{\varepsilon_0 k_{\mathrm{B}} T_e}{n_e q_e^2}} \qquad \text{Eq. 2.2}$$

where n_e is the electron density, q_e is the elementary charge and ε_0 is the vacuum dielectric permittivity. Effectively, a region of net charge is created around the test charge, called a *sheath*, whose spatial extent increases with electron temperature and decreases with electron density. An analogous argument holds for a conductive wall exposed to the plasma, like the walls of a reactor chamber (figure 2.5). The continuity of fluxes of ions and electrons at the wall's surface imply that a sheath with a higher density of ions will develop (hence of net positive charge, figure 2.5a). The wall's surface exposed to a plasma will be negatively charged and at a more negative potential (Φ_W) than the bulk of the plasma itself (Φ_P) (figure 2.5b).

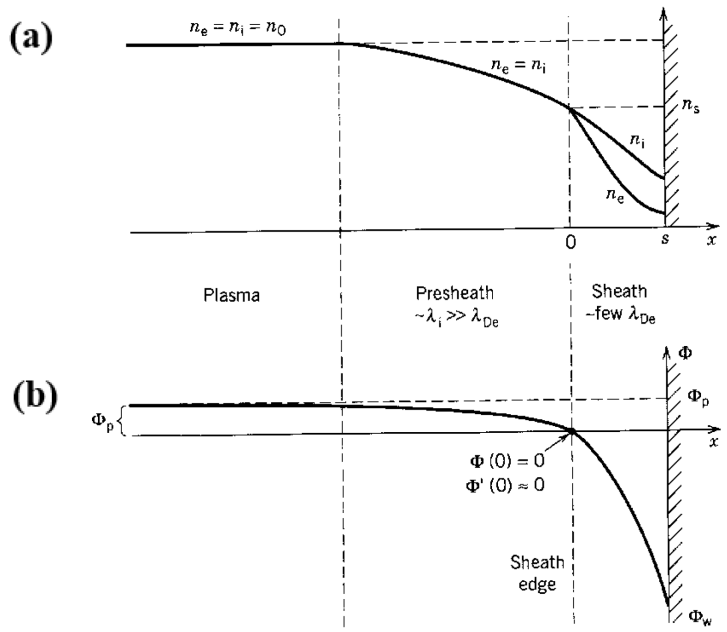

Figure 2.5 - (**a**) Density profile of electrons and ions for a plasma in contact with a conductive wall and (**b**) potential profile. A *pre-sheath* region is created for continuity reasons, a neutral region where still a weak electric field is formed, while the *sheath* is a region with net positive charge extended a few times the Debye length in ideal conditions.[1]

In the absence of collisions, the conservation of ion energy and continuity of flux determine that ions entering the sheath region will be accelerated to the Bohm velocity $u_B = \sqrt{eT_e/M}$ towards the wall, leading to the energetic ion bombardment at the surface.[1] The energetic ion bombardment at a plasma-surface boundary, has been exploited in low-pressure plasmas for sputtering of solid targets and for directional etching in microelectronic industry. At higher pressures the frequent collisions between ions and neutrals limits the velocity of ions at the sheath edge u_s by a factor that depends on the ion mean free path λ_i.[5] The properties of sheaths have been useful also for the development of diagnostic methods. *Langmuir probes* are biased conductive probes inserted into the plasma to attract currents of ions and electrons. The sheath formed at the probes surface is then manipulated through a bias V_B to selectively draw currents of ions or electrons. A typical plot of current-voltage (IV) characteristics of such a probe is shown in Figure 2.6. The *floating potential* Φ_F is the potential at which equal currents of ions and electrons are reaching the probe. For $V_B > \Phi_F$ the flux of electrons to the probe increases exponentially until reaching Φ_P, after which the probe is at the same potential as the bulk of the plasma. At this point the current is only due to electrons and tends to a saturation value (I_e^{sat}). For $V_B < \Phi_F$ the current is mainly from ions and quickly tends to a saturation value (I_i^{sat}). It is then straightforward to extract plasma parameters from the

IV plot: from the ion saturation current density it is possible to extract electron density or the electron temperature and in some cases it is also possible to evaluate ion density and the electron energy distribution function.[1]

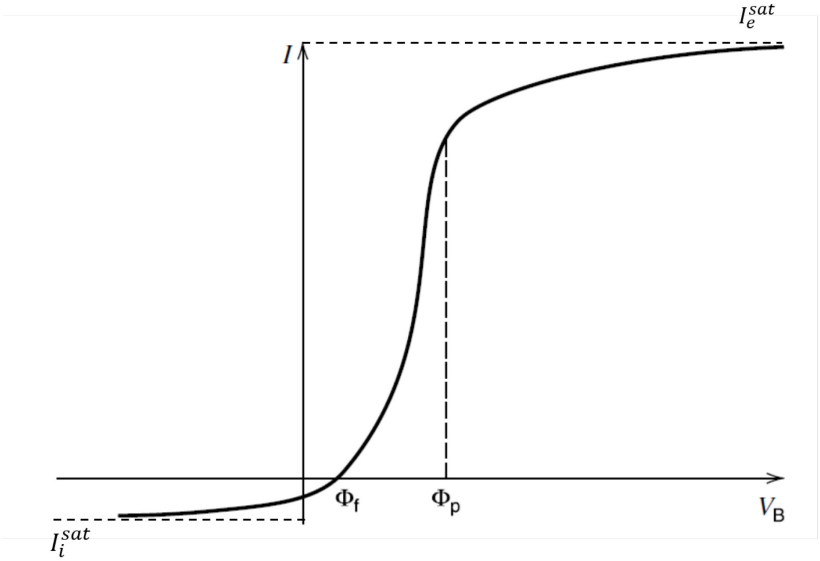

Figure 2.6 - Typical IV curve for a single Langmuir probe and indication of the quantities of interest for the extraction of plasma parameters mentioned in the text.[1]

2.1.5 Paschen law

The breakdown of a gas discharge always starts from the development of electron avalanches, where some randomly produced seeds electrons (from cosmic rays, radioactivity or pre-ionization) gain enough energy in the electric field to directly ionize other atoms of the gas via collisions. When ions, created by the first avalanche and reach the cathode, produce a source of secondary electron emission, the discharge can then be self-sustained (*Townsend breakdown mechanism*). Other mechanisms contributing to a secondary source of electrons can be also thermoionic emission or field emission by the electrodes, however the Townsend breakdown mechanism is valid only when ionization and secondary emission are the dominant sources of ions and electrons respectively. This is the main gas breakdown mechanisms leading to the formation of low density/low pressure discharges. The required voltage (*breakdown voltage*) to obtain a sustained discharge represents a universal scaling law for plasmas and reflects a trade-off between electron generation by avalanches, secondary emission, the loss of electrons due to collisions and the strength of the accelerating electric field. The breakdown voltage by

the Townsend mechanism was found to depend only on the product of the pressure p and the inter-electrode gap distance d and is described by the *Paschen law*:

$$V_b = \frac{B_p pd}{\left\{\ln(A_p pd) - \ln\left[\ln\left(1 + \gamma_{SE}^{-1}\right)\right]\right\}} \qquad \text{Eq. 2.3}$$

where B_p and A_p are gas-dependent constants and γ_{SE} is the secondary electron emission coefficient for the cathode material. The Paschen curves in Figure 2.7 illustrate the dependence of breakdown voltage in function of pd, and have the same shape for different gases: a concave curve with a minimum.[6] This relation shows how pressure and discharge gap should scale in order to reach the same breakdown voltage for different experimental conditions. For instance, by increasing the gas pressure the discharge gap must be reduced accordingly in order to reach the same breakdown conditions. In fact, typically, plasmas operated at atmospheric pressure have short discharge gaps (<1 cm). The product pd is also an indirect measure of the collisionality of the plasma in respect to its physical size, as the pressure p is inversely proportional to atoms mean free path. However, the Paschen law fails to describe the breakdown voltage for high pressures and large gap distances or at very low pressure where large electron avalanches cannot form due to insufficient gas density.[7]

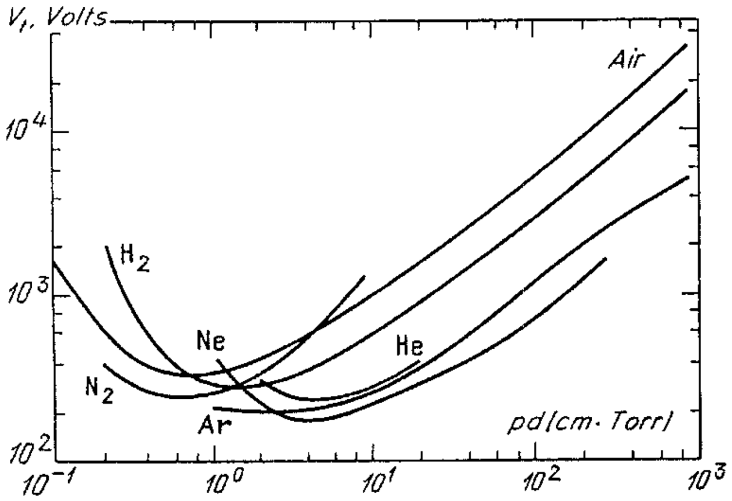

Figure 2.7 - Paschen curves for common discharge gases, showing the variation of breakdown voltage (ordinates) in function of pd (abscissas) for the Townsend breakdown mechanism.[6]

2.1.6 Plasma Chemistry

Plasmas are chemically active environments composed of highly reactive components and non-equilibrium conditions, especially when molecular gases are present. There is a large concentration of charged species as electrons and ions, excited atoms, radicals, clusters, molecules and high energy photons. Because of the non-equilibrium environment, these concentrations can easily exceed the equilibrium ones by orders of magnitude and the kinetics of chemical reaction can be profoundly affected.[8]

Electrons are the first species to acquire energy from the field in a plasma and the primary source of energy for all the other species through "secondary" mechanisms like excitation, ionization and dissociation of atoms and molecules. Their effect can be characterized by their number density, temperature and distribution in energy. Table 2.1 contains a brief description of the most common processes involving electrons in a plasma.

Direct and stepwise ionization by impact	$e^- + A \rightarrow e^- + e^- + A^+$	Electrons with energy higher than the ionization potential of an atom (or molecule) can knock out a valence electron from it, either directly or through a series of intermediate excited states
Dissociative molecular ionization by impact	$e^- + AB \rightarrow A + B^+ + e^- + e^-$	When the energy of electrons is much higher than the ionization energy of a molecule, they can drive it to an anti-bonding excited states that results in the dissociation of a molecule
Dissociative recombination	$e^- + AB^+ \rightarrow A + B^*$	Exothermic reaction that dissociate a molecular ion through exciting intermediate anti-bonding states
Three body recombination	$e^- + e^- + A^+ \rightarrow A^* + e^-$	The excess energy of this recombination pathway goes into

		the additional electron kinetic energy
Radiative recombination	$e^- + A^+ \rightarrow A + hv$	Recombination with the emission of photon
Three body electron attachment	$e^- + A + B \rightarrow A^- + B$	Reactions favorable at high pressure for low energy electrons
Dissociative electron attachment	$e^- + AB \rightarrow A + B^-$	Reactions happening through an intermediate anti-bonding states, favorable when products have positive electron affinities
Impact detachment	$e^- + A^- \rightarrow A + e^- + e^-$	An electron is detached from a negative ion by the impact of another electron, important for high ionization degree
Vibrational, rotational and electronic excitation	$e^- + AB \rightarrow AB^* + e^-$	Excitation of electronic, vibrational and rotational excited states of molecules from impact with electrons

Table 2.1 - Description of the most common processes induced by electrons with ions, radicals and neutrals.[8]

Ions are heavy particles that are important in the kinetics of plasma-chemical reactions, either because of the energy they acquire at the sheaths or because they have a strong influence on the activation barriers of chemical reactions [8]. The table 2.2 lists some important reactions involving ions in a plasma.

Elastic collisions	$A^+ + B^+ \rightarrow A^+ + B^+$	Coulomb scattering, efficient when ions have similar masses
Ion Conversion	$A^+ + A + A \rightarrow A_2^+ + A$	Fast formation of molecular ions happening at high pressures
Charge Exchange	$A^+ + B \rightarrow A + B^+$	An electron is transferred at the impact between an ion and a neutral, this process can be resonant and have a very large cross section for atoms of the same mass
Ion Molecular chemical reactions	$AB^+ + C \rightarrow A + CB^+$	Reactions involving the rearrangement of chemical bonds, with the exchange of one or more ions or neutrals
Ion cluster growth	$A^-_n + A^- \rightarrow A^-_{n+1}$	Reactions driven by the thermodynamic advantage of ion-clusters in respect to single ions
Associative detachment	$A^- + B \rightarrow AB + e$	Inverse process of dissociative attachment
Ion Ion recombination	$A^- + B^+ \rightarrow A + B^*$	Transfer of an electron between opposite sign ions, important in low pressure plasmas. Excess

		energy is spent in excited states of one species
Three body recombination	$A^+ + B^- + C \rightarrow A + B + C$	Ion – Ion recombination pathway for moderate and high-pressure discharges

Table 2.1 - Description of the most common processes induced by ions with radicals and neutrals.[8]

Vibrational and electronic excited states of molecules have also an important role, especially for the species with a long lifetime. Metastable states can transfer their energies to other species or lower the activation barriers of certain chemical reactions making them more energy efficient.[8] A notable example in high pressure plasmas is the *Penning ionization*, where an excited gaseous atom can ionize a target molecule whose ionization energy is smaller than energy of the excited state of the projectile. UV photons are also energetic enough to participate to the plasma chemistry via photoionization of neutral species, which serves also as a source of seed electrons.

The rate at which the reactions listed in Table 2.1 and 2.2 happen depend on number density of participating species and the cross-section ($\sigma(v)$) for that particular process. Cross-sections are generally energy dependent functions, so the energy distribution function of each participating species will determine which reactions will be dominant. For example, the cross sections for electronic processes among the different excitation channels with water molecules in a water vapour discharge is show in Figure 2.8. An electron with 1 eV of energy in such discharge would have a larger probability to provoke the vibrational excitation of water molecules, and a smaller probability of promote dissociative attachment. Instead, an electron with 4 eV of energy would provoke in order of probability the electronic excitation, ionization and dissociative attachment, and vibrational excitation of water molecules.

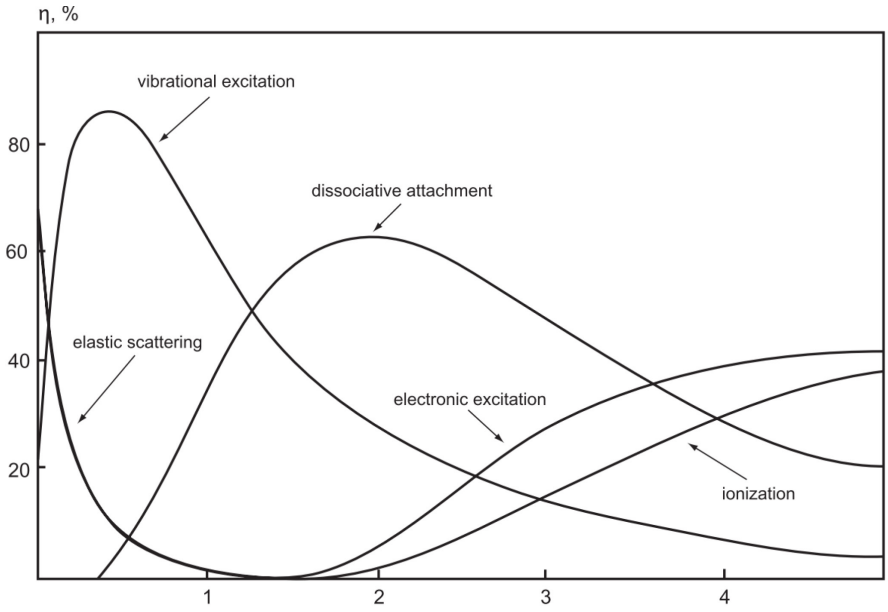

Figure 2.8. Relative cross sections for the different processes induced by electrons with water molecules in a water vapour discharge in function of energy (abscissa).[8]

In practice electrons have a distribution of energies (*f(v)*) in a plasma, hence more than one of the mentioned reactions will happen at the same time, each one at a rate (k_{A+B}) which depends on the integral in equation 2.4.

$$k_{A+B} = \int f(v)\sigma(v)v\,dv \qquad \text{Eq. 2.4}$$

If we imagine drawing the electron energy distribution function in Figure 2.8, then the rate in eq. 2.4 for each process would be proportional to the interception of the areas subtended by the cross section curve (of that particular process considered) and the distribution function curve.

Non-equilibrium discharges with molecular gases have typically average electron energies in the order of ~1 eV, hence the dominant reactions induced by electrons are excitation of molecular vibrational degrees of freedom and dissociative attachment, while electronic excitation and ionization generally happen from few high energy electrons (high energy tail of the distribution).

2.1.7 Plasma-surface interactions

Interactions of plasmas with the surfaces of materials is an important matter technologically. Most of the discharges of interest to science and industry are bound to reactor's walls and usually their influence on the plasma dynamics is determinant. At the same time plasmas can be used as deposition tools, as in plasma-enhanced chemical vapor deposition processes (PE-CVD) and understanding the plasma-surface interactions is vital for the quality of deposited thin films. Also, as happens in magnetron sputtering techniques or plasma-based etching techniques for microelectronic industry, these phenomena are the fundamental mechanisms behind the techniques. Surfaces are subject to modifications when in contact with a plasma, depending on the fluxes of neutrals, atoms, radicals, electrons, ions and photons. The specific path in which they are modified depends on the energy of the incoming projectiles as well as the temperature and chemical composition of the surface.

In general, high energy interactions (> 1 keV) are of interest to low-pressure plasmas, where the charged species can be accelerated by an external bias. Heavy charged species incoming on the surface can be accelerated to have energies up to tens of keV and if their mass is comparable or bigger than the material's individual atoms, they can enter a surface and lose energy within the material. Instead, lighter ones (in respect to target atoms) are more likely to backscatter from the surface. In the keV range, which is of interest for low-pressure plasma deposition processes, heavy species accelerated on the surface will mostly lose energy via nuclear elastic collisions creating a cascade of damaging events along its trajectory before stopping.[9] Most of these events involve the knocking of atoms, creation of vacancies, interstitials and other effects. Some of the knocked atoms may have enough recoil energy to escape the surface, a phenomenon called *sputtering* (Figure 2.9).

The latter process is used in low pressure plasmas to deposit thin films on a certain material, starting from the ion induced sputtering of a solid substrate.

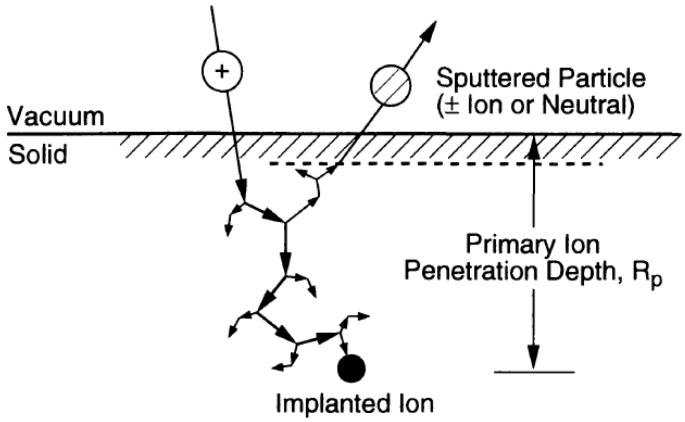

Figure 2.9 - Diagram showing a typical trajectory created by a 10-100 keV ion entering the surface of a material and a sputtered particle exiting the surface.

Lower energy processes (< 100 eV) instead are more important for higher pressure discharges or species with low energy even in low pressure discharges (e.g.: gas atoms in a discharge with T_g=2000 K have an energy of 0.17 eV), where the projectiles have energies lower than the binding energy of the target atoms at the surface. The fate of particles with low energy impinging on a surface will be determined by some elementary processes and the availability of surface sites. For the former reason, also mechanisms which are inherently surface processes (e.g.: surface diffusion) will have an influence (statistically) on the incoming particles, as some specific sites on the surface lattice will be occupied (see figure 2.10).[10]

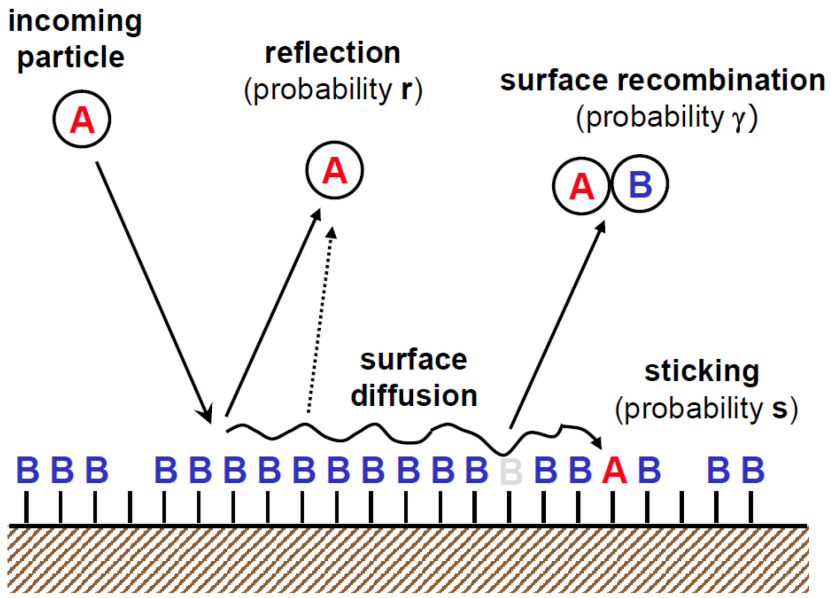

Figure 2.10 - Diagram showing some of the low energy processes happening to a particle impinging on a surface. A and B represent different atoms. Also indicated rates for generalized processes (r, s and γ), overall surface reaction probability (β) depends on the surface coverage of each species, and can be expressed in terms of the mentioned rates as $\beta = s + \gamma = 1 - r$.

A generic classification of involved phenomena can be made:

1) **Reflection (or backscattering)**: Particles may be directly reflected from the surface, especially if their mass is small with respect to individual atoms on the surface, and no kinetic energy is exchanged between them;

2) **Adsorption**: Particles can stick onto the surface by physical attractive forces (van der Waals or electrostatic forces) or by chemical reactions at specific sites (e.g.: surface recombination). The formers being much weaker (binding energies on the order of few meV) than the latter (binding energies on the order of 1 eV);

3) **Surface Diffusion**: Once a particle is adsorbed on a surface, it can diffuse in a temperature-activated motion against potential barriers. Surface corrugations, dangling bonds and other defects are examples of barriers for particles on the surface;

4) **Sticking:** Particles on the surface may have a certain probability to be captured by a potential well on the surface. Potential wells on the surface can be represented by dangling bonds, vacancies or topological inhomogeneities as steps and kinks in the superficial atomic structure. Particles are more likely to stick on the surface if their incoming kinetic energy is small or their mass is comparable to the atoms on the surface, which than permits a large exchange of kinetic energy through elastic collisions. Also, if the potential wells on the surface are deep the probability of sticking is larger;

5) **Desorption**: Particles can desorb from a surface either due to stochastic thermal agitation, surface recombination or chemical reactions whose products are volatile or not bonding with surface atoms.

These mentioned phenomena which are not specific for a particular kind of projectile-target combination are typical of low energy positive charges impinging on a surface, or neutral species (gas atoms, molecules, radicals, excited species) which are not influenced by the sheath and the surface potential. Instead, most of electrons will be mostly reflected by the sheath. Only high energy electrons can surpass the sheath, and have different fate depending on the conductivity of the surface. If the surface is an electrode for example, electron will likely go to the ground, while if it is an insulator they are accumulated as surface charges. In addition, high energy photons can induce ionization or excitation of photosensitive materials.

2.2 Microplasmas for Nanomaterials synthesis

2.2.1 Atmospheric pressure plasmas

Plasmas operated at atmospheric pressure present some clear economic advantages with respect to their low-pressure counterparts, because they do not need expensive vacuum equipment and corresponding maintenance costs are eliminated. Besides, non-equilibrium discharges at atmospheric pressure possess some unique features which are attractive for some applications. In fact, it is possible to maintain a non-equilibrium discharge with gas temperatures down to room temperature. When T_g is kept near room temperature, it becomes possible to treat materials which are not compatible with high temperatures or vacuum conditions (e.g. heat-sensitive materials like polymers, biomaterials or liquids). Moreover, there is the possibility of having a higher density of species than with low pressure discharges which open entirely new possibilities, such as, the condensation of nanoparticles from supersaturated vapors of a gaseous precursor element. However, some of the characterizing features of low-pressure discharges are lost in atmospheric pressure operation, for example the ability to sputter solid materials or to etch anisotropically, or the ability to manipulate charged species via external electric and magnetic fields.

Plasmas can be generated with different frequencies of alternate current (AC) electric fields. The perturbation of a collection of opposite sign charges with an AC field brings charge separation. From charge separation a counteracting electric field arises, which results in a restoring force. We can imagine the situation as an oscillator system driven by the electric field, with each species having a different characteristic eigenfrequency (plasma frequency ω_p) given the different inertia of the charged constituents (ions and electrons). For example, electrons in a collision-less plasma oscillate at the frequency:

$$\omega_p = \left(\frac{ne^2}{\epsilon_0 m} \right)^{1/2} \qquad \text{Eq. 2.5}$$

and a similar relationship exists for ions, except that the bigger mass makes the frequency much lower. Characteristic frequencies are commonly in the kHz for ions and GHz for electrons. An electric field sweeping too fast with respect to the characteristic frequency is not able to induce a net oscillation on the charge, effectively acting as a static DC field.

So that varying the AC field frequency, only certain species can efficiently respond to an alternating electric field and store energy from it. The most used driving frequencies are:

1. **DC and kHz plasmas**: a plasma is generated between two electrodes that drive a conductive current carried by both free ions and electrons. Mostly used for large scale or high-power applications because they can easily form spatially uniform discharges. Varying the frequency can be used to change the heat dissipated through electrodes or surfaces exposed to the plasma discharge.

2. **Radiofrequency (RF)**: the frequency of the applied electric field is in the MHz range and only electrons can respond to it. The current is mostly a displacement current that originates from oscillating electrons and makes it possible to treat insulating surfaces or to use them in front of the electrodes.

3. **Microwave**: frequencies are in the order of a GHz; ions are static, electrons strictly follow electric field oscillations and the plasma is ignited inside a microwave resonator, for better power coupling. It results in particularly high-density localized discharges.

At atmospheric pressure the breakdown happens in nanoseconds (~GHz) and cannot be explained by the Townsend mechanism, as in this timescale ions are static and cannot provoke secondary emission of electrons. However, Ionizing collisions are more frequent (given the higher gas density) and a space charge enhancing the applied electric field is created. This in turns triggers secondary avalanches and the fast formation of a conductive plasma channel called a *streamer,* which then propagates to the electrode. The formation of streamers is conditioned by the charge number density in the initial avalanche (*Meek criterion*), which at atmospheric pressure happens typically at $pd = 1000\ Torr \cdot cm$.

Besides, a plasma process operating at atmospheric pressure deals with other collisional and transport processes that span over 10 orders of magnitude in timescale (Figure 2.11) [4] and changing the frequency of the electric fields has a marked influence on their balance and the dynamics of the discharge. Probably the most important timescale determining the dynamics of plasmas species at atmospheric pressure is the frequency of collisions with neutrals (ν), which is in the order of THz (~10^{12} collisions/s) and have different

influences in the discharge characteristics. At first, the frequent collisions tend to restore thermal equilibrium between ions and electrons. Then, the drift motion of electrons under an applied electric field is influenced by collisions, and the power coupling between field and electrons depend on the ratio ω/ν, where ω is the angular frequency of the applied field. An ideal coupling would have a ratio near unity, hence even in the microwave regime (GHz) this coupling if far for ideal. Another important scaling factor is the ratio between electric field and gas density E/n called reduced electric field. It describes the energy gained by electrons in between collisional events.

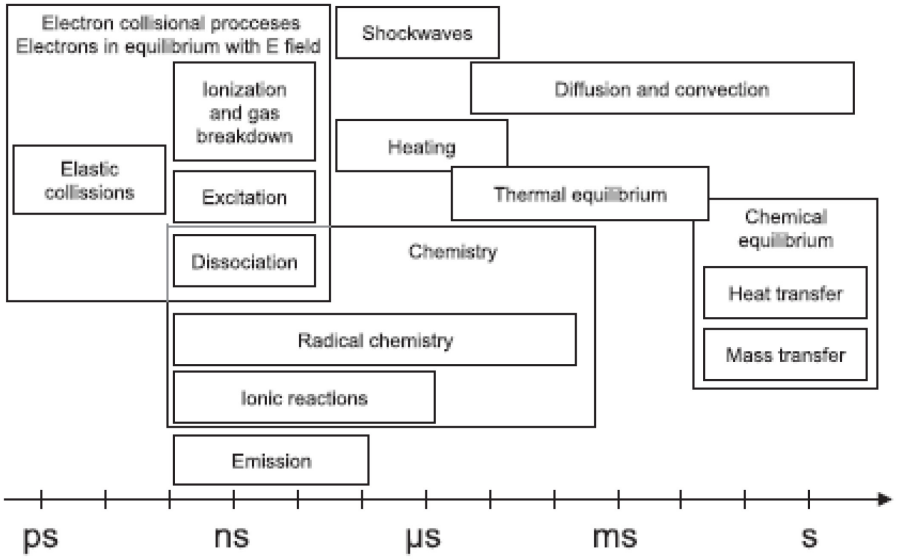

Figure 2.11 - Typical timescales of collisional and transport processes happening in a process plasma at high pressure.[4]

The mentioned breakdown mechanism and the thermalizing collisions with gas atoms often results in thermal instabilities and transitions to filamentary discharges, sparks or leaders.[3,4] Hence, different plasma generation schemes and strategies to prevent the transitions to sparks/arcs and maintain non-equilibrium in a steady state processs have been used;[4,11]

- **Current Limitation**: these are strategies to limit the charge available. A typical generation scheme in the DC case is the glow discharge shown in figure 2.12a. This consists of two bare electrodes facing each other at a fixed distance connected to a high voltage generator. When the breakdown happens, the plasma is low resistivity conductive channel which tend to increase the current in the circuit at a fixed applied voltage. In this case a ballast resistor in series with the high voltage generator limits the discharge current, preventing the formation of arcs and sparks. The dielectric barrier discharge (DBD) in figure 2.12b is based on an analogous concept. This configuration is based on using an insulating material covering at least one of the electrodes. In this case, the power supply must be AC as the only currents that can be sustained through a dielectric are displacement currents. The charge deposited on the dielectric surface limits the local electric fields, hence limiting the current densities when the plasma is formed. Instead the DC corona configuration in figure 2.12c is a self-limiting discharge. This design employs different shape electrodes, commonly a pin and a plane. The asymmetric electrode configuration gives strong electric fields near the pin which fade into lower fields nearer to the plane electrode. In this way, the field strength is enough for breakdown only at the pin and the discharge does not extend to the plane electrode, limiting the conductivity through the gap. However, continuity of current through the circuit is sustained by a flux of positive ions (or negative ions in case of electronegative gases in the reverse polarity) to the plane electrode.

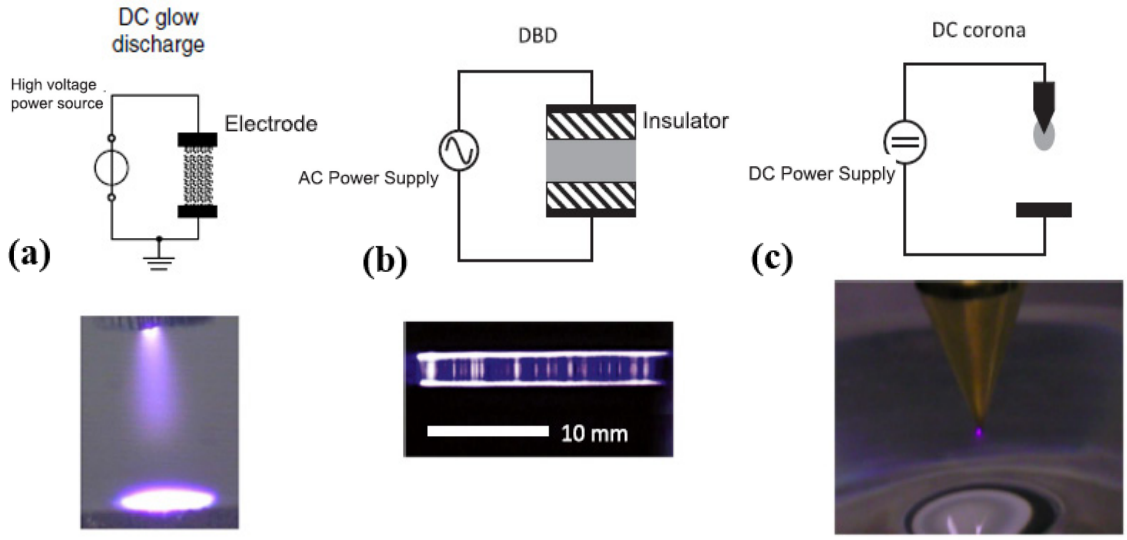

Figure 2.12 - Typical plasma generation schemes that use a current limiting strategy to avoid the formation of arcs/sparks, (**a**) DC glow discharge, (**b**) DBD and (**c**) DC corona. On top schematic diagrams of circuits involved where the black filled shapes are metallic elements, the striped ones insulators and the grey areas represent the formed discharges. At the bottom of each circuit a picture of the discharges in operation. Adapted from [4] and [11].

- **Cooled and gas-flow reactors**: these are strategies to counteract the gas heating which leads to thermal instabilities. In this respect, implementing active cooling of electrodes is a common strategy irrespectively of the plasma generation scheme. However, some design concepts are preventing heating in other ways. For example, the plasma jets (figure 2.13a) are reactors where a continuous gas flow is forced through the plasma, thus removing heat from the plasma zone. This concept can be adapted to all the excitation frequencies and is particularly useful for material science. Instead the gliding arc in figure 2.13b uses a divergent electrode configuration, where a quasi-thermal plasma is ignited in the smallest gap between electrodes and is pushed by a flow of gas or buoyancy to regions of larger separation of the electrodes. The quasi-thermal plasma then becomes non-thermal as the plasma length is increased.

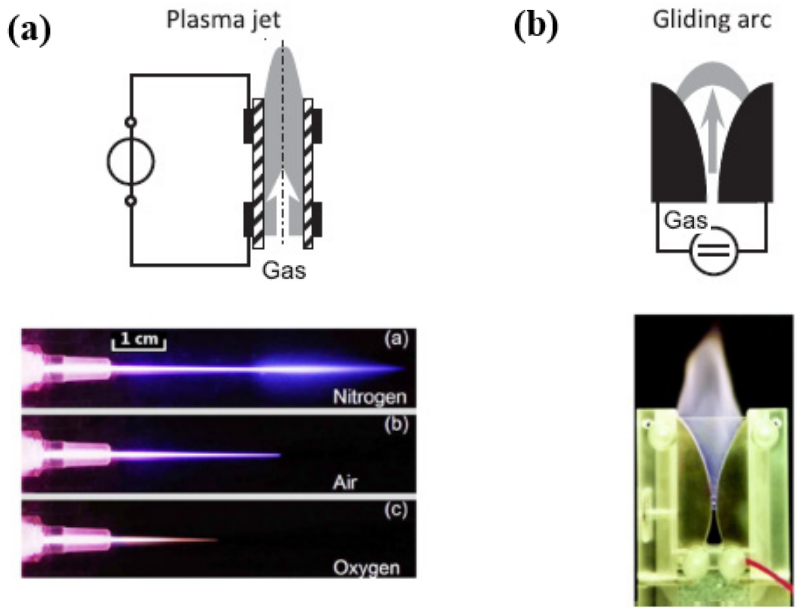

Figure 2.13 - Typical plasma generation schemes that use a flow-through concept to prevent heating of the gas in the plasma region, (**a**) Plasma jets, (**b**) Gliding-arc. On top the schematic diagrams of circuits involved where the black filled shapes are metallic elements, the striped ones insulators, the grey areas represent the formed discharges and the arrows symbolize the directional flow of gas. At the bottom of each circuit a picture of the discharges in operation. Adapted from [4] and [11].

- **Reducing the size**: These strategies are inspired by the *pd* scaling of Paschen law and enhanced heat dissipation through the facing electrode material. In fact, the small gap *d* would imply a lower breakdown voltage and a large surface/volume ratio to prevent heating. For example, the microhollow cathode discharges

(MHCD) in Figure 2.14a is a three electrode configuration, where the plasma ignited in the small d gap is used as a virtual cathode to sustain a bigger gap plasma with a 3rd positively biased electrode. The cathode fall is reduced, and the bigger plasma becomes more stable. Microplasmas are plasmas confined in sub-millimeter spaces and can work with different excitation frequencies as the microplasma array (DC to RF) in figure 2.14b or the microstrip resonator (microwaves) in figure 2.14c. These discharges have naturally low breakdown voltages and offer good heat dissipation through the walls in contact.

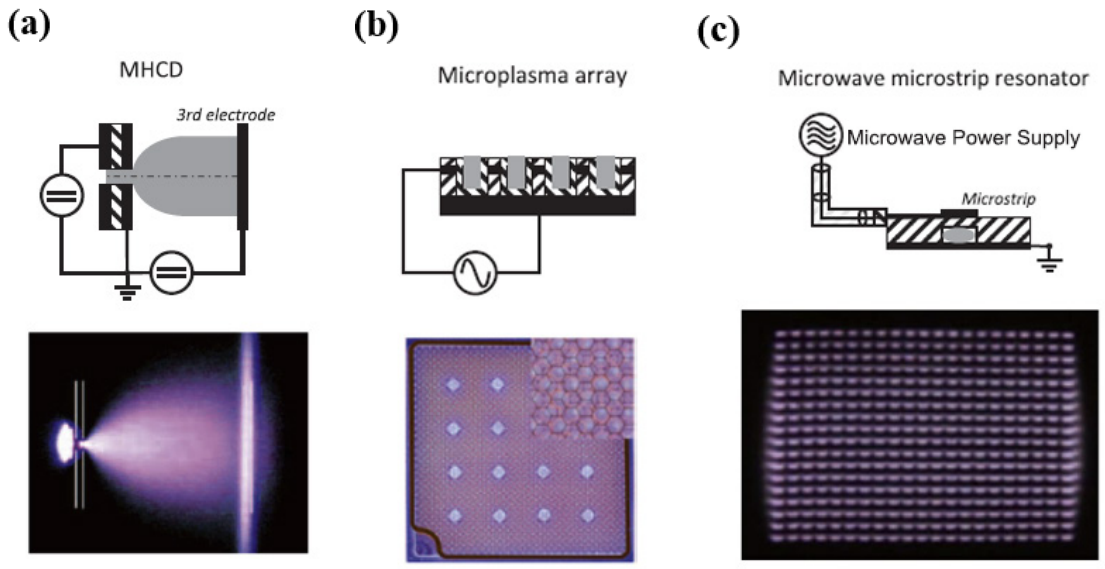

Figure 2.14 - - Typical plasma generation schemes that use a reduction of the discharge gap to prevent heating of the gas in the plasma region and the need og high breakdown voltages, (**a**) microhollow cathode discharge, (**b**) microplasma array and (**c**) microstrip resonator. On top the schematic diagrams of circuits involved where the black filled shapes are metallic elements, the striped ones insulators and the grey areas represent the formed. At the bottom of each circuit a picture of the discharges in operation. Adapted from [4] and [11].

- **Transient operation**: these strategies prevents the thermalization of electrons and ions through limiting the discharge duration (<100 ns @ P_{atm}) for example pulsing the power supply (ns-pulsed discharges).[4,11]

- **Use of pre-ionization and noble gases**: these strategies use gases that tend to breakdown at lower voltage and have high thermal conductivities, thus preventing the development of thermal instabilities. For example, by using He and Ne which are characterized by a high ionization coefficient at low electric field strengths. In alternative some designs use the admixture of gases which preferentially undergo

indirect ionization processes (e.g.: Penning ionization of NH_3 by Ar metastables) which result in lowering the needed breakdown voltage.

2.2.2 Peculiar physics of microplasmas

Microplasmas in flow-through reactor configurations, i.e. plasmas confined to sub-millimeter gaps with gases continuously fed through the discharge region, have shown to possess a great versatility for the synthesis of nanomaterials.[12–15] The flowing gas design in fact permits to modify the residence time of particles within the plasma region, a feature that commonly permits to control particle size. The confined configuration instead enables a controlled steady state non-equilibrium configuration, which until now has been operationally explained as the result of a lower breakdown voltage needed and the high surface to volume ratio. These features, though, derive from different physical phenomena peculiar of these discharges:

1. **Plasma confinement**: Expressing the power losses through collisional events and cooling by reactor walls by a plasma operated at pressure p and confined to a representative physical dimension D (reactor walls), is possible to derive a relashionship between T_e and T_g in function of the p and D. At the steady state it can be written as:[12]

$$p \propto \frac{T_g^{3/2}}{D^2 \varepsilon n_e K_e} \qquad \text{Eq. 2.6}$$

Where ε is the average energy per collisional event and K_e is the rate of such events, and both increase with T_e. The plot in Figure 2.15 shows qualitatively the equilibrium regimes of a plasma as a function of pressure p and D. In the figure, areas corresponding to different equilibrium regimes are identified through curves with different values of T_g and T_e. By varying the operative conditions as gas composition, flow, electrode geometry the curves shift up or down depending if they act increasing or decreasing the gas temperature through the mechanisms mentioned in section 2.2.1. Starting from a point in the non-equilibrium regime at low pressure (grey area in figure 2.15), then if the pressure is increased the point moves up, eventually reaching a thermal equilibrium condition. Conversely, the

diagram shows that at a certain pressure condition (e.g.: P_{atm}), the characteristic dimensions must be shrunk in order to maintain non-equilibrium conditions. This can be inferred also by eq. 2.6 where decreasing D at constant p leads to the decrease in gas temperature or the increase in electron temperature (through ε and K_e). This analysis shows that microplasmas offer a great versatility in controlling T_g and T_e through changing the characteristic size D (which determines the heat losses through the reactor walls), in addition to their other tuning capabilities already mentioned (electrode cooling, pulsing, gas composition, etc.);

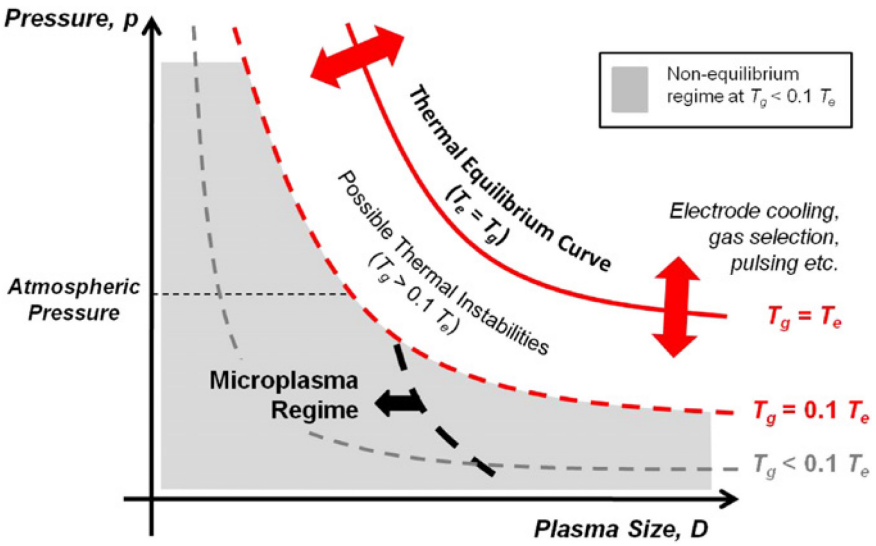

Figure 2.15 - Regimes of plasma equilibrium as a function of pressure p and gap size D, different regions are divided by both solid and dashed lines. The black dashed line represents a transition to the microplasma regime. The effect of additional cooling mechanisms is represented by red arrows expanding or contracting the areas pertaining to different regimes towards higher D and p or lower D and p values respectively.[12]

2. **Deviation from the Paschen law:** It has been demonstrated both theoretically and experimentally that when the interelectrode spacing reaches 10-100 μm distance, the breakdown mechanism (in the DC case) is strongly modified, and the breakdown voltage does not follow the Paschen law (e.g. Figure 2.16).[7,16–18] In fact, when the spacing reaches that this short size the field emission of electrons from the electrode material (tunneling) can become dominant, and strongly reduce the needed breakdown voltage to ignite the discharge. This effect then makes the breakdown voltage also dependent on the electrode material and the presence of impurities and adsorbates of environmental origin. In addition, the field emission effect is also enhanced by the space charge region formed in a sheath, hence it is an enhanced by ions, and the strong dependence on the field suggests also that the

pd scaling is not a universal scaling law as was believed from the Paschen law, instead the breakdown voltage in these conditions would depend on *p* and *d* separately.[7]

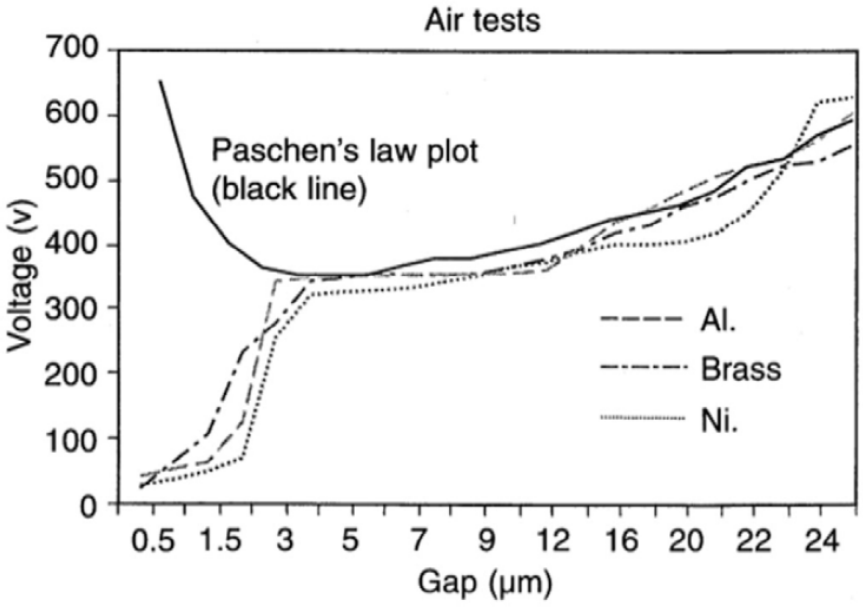

Figure 2.16 - Breakdown voltage as a function of gap size for a microplasma operated in air for different electrode materials. The measured values show a deviation from the Paschen law at low values of the gap.[7]

3. **Different Electron kinetics and electron energy distribution function (EEDF):** when the size of the discharge gap becomes comparable to the Debye length, it is calculated that the quasi-neutral region shrinks in proportion to the point of appearing only dynamically.[19–21] In these conditions the electron energy relaxation length can become comparable or bigger than the size of the confining ambipolar potential. As a result of the different heating, cooling and loss mechanisms in function of electron energy, the EEDF can deviate from the classical distributions used in plasma physics. For example it was found for a RF Helium plasma simulated by Monte Carlo algorithms that with a gap size below 200 μm EEDFs have a three-temperature profile pertaining to three different groups of electrons (Figure 2.17a).[22] The low energy ones are trapped in the potential well during the whole RF cycle and inefficiently heated by the electric field in the bulk (Figure 2.17b). The mid-energy ones are secondary electrons accelerated by the sheath due to the large electric fields at the cathode and do not last the whole RF cycle (Figure 2.17c). The high energy ones are strongly

accelerated by the sheath which lose energy quickly in the bulk (Figure 2.17d). These phenomena also result in the simultaneous increase of electron density and "effective" temperatures. The high energy tail in the EEDF is made of electrons which have energies > 20 eV.[19,22,23]

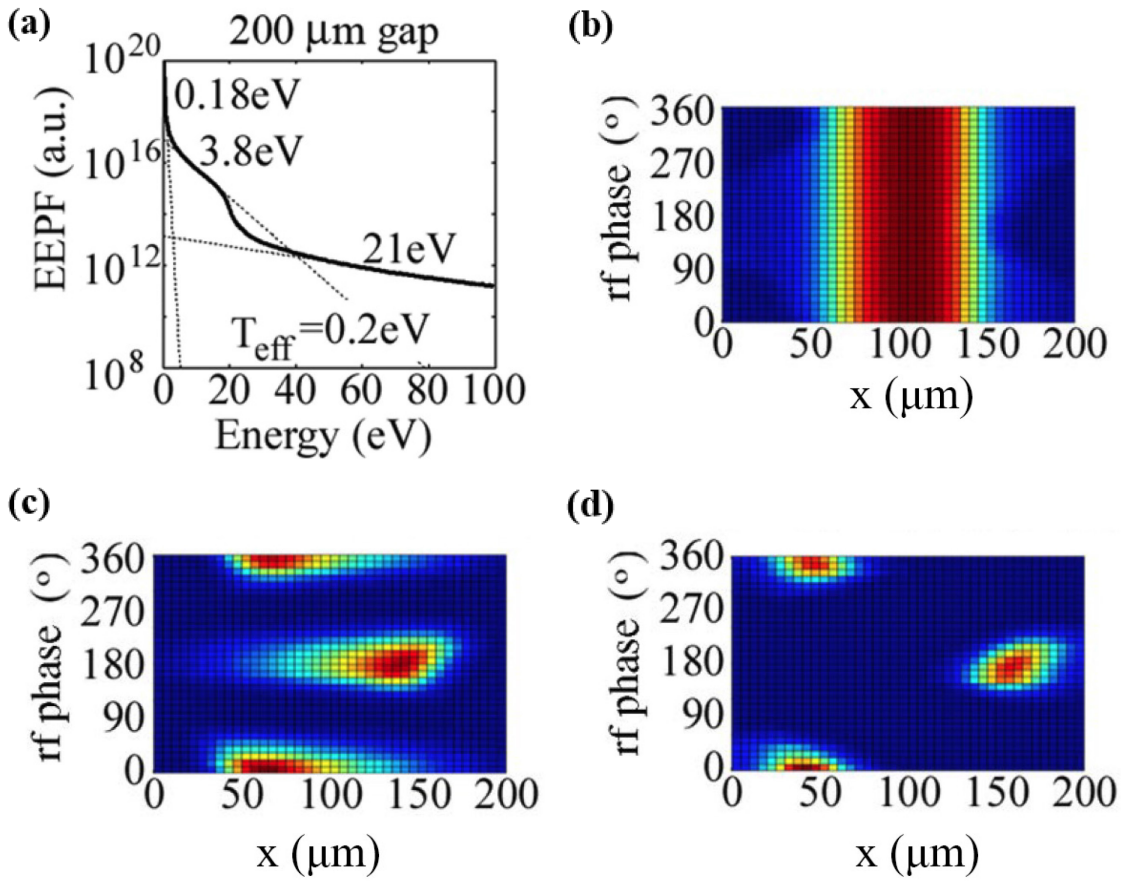

Figure 2.17 - (**a**) Space and time averaged electron energy probability functions of RF Helium discharge simulated with Particle-In-Cell Monte Carlo method for a 200 µm gap. Time evolution of normalized electron density in function of position *x* in the discharge gap (abscissas), distinguished per energy range (**b**) electrons with E< 4 eV (**c**) electrons with 4 eV < E < 20 eV (**d**) electrons with E> 20 eV.[19]

From these peculiar physics derive a lot of distinctive advantages of microplasmas for nanomaterials synthesis. For instance, the low breakdown voltage needed implies that plasma sustainment can be done with a lower power supply (in respect to other discharges), hence making them economically convenient. The presence of a significant population of high energy electrons have enormous implications for the plasma chemistry, because their energy is well beyond most of the molecular dissociation and ionization energies. Hence, molecular gases in microplasmas are efficiently dissociated, and these discharges are consequently populated by chemically reactive ions, radicals and

excited species. The ability to change the residence time of nanoparticles in the plasma and to tune T_g and T_e gives additional control on the plasma processes and material processes happening in the discharge. Microplasmas at atmospheric pressure possess similar characteristics to other atmospheric pressure non-equilibrium discharges from the point of view of ion-induced processes on surface. As already described, the high collisionality prevents the ions to acquire directional momentum from the accelerating field, hence they are not promising for anisotropic etching or sputtering of materials. Instead, microplasmas are more important as high-density discharges with high concentration of ions and radicals at low gas temperature. In respect to the chemical reactions involved, 3-body collisions are more frequent up to 6 orders of magnitude with respect to low pressure plasmas, determining a different chemistry. For example, it is easy to form dimers of ions and molecules in excited states (excimers), which lead to the emission of Vacuum Ultraviolet (VUV) radiation [24]. This VUV sources in conjunction with phosphors is at the basis of plasma displays technology. Also plasmas ignited in air are profoundly affected by the presence of water [25]. Moreover, in section 2.2.2 we saw that they possess an enhanced yield of high energy electrons which makes the discharges particularly reactive. Applications of microplasmas span over different fields, from destruction of volatile organic compounds and decontamination [26,27], surface treatments,[28–30] surface sterilization and biomedical applications,[31] UV sources,[32,33] spectroscopy and detection of trace elements[34] and synthesis and deposition of nanomaterials.[12,13,35,36]

2.2.3 Microplasmas for nanomaterial synthesis

It has been already mentioned that microplasma are particularly convenient for the deposition of nanostructured materials and the synthesis of free-standing nanoparticles. The combination of high density/small volumes and non-specific chemistry are particularly favorable conditions to produce small mono-disperse nanoparticles of different types of materials. In addition, the ability to treat liquids opens also unexplored possibilities for plasma-induced non-equilibrium electrochemistry and the functionalization of nanoparticles.[37,38] Since the first experiments on discharges of molecular gases, the formation of “dust” in the colder regions of low-pressure plasmas has been observed.[39,40] It was generally considered an unwanted effect for the deposition of conformal thin films. Since then, more studies have been done and interest in the

controlled formation of particles in discharges has blossomed both for material processing, fusion plasmas (plasma-walls interaction) and for astronomical plasmas (e.g. comet trails, planetary nebulae, interaction of solar radiation with planetary atmospheres).[41,42] Particles in a discharge region are generally charged by the flux of electrons and ions inside the plasma, and while this can be advantageous in some cases (e.g. for the synthesis of non-aggregated nanoparticles) it can substantially influence the charge distribution and the dynamics of a discharge. They are of particular interest for materials processing, as a controlled bottom-up process to deposit nanostructures would overcome the intrinsic limitations of nanoscale top-down processes.[43] The synthesis of nanoparticles has been studied more in depth in low pressure plasmas, especially to produce silicon nanoparticles from Ar discharges containing gaseous silane (SiH_4). [40,44] A formation mechanism based on the *polymerization/clustering of negative ions* is now the generally accepted theory behind nanoparticle formation in low pressure discharges for various processes.[45–48]

More recently the production of silicon nanoparticles was also demonstrated from argon/silane mixtures at atmospheric pressure,[49–51] using flow-through RF discharges in various electrode configurations,[52] which resulted in smaller particles (1-5 nm) with respect to the analogous process in low-pressure experiments. The formation in this case seems unlikely to proceed via the anion cluster growth, as the ionization degree is expected to be lower at atmospheric pressure. However, a similar polymerization mechanism involving radicals could explain the formation. Some authors claim also that in atmospheric pressure discharges, the gas density can be so high to promote heteromolecular homogenous nucleation from a supersaturated vapour,[50,53] though no strong evidence has yet been presented. This kind of flow-through reactor has been a common design to synthesize aerosols of nanoparticles from gas-phase precursors (Figure 2.18a).[13,54] It has also been demonstrated that microplasma jets are able to deposit thin films and patterned nanostructures (Figure 2.18b),[36,43,55–57] even though the difficulty of having large volume homogeneous discharges at atmospheric pressure poses big constraints to their use for this specific application. Other experiments demonstrated the synthesis of metal, metal oxides and alloys from pure solid precursors (Figure 2.18c),[13,58–62] usually in the form of fine wires acting as an electrode in RF microplasmas. Also in this case the formation mechanism in this case is still unknown, and experimental results from different groups are inconsistent. For example, some studies speculate that a ion bombardment process may be possible if the wire reaches temperatures near the melting

point,[62] while some others demonstrated that a small amount of reactive gases are needed in order to obtain particles.[63,64] Another way to form nanoparticles with atmospheric pressure microplasmas is using liquid precursors (Figure 2.18d),[37,65,66] with one electrode immersed in a conductive solution of precursors and hollow metallic cathode very near to the surface of the liquid in a DC configuration. This technique allows to use liquid chemistry methods to synthesize small nanoparticles and control their surface at the synthesis stage.

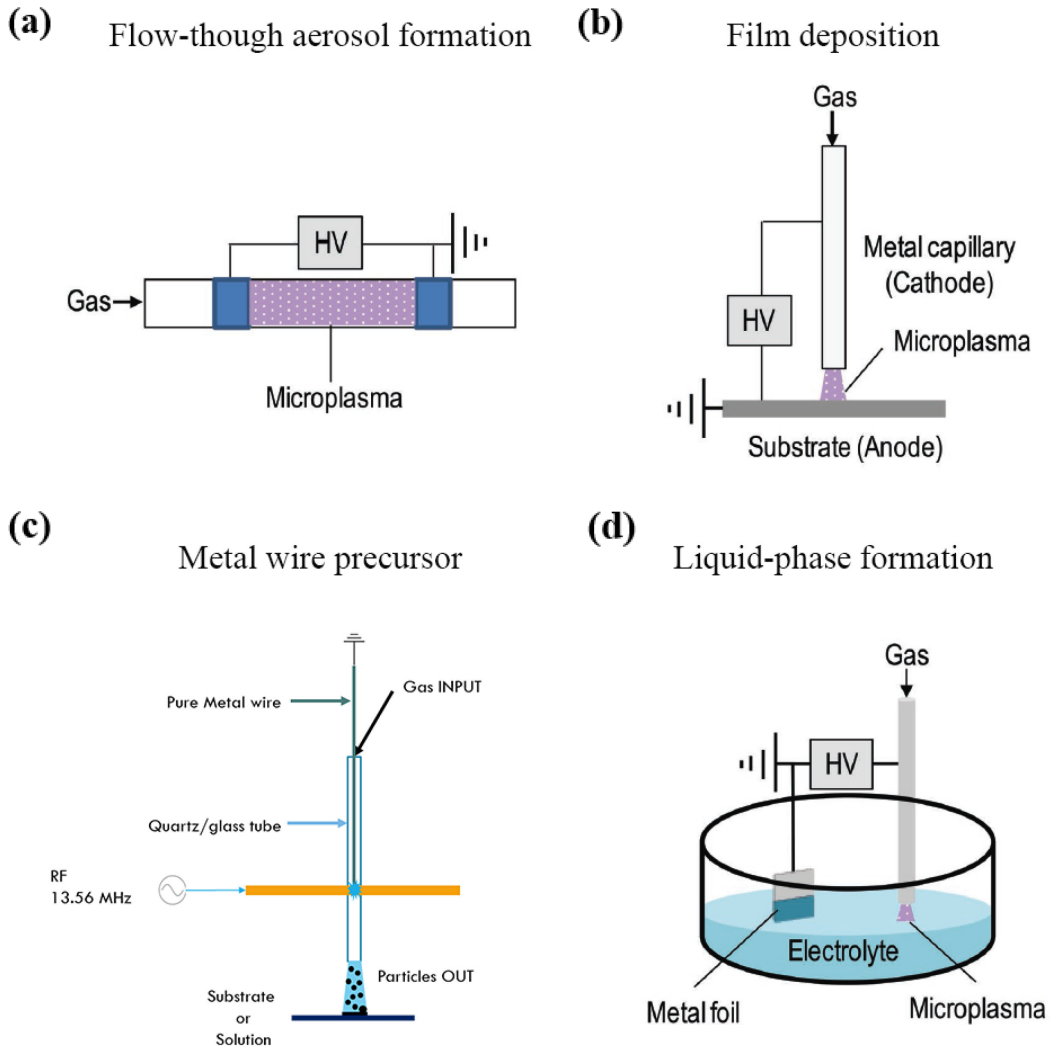

Figure 2.18 - Schematic diagrams of some common microplasma reactor designs for the synthesis of nanomaterial (**a**) flow-through reactor forming aerosols of nanoparticles, (**b**) microplasma jet to deposit nanopatterned films, (**c**) reactor using a solid wire as a precursor, (**d**) microplasma-liquid reactor to synthesize nanoparticles from liquid precursors.[54]

2.2.4 Nanoparticle-related phenomena in the discharge

There are some mechanisms inherently related to the presence of nanoparticles in the discharge which are particularly important to understand the material processes happening inside a plasma. Nanoparticles suspended in a plasma are charged by the flux of charged species flowing onto their surfaces. Depending on the density of particles, their size and the charge accumulated on their surface, they can affect the plasma considerably, by affecting the charge balance in it.[67] For plasma processes of interest to nanoparticle synthesis, the particles are usually diluted with respect to the density of ions or electrons (typically 10^{10} m^{-3}) and small enough not to acquire a conspicuous amount of charge (in the order of 1-10 *e*), hence can be considered electrostatically isolated from themselves and not perturbing the plasma quasi-neutrality. Nevertheless, the charge balance on the surface of nanoparticles also determine the energy exchanges with the plasma species. Calculation of the particle charge can become very complex, especially for atmospheric pressure plasmas, because of all the other collisional phenomena that influence the flux of ions and electrons approaching its surface.[68] The main result is that in this condition nanoparticles usually are negatively charged and are easily trapped in the plasma region far from the walls, that are at a more negative potential than the bulk plasma region. This fact has a big importance for nanoparticle synthesis, because it implies that particles are not lost to the walls of the reactor and do not tend to agglomerate.

It has been observed that particles in non-equilibrium plasmas can undergo some processes which usually happen at higher temperatures than the plasma gas temperature (e.g. the crystallization of amorphous Si nanoparticles [49,69]). Theoretical investigations estimate that the energy balance on the particle surface depends strongly on their charging state, by affecting the rate of heat deposited by recombination processes and on the presence of exothermic surface chemical reactions for the deposition of the excess energy [70,71]. The charging and consequent heating of nanoparticles are important phenomena to be understood for the sake of controlling the properties of synthesized particles. The comprehension of these phenomena is still limited up to date and will be treated in detail in the chapter 2.

2.2.5 Comparison of gas-phase discharges for synthesis of NPs

In figure 2.19a electron density and temperature values are shown for the typical discharges used to synthesize nanoparticles, irrespectively of their thermal equilibrium character.[4,72] Microplasmas operate in conditions of intermediate average electron energies (~1 eV) but high electron densities in respect to low-pressure discharges. At the same time, among the atmospheric pressure discharges (figure 2.19b) they are the only kind of discharges which can reach high electron densities keeping the gas temperatures low, so with a remarkable non-equilibrium character.

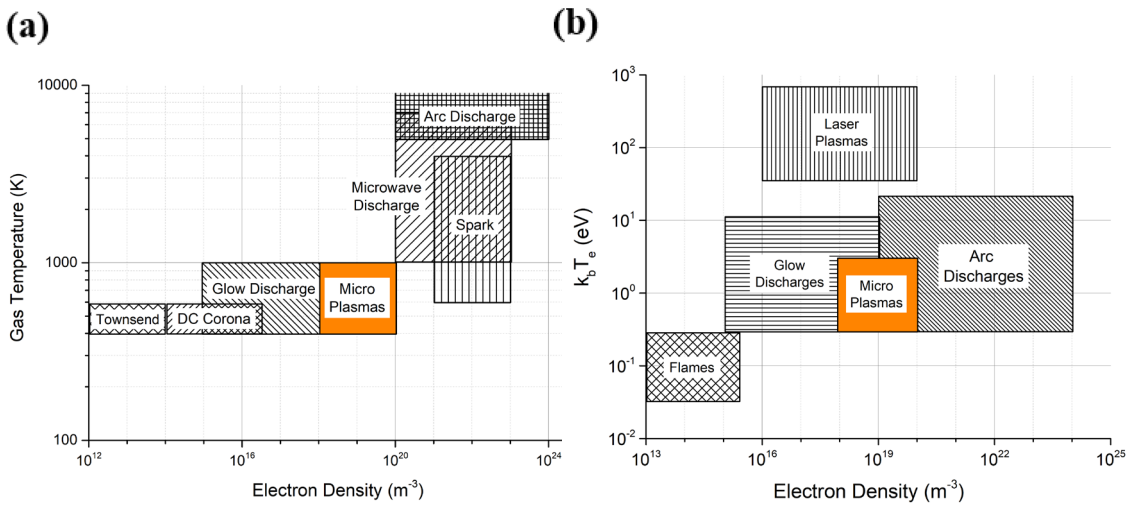

Figure 2.19 - (**a**) Areas in the n_e - T_e parameter space covered by the most common discharges of interest for nanoparticles synthesis and (**b**) common atmospheric pressure discharges distinguished by gas temperature and electron density.

In table 2.2 a list of additional parameters of interest to particle-forming discharges is presented. Looking at the values listed in table 2.2 it is possible to have an idea of the potential of microplasmas for nanoparticle synthesis, in comparison to both thermal discharges, as arc or spark discharges or flames, and non-equilibrium ones at lower pressures, as Glow Discharges at RF or microwave frequencies. The most important disadvantage is the low throughput of the process, given the small volume of the discharge. This is intrinsic of the kind of discharge because a bigger discharge gap at atmospheric pressure would result in thermal discharges. The potential scalability of the process, for example operating multiple discharges in parallel, is still under investigation.[14] However, the latter disadvantages could be overwhelmed by the lower

costs associated to vacuum equipment and supply of power for the same amount of synthesized material.

Symbol	Definition (unit)	Low-P Glow Discharge	Arc Discharge	RF Microplasma
P	Pressure (Pa)	10	10^5	10^5
f	AC frequency (MHz)	13.56	DC	13.56
n_g	Gas density (m^{-3})	10^{15}	10^{19}	10^{19}
d	Gap distance (cm)	10 - 100	> 1	< 0.1
E_i	Ion energy (eV)	10^2 - 10^3	10^2 - 10^3	0.1 - 10
ν	Collision freq. (MHz)	150	10^3	10^3
λ_i	Mean free path (cm)	0.1 - 100	10^{-3} - 10^{-5}	10^{-5}
λ_D	*e* Debye length (μm)	1	0.1 - 1	1 - 10
Q_p	Average charge (*e*)	100 - 500	-	1 - 10
t_p	Residence Time (ms)	10^3 - 10^4	10^3 - 10^4	1
r	NP size (nm)	10 - 100	20 - 1000	1 - 10
δr	NP Size Dispersion (nm)	10 - 50	100 - 200	1 - 5
R_m	Deposition rate (mg/min)	1 - 10^3	1 - 10^3	10^{-3} - 1

Table 2.2 - Typical values of physical quantities of interest for common gas phase discharges used for nanoparticles synthesis.[4]

Given the short residence times in the discharge region, the particles have little chance to grow and have smaller size and size dispersion than what is commonly achievable with

low-pressure discharges, which is an important feature for synthesizing quantum dots. In addition, the unprecedented control capabilities over T_e and T_g together with the unique physical characteristics which have been detailed throughout this chapter, make microplasma more versatile than any other particle-forming discharge. Controlling and tailoring particles properties as size, crystalline phase and composition is of extreme importance for applications. For example, quantum confinement effects on near fermi level electron states are strongly dependent on the physical size of nanoparticles, and affects all the electric, thermal, and optical properties of the synthesized material. Only few cases have been reported of a good degree of control over particles features from plasma parameters. For example, changing nanoparticles size by modifying the total flow of gas through the reactor[73] (thus influencing the residence time in the active region) or acting on the concentrations of precursors and reactive admixtures (e.g. H_2, O_2) in the discharge gas mixture.[50,74] For some systems the control of the crystalline phase can be achieved, as well as the doping and alloying by careful admixture of other precursors[13,59,75] or by changing the power.[73] Nevertheless, a satisfactory knowledge of the interplay between plasma processing parameters and the properties of the final nanoparticles is still lacking and generally dependent on the detailed mechanism of formation, hence very specific for each material to be processed and the properties of the discharge.

2.2.6 Relevant Diagnostics

Knowing the discharge characteristics is important to control the outcome of a plasma process and some established diagnostic methods for low-pressure plasmas have some obvious limitations when applied to atmospheric pressure plasmas. For instance, because of the typical small size of microplasmas, physical probes inserted in the plasma region induce strong perturbations and can no longer be used to directly extract plasma parameters (e.g.: simple Langmuir probes), without technological developments and hard modeling efforts. Hence, in this context, less invasive techniques as with optical probes are more suitable. The complexity of these plasmas though requires particular care for the interpretation of data and a detailed understanding of the models used to extract meaningful quantities. In fact, it is very common to need simplifying assumptions in order to understand the underlying phenomena, simply because in most of the cases there is no

established theory able to grasp the complex aspects of these discharges. In this section, a short review of the most relevant diagnostic techniques for microplasmas will be made.

Optical probes have been the most useful tools for diagnostics of APPs and can be divided in two subgroups:

1. **Passive**: collection of light from emitting species in the plasma, usually the most affordable methods but limited to the analysis of light-emitting species.

2. **Active**: based on laser sources and the relative absorption, fluorescence and scattering induced in the plasma. Better for quantitative analysis but much more complicated and expensive.

Direct imaging with intensified charge-coupled devices (ICCD) is used for monitoring the discharge development and spatial characteristics. Modern ICCDs have gating times of about 100 ps, so with the proper triggering (e.g. synchronized to the voltage cycle) and a suitable spatial resolution (down to 10 μm) can show the inception, the structure and the spatial evolution of discharges. The experimental difficulties here consist in the low intensity of signal at the spatial resolution of interest.

Optical emission spectroscopy (OES) is by far the most applied method, even though for microplasmas the interpretation of data usually requires using extensive modeling. The light emitted from light-emitting species in the plasma is analyzed in intensity and wavelength. The typical spectrum shows different features, which appears at characteristic wavelengths characteristic of each emitting species. The analysis of the spectra yields information on relative content of radiating species, electron density, electron temperature, gas temperature and in few cases the electric field strength within the discharge. OES is the main diagnostic tool used to extract plasma parameters in the present study, so a full chapter (chapter 3) is devolved to the physics principles and the modeling behind this technique.

Laser-induced fluorescence (LIF), *absorption spectroscopy and Raman Spectroscopy* are all techniques that require shining a light source on or through the discharge region. They are all able to excite optical transitions from the ground state of atoms and molecules and

if the line profiles of the transitions are known, they can be used either to identify the species present in the plasma whether they are emitting light or not and quantify their density in absolute values. These techniques can be used to estimate the gas temperatures, concentration of molecules, radicals and metastable densities with a good spatial resolution.[76]

More advance techniques based on similar phenomena are *cavity ring-down spectroscopy (CRS)*, *two-photon absorption LIF (TALIF)* and *coherent anti-stokes raman scattering (CARS)*. CRS measures the time-dependent fluorescence decay of a pulsed or continuous wave laser shone on a plasma source encapsulated in an optical cavity to assess the concentration of trace elements absorbing the laser light,[77,78] pushing the lower limits of detectable densities at the expense of a more complicated setup. TALIF instead is able to have better fluorescence signals from forbidden transitions and avoid using VUV lasers.[78] CARS push the sensitivity of Raman spectroscopy, which is based on spontaneous Raman scattering, by guiding two ns-lasers to produce a coherent IR beam, it is a good technique for spatially resolved species density estimation. In addition, the resulting signal intensity depends on the local electric field strength and the incoming beam intensities, thus enabling to measure the internal electric fields of discharges.[79–81]

Other useful diagnostics are based on light scattering techniques. *Thomson scattering* is the scattering of laser light from free electrons and can give direct information about n_e and T_e, especially for weakly coupled (i.e. low electron density) discharges.[82] Also, the intensity profile is related to the electron velocity distribution function, thus enabling to assess the EEDF of a discharge.[83] Another technique recently introduced for measuring the electron density is *heterodyne interferometry*. It is based on the measurement of the phase shift introduced by an optically thin plasma on a laser beam in an interferometric arrangement. The plasma introduces a change in the refractive index which depends both on heavy particles and electrons and the two contributions can be separated because of different timescales. The advantage of this technique is the good spatial resolution and a general applicability to different type of discharges.[84]

In addition to optical methods, practically all the classical quantitative chemistry methods in the gas phase can still be applied to characterize the gas composition (FT-IR, gas chromatography, residual gas analysis, Schlieren imaging...), as long as they introduce small perturbations to the plasma. Apart from the diagnostics that probe the discharges in situ, some useful techniques have been applied to measure the composition of the

plasma effluent as well as the influence of exposure of surfaces to the electric fields and particle fluxes from the plasma. These methods can give valuable information about the plasma chemistry, the interaction of plasmas with surfaces which is of interest for thin-film deposition or surface treatments and the electrical interaction between plasmas, gas flow and substrates. A particularly important one which has been transferred to atmospheric pressure discharges is *Mass spectroscopy*. It is a technique that can analyze ions, neutrals, metastables and radicals coming from the plasma effluent and can be used to characterize the plasma chemistry upstream from the products collected downstream. Usually species are sampled from a small orifice, ionized, focused, analyzed in energy, sent to charge/mass selectors and finally to ion counters. The selectors manipulate the trajectory of particles either with magnetic fields or with DC and RF-biased electric quadrupoles depending on their charge/mass ratio. With careful calibration it is possible to quantify the amount of species also in a time-resolved manner (~µs resolution). The difficulty of using this technique at high pressure consists in the lower mean free path imposed by collisions, hence, to apply this technique multiple differential pumping stages must be implemented in the setup. The multiple pumping stages and an especially designed sampling stage are important for short-lived species as radicals and metastables, for which the expansion into a molecular beam prevents most of the collisions from happening ("*molecular beam mass spectroscopy*").[85–87]

2.3 Summary

In this chapter the main physical characteristics of atmospheric pressure microplasmas have been introduced, stressing their potential for the synthesis of nanomaterials. The main established advantages of using these plasma sources to the purpose rely on their high reactivity, reduced cost and flexibility in the design of reactors and the precursors that can be used as well as the ability to produce nm-size particles free from aggregation. In addition, the ability to control gas temperature and electron temperature can give unprecedented control over the synthesis process and the synthesized products. The possibility to have low gas temperature at atmospheric pressure makes them also suitable for treating biomaterials, polymers, liquids and other temperature-sensitive materials which could never have been used before. In addition, the collisional yet non-equilibrium character of these discharges opens novel opportunities for in-process control of nanoparticles size, crystallinity, and composition.

Besides, there are some challenges to unleash their full potential, only partially of technical nature. For example, the impossibility of bombarding material directionally with high energy ions is intrinsic to the discharge's nature, an appealing feature that made the success of low-pressure plasmas. The low volume of reactors and the coupling of discharges to the flowing gas put into question the scalability of this technology at industrial levels. In addition, a better understanding of the interactions between the complex processes happening inside the discharge is needed in order to achieve a good control of the process.

References

1. Lieberman, M. A. & Lichtenberg, A. J. *Principles of Plasma Discharges and Materials Processing: Second Edition*. (2005).

2. Meichsner, J., Schmidt, M., Schneider, R. & Wagner, H. *Nonthermal Plasma Chemistry and Physics*. (Taylor & Francis Group, 2013).

3. Von Keudell, A. & Schulz-Von Der Gathen, V. Foundations of low-temperature plasma physics - An introduction. *Plasma Sources Science and Technology* vol. 26 (2017).

4. Bruggeman, P. J., Iza, F. & Brandenburg, R. Foundations of atmospheric pressure non- equilibrium plasmas. *Plasma Sources Sci. Technol* **26**, (2017).

5. Godyak, V. A. & Sternberg, N. Dynamic model of the electrode sheaths in symmetrically driven rf discharges. *Phys. Rev. A* **42**, 2299–2312 (1990).

6. Raizer, Y., Allen, J. & Kisin, V. *Gas Discharge Physics*. (Springer London Limited, 2012).

7. Go, D. B. & Venkattraman, A. Microscale gas breakdown: Ion-enhanced field emission and the modified Paschen's curve. *J. Phys. D. Appl. Phys.* **47**, (2014).

8. Fridman, A. *Plasma Chemistry*. (Cambridge University Press, 2008).

9. Nastasi, M., Mayer, J. & Hirvonen, J. *Ion-solid interactions: fundamentals and applications*. *Materials Research Society Symposium Proceedings* (Cambridge University Press, 1996).

10. Hutchinson, I. H. Principles of Plasma Diagnostics: Second Edition. *Plasma Phys. Control. Fusion* **44**, 2603–2603 (2002).

11. Bruggeman, P. & Brandenburg, R. Atmospheric pressure discharge filaments and microplasmas: Physics, chemistry and diagnostics. *J. Phys. D. Appl. Phys.* **46**, (2013).

12. Mariotti, D. & Sankaran, R. M. Microplasmas for nanomaterials synthesis. *J. Phys. D. Appl. Phys.* **43**, (2010).

13. Chiang, W. H., Richmonds, C. & Sankaran, R. M. Continuous-flow, atmospheric-

pressure microplasmas: A versatile source for metal nanoparticle synthesis in the gas or liquid phase. *Plasma Sources Sci. Technol.* **19**, (2010).

14. Mariotti, D. & Sankaran, R. M. Perspectives on atmospheric-pressure plasmas for nanofabrication. *J. Phys. D. Appl. Phys.* **44**, (2011).

15. Mariotti, D. *et al.* Low-Temperature Atmospheric Pressure Plasma Processes for 'Green' Third Generation Photovoltaics. *Plasma Process. Polym.* **13**, 70–90 (2016).

16. Mariotti, D., McLaughlin, J. A. & Maguire, P. Experimental study of breakdown voltage and effective secondary electron emission coefficient for a micro-plasma device. *Plasma Sources Sci. Technol.* **13**, 207–212 (2004).

17. Loveless, A. M. & Garner, A. L. A universal theory for gas breakdown from microscale to the classical Paschen law. *Phys. Plasmas* **24**, (2017).

18. Garner, A. L., Loveless, A. M., Dahal, J. N. & Venkattraman, A. A Tutorial on Theoretical and Computational Techniques for Gas Breakdown in Microscale Gaps. *IEEE Trans. Plasma Sci.* **48**, 1–17 (2020).

19. Choi, J., Iza, F., Lee, J. K. & Ryu, C. M. Electron and ion kinetics in a DC microplasma at atmospheric pressure. *IEEE Trans. Plasma Sci.* **35**, 1274–1278 (2007).

20. Shi, J. J. & Kong, M. G. Evolution of discharge structure in capacitive radio-frequency atmospheric microplasmas. *Phys. Rev. Lett.* **96**, 1–4 (2006).

21. Wagner, A. J., Mariotti, D., Yurchenko, K. J. & Das, T. K. Experimental study of a planar atmospheric-pressure plasma operating in the microplasma regime. *Phys. Rev. E - Stat. Nonlinear, Soft Matter Phys.* **80**, 1–4 (2009).

22. Iza, F., Lee, J. K. & Kong, M. G. Electron kinetics in radio-frequency atmospheric-pressure microplasmas. *Phys. Rev. Lett.* **99**, 2–5 (2007).

23. Wilson, C. G., Gianchandani, Y. B., Arslanbekov, R. R., Kolobov, V. & Wendt, A. E. Profiling and modeling of dc nitrogen microplasmas. *J. Appl. Phys.* **94**, 2845–2851 (2003).

24. Park, S. J., Herring, C. M., Mironov, A. E., Cho, J. H. & Eden, J. G. 25 W of

average power at 172 nm in the vacuum ultraviolet from flat, efficient lamps driven by interlaced arrays of microcavity plasmas. *APL Photonics* **2**, (2017).

25. Bruggeman, P. *et al.* Electronic quenching of OH(A) by water in atmospheric pressure plasmas and its influence on the gas temperature determination by OH(A-X) emission. *Plasma Sources Sci. Technol.* **19**, (2010).

26. Becker, K. *et al.* Environmental and biological applications of microplasmas. *Plasma Phys. Control. Fusion* **47**, (2005).

27. Becker, K. H., Schoenbach, K. H. & Eden, J. G. Microplasmas and applications. *J. Phys. D. Appl. Phys.* **39**, (2006).

28. Shimizu, K., Fukunaga, H., Tatematsu, S. & Blajan, M. Atmospheric microplasma application for surface modification of biomaterials. *Jpn. J. Appl. Phys.* **51**, (2012).

29. Blajan, M., Umeda, A. & Shimizu, K. Surface treatment of glass by microplasma. *IEEE Trans. Ind. Appl.* **49**, 714–720 (2013).

30. Teli, M. D., Pandit, P. & Samanta, K. K. Application of atmospheric pressure plasma technology on textile. *J. Text. Assoc.* **75**, 422–428 (2015).

31. Shimizu, K., Fukunaga, H. & Blajan, M. Biomedical applications of atmospheric microplasma. *Curr. Appl. Phys.* **14**, S154–S161 (2014).

32. Park, S. J. & Eden, J. G. 13-30 micron diameter microdischarge devices: Atomic ion and molecular emission at above atmospheric pressures. *Appl. Phys. Lett.* **81**, 4127–4129 (2002).

33. Kurunczi, P., Martus, K. E. & Becker, K. Neon excimer emission from pulsed high-pressure microhollow cathode discharge plasmas. *Int. J. Mass Spectrom.* **223**–**224**, 37–43 (2003).

34. Ichiki, T., Koidesawa, T. & Horiike, Y. An atmospheric-pressure microplasma jet source for the optical emission spectroscopic analysis of liquid sample. *Plasma Sources Sci. Technol.* **12**, (2003).

35. Kortshagen, U. Nonthermal plasma synthesis of semiconductor nanocrystals. *J. Phys. D. Appl. Phys.* **42**, (2009).

36. Benedikt, J., Focke, K., Yanguas-Gil, A. & Von Keudell, A. Atmospheric pressure

microplasma jet as a depositing tool. *Appl. Phys. Lett.* **89**, 3–5 (2006).

37. Bruggeman, P. J. *et al.* Plasma-liquid interactions: A review and roadmap. *Plasma Sources Sci. Technol.* **25**, (2016).

38. Velusamy, T., Mitra, S., Macias-Montero, M., Svrcek, V. & Mariotti, D. Varying Surface Chemistries for p-Doped and n-Doped Silicon Nanocrystals and Impact on Photovoltaic Devices. *ACS Appl. Mater. Interfaces* **7**, 28207–28214 (2015).

39. Selwyn, G. S., Singh, J. & Bennett, R. S. Insitu laser diagnostic studies of plasma-generated particulate contamination . *J. Vac. Sci. Technol. A Vacuum, Surfaces, Film.* **7**, 2758–2765 (1989).

40. Bouchoule, A., Plain, A., Boufendi, L., Blondeau, J. P. & Laure, C. Particle generation and behavior in a silane-argon low-pressure discharge under continuous or pulsed radio-frequency excitation. *J. Appl. Phys.* **70**, 1991–2000 (1991).

41. Evans, A. *The Dusty Universe*. (Journal of the British Astronomical Association, 1993).

42. Verheest, F. Plasma Physics and Controlled Fusion Related content Strongly coupled dusty plasmas : crystals , liquids , clusters and waves. *Plasma Phys. Control. Fusion* **41**, (1999).

43. Sankaran, R. M. *Plasma Processing of Nanomaterials*. (2011).

44. Bouchoule, A. & Boufendi, L. Particulate formation and dusty plasma behaviour in argon-silane RF discharge. *Plasma Sources Sci. Technol.* **2**, 204–213 (1993).

45. Hollenstein, C. *et al.* Anionic clusters in dusty hydrocarbon and silane plasmas. *J. Vac. Sci. Technol. A Vacuum, Surfaces, Film.* **14**, 535–539 (1996).

46. Watanabe, Y. *et al.* Contribution of short lifetime radicals to the growth of particles in SiH 4 high frequency discharges and the effects of particles on deposited films . *J. Vac. Sci. Technol. A Vacuum, Surfaces, Film.* **14**, 995–1001 (1996).

47. Watanabe, Y. *et al.* Growth processes of particles in high frequency silane plasmas. *J. Vac. Sci. Technol. A Vacuum, Surfaces, Film.* **14**, 540–545 (1996).

48. Mao, M., Benedikt, J., Consoli, A. & Bogaerts, A. New pathways for nanoparticle

formation in acetylene dusty plasmas: A modelling investigation and comparison with experiments. *J. Phys. D. Appl. Phys.* **41**, (2008).

49. Askari, S., Levchenko, I., Ostrikov, K., Maguire, P. & Mariotti, D. Crystalline Si nanoparticles below crystallization threshold: Effects of collisional heating in non-thermal atmospheric-pressure microplasmas. *Appl. Phys. Lett.* **104**, (2014).

50. Nozaki, T., Sasaki, K., Ogino, T., Asahi, D. & Okazaki, K. Microplasma synthesis of tunable photoluminescent silicon nanocrystals. *Nanotechnology* **18**, (2007).

51. Sankaran, R. M., Holunga, D., Flagan, R. C. & Giapis, K. P. Synthesis of blue luminescent Si nanoparticles using atmospheric-pressure microdischarges. *Nano Lett.* **5**, 537–541 (2005).

52. Barwe, B., Riedel, F., Cibulka, O. E., Pelant, I. & Benedikt, J. Silicon nanoparticle formation depending on the discharge conditions of an atmospheric radio-frequency driven microplasma with argon/silane/hydrogen gases. *J. Phys. D. Appl. Phys.* **48**, (2015).

53. Borra, J. P. Charging of aerosol and nucleation in atmospheric pressure electrical discharges. *Plasma Phys. Control. Fusion* **50**, (2008).

54. Chiang, W. H., Mariotti, D., Sankaran, R. M., Eden, J. G. & Ostrikov, K. Microplasmas for Advanced Materials and Devices. *Adv. Mater.* (2019).

55. Mackie, K. E. *et al.* Microplasmas for direct, substrate-independent deposition of nanostructured metal oxides. *Appl. Phys. Lett.* **109**, (2016).

56. Demaude, A. *et al.* Atmospheric Pressure Plasma Deposition of Hydrophilic/Phobic Patterns and Thin Film Laminates on Any Surface. *Langmuir* **35**, 9677–9683 (2019).

57. Benedikt, J., Raballand, V., Yanguas-Gil, A., Focke, K. & Von Keudell, A. Thin film deposition by means of atmospheric pressure microplasma jet. *Plasma Phys. Control. Fusion* **49**, (2007).

58. Shimizu, Y., Kawaguchi, K., Sasaki, T. & Koshizaki, N. Generation of room-temperature atmospheric H2/Ar microplasma jet driven with pulse-modulated ultrahigh frequency and its application to gold nanoparticle preparation. *Appl. Phys. Lett.* **94**, 2007–2010 (2009).

59. Askari, S. *et al.* Ultra-small photoluminescent silicon-carbide nanocrystals by atmospheric-pressure plasmas. *Nanoscale* **8**, 17141–17149 (2016).

60. Shimizu, Y., Sasaki, T., Chandra Bose, A., Terashima, K. & Koshizaki, N. Development of wire spraying for direct micro-patterning via an atmospheric-pressure UHF inductively coupled microplasma jet. *Surf. Coatings Technol.* **200**, 4251–4256 (2006).

61. Mariotti, D., Lindström, H., Bose, A. C. & Ostrikov, K. Monoclinic β-MoO3 nanosheets produced by atmospheric microplasma: Application to lithium-ion batteries. *Nanotechnology* **19**, (2008).

62. Stauss, S., Imanishi, Y., Miyazoe, H. & Terashima, K. High rate deposition of ZnO thin films by a small-scale inductively coupled argon plasma generated in open air. *J. Phys. D. Appl. Phys.* **43**, (2010).

63. Shimizu, Y. *et al.* Localized deposition of metallic molybdenum particles in ambient air using atmospheric-pressure microplasma. *Dig. Pap. - Microprocess. Nanotechnol. 2007; 20th Int. Microprocess. Nanotechnol. Conf. MNC* **4256**, 174–175 (2007).

64. Shimizu, Y., Koga, K., Sasaki, T. & Koshizaki, N. Dense growth of multiply-twinned star-shaped molybdenum particles by atmospheric H2/Ar microplasma jet. *CrystEngComm* **11**, 1940–1946 (2009).

65. Velusamy, T. *et al.* Ultra-small CuO nanoparticles with tailored energy-band diagram synthesized by a hybrid plasma-liquid process. *Plasma Process. Polym.* **14**, 1–8 (2017).

66. Carolan, D. *et al.* Environmentally friendly nitrogen-doped carbon quantum dots for next generation solar cells. *Sustain. Energy Fuels* (2017).

67. Shukla, P. K. & Mamun, A. A. Introduction to Dusty Plasma Physics. *Plasma Phys. Control. Fusion* **44**, 395–395 (2002).

68. Khrapak, S. A. *et al.* Grain charge in the bulk of gas discharges. *Phys. Rev. E* **72**, 016406 (2005).

69. Kramer, N. J., Aydil, E. S. & Kortshagen, U. R. Requirements for plasma synthesis of nanocrystals at atmospheric pressures. *J. Phys. D. Appl. Phys.* **48**, (2015).

70. Daugherty, J. E. & Graves, D. B. Particulate temperature in radio frequency glow discharges. *J. Vac. Sci. Technol. A Vacuum, Surfaces, Film.* **11**, 1126–1131 (1993).

71. Mangolini, L. & Kortshagen, U. Selective nanoparticle heating: Another form of nonequilibrium in dusty plasmas. *Phys. Rev. E - Stat. Nonlinear, Soft Matter Phys.* **79**, 1–8 (2009).

72. Belmonte, T., Arnoult, G., Henrion, G. & Gries, T. Nanoscience with non-equilibrium plasmas at atmospheric pressure. *J. Phys. D. Appl. Phys.* **44**, (2011).

73. Gresback, R., Holman, Z. & Kortshagen, U. Nonthermal plasma synthesis of size-controlled, monodisperse, freestanding germanium nanocrystals. *Appl. Phys. Lett.* **91**, (2007).

74. Kumar, A. *et al.* Formation of nanodiamonds at near-ambient conditions via microplasma dissociation of ethanol vapour. *Nat. Commun.* **4**, 1–8 (2013).

75. Pi, X. D. & Kortshagen, U. Nonthermal plasma synthesized freestanding silicon-germanium alloy nanocrystals. *Nanotechnology* **20**, (2009).

76. Verreycken, T., Van Der Horst, R. M., Baede, A. H. F. M., Van Veldhuizen, E. M. & Bruggeman, P. J. Time and spatially resolved LIF of OH in a plasma filament in atmospheric pressure HeH 2O. *J. Phys. D. Appl. Phys.* **45**, (2012).

77. Laux, C. O., Spence, T. G., Kruger, C. H. & Zare, R. N. Optical diagnostics of atmospheric pressure air plasmas. *Plasma Sources Sci. Technol.* **12**, 125–138 (2003).

78. Stancu, G. D., Kaddouri, F., Lacoste, D. A. & Laux, C. O. Atmospheric pressure plasma diagnostics by OES, CRDS and TALIF. *J. Phys. D. Appl. Phys.* **43**, (2010).

79. Ito, T. *et al.* Electric field measurement in an atmospheric or higher pressure gas by coherent Raman scattering of nitrogen. *J. Phys. D. Appl. Phys.* **42**, 1–5 (2009).

80. Ochkin, V. N. *et al.* Nonlinear optical techniques for plasma diagnostics. *IEEE Trans. Plasma Sci.* **26**, 1502–1513 (1998).

81. Ito, T., Kobayashi, K., Czarnetzki, U. & Hamaguchi, S. Rapid formation of electric field profiles in repetitively pulsed high-voltage high-pressure nanosecond discharges. *J. Phys. D. Appl. Phys.* **43**, 1–6 (2010).

82. Van Gessel, A. F. H., Carbone, E. A. D., Bruggeman, P. J. & Van Der Mullen, J. J. A. M. Laser scattering on an atmospheric pressure plasma jet: Disentangling Rayleigh, Raman and Thomson scattering. *Plasma Sources Sci. Technol.* **21**, (2012).

83. Muraoka, K. & Kono, A. Laser thomson scattering for low-temperature plasmas. *J. Phys. D. Appl. Phys.* **44**, (2011).

84. Choi, J. Y., Takano, N., Urabe, K. & Tachibana, K. Measurement of electron density in atmospheric pressure small-scale plasmas using CO2-laser heterodyne interferometry. *Plasma Sources Sci. Technol.* **18**, (2009).

85. Benedikt, J., Hecimovic, A., Ellerweg, D. & Von Keudell, A. Quadrupole mass spectrometry of reactive plasmas. *J. Phys. D. Appl. Phys.* **45**, (2012).

86. Ellerweg, D., Benedikt, J., Von Keudell, A., Knake, N. & Schulz-Von Der Gathen, V. Characterization of the effluent of a He/O2 microscale atmospheric pressure plasma jet by quantitative molecular beam mass spectrometry. *New J. Phys.* **12**, (2010).

87. Große-Kreul, S. *et al.* Mass spectrometry of atmospheric pressure plasmas. *Plasma Sources Sci. Technol.* **24**, (2015).

Chapter 3 - Plasma Modeling

3.1 APPs for nanoparticles synthesis

3.1.1 Introduction

In this chapter, models and diagnostic techniques used in the experimental chapters will be introduced. These are developed to describe the plasma conditions and interactions with laden particles inside the active plasma region. In a first instance, the principles of optical emission spectroscopy (OES) applied to atmospheric pressure plasmas will be outline and more in detail the analytical methods to extract key plasma parameters, such as gas temperature (T_g), electron temperature (T_e) and electron density (n_e) for experimental spectra. Secondly a collisional model will be described for calculating nanoparticles' surface potential and surface temperature from OES-derived parameters, in order to establish the basis for process control through all-optical diagnostics. This model will be also useful to understand the material processes happening to nanoparticles in the plasma environment during the synthesis and later stages of the plasma process and justifies some of the advantages of microplasmas for the synthesis of nanoparticles as a result of non-equilibrium and collisional events.

3.1.2 Diagnostics and modeling for process control

Despite the potentialities of microplasmas for nanoparticle synthesis presented in the literature review (Chapter 2), the experimental efforts in this thesis will show that process control is only partially satisfactory. This is due to both the lack of knowledge regarding the plasma physics and chemistry of these complex discharges and the non-suitability of the diagnostic methods established for low-pressure or thermal discharges. Plasma diagnostics can be classified depending on the basic mechanism they exploit, from electrical probes like Faraday cups or Langmuir probes to optical probes like optical emission/absorption spectroscopies or Thompson scattering. These are not readily applicable for atmospheric pressure plasmas confined to sub-millimeter spaces, either because they are physically too invasive or because the charged species in these plasmas are not easily manipulated with external electric and magnetic fields.

Optical emission spectroscopy (OES) stands out in this context, because it is a non-invasive technique which is not affected by the extreme environments found in reactors, such as intense electric and magnetic fields or high temperatures, and where the spatial resolution depends only on the optics and the sensitivity of the spectrometer. As long as spatially resolved information is not necessary, the experimental setup is relatively simple and inexpensive and can be easily adapted for real time in-situ diagnostics. The basic mechanism is to acquire ultraviolet (UV), visible (VIS) and infrared (IR) light emitted from radiating ions, atoms and molecules excited within the discharge. The analysis of the spectra can yield information about plasma parameters, the chemical state and processes happening to species active in a discharge. Despite the simple experimental practice for OES, the interpretation of data is not always straightforward for non-equilibrium discharges. The non-equilibrium character complicates the interpretation of OES spectra because some assumptions on the energetics of exciting electrons are not fulfilled. In addition, a coherent understanding of the thermodynamic conditions of microplasmas at atmospheric pressure has not yet been achieved. The next sections will deal with the characterization of nanoparticles synthesis in microplasmas through the analysis of OES.

3.2 Optical Emission Spectroscopy (OES)

3.2.1 Anatomy of OES spectra for discharges of molecular gases

Spectral features of OES in the visible region for gas-phase discharges of molecular gases arise mostly from the de-excitation of atomic and molecular excited transitions. The peaks positions in wavelengths are unique fingerprints of particular species radiating from inside the plasma, while the spectral line intensities and corresponding broadening are affected by discharge parameters. The two different kinds of spectral features have different characteristics. Figure 3.1 shows a typical OES spectrum for an 80 W Ar plasma with a small admixture of benzene vapor, comprehensive of both type of transitions. The sharp peaks from 680 nm to 960 nm are atomic lines coming from Argon excited states. While the weak broader features between 300 nm and 680 nm are transitions involving molecular species, in part coming from the dissociation of benzene in the discharge (CH-related and C_2 swan bands) and in part from environmental species present as impurities in the gas lines (N_2).

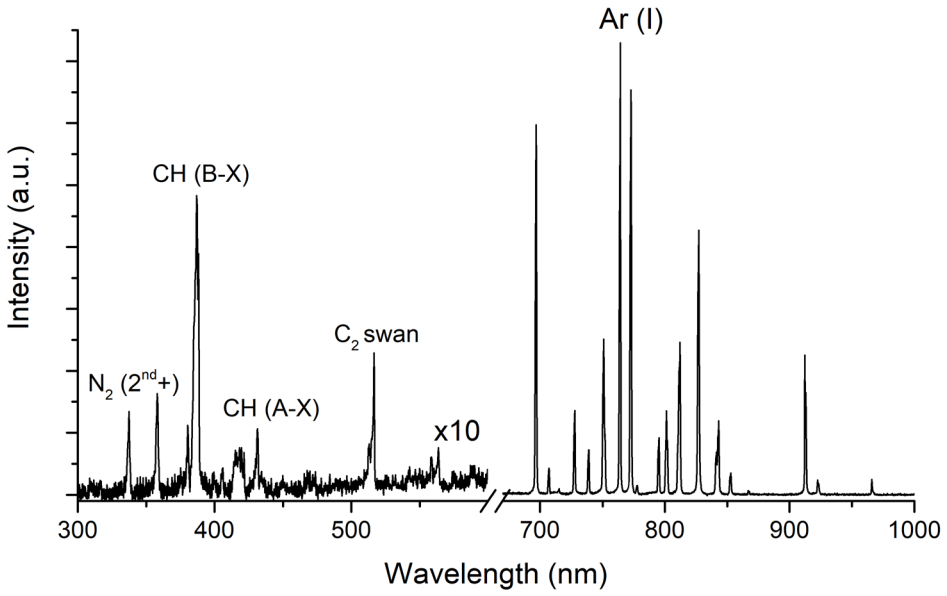

Figure 3.1 – Example of OES spectrum from a 80W (applied power) Ar discharge with a small addition of a benzene (C_6H_6) vapor, showing both emission from atomic species like excited Argon atoms (680 nm to 960 nm) and different molecular excited species (300 nm to 680 nm), some of them come from the dissociation of Benzene (CH and C_2) and others coming from the intermixing of air within the reactor (N_2).

Atomic transitions are transitions between excited levels of an atomic species result in the emission of light. The distribution wavelength of peaks reflects the energy-level structure

of electrons in excited states of atoms, while the distribution of intensities in the different peaks reflect the populations of such levels. These transitions appear as structures of sharp peaks (e.g.: Argon emissions between 680 nm and 960 nm in Figure 3.1), usually spread across a large range wavelength range (in respect to molecular transitions). In figure 3.2, the atomic energy level diagram for helium is depicted, with indication of the corresponding radiative transitions.[1] The transition from energy level E_k to E_i (with $E_k > E_i$) results in the emission of light with wavelength λ_{ki} such that $\lambda_{ki} = \frac{hc}{E_k - E_i}$, where h is the Planck constant and c is the speed of light in vacuum. The allowed transitions among atomic levels satisfy selection rules for which $\Delta L = 0, \pm 1$, $\Delta J = 0, \pm 1$ and $\Delta S = 0$, where L denotes the orbital angular momentum, S the spin and J the total angular momentum of the electron levels involved in the transition ($\Delta L=0$ and $\Delta J=0$ only for non-null angular momenta). Only the allowed optical transitions which lie in the UV, visible and IR range will result in emission of light detectable in the most common OES setups. Moreover, in most cases these transitions are among higher excited levels, as transitions to the ground levels usually lie in the deep UV range.

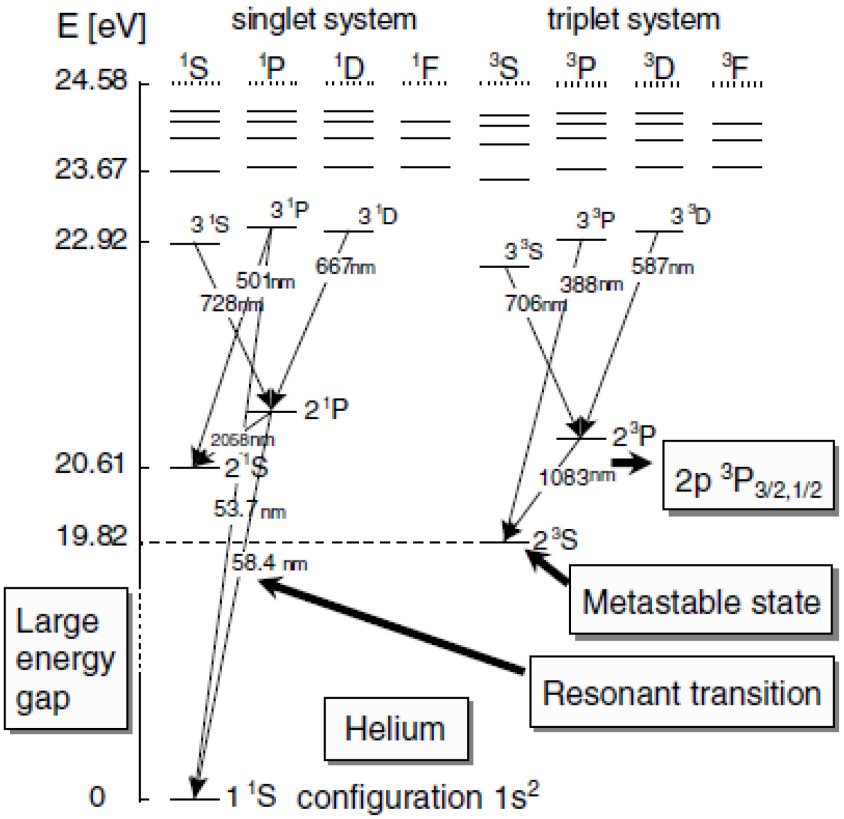

Figure 3.2 – Example of atomic energy level diagram for He. Transitions between states are represented by arrows, and generally follow the dipolar selection rules described in the text. Fine structure is shown for some common lines of interest to He atmospheric pressure plasmas, with indication of the emitted light wavelength.[1]

Molecular transitions are radiative transitions originating from vibrational and rotational levels in excited molecules and their ionic forms. In OES spectra they appear as broader peaks (in respect to atomic transitions) which relate to transitions among vibrational levels (e.g.: region between 300 and 680 nm in Figure 3.1). Each transition among vibrational states has then a closely separated fine structure of peaks due to rotational states of a molecule (an example in Figure 3.5). Molecular orbitals have sublevels which relate to vibrational degrees of freedom (distinguished by the quantum number ν) and each vibrational level has rotational sublevels (distinguished by the quantum number J) of increasingly lower energy (Figure 3.3).[2] Once molecular species are in an excited state, the allowed optical transitions for de-excitation do not have restrictions on the vibrational quantum number between initial and final states, but they are subject to selection rules between rotational sublevels, which are restricted by similar dipole selection rules as in the atomic case (ΔJ=0, ±1). The distribution of intensities among the peaks for vibration and rotational transitions, reflect the relative population of levels. However, while single

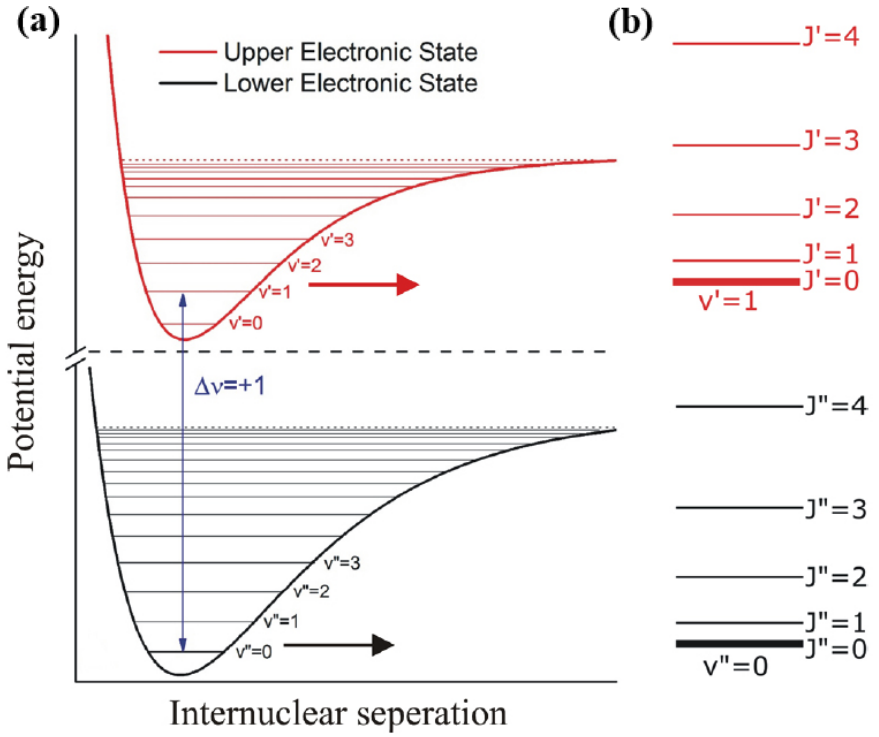

Figure 3.3 – (a) Energy diagram for a diatomic molecule with upper and lower state potential energies for two electronic levels (molecular orbitals), shown plotted against the internuclear separation. The first four vibrational levels distinguished by the quantum number ν for each electronic state are labelled. The blue arrow represents a transition between vibrational states with Δν=+1. (b) An expanded view of the vibrational manifold for the two vibrational levels involved in the transition corresponding to the blue arrow in panel a. The first 4 rotational levels within each respective vibrational manifold are labelled with the quantum number J.[2]

vibrational transitions are easy to observe with common spectrometers, for rotational transitions a good resolution is needed to distinguish single peaks. Nevertheless, a different population in rotational levels will affect the shape of each vibrational transition.

There are other possible features in OES spectra which have different origin, as *free-electrons ions recombination*, *Bremsstrahlung radiation*, and *black body radiation* which produce continuous background features, but are less common for non-thermal atmospheric pressure discharges.

Throughout the experimental work in this thesis, plasma parameters have been evaluated from OES spectra by analysing some of the mentioned spectral features for the different process plasmas. In particular the information extracted are:

- **Identification of species** from the position and structure of peaks measured. In some cases, this analysis can give some hints on the dissociation of precursors, or the evolution of the chemistry within the discharge.

- **Effective electron temperature (T_e)** from the analysis of intensities of selected Argon emission lines. In fact, for some transitions the population of levels is related to the energy distribution of free electrons in the plasma. Hence, an indirect estimation of the effective electron temperature can be obtained.

- **Electron density (n_e)** from the broadening of H_α line. The broadening of such emission line can be related to the electron number density due to the Stark effect. Whenever there is atomic hydrogen identified in the OES spectra, it is possible to extrapolate the electron density by deconvoluting this peak into its different contributions.

- **Gas temperature (T_g)** from intensity distribution of selected molecular transitions. By simulating spectra, the resulting rotational population distribution obtained can be, in some circumstances, approximated to the gas temperature of the discharge.

3.2.2 Effective electron temperature

The plasma electron temperature is a parameter associated to the distribution of energies that free electrons have in the discharge. As described in chapter 2, knowing the number of electrons in a certain energy range is important to understand which processes will be happening to plasma species interacting with electrons and with what efficiency for a given discharge. For example, it will determine which excited states of gaseous atoms will be populated, and in which proportion. Vice versa, by analyzing the emission of excited states of a certain atom, it is possible to retrieve information about the distribution of energy levels of the plasma electrons, through some models which describe the excitation mechanism. The emission intensity of each line from an excited atomic species depends on the statistical population of that particular level. If a Boltzmann-like distribution of excited levels with temperature T is assumed, then the population n_i of each excited level *i* follows equation 3.1:

$$n_i = \frac{g_i}{g_0} e^{-\left(\frac{E_i}{k_b T}\right)} \qquad \text{Eq. 3.1}$$

where g_i and g_0 are the multiplicity of the level *i* and the ground state, E_i is the energy of the level *i*, k_b is the Boltzmann constant and *T* is the temperature associated to the distribution. In some simple cases as thermal discharges, this temperature can be readily identified to the electron temperature of electrons in the plasma.[3] In atmospheric pressure non-equilibrium discharges as microplasmas, collisional processes among heavy species influence the population/depopulation of atomic excited states, hence the population of radiating excited states does not directly reflect the distribution of electrons in the plasma. Furthermore, it is also common for the EEDF in microplasmas to deviate significantly from a MB distribution, hence the electron temperature is not always a well-defined quantity.[4] In this context the parameter extracted from our analysis will be treated as an *effective electron temperature*. Some collisional-radiative (CR) models have been developed in literature in order to relate the temperature associated to the distribution of excited states in eq. 3.1 and the plasma effective electron temperature. These models calculate rate balance equations that relate the concentration of electrons, ions and neutrals and the most important processes populating and depopulating excited levels. The model used for extraction of T_e in this work was developed by *Zhu et al.*[5] for a microwave atmospheric pressure Ar microplasma and considers only processes involving 4p and 5p excited states of Ar atoms and their relative cross sections.

The processes considered are:

1. *Electron impact excitation*
2. *Atomic collisional relaxation*
3. *Stepwise ionization*
4. *Radiative transitions between excited levels*

The result of the calculation is a relationship connecting T and T_e which shows a weak dependence on electron density and gas temperature that reads:

$$T_e = C_0 \, e^{\frac{T}{\beta}} \qquad \text{Eq. 3.2}$$

C_0 and β are scaling constants that have been then fitted to various data points relative to different experiments,[5] and estimated to be $C_0 = 0.03$ eV and $\beta = 0.11$ eV valid for electron densities between 10^{19} m^{-3} and 10^{20} m^{-3} and gas temperatures between room temperature and 800 K. The model mentioned assumes that only electron-atom collisions and atom-atom collisions are the only sources of population/depopulation of the 4p and 5p excited level of Ar neutrals and the radiative processes to the ground state are neglected because of the strong radiation trapping effect. Another assumption made is a Maxwellian EEDF for the calculation of electron impact rates. While this assumption may be particularly inappropriate for an high density microplasma, it is likely to affect more the error on the calculation of the population of the ground state or when the excitation energies span over a wide range of energies.[6] In this case, the ground state effect is neglected and the levels involved are closely spaced in energy, hence the effects of this assumption are neglected. A third assumption of the model, which is likely to have more weight in the calculation of the estimated error, is that the kinetics of excited Ar levels are not affected by the presence of H_2O. It is known that the presence of O_2, CO_2 and H_2O can strongly affect Ar excitation kinetics due to strong energy transfer processes.[7] Even though for most of the plasma processes some specific strategies have been adopted for the removal of water vapour from the chamber, it was not possible to estimate the residual amount of it and the relative errors introduced in the estimation of the effective electron temperature, under these conditions the error introduced is no less than 10 % of the estimated values.[5] Hence, while the absolute values make sense only as an estimation of the order of magnitude, the

calculated values will be meaningful only to show trends with varying experimental parameters, if the relative variation is bigger than 10 %.

The intensity of the final emission I_{ik} is then linked to the population of single excited levels n_i through the Einstein spontaneous emission coefficients A_{ik} and the energy of the photon emitted $h\nu_{ik}$ as:

$$I_{ik} = h\nu_{ik}\, A_{ik}\, n_i \qquad \text{Eq. 3.3}$$

By eq. 3.1 it results an equation relating the intensity of emission lines to the energy of the starting level E_i. By plotting the measurable emission lines pertaining to 4p and 5p levels of Argon and taking the natural logarithm results in a scatter plot (*Boltzmann plot*) whose slope of the best fit is inversely proportional to the distribution temperature in eq. 3.1 (e.g.: figure 3.4).

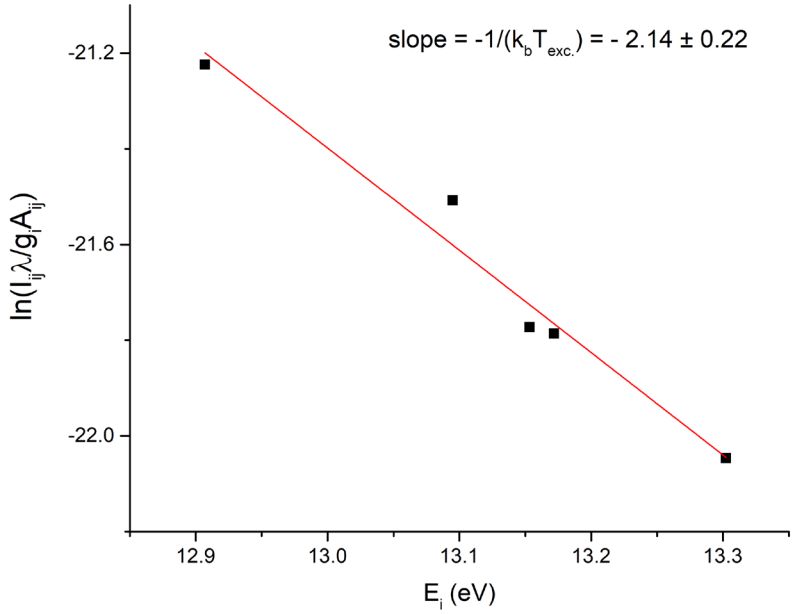

Figure 3.4 - Example of Boltzmann plot used to extract the distribution temperature from the slope of the linear fit. The points are ratios between measured intensities of Ar lines listed in table 3.2 and the intensity of the 750 nm line.

The extrapolated value of T is then converted into an effective electron temperature via the equation 3.2. In table 3.2 the lines used for our studies are listed along with the multiplicity factors, energy of starting levels and the Einstein coefficients.[8]

Wavelength (nm)	g_kA_{ki} (x10^7 s^{-1})	Upper Energy Level E_i (eV)
706.7	1.90	13.302
738.4	4.20	13.302
794.8	5.58	13.283
801.5	4.60	13.095
912.0	5.67	12.907

Table 3.2 – Summary of the lines chosen for calculating T_e and relative coefficients. Columns are in order, wavelength of emitted light, combined Landè factor g and Einstein coefficients A and energy of the starting level.8

3.2.3 Electron density

The width of each emission line in an OES spectrum is determined by different mechanisms which reflect the interaction of radiating excited species with the surrounding plasma environment. It is possible in some conditions to rule out which mechanism is more important and de-convolute a certain peak in the respective components, each one having a certain line shape. The importance of each broadening mechanism depends on the conditions of a plasma in terms of pressure, temperatures, neutrals and electrons density. At atmospheric pressure the most relevant are:

- **Doppler Broadening $\Delta\lambda_D$**: appears due to the thermal motion of the emitting atoms in the plasma. Their velocity relative to the observer frame imposes a spread of the original wavelength λ_0, which is described as a Gaussian distribution (if a Maxwellian distribution of atoms thermal velocity is assumed) whose width increases with T_g and decreases with the mass of the involved atoms. [9]

$$\Delta\lambda_D = 7.126 \cdot 10^{-7}\ \lambda_0 \sqrt{\frac{T_g}{M}} \qquad \text{Eq. 3.4}$$

- **Van der Waals Broadening $\Delta\lambda_W$**: the high collision rate causes the Van der Waals interactions between excited atoms and neutral species to be relevant, so a dipolar interaction between the excited species emitting and the dipole induced on neutral atoms. It results in a broadening of emission lines described by a Lorentzian profile whose full width at half maximum (FWHM) increases with the polarizability α and the number density *N* of the perturbing neutral atoms. It also increases with gas temperature and the difference in the mean square radii of the two species $<R^2>$, while it decreases for larger reduced mass values of the combined emitter-perturber system μ.[10] Alternatively, it can be described in terms of the pressure *P*, using its relationship with *N* and T_g.

$$\Delta\lambda_W = 8.2 \cdot 10^{-12}\ \lambda_0^2\ (\alpha\langle R^2\rangle)^{2/5} \left(\frac{T_g}{\mu}\right)^{3/10} N = 3.6 \cdot \frac{P}{T_g^{0.7}} \qquad \text{Eq. 3.5}$$

- **Stark Broadening $\Delta\lambda_S$**: is provoked by the splitting of levels due to the electric field of plasma electrons (Stark effect). This effect brings about a Lorentzian shape to the emission line, whose FWHM increases with electron density and is dominant for lower Z emitters in a plasma with high electron densities ($> 10^{19}$ m^{-3}).[11]

$$\Delta\lambda_S = 2 \cdot 10^{-11} n_e^{2/3} \qquad \text{Eq. 3.6}$$

- **Instrumental Broadening $\Delta\lambda_I$**: This source of broadening depends on the optics of the collection system and it is evaluated experimentally through calibrating the spectrometer with a standard emission line, usually from a peak emission of a halogen lamp.

- **Other Broadenings**: Resonant charge exchange mechanisms must be taken into account when the masses of emitters and neutrals are very similar, for example when considering an emission line from Ar ions in an Ar plasma (*Resonance Broadening*). Other broadening sources usually results from energy loss of emitted light while propagating or from the spread in energy of the original radiating levels (due to uncertainty relation). These effects are usually described

as a damping in an oscillator system (*Natural Broadening*) and are negligibly small at atmospheric pressure in respect to other broadening mechanisms.

Using the emission of hydrogen alpha Balmer line H_α at 656.4 nm whenever some hydrogen is introduced in the discharge or is dissociated from a molecule permits to estimate the electron number density by deconvoluting the emission line. This is possible because the plasma sources used in this work commonly show electron densities in the range of 10^{19}-10^{20} m^{-3}, conditions for which the Stark broadening is linear and the leading broadening mechanism.[12] Also, the resonance broadening can be neglected if the base plasma species is Argon. The deconvolution of the emission line has to consider all the different line shapes which accompany the single effects; combining Lorentzian and Gaussian distributions results in a so-called *Voigt profile* whose width can be related to the single broadening sources as in equation 3.7:

$$\Delta\lambda_{Tot} = \left[\left(\frac{\Delta\lambda_S+\Delta\lambda_W}{2}\right)^2 + \Delta\lambda_D^2 + \Delta\lambda_I^2\right]^{1/2} + \frac{\Delta\lambda_S+\Delta\lambda_W}{2} \qquad \text{Eq. 3.7}$$

For a high-density Argon RF discharge at atmospheric pressure the most important contributions to the H_α line broadening are found to be the Stark broadening (0.5 – 1 nm) and the intrinsic broadening brought up by the spectrometer (0.1 - 0.3 nm), while Resonance and Van der Waals broadening are on the order of 10^{-2} nm and the Doppler broadening is on the order of 10^{-3} nm. Natural line broadening is of the order of 10^{-5}, hence will be neglected in the present calculations.[13]

Values of T_g are then inserted in the model to calculate the resulting global width of the Voigt distribution, leaving the electron density as a parameter. The value of n_e is then extrapolated from fitting the resulting distribution to the measured H_α emission line.

3.2.4 Gas temperature

Molecules have internal degrees of freedom consisting in discrete vibrational and rotational modes. Transitions between vibrational and rotational states are likely to happen alongside electronic transitions when they are excited inside a plasma. The intensity of the emission lines relative to transitions between rotational states can be written as:

$$I \propto \frac{A_{JJ'}(2J+1)}{\lambda_{JJ'}} \, e^{-\left(\frac{E_J}{k_b T_{rot}}\right)} \qquad \text{Eq. 3.8}$$

where $A_{JJ'}$ are Einstein coefficients, J and J' are rotational quantum numbers of upper and lower levels, and T_{rot} is the temperature associated to the distribution of rotational states. [11] In certain circumstances, for atmospheric pressure plasmas, the lifetime of rotational excited states is shorter than the average time between successive collisions with the neutral in the gas. With this assumption, the distribution of rotational excited states is quickly thermalized by collisions and T_{rot} can be a good approximation of the gas temperature T_g.[14] In figure 3.5 a measured emission spectrum of the $\Delta v=0$ C_2 swan band ($D^3\prod_g \rightarrow A^3\prod_u$) transition for an Ar/$CO_2$ APP for two different rotational temperatures is presented.[15] It shows how the intensities of the various rotational peaks changes with rotational temperature, when the spectrometer can resolve the single lines. A spectrum acquired through a lower resolution spectrometer would see the main peak at 516.5 nm

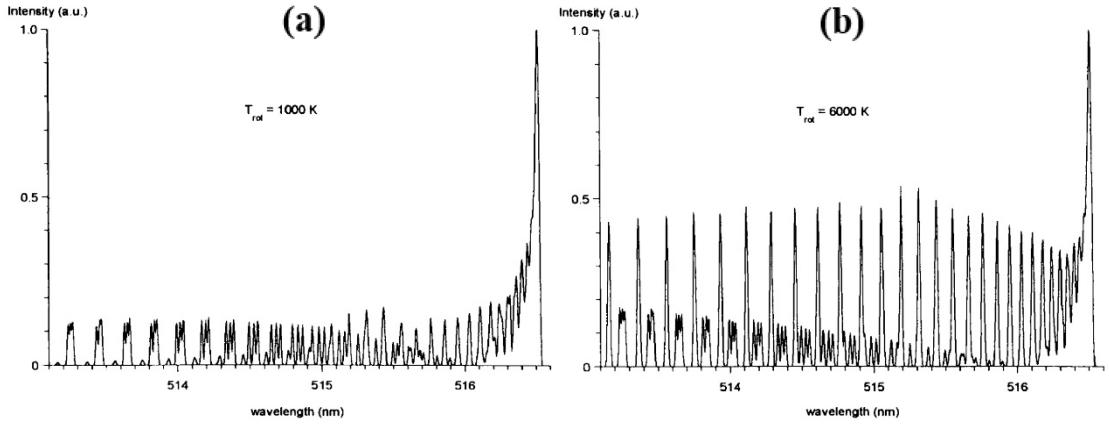

Figure 3.5 - Emission spectrum of the $\Delta v=0$, C_2 swan band ($D^3\prod_g \rightarrow A^3\prod_u$) for two different temperatures (**a**) 1000 K and (**b**) 6000 K, with resolved rotational transition fine structure. The intensity of each rotational transition changes with rotational temperature, reflecting different population of excited states. [11]

broadened in the higher temperature case, with a tail at smaller wavelengths as would appear the convolution of rotational peaks.

The extraction of T_{rot} from the OES spectra can be done different ways, in the context of this work two ways have been considered:

1. **Global simulations**: A full parametric simulation of the rotational and vibrational molecular levels via SpecAir or MassiveOES software using available algorithms for the analysed species. The synthetic spectra, based on separate single-temperature MB distributions for vibrational and rotational excited states, are fitted to experimental spectra through minimizing the residuals with a least square method.

2. **Partial simulations**: Taking the simulated spectrum in 1) and plotting the logarithm of intensity of the single fitted peaks against the energy of starting level it is possible to build Boltzmann plots in analogy to what has been done in section 3.2.2 using the eq. 3.8 for rotational transitions pertaining a single vibrational peak. An example of an analogous routine applied to the Δv=0 OH (A-X) transition is shown in figure 3.6.[16] It is possible to notice that in non-equilibrium conditions, in the case in figure a dc discharge in water, deviations from a single-temperature MB distribution can be evident. Data points tend to accumulate along different lines, and at each line corresponds a distribution temperature. Typically, excited states at lower J tend to be more easily thermalized, even if it may strongly depend on the formation mechanism of the particular species involved.[14,16] Hence, by taking the slope relative to the linear fit of lowest lying J components, it is possible to extract a T_{rot} which is more likely to be a good approximation of T_g.

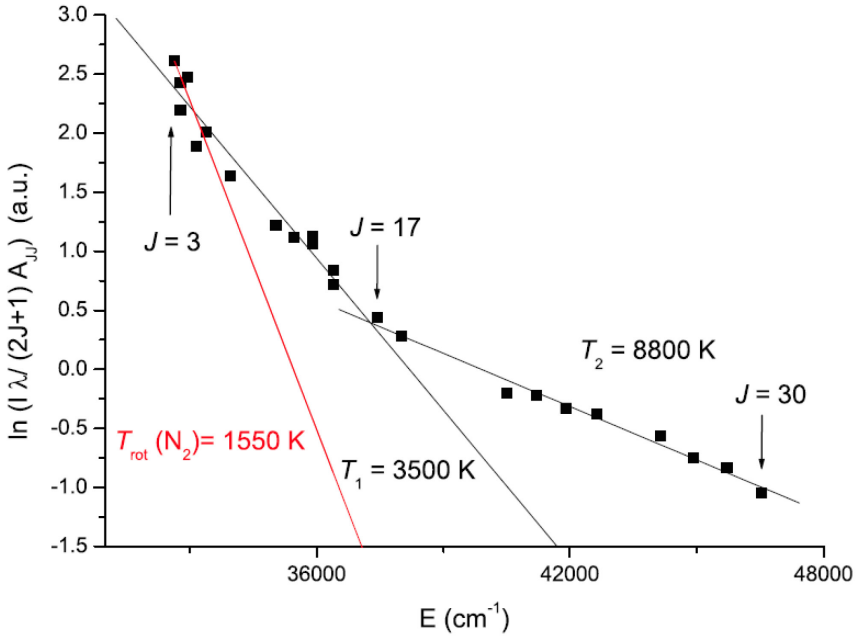

Figure 3.6 - Boltzmann plot for the Δv=0 OH (A-X) transition relative to a water bubble discharge. The different formation pathways of OH in the discharge are reflected in a 3-temperature distribution of rotational excited states, which can be seen in such diagrams as the accumulation of data points along lines with different slopes. Indicated in red the simulated T_{rot} for N_2 in the same spectrum, showing that low lying (in J) rotational levels are more likely to be thermalized and approximate better T_g. [16]

The transitions commonly used for the measurement of gas temperature are OH(A-X) at 306-309 nm, N_2(C-B) at 337nm , N_2^+ (B-X) at 391 nm because they are easily present in atmospheric pressure processes as residual water from moisture and air in the gas lines. Alternatively other studies have been using CN(BX), CH(A-X), CF (B-X), O_2(b-X), CO(B-A), C_2 swan band, NO (A-X), H_2 Fulcher band because their emission is in the visible and near UV and usually are part of the chemistry of the plasma processes under study. The assumption of thermalize rotational distribution, though, is not always satisfied even at atmospheric pressure. In fact, there is a multitude of phenomena which can lead to depopulation/population of rotational levels. In all these cases the distribution of rotational states obtained from optical emission is a result of the details of the formation process.[14] So, whenever a certain set of transitions is chosen for estimating the gas temperature from rotational lines, it is good practice to understand the formation process of the analyzed species to have a meaningful identification of gas temperature with the rotational temperature. *Dissociation reactions, dissociative excitation/recombination, dissociative charge transfer and chemical reactions* (induced by photons, electrons, metastables, ions and neutrals in the plasma) may form species in excited states with very high quantum numbers, unable to thermalize quickly through collisions. *Collisions at the*

reactor walls can also affect the distribution of excited rotational states if the mean free path of species in excited states is bigger than the size of the vessel or the confinement space.[14] In general, these phenomena imply that is better to choose species which are not actively involved in the plasma chemistry of the process, and in non-equilibrium conditions a multi-temperature distribution of rotational states has to be expected. If the spectra can be resolved in the single rotational lines, though, the partial simulation method (method 2) can be applied to low J rotational quantum numbers and still give reasonable results even if equilibrium conditions are not strictly met or the formation process of the target species is unknown.

3.3 Particle heating models in collisional plasmas

3.3.1 Particle charging model: orbital motion limited (OML) theory

Nanoparticles surface temperature can be higher than the background gas temperature in an atmospheric pressure plasma. This is critically important when frequent collisions between ions and neutrals result in a higher current of ions to the particles surface, influencing the energy balance on the particle surface. In fact, the energy balance on the particles surface depends on electron-ion recombination events, collisions with plasma species and chemical reactions. Most of these phenomena strongly depend on the fluxes of ions, electrons and neutrals on the particles surface. Nanoparticle heating is particularly important on the surface of a small particles and have been proved important to understand the formation of various crystalline particles which would otherwise need higher gas temperatures.[17] In this section we will lay out a model to calculate the temperature at the surface of nanoparticles immersed in the plasma volume during the synthesis process and characterize this phenomenon as a unique feature of atmospheric pressure plasmas in respect to low pressure plasmas.

The electrostatic environment of unbiased objects exposed to a low-pressure plasma is commonly modelled using the orbital motion limited (OML) model.[18] It provides an adequate evaluation of the electric potential at the surface of the object immersed in the plasma and can be applied to probes, particles or whatever material facing the plasma and not electrically coupled to the electrodes.[18] In general, every surface exposed to the plasma becomes negatively charged, a fact that is responsible for the non-agglomerating behavior of plasma-synthesized particles and can be traced back to the lower inertia of electrons in respect to ions in the plasma. This implies a higher instantaneous density of electrons near the surface. The particle potential is calculated assuming it equal to the floating potential when electron and ion currents are equalized, i.e. $I_e = I_i$. Assuming a MB distribution of electrons velocities and that charges are present on the particles surface giving rise to the potential difference V_p, the electron current to the particle surface is determined by the probability of an electron to collide with the particle of diameter a:[19]

$$I_e = \pi a^2 n_e \sqrt{\frac{8 k_b T_e}{\pi m_e}}\, e^{\frac{eV_p}{k_b T_e}} \qquad \text{Eq. 3.9}$$

where m_e is the rest mass of electrons. A similar argument holds for the collisionless current of plasma ions subject to the attraction of a charged sphere, which yields:

$$I_i^{OML} = \pi a^2 n_i \sqrt{\frac{8k_bT_i}{\pi M}} \left[1-\left(\frac{eV_p}{k_bT_i}\right)\right] \qquad \text{Eq. 3.10}$$

where T_i is the temperature of ions in a Maxwellian distribution of velocities, M the mass of involved ions in atomic units, n_i is the number density of ions. At atmospheric pressure collisions between ions and neutrals are very efficient, so the ions are in thermal equilibrium with the non-ionized counterparts and ions temperature can be approximated to the gas temperature $T_i \approx T_g$. Moreover, for the conservation of charge $n_e = n_i - qn_p$ where q is the average charge deposited on particles and n_p is the density of particles in the plasma. Relevant values for the work carried out here can be ~ 1 - 10 nm for the nanoparticles diameter and 10^{10} cm^{-3} for the nanoparticle number density, while typical electron densities for the discharges used in this study are on the order of 10^{14} cm^{-3} and the average charge per particle is on the order of 1 to 5 elementary charges (e); hence the contribution of particles charge on the overall plasma neutrality can be neglected and the ion number density is approximately equal to the electron number density $n_e \approx n_i$. Equating expressions 3.9 and 3.10 gives a transcendental equation which can be solved computationally to obtain the particles potential V_p.

3.3.2 Applicability range of OML model

The OML model is meaningful only when the condition $\lambda_i \gg \lambda_d \gg a$ is satisfied,[20,21] where λ_i is the ion mean free path, λ_d the plasma screening length (electron Debye length) and a is the particle diameter. In these conditions the motion of ions and electrons can be considered as collisionless. For APPs λ_i is of the same order of λ_d and the effect of ion collisions and charge-exchange with neutrals plays an important role on calculating the ion current on the particles surface, hence a collision-corrected model (CCM). The CCM model that is presented in the section 3.3.3 and used throughout this work is valid when $\lambda_i \approx \lambda_d$, but both quantities are still bigger than the particle size. As introduced in chapter 1, the ion mean free path changes in function of the gas temperature, while the electron Debye length depends on the electron temperature and electron density by a factor $\propto$

$\sqrt{T_e/n_e}$. In figure 3.7 the regions of validity for the OML and CCM models at atmospheric pressure are presented in function of T_e and n_e for different gas temperatures, in the ranges of interest for nanomaterial synthesis. At low gas temperatures the OML model is valid only when electron temperature is very high (>6-7 eV) even at low electron density (10^{16} m^{-3}). The region of validity of OML is expanded to lower electron temperatures and higher electron densities with increasing gas temperature, given the increasing value of ion mean free paths. At lower pressures, for example those typical of glow discharges for magnetron sputtering (10^{-1} Pa) the conditions for OML are always met (not shown), as the values of mean free path reach the meter range. For bigger particles, when the Debye length or the ion mean free path become comparable to the particle size, neither OML nor CCM are valid models, as for example would happen for 100 nm particles in a low gas temperature discharge lying near the $\lambda_i = \lambda_d$ line.

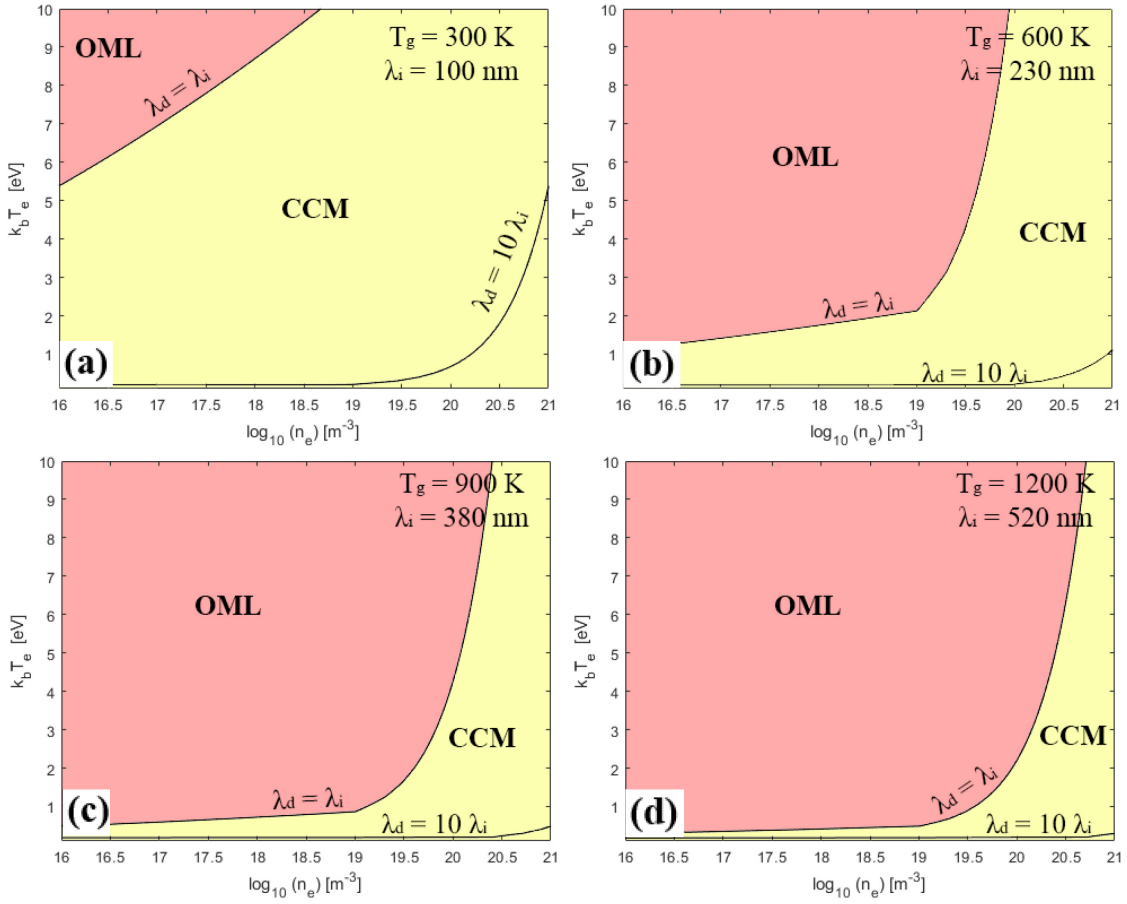

Figure 3.7 - Regions of validity for the OML (red shaded area) and CCM model (yellow shaded area) in function of electron density (log scale) and electron temperature for different gas temperatures, (**a**) 300 K (**b**) 600 K (**c**) 900 K and (**d**) 1200 K. Also values of ion mean free path relative to the corresponding gas temperature is indicated in each panel, as well as countour lines corresponding to values of the electron debye length equal to the ion mean free path and ten times its value.

Nevertheless, these conditions are hardly met for plasma reactors of interest to materials synthesis.

3.3.3 Particle charging model: CCM

When collisional effects start to become important the current of ions to the particles surface is reduced due to the highly probable collisions with neutral particles and the efficient charge exchange phenomena. Other authors developed models to calculate the current of ions under these conditions[22–24] introducing the concept of Capture Radius (R_0). The effect of charge exchange between neutrals and ions in the vicinity of a particle can be described as a potential well around the particle where the slow ions resulting from collisions are captured. The capture radius is calculated in analogy to an impact parameter, as the distance at which ions kinetic energy equals the attractive electrostatic potential of the charged particle $E_{kin} + U(R_0) = 0$. If $U(R)$ is taken as the screened Coulomb potential, then R_0 reads:

$$R_0(E_{kin}) = \frac{e|V_p|\, a\left(1+\frac{a}{\lambda_d}\right)}{E_{kin}+e|V_p|\frac{a}{\lambda_d}} \quad \xrightarrow{a \ll \lambda_d} \quad \frac{e|V_p|\, a}{E_{kin}} \qquad \text{Eq. 3.11}$$

The last approximation of expression 3.11 is valid for small particles or low electron temperature discharges (typically <100 nm at P_{atm} and $n_e=10^{20}$ m^{-3}, <10 nm for RF glow discharges at P=0.1-0.01 atm).[24] The additional contributions to the ion current due to collisions can be divided in two regimes, a weakly collisional term (WC or "collision-enhanced") that describes a regime where each ion has a non-negligible probability to undergo one collision before reaching the particle, and a strongly collisional term (SC or "hydrodynamic") where each ion can undergo more than one collision before reaching the particle's surface. The last case is analogous to a continuum limit, where the ion is described by a mobility μ_i in a diffusion-limited motion.[25] Table 3.3 summarizes the equations used for ion flux in each regime and the expression for collision probability in each regime.[22]

Regime	Ion Flux	Probability
No collisions I_{OML}	$\pi a^2 n_i v_{i,th}\left[1-\left(\frac{eV_p}{k_b T_i}\right)\right]$	$P_0 = e^{-\frac{\alpha R_0}{\lambda_i}}$
Weakly collisional I_{WC}	$\pi(\alpha R_0)^2 n_i v_{i,th}$	$P_1 = \frac{\alpha R_0}{\lambda_i} e^{-\frac{\alpha R_0}{\lambda_i}}$
Strongly collisional I_{SC}	$4\pi a n_i \mu_i$	$P_{>1} = 1-(P_0+P_1)$

Table 3.3: Equations for the ion current in each regime and the relative collision probability.

In table 3.3 $v_{i,th}$ is the thermal velocity of ions with a Maxwell-Boltzmann distribution, and μ_i is the ion mobility for a thermal diffusion-like flow of ions, α is a constant that depends on the energy dependence of the capture radius (= 1.22 in the case of MB distributed ion energies). As already mentioned, the plasma will be considered quasi-neutral ($n_i \approx n_e$) and ions are in thermal equilibrium with neutrals ($T_i \approx T_g$). These conditions are met as long as the gas is partially ionized (as in process plasmas) and the charging of particles does not influence the quasi-neutrality (e.g.: for $n_e = 10^{20}$ m^{-3}, particle density $n_p < 10^{18}$ m^{-3} and 1e to 10e charge on each particle). Moreover, the ion mobility in the SC regime can be expressed in function of thermal velocity and mean free path of ions.[22] In addition, the ion mean free path at atmospheric pressure can be considered limited by ion-neutral collision events, and is defined as $\lambda_i = 1/\sigma_i n = k_B T_i / P\sigma_i$ where n is the gas density, P is the pressure and σ_i is the ion-neutral collision cross-section ($= 40.9 \cdot 10^{-20}\ m^2$ for Argon). The total current of ions is then obtained by weighting each ion current term with the respective probability of collision:

$$I_i = P_0 I_{OML} + P_1 I_{WC} + P_{>1} I_{SC} \qquad \text{Eq. 3.12}$$

The floating potential is then obtained from matching the expressions for electron current (equation 3.9) and ion current (equation 3.12) once the values for n_e, T_e, T_g are supplied.

The original contribution of the present work, in respect to the CCM model developed by *Askari et al.*[17] is to consider the total ion current as calculated in eq. 3.12. The main

difference with the model introduced by *Askari et al.* is to consider collision events as being weighted by the collision probability defined in table 3.3, in analogy to the work of *Gatti et al.* [22]. In the previous work instead, the total ion current was calculated as $I_i^{-1} = I_{OML}^{-1} + I_{WC}^{-1} + I_{SC}^{-1}$, so as a rate equation where all the three events (no collision, one collision and more than one collision) could happen at the same time, and the less frequent kind of collision acting as a rate limiting step. The comparison between the two models can be done only in a narrow parameters window, as only in the present work the functional dependence of gas parameters on gas temperature has been considered. However, for a 300 K T_g, 10^{20} m^{-3} n_e Ar plasma it is found that the weighted average procedure introduced in the present work results in total ion currents larger by one order of magnitude at least, and the discrepancy is larger for smaller particles, as shown in figure 3.8. It will be clear further in the text that this implies the same amount of charging on the particles surface (ions and electrons fluxes are balanced) but systematically higher temperatures on the particles surface, mostly due to an increased contribution from the kinetic energy of ions colliding on the particles surface.

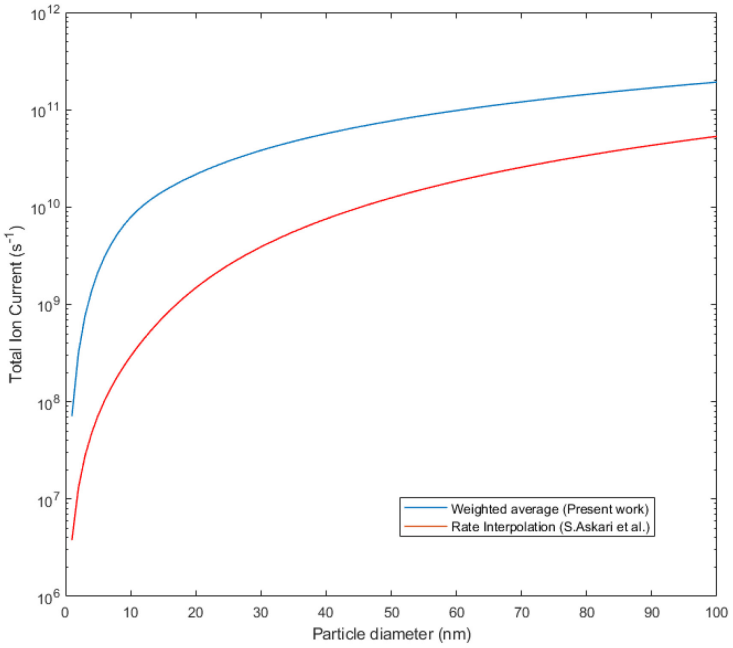

Figure 3.8 - Semilogarithmic plot of total ion currents calculated with the rate interpolation method by Askari et al. (red) [16] and the method developed in the present work (blue). The values are larger for the model developed in the present work, especially for smaller particles (< 10 nm).

The further calculations used to show the general characteristics of this model are based on atmospheric pressure Ar plasmas. The reduced potential $z\ (= -eV_p/k_bT_e)$ is always smaller than in the OML case, reflecting the fact that the ion flux to the particle surface is always large in the collisional case and the net charge accumulated (calculated assuming a homogeneous distribution on the surface of a sphere through the Poisson equation $V_p = Q/(4\pi\varepsilon_0 a)$) on the particles surface is smaller. Also, OML reduced potential is independent of particle size while the CCM reduced potential is a function of particles size. Higher z result in more net charge per particle.

The plots reported in figure 3.9 shows the variation of reduced potential and charge per particle as a function of particles size for different background gas temperatures (panels **a** and **b**, T_e=1 eV) and different electron temperatures (panels **c** and **d**, T_g=300 K). As a consequence of charge neutrality and the equal electron and ion currents on the particle surface, the potential and net charge per particle do not change with electron density. From figure 3.9 it is observed that the resulting reduced potential in function of particle size is a concave function which has a minimum, while the net charge per particle is monotonously increasing with particles size (due to the dependence on particle diameter a in Poisson equation). z and Q increase with both T_g and T_e, but more strongly with electron temperature for particles bigger than 10 nm. The minimum of z curves also shifts at higher particles size for higher T_g and T_e. While this minimum particle size changes from 8 nm to 10 nm for a significant variation in T_e (0.5 eV to 4 eV), it goes from 5 nm to 70 nm changing gas temperature from 300 K to 1200 K. However, the functional dependence on particles size has stronger variations with T_e, as the curves become increasingly concave at higher values of T_e. The net charge per particle results always within 1 to 10 elementary charges (e) for particle radii smaller than 10 nm, while is of an order of magnitude bigger for 100 nm particles. For high T_e (>1 eV) net charge per particle can be as high as 300e for such big particles (panel **d**).

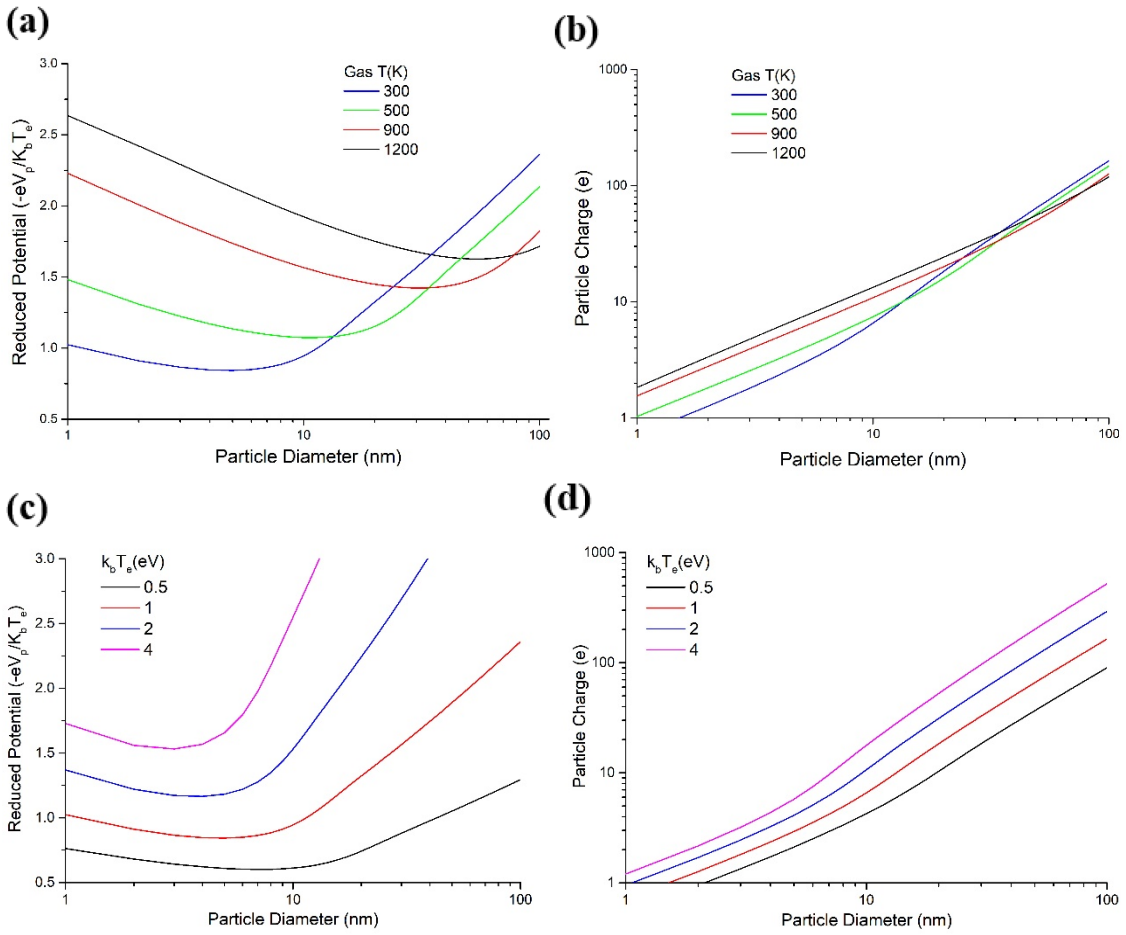

Figure 3.9 - Semilogarithmic plot of reduced potential (**a**-**c**) and loglog plots of net charge per particle (**b**-**d**) in function of particle diameter, (**a**) and (**b**) varying gas temperature, (**c**) and (**d**) varying electron temperature of the discharge.

Having estimated the reduced potential, it is possible to calculate each term in eq. 3.12 and study the effect of varying plasma parameters on the model specific contributions to the ion currents and the relative probabilities. Figure 3.10 shows the various contributions to the total ion current from the different terms weighted by their respective probability in function of particle size and for varying plasma parameters. In respect to panel (**a**), panel (**b**) introduces a change in n_e, panel (**c**) a change in T_e and panel (**d**) a higher T_g. All the plots are relative to atmospheric pressure operation. For the conditions explored it is noticed that the contribution of collisional terms (SC and WC) is always a large fraction of the total current, and 1 or 2 orders of magnitude higher than the OML contribution for significant variation of electron densities (comparing **a** and **b**) and electron temperature (comparing **a** and **c**). For smaller particles (<10 nm) at higher gas temperatures (panel **d**) the OML contribution to the total current becomes comparable in magnitude to the collisional terms and becomes even larger for particles with diameter smaller than 2 nm.

Hence, the relative contribution of collisional components compared to OML ones is more strongly affected by variations in the gas temperature.

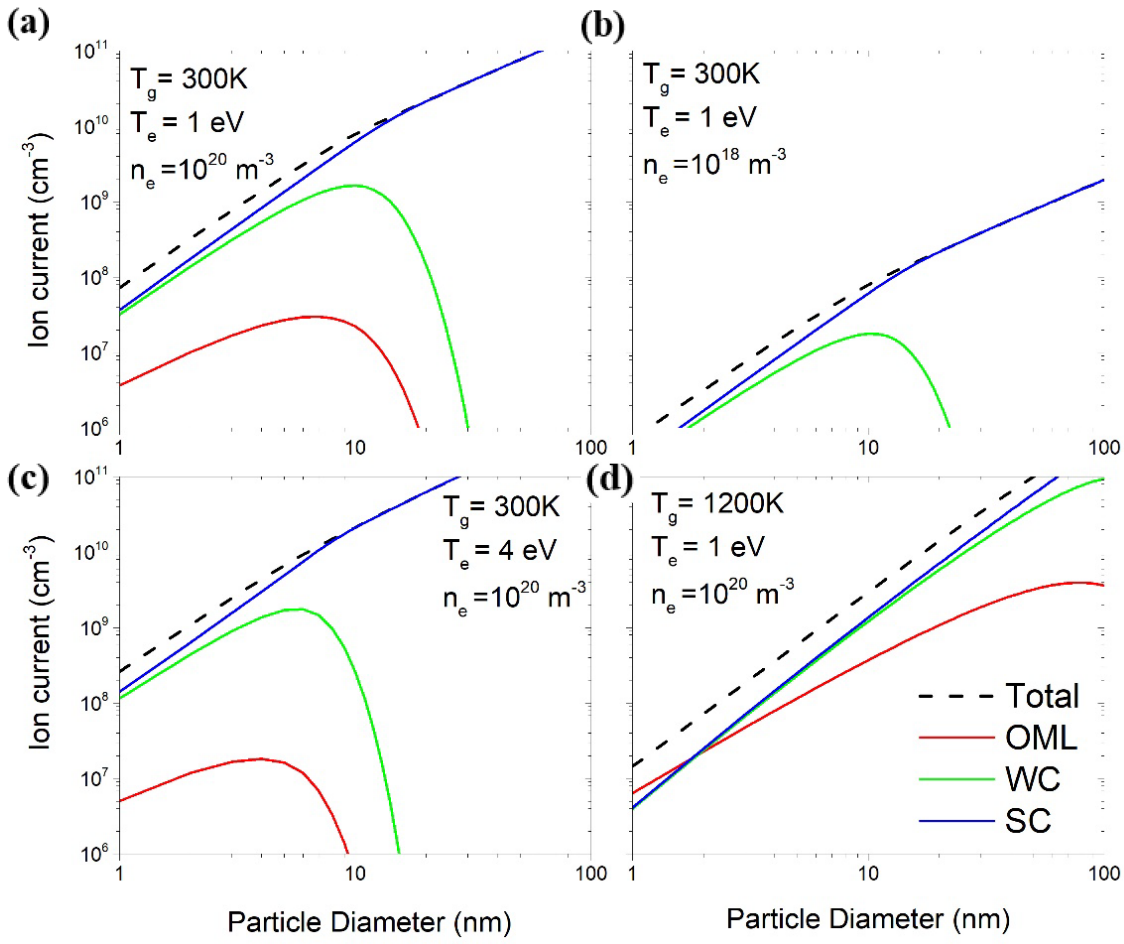

Figure 3.10: log-log plots of total ion currents in function of particles size, showing the contribution of OML current (no collisions) Weakly Collisional (1 collision) and Strongly Collisional (more than 1 collision) terms weighted by their respective probability. (**a**) T_g = 300 K T_e = 1 eV and n_e =10^{20} m^{-3} taken as a reference to show variation in (**b**) electron density $10^{18}m^{-3}$, (**c**) electron temperature 4 eV and (**d**) gas temperature 1200 K.

Within the contributions relative to CCM, for particles smaller than 10-15 nm the WC and SC are comparable in magnitude, while for bigger particles the ion current is all determined by the strongly collisional terms. This is a direct consequence of collision probabilities, for which bigger particles will be likely suffer more than one collision at a time. From comparing all the panels, it is apparent that the threshold size for which the SC contribution becomes dominant changes more significantly with the gas temperature (panel **d**). Another fact that can be observed is that the magnitude of total current is strongly affected by variations in n_e (e.g.: compare panel **a** with **b**), dropping of three orders of magnitude by changing the electron density from 10^{20} m^{-3} to 10^{19} m^{-3}. A variation

in gas temperature from 300 K to 1200 K (**a** vs **d**) introduces a one order of magnitude difference in the total current, while a variation in the electron temperature from 1 eV to 4 eV (**a** vs **c**) a more negligible difference.

For experiments performed in this work, the plasma reactor used is expected to operate in conditions such that $T_e \cong 1\ eV, n_e \cong 10^{20}\ m^{-3}$, as estimated from previous experiments,[17] while T_g may vary strongly depending on the specific process involved. The processes explored in the experimental chapter will result in the synthesis of 2 to 10 nm - diameter nanoparticles, and as estimated from OES measurements T_g never surpasses 1200 K (in the "worst" case). Hence, as can be concluded from the previous analysis, it is expected for the nanoparticles processed in the present reactor design to be confidently described by the collision corrected model even when assuming a possible broader variation of the base plasma parameters or a larger uncertainty in the estimated values.

3.3.4 Heat balance and particle temperature with the CCM model

It has been mentioned that the effect on collisionality as described by the CCM model bring to a higher temperature on the particles surface. To understand how it is happening a model is introduced to calculate the energy balance of particles' surface interacting with the surrounding plasma. In general, there are different phenomena that influence the energy balance (or exchange of heat) on a surface exposed to a plasma, the main ones are listed in table 3.4.

Heat sources	Heat sinks
e^-- ion surface recombination	Heat Conduction
Collisions with ions, electrons and neutrals	Emission of Radiation
Exothermic surface reactions	Endothermic surface reactions

Table 3.4 - List of the most important phenomena contributing to the energy balance on the surface of a particle immersed in the volume of a plasma.

Electrons and ions recombining at the particles surface release the excess energy as thermal agitation of the particle, while species in plasma colliding with the particle can transfer their kinetic energy. Chemical reactions happening at the surface of the particles can also affect the energy balance, leading to the release of excess energy or the inverse process depending on the energetics of the reactions involved. At the first approximation we neglect few of these processes, in order to build a simple steady state model which considers the dominant contributions to the particle's energy balance. Radiation losses will be neglected as can be assumed to be small, given the low temperatures involved. Surface chemical reactions contribution can be substantial, and in some cases has been pointed has the main heating mechanism for small nanoparticles at pressure slightly lower than atmospheric,[24] given the small surface area of particle and the significant amount of energy per event (for example H reaction with a dangling bond in Si brings about 3.1 eV per reaction); however in the present CCM model the impact of these reactions is not taken into account, either to preserve the non-specificity of the presented heating mechanism and show that even without considering these surface chemical reactions a steady-state calculation of particle temperatures based on the model in section 3.3.3 results in higher temperatures than the T_g. It will also be demonstrated in chapter 5 that this model is able to explain the experimental results for crystallization of Si nanoparticles with low temperature discharges, which has been the main reason (historically) driving the scientific community on developing particle heating models for industrial-relevant plasmas.[17,22–24,26,27] In these conditions the steady-state heat balance reads:[28]

$$q_{con} = q_{kin} + q_{rec} \qquad \text{Eq. 3.13}$$

where q_{con}, q_{kin} and q_{rec} are terms describing heat conduction to the background gas, kinetic contribution from collisions with electron and ions, and electron-ion recombination events on the particle's surface respectively. The average kinetic energy of ions and electrons reaching the particles can be estimated from the electron temperature and the floating potential as:

$$q_{kin} = I_i(2k_bT_e - eV_p) \qquad \text{Eq. 3.14}$$

The energy due to recombination of ions and electrons at the particle surface involves the ionization energy of the specific process gas. In our case we will consider only singly ionized Argon discharge, so the contribution to the total balance is:

$$q_{rec} = I_i \epsilon_i \qquad \text{Eq. 3.15}$$

Where ε_i = 15.76 eV is the first ionization energy of Argon. The evaluation of the contribution from heat conduction, instead, requires some considerations about the heat transport regime. In fact, depending on the relative scale between mean free path λ_g of gaseous atoms and the size of the particles a, the heat flux on the particle surface is described in different ways. The most used discriminating parameter is the Knudsen number defined as the ratio $K_n = \lambda_g / a$. Three different regimes are distinguished:

- $K_n \gg 1$ "*Free Molecular Regime*" in this case $\lambda_g \gg a$ so gas atoms or molecules do not suffer any collisional event on the length scale of the particle, and the heat flux does not depend on the geometry of the problem.

- $K_n \ll 1$ "*Continuum Regime*" in this case $\lambda_g \ll a$ gaseous atoms stochastically experience many collisions with particles, and the heat flux can be derived by Fourier heat conduction law. It depends on the geometry of the system, the temperature gradient and the thermal conductivity of the gas involved.

- $K_n \cong 1$ "*Transition Regime*" in this case $\lambda_g \cong a$ and the conditions are intermediate between the other cases

In the case of atmospheric pressure Ar plasma and nm-range particles the conditions are always between the transition regime and the Free molecular regime. A relation that has been used to describe the conductive heat flux in both regimes is:[29]

$$q_{con} = \frac{8\pi a^2 K}{2a + \lambda_g G} (T_p - T_g) \qquad \text{Eq. 3.16}$$

where K is the temperature-dependent conductivity of Ar at atmospheric pressure, G is a geometrical factor and T_p is the particle surface temperature. We use this definition of the mean free path for a non-ideal gas developed by McCoy and Cha, which is valid in both transport regimes:[30]

$$\lambda_g = (\gamma - 1)\frac{K}{Pf}\sqrt{\frac{\pi M T_g}{2k_b}} \qquad \text{Eq. 3.17}$$

Where P is the gas pressure, γ is the heat capacity factor and M is the mass of the gaseous atoms. The table 3.5 describes the other parameters in eq. 3.17 in terms of measurable or known physical properties:

Symbol	Definition	Expression
K	Heat conductivity	$K(T_g, P)$
G	Geometry-dependent heat transfer factor	$\frac{8f}{\alpha(\gamma+1)}$
f	Eucken factor	$\frac{9\gamma-5}{4}$
γ	Heat Capacity factor	$\frac{C_p}{C_v}$
α	Thermal accommodation factor	$\frac{\langle E_i\rangle - \langle E_r\rangle}{\langle E_i\rangle - \langle E_s\rangle} \approx 1\ (Ar)$

Table 3.5 - Definition of parameters appearing in equations 3.16 and 3.17 and relative expressions in function of known or measurable gas parameters. C_p and C_v are the known heat capacities at constant pressure and volume respectively. $\langle E_i\rangle$, $\langle E_r\rangle$ and $\langle E_s\rangle$ are mean energies of incident, reflected and fully accommodated gas atoms at the surface of the particle. It can be approximated to 1 for Ar at P_{atm}.

Using equation 3.13 and the dependence of the conduction heat flux (Eq. 3.16) on T_p, we can extract the particle surface temperature using the ion currents supplied by the CCM

model and the parameters relative to the discharge gas. Figure 3.11 shows solutions of equation 3.13 in terms of temperature difference with the background gas (panel **a**) and absolute temperatures (panel **b**) function of particle size for different T_g (constant T_e=1eV and $n_e = 10^{20}$ m^{-3}).

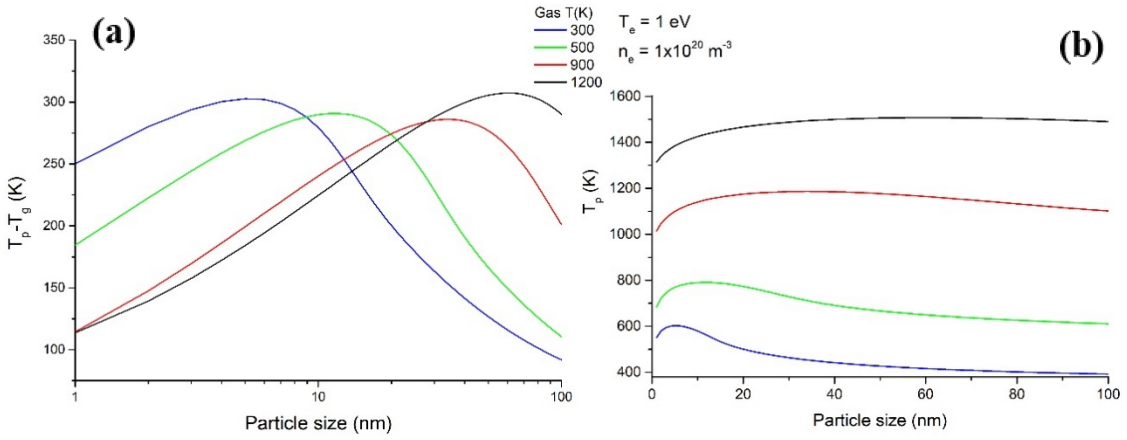

Figure 3.11 - (**a**) Semilogarithmic plot of temperature differential between particles surface and gas in function of particles size calculated with the collision-corrected model for different values of gas temperature. (**b**) Absolute values of particle temperature in function of particle size, for different gas temperature.

The temperature differential is a peaked function of particle size, and it remains in the same order of magnitude at different T_g. In correspondence to the minimum in reduced potential (figure 3.10a) there is a maximum in the temperature differential and shifting in analogous way to higher particle size with increasing T_g. At the same time the value of temperature differential at constant particle size is an increasing function of gas temperature at small particle size, and a decreasing function of gas temperature at bigger particle size. Hence when particles in the plasma are small, as it is for the present experimental work, the effects of collision heating mechanisms are more important for lower gas temperatures. This is clearer in terms of absolute values for particle temperature (panel b) where it is possible to see that a 10 nm particle in a cold plasma (T_g=300 K) can reach temperatures of 600 K on its surface. While the same particle in a "warmer" plasma (T_g=1200 K) reaches a temperature of 1400 K, hence a much smaller relative variation in respect to the gas temperature.

In figure 3.12 the effect of T_e and n_e on the temperature differential is shown (for fixed T_g at 300 K). By increasing the electron temperature (panel a) the temperature differential increases also, always with a larger relative increase for smaller particles. Instead it is

evident that the magnitude of the temperature differential is a strong function of electron density (notice the log-log scale in panel **b**), as it grows of an order of magnitude as electron density does.

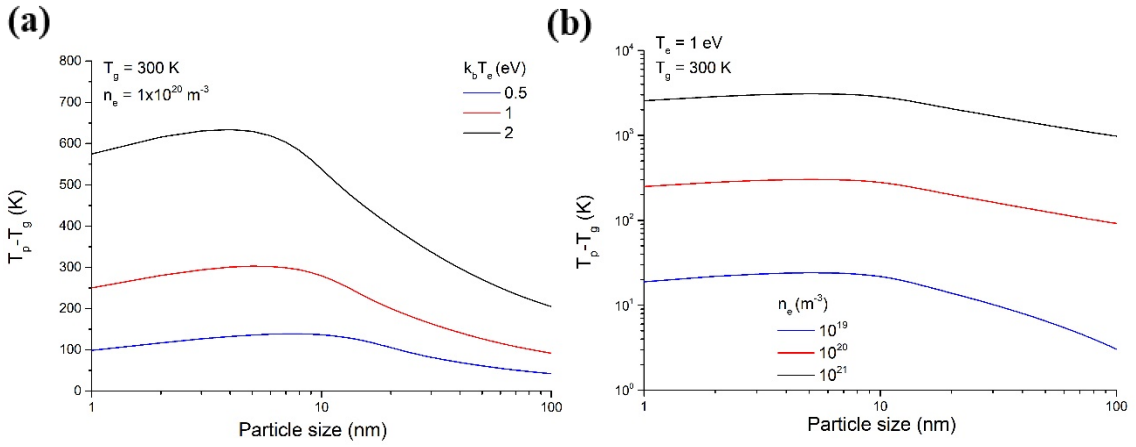

Figure 3.12 - Temperature differential between particles surface and gas in function of particles size calculated with the collision-corrected model for different values of plasma parameters. (**a**) semilogarithmic plot for different values of electron temperature and (**b**) loglog plot for different values of electron density.

The results of the model reflect the balance between different contribution of ion currents and their respective probabilities. The dependence on electron density is easily explained considering the approximation of quasi neutrality that we used ($n_e \approx n_i$), which has the result of increasing the total ion current regardless of the involved collisional regime. The electron temperature is affecting mostly the current of electrons on the particle's surface temperature, while gas temperature affects at the same time the total ionic currents and the probability of collisions with ions. In fact the increased gas temperature (related to the average kinetic energy of gas atoms) implies an increase of average velocities of gas atoms and the number of collisions per unit time with ions, hence an increased ion current on the particle surface, is balanced by a reduced ability of the particles attractive potential to capture ions.

3.4 Conclusion

An experimental routine based on optical emission spectroscopy has also been discussed as a way towards understanding better the physics and chemistry behind the formation of particles in discharges with molecular precursors and as a tool to achieve a better control on the synthesis process. This has been done by studying methods to obtain plasma parameters as gas temperature, effective electron temperature and electron density starting from distinctive features in OES spectra of molecular gases.

A steady state collision-corrected model has been proposed and studied in function of the plasma parameters of interest to atmospheric pressure plasmas, in order to understand the synthesis conditions of nanoparticles in such discharges. This model is independent on the nanoparticles' material and can be used with OES-derived parameters. It is found that very small particles (1-10 nm) can have surface temperatures way larger than the background gas temperature due to charge-exchange mechanisms influencing the ion currents on the particles surface and the overall energy balance. At the same time, the monopolar charging of nanoparticles prevents their agglomeration, which is important for obtaining dispersed colloids and free-standing nanoparticles.

These increased temperatures can stimulate material processes as crystallization or the formation of high temperature polymorphs in a relatively cold plasma discharge. Moreover, the result of the study highlights that the contribution of collisional heating on very small nanoparticles (< 10 nm) is more important the higher the non-equilibrium (difference between T_g and T_e) at low gas temperatures and the higher the electron density of the discharge, hence justifying the unique features of microplasmas for nanoparticle synthesis.

References

1. Fantz, U. Basics of plasma spectroscopy. *Plasma Sources Sci. Technol.* **15**, (2006).

2. Harilal, S. S., Brumfield, B. E., Lahaye, N. L., Hartig, K. C. & Phillips, M. C. Optical spectroscopy of laser-produced plasmas for standoff isotopic analysis. *Appl. Phys. Rev.* **5**, (2018).

3. Yanguas-Gil, A., Cotrino, J. & González-Elipe, A. R. Measuring the electron temperature by optical emission spectroscopy in two temperature plasmas at atmospheric pressure: A critical approach. *J. Appl. Phys.* **99**, (2006).

4. Iza, F., Lee, J. K. & Kong, M. G. Electron kinetics in radio-frequency atmospheric-pressure microplasmas. *Phys. Rev. Lett.* **99**, 2–5 (2007).

5. Zhu, X.-M., Chen, W.-C. & Pu, Y.-K. Gas temperature, electron density and electron temperature measurement in a microwave excited microplasma. *J. Phys. D. Appl. Phys.* **41**, 105212 (2008).

6. Zhu, X.-M. & Pu, Y.-K. A simple collisional radiative model for low-pressure argon discharges. *J. Phys. D* **40**, 2533 (2007).

7. Sadeghi, N., Setser, D. W., Francis, A., Czarnetzki, U. & Döbele, H. F. Quenching rate constants for reactions of Ar(4p′ [1/2]0, 4p[1/2]0, 4p[3/2]2, and 4p[5/2]2) atoms with 22 reagent gases. *J. Chem. Phys.* **115**, 3144–3154 (2001).

8. NIST Atomic Spectra Database (version 5.7.1), [Online]. available: https://physics.nist.gov/asd.

9. Djurović, S. & Konjević, N. On the use of non-hydrogenic spectral lines for low electron density and high pressure plasma diagnostics. *Plasma Sources Sci. Technol.* **18**, (2009).

10. Muñoz, J., Dimitrijević, M. S., Yubero, C. & Calzada, M. D. Using the van der Waals broadening of spectral atomic lines to measure the gas temperature of an argon-helium microwave plasma at atmospheric pressure. *Spectrochim. Acta - Part B At. Spectrosc.* **64**, 167–172 (2009).

11. Hofmann, S., Van Gessel, A. F. H., Verreycken, T. & Bruggeman, P. Power dissipation, gas temperatures and electron densities of cold atmospheric pressure

helium and argon RF plasma jets. *Plasma Sources Sci. Technol.* **20**, (2011).

12. Gigosos, M. A., Gonzàles, M. & Cardenoso, V. Computer simulated Balmer-alpha, -beta and -gamma Stark line profiles for non-equilibrium plasmas diagnostics. *Spectrochim. Acta Part B* **58**, 1489–1504 (2003).

13. Balcon, N., Aanesland, A. & Boswell, R. Pulsed RF discharges, glow and filamentary mode at atmospheric pressure in argon. *Plasma Sources Sci. Technol.* **16**, 217–225 (2007).

14. Bruggeman, P. J., Sadeghi, N., Schram, D. C. & Linss, V. Gas temperature determination from rotational lines in non-equilibrium plasmas: A review. *Plasma Sources Sci. Technol.* **23**, (2014).

15. Coitout, H. & Faure, G. Measurement of rotational temperature by simulated molecular spectra. *Spectrosc. Lett.* **29**, 1201–1214 (1996).

16. Bruggeman, P. *et al.* Characterization of a direct dc-excited discharge in water by optical emission spectroscopy. *Plasma Sources Sci. Technol.* **18**, (2009).

17. Askari, S., Levchenko, I., Ostrikov, K., Maguire, P. & Mariotti, D. Crystalline Si nanoparticles below crystallization threshold: Effects of collisional heating in non-thermal atmospheric-pressure microplasmas. *Appl. Phys. Lett.* **104**, (2014).

18. Allen, J. E. Probe theory-The orbital motion approach. *Phys. Scripta.* **45**, 497 (1992).

19. Vladimirov, S. V., Ostrikov, K. N., Yu, M. Y. & Stenflo, L. Evolution of Langmuir waves in a plasma contaminated by variable-charge impurities. *Phys. Rev. E - Stat. Physics, Plasmas, Fluids, Relat. Interdiscip. Top.* **58**, 8046–8048 (1998).

20. Lampe, M., Gavrishchaka, V., Ganguli, G. & Joyce, G. Effect of trapped ions on shielding of a charged spherical object in a plasma. *Phys. Rev. Lett.* **86**, 5278–5281 (2001).

21. Zobnin, A. V., Nefedov, A. P., Sinel'shchikov, V. A. & Fortov, V. E. On the charge of dust particles in a low-pressure gas discharge plasma. *J. Exp. Theor. Phys.* **91**, 483–487 (2000).

22. Gatti, M. & Kortshagen, U. Analytical model of particle charging in plasmas over

a wide range of collisionality. *Phys. Rev. E - Stat. Nonlinear, Soft Matter Phys.* **78**, 1–6 (2008).

23. Kramer, N. J., Aydil, E. S. & Kortshagen, U. R. Requirements for plasma synthesis of nanocrystals at atmospheric pressures. *J. Phys. D. Appl. Phys.* **48**, (2015).

24. Mangolini, L. & Kortshagen, U. Selective nanoparticle heating: Another form of nonequilibrium in dusty plasmas. *Phys. Rev. E - Stat. Nonlinear, Soft Matter Phys.* **79**, 1–8 (2009).

25. Khrapak, S. A. *et al.* Grain charge in the bulk of gas discharges. *Phys. Rev. E* **72**, 016406 (2005).

26. Kortshagen, U. Nonthermal plasma synthesis of semiconductor nanocrystals. *J. Phys. D. Appl. Phys.* **42**, (2009).

27. Kramer, N. J., Anthony, R. J., Mamunuru, M., Aydil, E. S. & Kortshagen, U. R. Plasma-induced crystallization of silicon nanoparticles. *J. Phys. D. Appl. Phys.* **47**, (2014).

28. Maurer, H. R. & Kersten, H. On the heating of nano- and microparticles in process plasmas. *J. Phys. D. Appl. Phys.* **44**, (2011).

29. Liu, F., Daun, K. J., Snelling, D. R. & Smallwood, G. J. Heat conduction from a spherical nano-particle: Status of modeling heat conduction in laser-induced incandescence. *Appl. Phys. B Lasers Opt.* **83**, 355–382 (2006).

30. McCoy, B. J. & Cha, C. Y. Transport phenomena in the rarefied gas transition regime. *Chem. Eng. Sci.* **29**, 381–388 (1974).

Chapter 4 - Nanodiamonds

4.1 Introduction

4.1.1 Interest in Nanodiamonds

Carbon comes in different forms at the solid state because of its ability to form bonds in different hybridized bonds such as sp, sp^2 and sp^3 configurations,[1] with graphite being the most thermodynamically stable for bulk specimens at atmospheric pressure and room temperature. Today there is a lot of interest in nanometric forms of carbon for the most diverse applications. Graphene sheets and carbon nanotubes exhibit exceptional properties such as switchable high electrical conductivity and mechanical strength[2,3] while fullerenes for instance have found wide application in biology and polymer-based solar cells.[4] Nanodiamonds (NDs) are of particular interest as a photoluminescent biomarkers[5] for drug delivery systems[6] and more recently in the field of quantum information,[7] quantum optics[8] and nanoscale metrology,[9,10] usually along with dopant engineering or surface functionalization.[11] Moreover, understanding the details of the synthesis condition is particularly important for astrophysics to provide suggestions on the thermodynamic environment of forming planets as NDs have been found in meteorites and planetary nebulae.[12–14] Theoretically, a thermodynamic stability crossover at the nanoscale has been predicted, for which clusters below 3-5 nm in diameter are more stable in the cubic diamond phase.[15,16] This picture is complicated by the fact that the stability window for the formation of NDs is sensitive to strain, surface terminations and the interaction with the environment during growth, as suggested by thermodynamic modelling[15,17] and experiments about post-synthesis processing.[18,19]

4.1.2 Synthesis of NDs

Most synthesis methods rely on high pressures and temperatures or extreme non-equilibrium conditions, e.g. detonation of carbon containing explosives,[20] plasma-enhanced chemical vapor deposition,[21] laser ablation of non-diamond carbon targets[22] and other less common methods.[23–25] Moreover, these methods often result in the coexistence of soot made up by different carbonaceous phases[26–28] or the presence of defective crystals.[29,30]

Few groups reported on the synthesis in atmospheric conditions, still relying on highly non-equilibrium processes such as direct femtosecond laser ablation[31] or using a microplasma reactor,[32] and in both cases using ethanol as precursor. In the latter study, *Kumar et al.* [32] demonstrated the synthesis of NDs by feeding vaporized ethanol into a direct-current plasma sustained in a millimetre scale hollow cathode reactor operated at atmospheric pressure. They reported the simultaneous synthesis of nanocrystals with cubic (c-diamond), hexagonal (h-diamond) and face centred cubic (n-diamond) structures along with some non-diamond phases. The authors were also able to selectively etch non-diamond phases by introducing hydrogen gas in the process plasma. Importantly, this work demonstrates that pure NDs can be synthesized in an atmospheric pressure gas phase reactor, although the low production rates and the small volume of the microplasma reactor still limit the research to purely lab-scale scientific investigation.

The formation of NDs in atmospheric pressure plasmas has not been understood. *Kumar et al.*[32] for example, advance the idea that NDs may nucleate from solid precipitation of C from a volatile organic precursor with suitable C:H:O ratios and particularly fast quenching rates. Also, they pinpointed the role of atomic hydrogen in the discharge as a selective non-diamond carbon etchant. Their views suit well with the results of a more comprehensive study by *Bachmann at al.*[33] on the chemical vapour deposition (CVD) synthesis of NDs from different precursors and reactor designs, however they provided no verification of the independence of their processes from precursors chemistry. The authors compared the synthesis of ND films as a function of the precursor's composition and the kinetic aspects of different methods such as hot-filament CVD, plasma enhanced CVD (PE-CVD), thermal CVD and combustion flames. Their analysis showed the existence of a narrow region in the ternary C:H:O diagram, referring to the composition of the precursors, where NDs were preferentially grown, between a no-growth region at the O-abundant side and a non-diamond growth region near the C-abundant side of the diagram. The striking conclusion was that the elemental composition of the precursor had a more important role than its molecular configuration or the kinetics of the synthesis process. Moreover, high temperature processes (but below 1300 °C where bulk graphite becomes more stable) can increase the deposition rates.

4.1.3 Present work

Herein, we demonstrate the synthesis of ultra-small nanocrystals of diamond using a gas phase atmospheric pressure radiofrequency (RF) microplasma process that employs a metalorganic precursor, ferrocene, $Fe(C_5H_5)_2$. This process exhibits higher production rate and versatility compared with previous work on microplasma synthesis of NDs.

In the present study the products of a microplasma process have been studied where, for the first time, ferrocene is used as a precursor for NDs synthesis. Therefore, the formation of NDs from this precursor can contribute to the understanding of the synthesis conditions as well as define new related scientific questions. We report the presence of dispersed nanocrystals of different crystalline phases of diamond along with fewer amounts of other carbonaceous species. We first study the effect of changing the precursor input concentration. Along with these experiments we use optical emission spectroscopy (OES), in order to frame the conditions under which NDs are formed, both thermally and chemically.

Ferrocene is a metal-organic compound which comes as a volatile powder and is mainly used for the catalytic formation of C nanotubes in CVD furnaces, and its chemical composition is not simply compatible with the view of *Bachmann et al.*[33] as there is no oxygen in ferrocene. Hence, to understand the role of precursor chemistry and the plasma conditions on the formation process, complementary experiments were performed. First by introducing molecular hydrogen in the ferrocene process, in order to study the etching properties of atomic hydrogen in the plasma discharge, and the effects of a H-rich environment on the synthesis products. Secondly, by using benzene as a precursor, a volatile liquid compound which has the same C:H ratio (1:1) as ferrocene but does not contain Iron and has a different molecular configuration of C-H bonds (benzenic rings vs cyclopentadienyl groups).

NDs were only obtained with ferrocene. This result in combination with the observations about the influence of plasma parameters on the synthesis products helped understanding some of the aspects of the synthesis of NDs within the present plasma process.

4.2 Experimental Setup

4.2.1 Reactor

The experimental setup is composed by a sealed stainless-steel chamber filled with nitrogen reaching atmospheric pressure. The chamber is equipped with a reactor wherein gaseous species are injected (Figure 4.1). The reactor is composed by a pair of rectangular copper electrodes (40 mm x 20 mm × 5mm) sandwiching a hollow glass capillary with rectangular cross section (0.3 mm wall thickness, 0.5 mm gap). RF power at 13.56 MHz is applied to one of the electrodes through an impedance matching network (80 W applied power for ignition), while the opposite electrode is grounded. The flow of the gaseous species from pre-mixed gas cylinders is controlled through mass flow controllers and a mixing circuit.

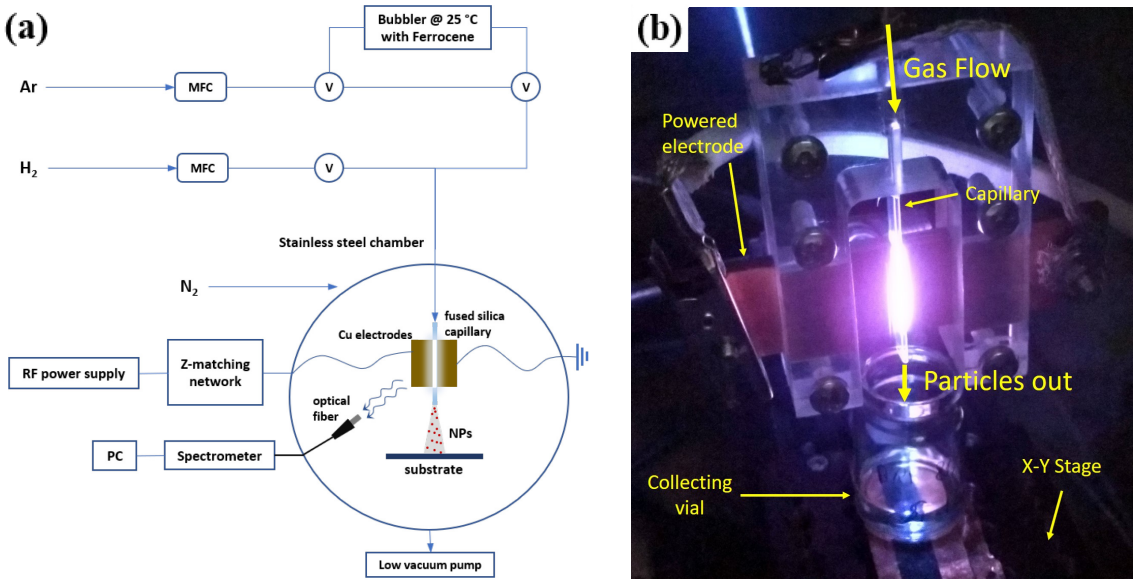

Figure 4.1 - (**a**) Schematics of the experimental setup: gas mixing circuit, reactor chamber and setup for OES. The optical fiber is pointing perpendicularly to the capillary in the middle of the visible discharge to capture a horizontal line of sight, (**b**) photograph of the microplasma reactor operating an 80 W Ar plasma, an ethanol vial is placed directly below the capillary exit.

A bubbler cylinder in parallel to the carrier gas supply line under a thermostatic bath set at 25 °C is used for delivering aerosols of the volatile precursors. The main experiments are performed by placing a few mg of ferrocene powder (98% purity, Sigma Aldrich) in the bubbler. Another bubbler cylinder with 5 mL of anhydrous benzene (99.8% purity, Sigma Aldrich) was used for the complementary experiments. In both cases the precursors were not depleted from the bubbler after all the experiments presented. Ar (N6,

BOC) flows through the bubbler housing the precursor and the resulting vapour is delivered to the reactor. Two additional supply lines are accommodated, one flowing Ar to permit changing the relative flow ratio of precursors mixture keeping the total flow constant (800 sccm) and another one for introducing hydrogen from a premixed cylinder (2% in Ar, BOC) in the discharge.

4.2.2 Characterization techniques

Structural characterization is done with a transmission electron microscope (TEM) (JEOL JEM-2100F) equipped with an EDX spectrometer. The TEM analysis includes bright-field imaging to observe the morphology of the particles and selected area electron diffraction (SAED) to characterize their crystallinity.

Chemical bond characterization was done through X-ray photoemission spectroscopy (XPS) and Raman scattering spectroscopy. XPS was carried out with a Kratos Axis Ultra DLD spectrometer. The X-ray source was an Al k_α anode (1486.6 eV) held at a potential within the range of 12-15 kV at a current of 10 mA. The operating pressure of the system maintained at 10^{-9} bar for all experiments. High-resolution scans were carried out with a resolution of 0.05 eV and a pass energy of 20 eV. Wide-energy scans carried out with a resolution of 1 eV and a pass energy of 160 eV. Raman measurements were obtained with a Horiba LabRAM 300 spectrometer. A helium-neon laser is used to produce a laser beam with 632.81 nm wavelength. The collimated light beam is scattered by the sample and passed through a notch filter to remove the elastic scattering contribution before interacting with a diffraction grating and received by a charge couple device (CCD) detector.

The plasma conditions are characterized using optical emission spectroscopy (OES). The equipment used to acquire the emission spectra is an Ocean Optics HR4000CG UV-NIR spectrometer (range 194-1122 nm) coupled with a 50 µm optic fiber. These measurements are carried out locating one end of the optic fiber perpendicular to the plasma 10 mm away.

4.2.3 Experimental Procedure

The plasma is first ignited at 60 W (as applied from the power supply) with He. After 10 minutes of He plasma on-time, the gas is switched to Ar and kept for other 5 minutes. This initial procedure is meant to clean the capillary from residual contaminants and to deplete gas lines from any residual extraneous gas. Then, the bubbler line is opened slowly, as usually a sudden pressure drop provokes the quenching of the plasma. After 10 min to 15 min from the introduction of the precursors, the stage is moved below the capillary exit to collect the products, the reason will be clarified when characterizing the process plasma from OES measurements in section 4.4. For most of the synthesis conditions, a useful amount of sample for characterization techniques is produced within 30 minutes of processing, which is currently the limit for repeatability due to deposition on the capillary walls. Synthesis with hydrogen is limited to 10-15 min due to the development of high temperature hotspots that can cause capillary damage and melting.

Samples for TEM are synthesized and collected directly into a 2 cm diameter glass vial containing 5 mL of anhydrous ethanol (max. 0.01 % H_2O, Sigma-Aldrich). The exit nozzle of the capillary is right at the top of the vial's orifice, and at the beginning of the process the surface of the liquid is 1 cm far from it. During the plasma process ethanol evaporates and at the end of each experimental trial its volume is approximately halved. The solution is then drop-casted and dried onto an ultrathin (3 nm) lacey carbon film supported on a Cu grid (Agar Scientific). Samples for Raman and XPS characterization are directly deposited from the plasma on a Si substrate placed on a scanning X-Y stage 1 cm below the exit of the capillary and then, in the case of XPS samples, partially coated with gold with a sputtering system in order to compensate for surface charge and use Au 4f levels as a calibration standard for binding energies.

In order to explore the effect of different synthesis conditions on the particles features and to understand the formation mechanisms the experiments have been divided in three different sets:

1. Varying the ferrocene concentration, with constant total flow and applied power; two variations of the sample that gave the best results (ND400) with different total flow and power settings are also presented, to show the sensitivity of synthesis products to the operative parameters;

2. Adding hydrogen in different concentrations, with constant ferrocene flow and power;
3. Using benzene as precursor.

4.3 Characterization of products

4.3.1 Varying ferrocene Flow

The first set of experiments involves changing the relative flow ratio of a ferrocene vapour to an argon background keeping a fixed total flow, thereby varying the precursor concentration in a fixed gas flow pattern. As ferrocene is a powdery solid which sublimates at low temperatures, the temperature of the thermal bath was chosen to have a saturated vapour while flowing 100 sccm to 500 sccm of Argon through the bubbler line. These conditions were obtained by monitoring the OES emission from C_2 species after 15 minutes of plasma on-time (plasma reaches an operative stability, see section 4.4) and varying the temperature of the thermal bath. Below 25 °C the C_2 emission varied with the thermal bath temperature. Instead, above 25 °C no variation of the emission intensity was observed by varying the thermal bath temperature. These conditions are interpreted as the achievement of a saturated vapour for which there is no difference in the vapour concentration of ferrocene inside the bubbler by increasing the thermal bath temperature. The estimation of ferrocene volumetric concentrations is carried out through the following relation:

$$\phi_{fer} = \frac{p_{fer}^{vap}(T)}{10^5 - p_{fer}^{vap}(T)} \cdot \phi_{bubbler} \approx 10^{-5} \cdot \phi_{bubbler} \qquad \text{Eq. 4.1}$$

where $\phi_{bubbler}$ is the flow of Ar through the bubbler line and $p_{fer}^{vap}(T)$ is the temperature-dependent vapour pressure of ferrocene (1.03 Pa at 25 °C [34]). Then, the concentration of ferrocene within the process is obtained by taking the ratio of actual ferrocene flow to the total flow through the reactor, $[Fe(Cp)_2] = \phi_{fer}/\phi_{tot}$.

The estimated concentrations are in the order of few parts per million (ppm), given the low vapour pressure of ferrocene at 25 °C. Nevertheless, the samples will be distinguished by the flow through the bubbler throughout the experimental results. Table 4.1 lists the different conditions explored and corresponding labelling of the samples (power 80 W and total flow 800 sccm constant for all the samples).

Sample	$\phi_{bubbler}$ (sccm)	ϕ_{Ar} (sccm)	[Fe(CP)$_2$] (ppm)
ND100	100	700	1.25
ND200	200	600	2.5
ND300	300	500	3.75
ND400	400	400	5
ND500	500	300	6.25

Table 4.1 – Sample labelling along with corresponding flow of Ar through the bubbler and through the dilution line and estimated Ferrocene concentration. Total flow is kept constant at 800 sccm.

Upon introducing ferrocene as described in section 4.2.3 the whiteish Ar discharge turns bluish by the time ferrocene diffuses inside the capillary. After 5 min to 10 min it develops a greener portion on its top during the process, where the flowing gas enters the visible plasma region. A dark brown/black material deposits on the walls of the capillary during the process (Figure 4.2b). When the products are collected on a Si substrate, we observe a deposition which is light brown/yellow at the centre in correspondence of the capillary exit (approximately 1 cm far), and a whiteish film around (Figure 4.2a).

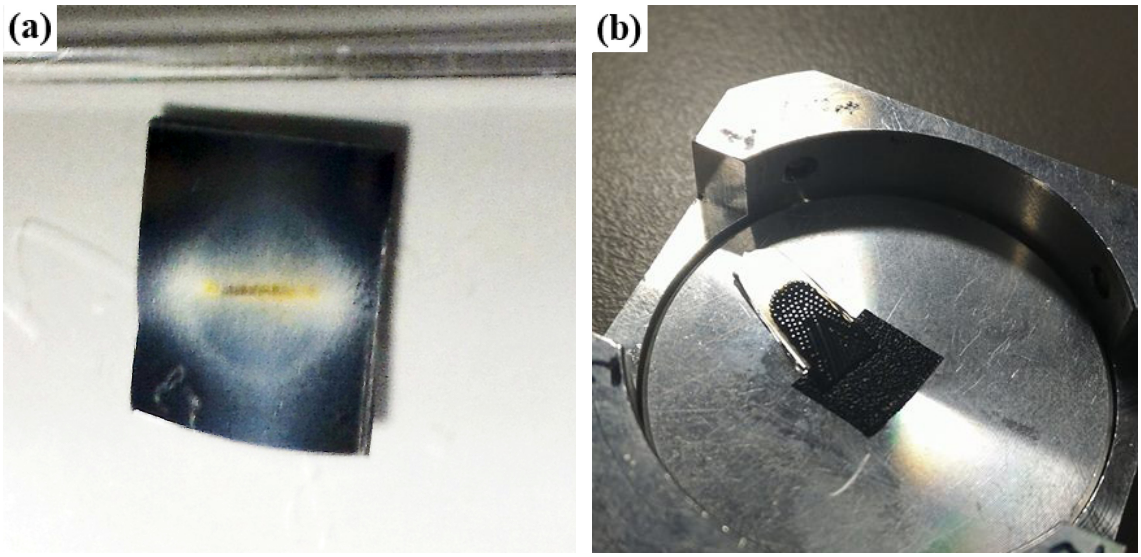

Figure 4.2 - (**a**) Picture of a sample in the ND400 conditions deposited on a Si substrate without scanning the stage (**b**) photograph of a fragment of a capillary used for a long test process mounted on a SEM sample holder, showing the black deposit on its inner surface. The dots have a metallic reflection appearance and are due to filamentary discharges appearing over 1 hour of processing time.

Also, the throughput of the process appears to be increasing with increasing flow of ferrocene through visual estimation. In fact, for the same processing time, the amount of deposit directly collected on a Si substrate placed underneath the capillary exit is clearly visible for ND500, losing visibility for lower flows. When the product is directly collected on pure ethanol, the solvent remains transparent.

Transmission electron microscope is used to study the structure and morphology of the products. In this case, only 3 mL of ethanol is used in the vials for collection, in order to reach a good concentration for drop casting on TEM grids, without incurring in unnecessary contamination and avoiding drying artefacts. Bright-field images reveal that the outcome of the process is mostly composed by well dispersed nanocrystals. Figure 4.3a shows a region highly populated of particles for the ND400 conditions, along with an energy dispersive x-ray (EDX) spectrum of the same area. The EDX in this area shows that most the signal comes from carbon species, along with a minor presence of Si, Fe and Cu. It is not possible to estimate the composition of particles from this spectrum though, because the particles are supported on a carbon film. The Cu signal originate from the grid material, while silicon probably originates from the etching of the glass capillary during the plasma process. Iron is found in low contents, always within 1.5 %at. from EDX spectra. A close-up image reveals that the majority of the particles have regular spherical shape as testified by higher magnification images (Figure 4.3b), but there are also irregular particles that show twin boundaries and faceted particles.

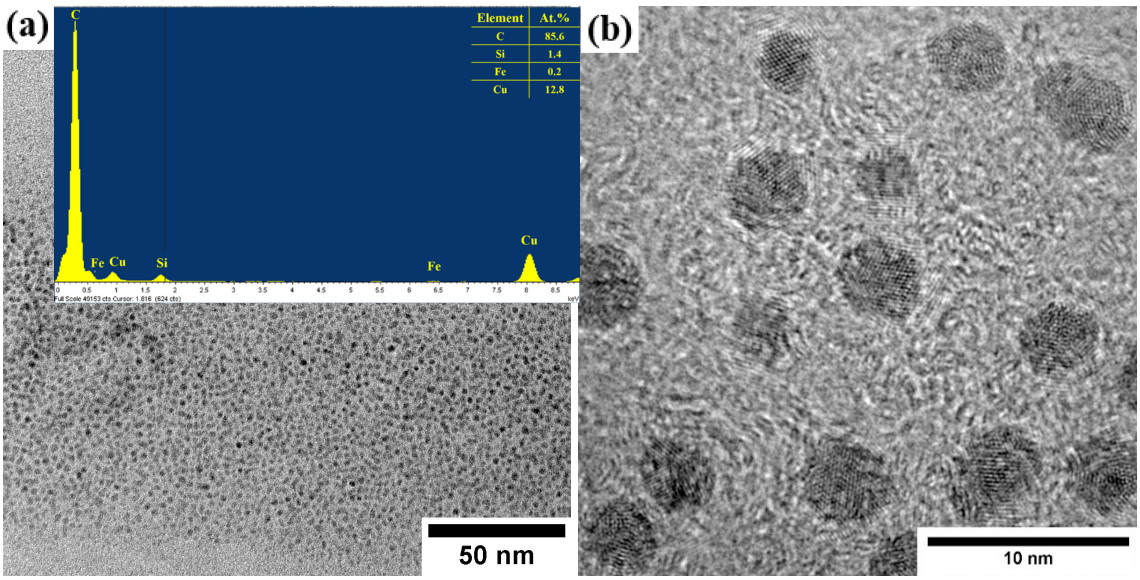

Figure 4.3 – TEM bright field image showing the morphology and crystallinity of nanoparticles. (**a**) low magnification picture showing a numerous population of well dispersed particles, the inset shows an EDX spectrum of the same area. (**b**) high magnification image showing the crystalline nature of particles, where it is possible to notice some faceted or twinned particles through the diffraction fringes

A collection of low magnification images for all the experimental conditions are used to determine average diameter of particles, measuring at least 500 particles (irrespectively of their crystalline nature) with the image analysis software ImageJ. The software helps cleaning the images from the background noise and enhancing the contrast and the measurements are carried out by determining the area of lower contrast regions with a threshold size determined by the size of background noise speckles (usually only features bigger than 1 nm are accounted for). Then by assuming a spherical shape, a diameter is extracted for each particle. A statistical distribution is then calculated by counting the number of particles per diameter range (Figure 4.4). The size distributions obtained are fitted well with lognormal distributions. Lognormal distributions usually represent the size distribution of small particles which undergo growth phenomena, hence showing a pronounced tail at higher size values. However, the better fit of lognormal distributions of our data can be artificial, because of the low size threshold that has been imposed to distinguish particles from noise speckles in the image analysis software.

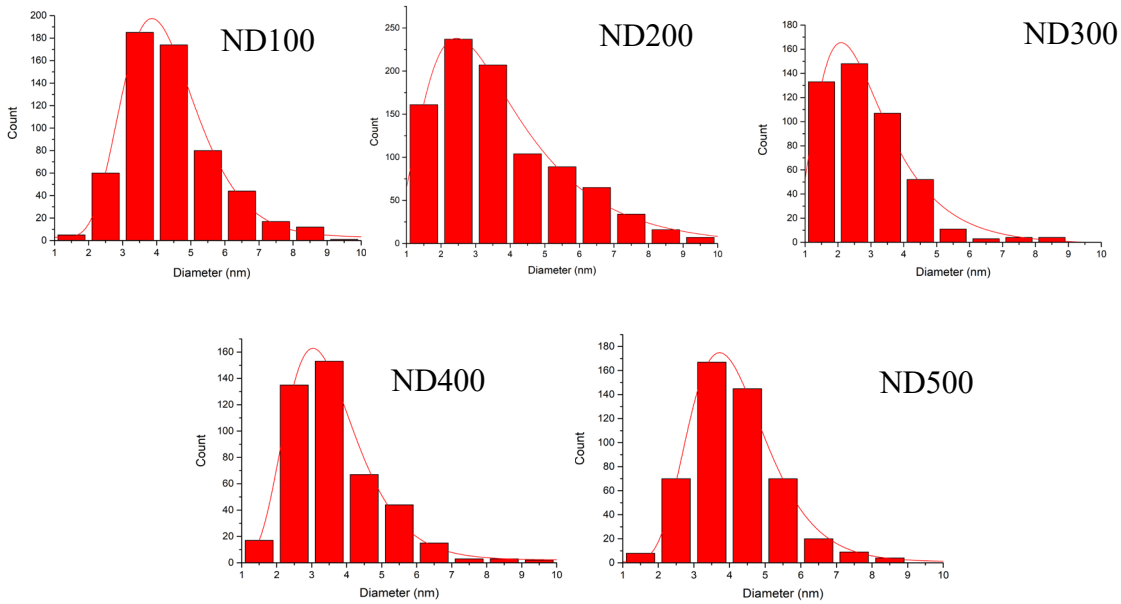

Figure 4.4 – Particle diameter frequency distribution obtained from low magnification TEM images counting approximately 500 particle per sample, measuring the area through ImageJ software, and calculating the diameter assuming a spherical shape and relative log-normal fitting of the histograms.

For this reason, the mode of the distribution (the value corresponding to the more frequent diameter in the distribution) has been chosen as the value for comparing samples synthesized with different precursor flow (Figure 4.5), instead of the mean diameter. The diameter is found to slightly vary with the precursor concentration in a non-linear fashion. It shows bigger particle size above 4 nm in the extreme cases (ND100 and ND500) and a

minimum diameter of 2.6 nm for ND300 conditions, hence at intermediate precursors concentration. Size distributions show a small variance between 1 nm and 2 nm (Figure 4.5) which means that the sizes are distributed in a narrow range in most of the cases. The ND200 sample shows a quite different distribution, with an increased number of smaller as well as larger particles, with the latter ones being cumulatively more numerous.

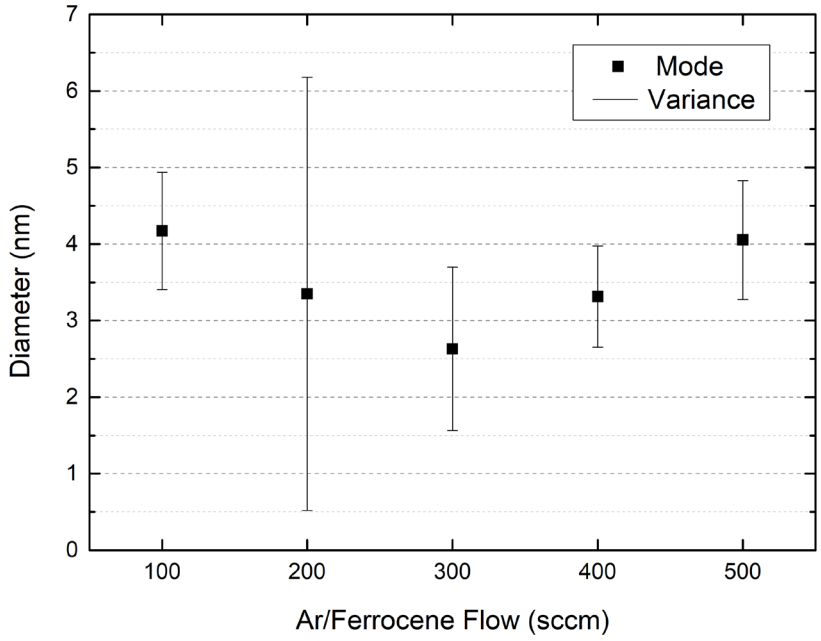

Figure 4.5 – Mode (symbols) and variance (error bars) of the fitted lognormal distributions with relative standard errors as a function of the precursor flow. The distribution modes show a minimum at intermediate flow conditions. Apart from the ND200 conditions the variance of the distributions is within 2 nm, so particles are all very similar in size.

Table 4.2 reports the fitting parameters values and the statistical significance of the log-normal distributions.

Sample	Mode	Std. Err.	Mean	Std. Err.	Variance	Std. Err.	Adj. R-Square
ND100	4.17	0.03	4.34	0.03	1.5	0.1	0.994
ND200	3.3	0.2	3.9	0.2	5.6	0.5	0.980
ND300	2.63	0.07	2.94	0.09	2.1	0.4	0.985
ND400	3.31	0.06	3.49	0.07	1.3	0.2	0.985
ND500	4.05	0.03	4.2	0.03	1.5	0.1	0.996

Table 4.2 – Output of the lognormal fitting, mode and mean differ significantly only when the distribution is particularly asymmetric, the adjusted R^2 coefficient is computed to show the statistical significance of the log-normal fitting.

Along with the particulate product, polycrystalline agglomerates (Figure 4.6a) and some regions where there are onion-like and tube-like "particles" (Figure 4.6b) are also present, with relatively low frequency. However, in the lowest and highest precursor flow conditions (ND100 and ND500 respectively) these features are more common. In both cases it is easy to spot phase contrast fringes typical of graphite (002) planes with 3.3 Å d-spacing.

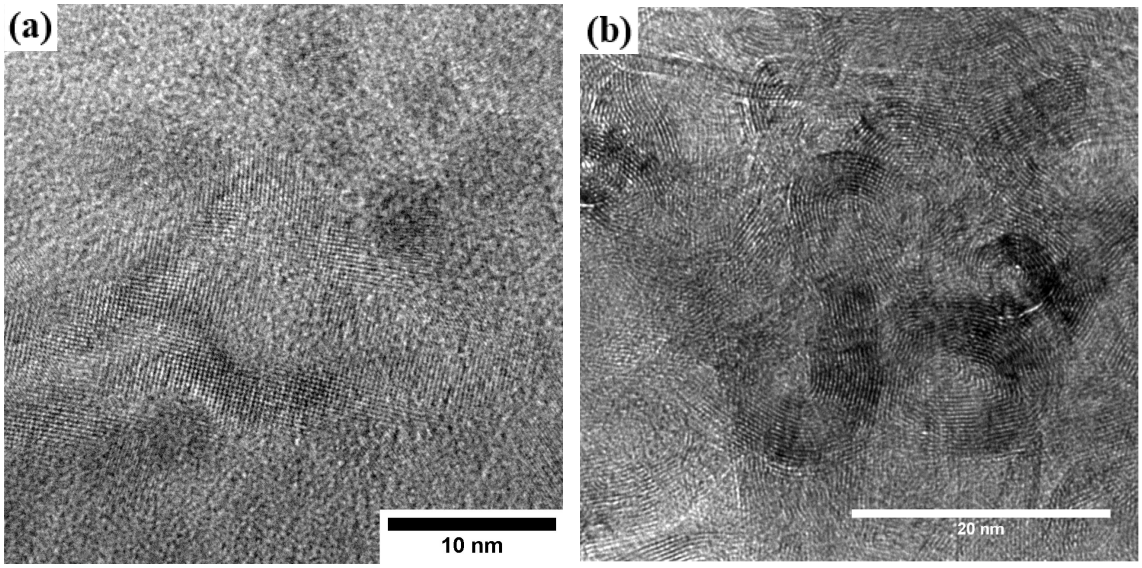

Figure 4.6 – Examples of (**a**) graphitic (**b**) and onion-/tubular- like formations found on samples. While for most of the conditions are rare, in the minimum and maximum precursor flow conditions they are more common.

From high-resolution TEM (HRTEM) imaging and selected area electron diffraction (SAED) patterns it is possible to understand the crystalline phase of particles. Particles commonly show three different fringe spacings in HR images (Figure 4.7), the most common belonging to electron diffraction from atomic planes with interplanar spacings of 2.06 Å, 1.77 Å and 2.17 Å, in order of occurrence frequency (see Table 4.3) and no clear relationship with size or shape. The crystalline planes observed are consistent with different crystalline phases of diamond, which have been reported[32,35–39] for small particles in both natural and synthetic samples; the d-spacing values that have been measured after fast Fourier transform (FFT) filtering and line profiling are summarized in table 4.3. The majority of particles show reflections from a set of planes with 2.06 d-spacing which can be associated to the reflection from (111) planes of either the common cubic phase (*c*-) of diamond or the hexagonal phase (denoted as *h*- also known as *lonsdaleite*) or a less known face centred cubic phase (FCC) which is of recent discovery called new-diamond (*n*-). Less frequently the particles show 1.77 Å and 2.17 Å d-spacing,

which can be assigned to n-diamond (200) and h-diamond (100) crystal planes respectively.

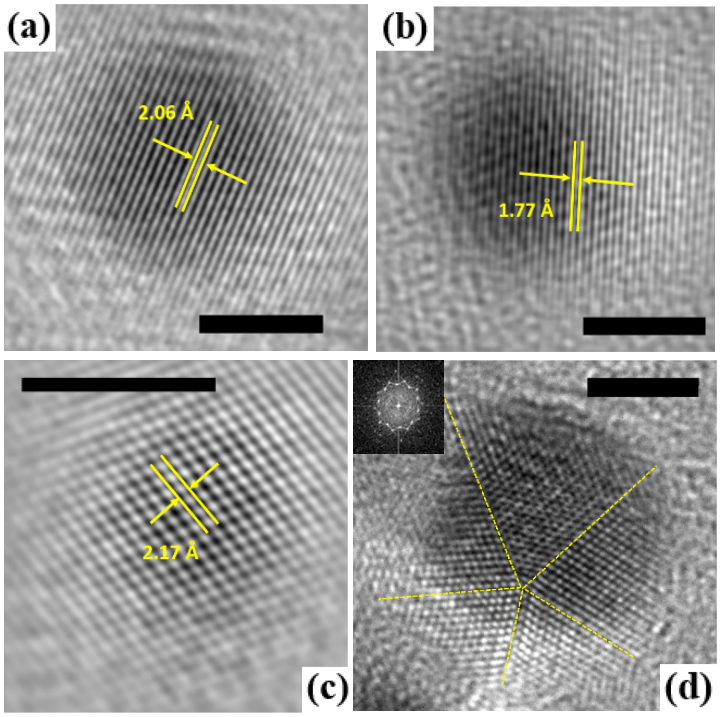

Figure 4.7 – FFT-filtered HR-TEM images of selected particles showing fringes assignable to different polymorphs diffracting family of planes (**a**) c- or n- diamond (111) or h-diamond (002) (**b**) n-diamond (200) (**c**) h-diamond (100) and (**d**) multiple twinned particle with decahedral symmetry, the broken lines mark the twin boundaries between (111) planes and the inset shows the images power spectrum. The scale bars are 3 nm long.

d-spacing (Å)	Cryst. Planes/Phase	Occurrence (%)	Literature
2.06	c-(111), n-(111), h-(002)	80	2.06
1.77	n-(200)	15	1.78
2.17	h-(100)	5	2.18

Table 4.3 – Summary of the three common diffraction fringes shown by particles in HR-TEM, associated crystal phases and planes, approximate occurrence frequency and reference values from literature. The total number of particles analysed for these statistics is approximately 20 per sample from different areas of each grid. Only spherical particles with clear diffraction fringes were considered, thereby ignoring twinned particles and irregularly shaped ones.

Also, there is a considerable number of particles which show different numbers of twin boundaries, the most numerous having icosahedral and decahedral symmetry (an example of a particle displaying the 5-fold twinning vertex is shown in figure 4.7d). This

configuration typically happens along the (111) planes of an FCC particles, and may arise from the association of tetrahedral subunits under strained conditions.

Selected area diffraction patterns in particle-abundant areas always show diffraction rings composed of bright spots, which is the signature of large numbers of randomly oriented crystalline particles (Figure 4.8). The SAED patterns (ND100 in Figure 4.8a, ND200 in Figure 4.8b, ND300 in Figure 4.8c, ND500 in Figure 4.8d and ND400 apart in Figure 4.9a) are similar for most of the samples as the rings have similar distribution and the same radius. For this reason, only the analysis of ND400 SAED pattern will be shown (Figure 4.9a), as it has a clearer and more informative pattern. The SAED patterns can be fitted very well by the diffraction pattern of an FCC lattice with 3.55-3.58 Å parameter (Figure 4.9a). The ND500 case is an exception as it was not possible to identify a clear pattern for all the SAED patterns acquired, in Figure 4.8d there is an example of such

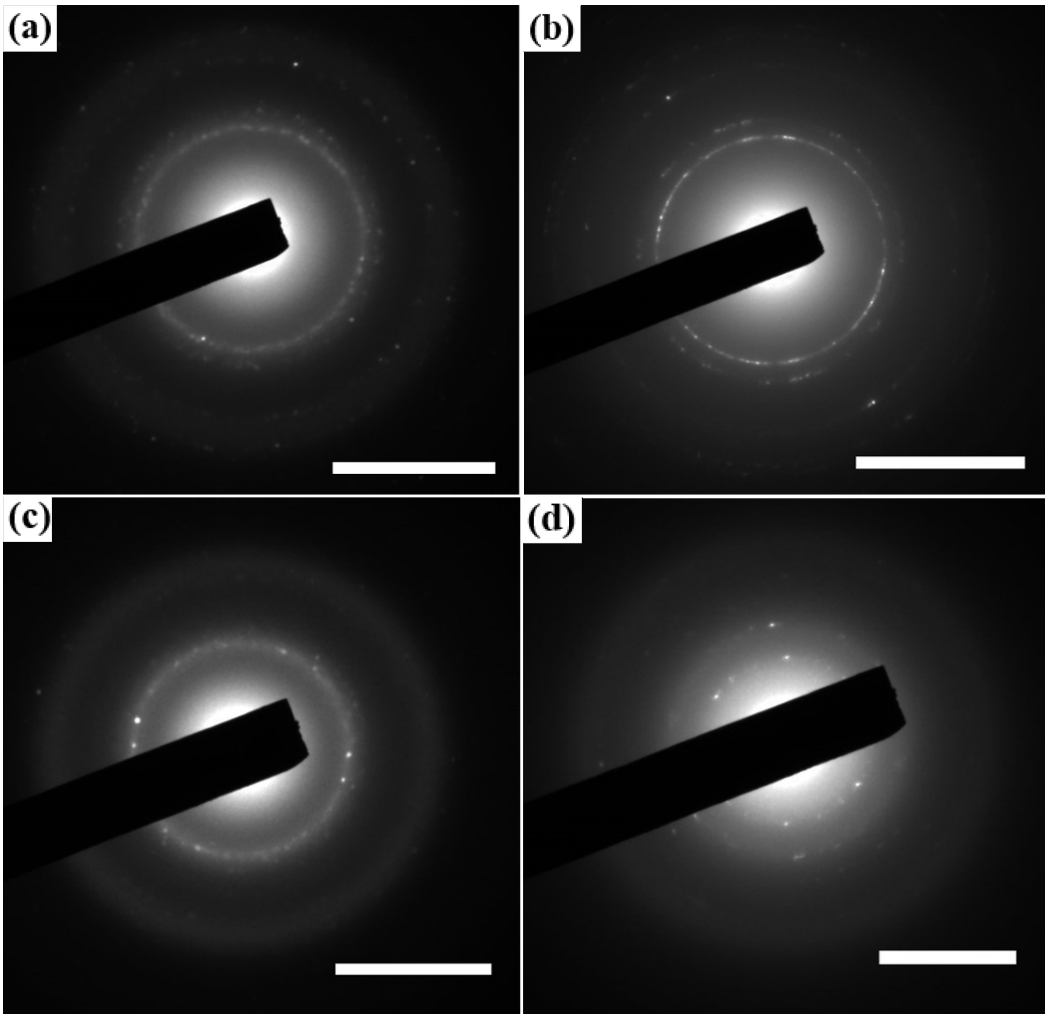

Figure 4.8 – SAED patterns of sample area densely populated with nanoparticles for different conditions (**a**) ND100 (**b**) ND200 (**c**) ND300 (**d**) ND500. The patterns show similar features except in the ND500 case. Scale bars are all 5 nm^{-1}.The SAED pertaining to ND400 conditions is shown in figure 4.9, as it is the clearest of the patterns acquired and will be analysed as representative for most of the samples.

unidentified diffraction pattern, while in Figure 4.9b a clear pattern from graphitic crystal phases.

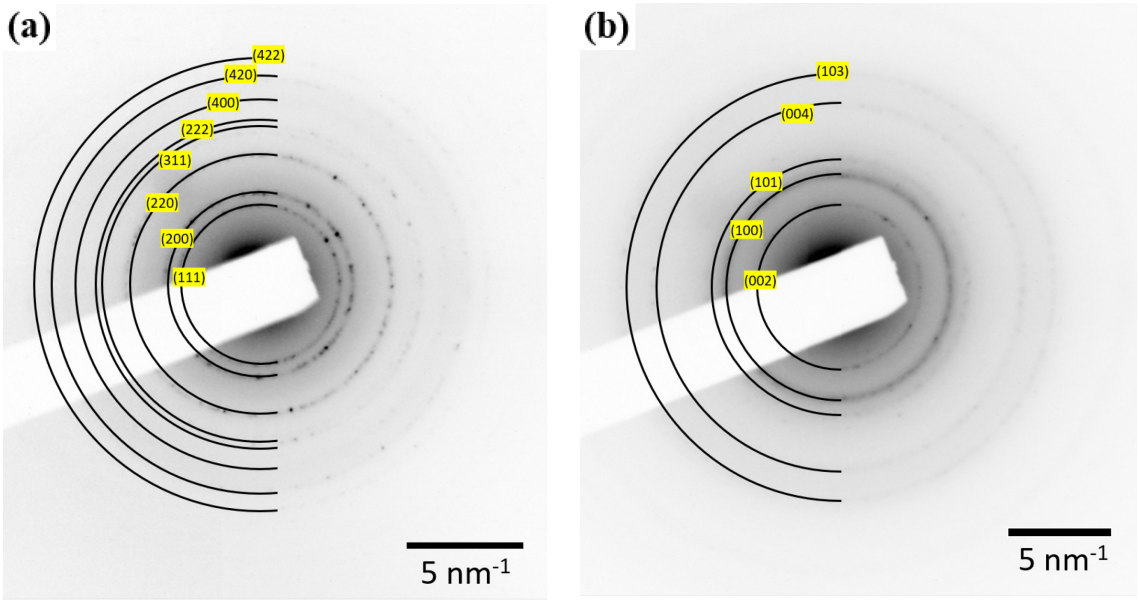

Figure 4.9 - Analysis of SAED patterns of collections of particles for (**a**) ND400 labelled to an fcc structure with a= 3.56 Å, recognised as the n-diamond phase. (**b**) Pattern found in some areas of ND100 and ND500 samples, assignable to graphite.

The common bulk diamond cubic structure (called *diamond cubic structure*, same as c-Si) is described as two compenetrated FCC lattices translated by a quarter of diagonal of the unit cube with lattice parameter of 3.57 Å. It can be seen also as an FCC with two C atoms per unit cell. Diffraction selection rules for the diamond cubic structure do not allow the reflections with even Miller indexes whose sum is not multiple of 4 (which gives destructive interference between diffracting waves).[40] In the SAED patterns measured the (200), (222) and (420) rings should not be present if the crystal structure was the common diamond cubic structure. Recently, different groups reported the occurrence of such forbidden reflections[32,35,41–43] for nanocrystalline diamond. Hence, it was inferred that a FCC phase of diamond (*n-diamond*) can exist at the nanoscale, even though the nature of this polymorph is still debated.[44,45] In fact, some authors explain these diffraction features associated to n-diamond as the result of multiple diffraction events on twin boundaries of multiple twinned particles in HR-TEM studies.[45] Also the hexagonal phase is still debated in its nature as a separate polymorph.[44]

In the present study, the presence of non-twinned particles which show directly a d-spacing of 1.77 Å in HR-TEM images (e.g. Figure 4.7b) would be consistent with the existence of n-diamond as a distinct crystalline phase. However, a big number of particles

that show multiple twins are found in the samples (e.g. Figure 4.7d). The analysis cannot be conclusive, as the error associated to d-spacings from the measured SAED is on the order of 2% and does not permit the unambiguous determination of this phase as a separate one, as features may be undistinguishable from graphitic ones or eventually other predicted polymorphs of carbon at the nanoscale. At the same time HR-TEM images of single particles show diffraction fringes of family of planes casually oriented in the right way with respect to the beam and usually are not enough to identify a certain crystalline phase alone.

X-ray photoelectron spectra were recorded after the samples were inevitably exposed to the atmosphere. Given the surface sensitivity of this analytical technique (~10 nm), adventitious carbon and oxygen may complicate the analysis. In order to avoid ambiguities, a layer of gold is sputter-deposited on the samples and use Au 4f core levels at 88 eV binding energy as calibration value. The gold is sputtered on the sample through a mask which leaves undeposited areas for the XPS measurements. In this way, the deposited gold and the sample share the same electrical potential and if charging occurs, the binding energy values can be shifted according to the reference Au 4f peak shift. Only the samples synthesized with higher precursor concentration were analysed (ND300, ND400 and ND500) by XPS because of the low throughput of the lower precursor flow conditions which do not produce significative amounts of material and increasing the deposition time would result in poor repeatability given the deposition of material at the

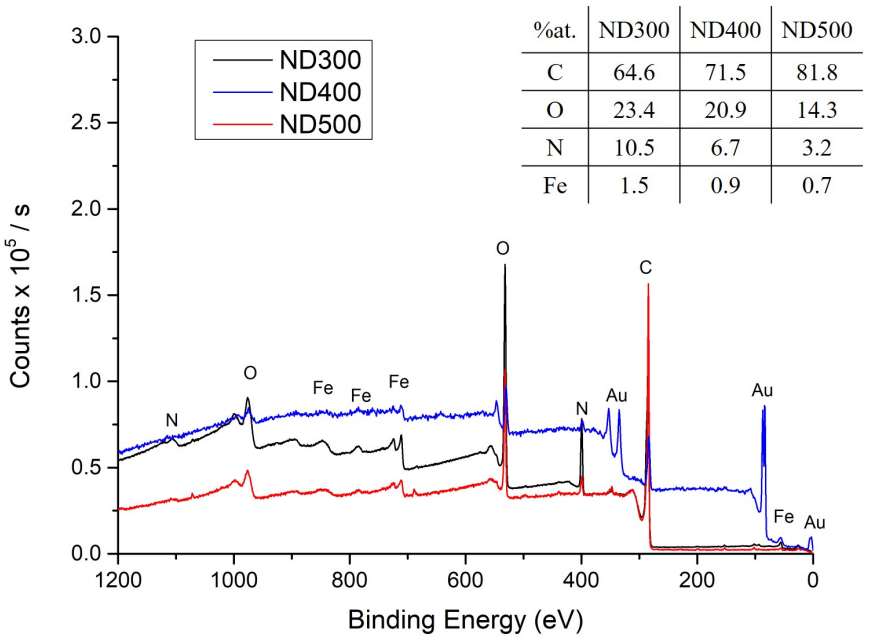

%at.	ND300	ND400	ND500
C	64.6	71.5	81.8
O	23.4	20.9	14.3
N	10.5	6.7	3.2
Fe	1.5	0.9	0.7

Figure 4.10 – XPS survey spectra of the analysed samples. Quantification of atomic percent is made by peak area analysis of the indicated peaks. In the ND400 spectrum, also the Au-related peaks are visible, hence the relative Au peaks were excluded from atomic percent calculations.

capillary walls. XPS survey spectra (Figure 4.10) and relative peak area analysis estimates the composition of samples as mostly C together with O (10-24 at.%), Fe (<1.6 at.%), and N (<11 at.%).

The acquired XPS high resolution spectra show different features which unambiguously indicate the presence of sp^3 bonding in the samples (figure 4.11a). The high resolution XPS spectra in the C 1s region have been de-convoluted in two different orbital hybridisations, sp^3 at 284.8 eV and sp^2 at 284 e V and C in the C-O bonding relative to common air-borne adventitious species.

The peak area ratio of the resulting deconvoluted peaks shows a trend with increasing precursor flow, giving an increased proportion of sp^3 species in the higher precursor flow conditions (Figure 4.11b). High resolution of the Fe 2p region shows a weak signal (figure 4.11c) whose peaks are suggest also the presence of iron oxide phases (FeO at 709.6 eV, Fe_2O_3 at 710.8 eV, metallic Fe at 706 eV and relative spin-orbit components).

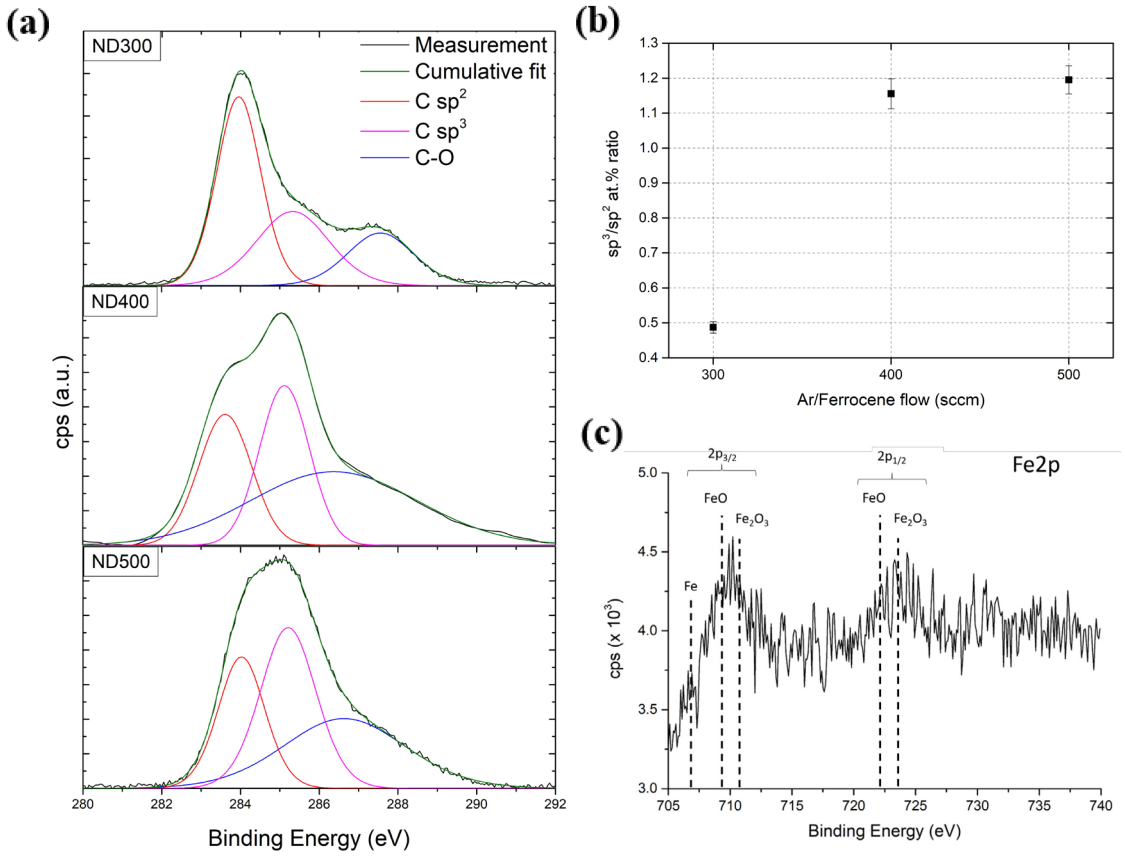

Figure 4.11 – (**a**) XPS C 1s region spectra for the samples considered clearly showing peaks assignable to sp^2, sp^3 C-C bonds and others linked to oxygen usually found for samples exposed to atmosphere. The same peaks have been used for fitting. (**b**) Peak area ratios for sp^2 and sp^3 C-C bonds extracted from the fitting of C 1s spectra showing a higher ratio for samples with higher precursor flow, the analysis does not distinguish adventitious carbon, inevitably present after exposure to the atmosphere. (**c**) Traces of iron found in the Fe 2p region show weak peaks whose binding energy is typical of iron oxide phases.

Raman spectra of bulk phases of carbon have some distinctive features that permit their straightforward identification. Instead, Raman spectra of carbon nanostructures are somewhat more complex because phonon confinement at the nanoscale introduces substantial modifications.[46] Furthermore, mixed phases may show a large variety of peaks when more than one phase is present.[47] The spectra acquired in this study (Figure 4.12a) indeed show broad features, which can be either attributed to the presence of small particles or to the co-presence of amorphous materials with various kinds of bonds. However, some peaks in the spectra acquired for the samples in this study can be distinguished, analysed and compared with previous studies.[32,46,47] It is worth noting that the cross section for Raman scattering of carbon is wavelength-dependent, with the sp^3-associated scattering portion being more intense when excited at UV wavelengths. So the excitation wavelength in use in this case (He-Ne 632.8 nm) is not ideal to selectively excite sp^3 related vibrations[47] while the sp^2 components will be dominant in determining the overall scattered light intensity, nevertheless peaks which are readily associated to sp^3 vibrations can be observed.

The typical nanocrystalline diamond spectrum is generally analysed in 5 peaks, a small diamond peak at 1330 cm^{-1}, D and G bands related to sp^2 components at 1350 cm^{-1} and 1550 cm^{-1}, and two peaks at 1150 cm^{-1} and 1480 cm^{-1} which have been recently assigned to trans-polyacetylene vibrations.[47] In this study the spectra show two broad peak structures near 1330 cm^{-1} and 1580 cm^{-1} and a shoulder peak at 1150 cm^{-1}. The spectra have been deconvoluted in the mentioned five contributions with Voigt profiles (convolution of Gaussian and Lorentzian distributions). The reported Raman shift and full width at half maximum (FWHM) for bulk single crystal diamond are 1332 cm^{-1} and 1-2 cm^{-1} respectively. At the nanoscale both quantities change as the shape of the diamond related peak becomes asymmetric and the Raman shift decreases (e.g. 1326 cm^{-1} for 7 nm, 1300 cm^{-1} for 3 nm)[46] and FWHM increases (> 30 cm^{-1}) with respect to bulk values, in a size-dependent fashion (see Figure 4.13a). The numeric values, though, vary significantly depending on the model adopted and the samples considered. Recently, *Osswald et al.*[46] made an extensive study of Raman spectra of nanodiamonds as a function of increasing size. This is the only modelling effort valid for nanoparticles, while previous studies focused on microstructured films. They put forward a semiempirical relationship to calculate the broadening of the diamond peak as a function of particles size, caused by the change in phonon lifetime:[46]

$$\Gamma = A + \frac{B}{L^2} \qquad \text{Eq. 4.2}$$

where Γ is the FWHM of the peak, L is the crystal size in nm, A = 11 cm^{-1} and B = 491.25 cm^{-1} nm^2 are proportionality constants. The same authors report also that the presence of defects as the twinnings we observe, result in smaller coherence domains for Raman scattering and systematically smaller calculated L with respect to the actual crystal size. In all spectra acquired in this study (Figure 4.12a), the fitted diamond peak show Raman shifts smaller than 1332 cm^{-1} (Figure 4.12b), especially for the ND400 sample (1307 cm^{-1}) and particularly large FMWH values (Figure 4.12c) from 100 cm^{-1} to 150 cm^{-1}.

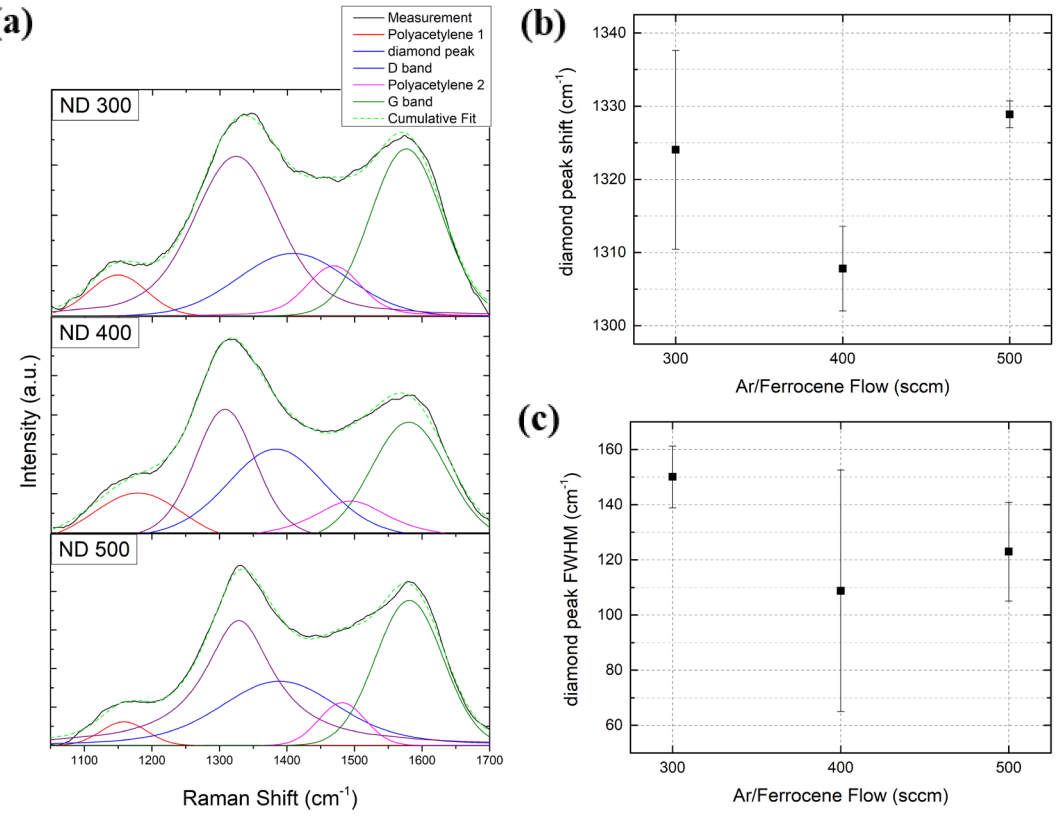

Figure 4.12 – (**a**) Visible Raman spectra of the considered samples in the range of interest for Carbon polymorphs and relative deconvolution. Plots of the values relative to the diamond peak extracted from the fit: (**b**) Raman shift and (**c**) full width at half maximum. Error bars represent std. errors on the fit.

By calculating the crystal size from equation 4.2 values of 1.9 nm , 2.2 nm and 2 nm are obtained respectively for ND300, ND400 and ND500 (Figure 4.13b). By comparing these values with the ones obtained from TEM size distribution statistics, it is evident that the trend in diamond peak shift and FWHM does not correlate very well with observation in

TEM. The ambiguity of interpretation of Raman spectra in respect to TEM size evaluation can be due to different reasons:

1. Underfitting of Raman spectra due to the presence of different polymorphs, size dispersion or the presence of twinned particles;
2. TEM size evaluation does not distinguish on the possible phases in which particles are found, and the portion of higher diameter particles counted in the size distribution could be entirely due to graphitic particles

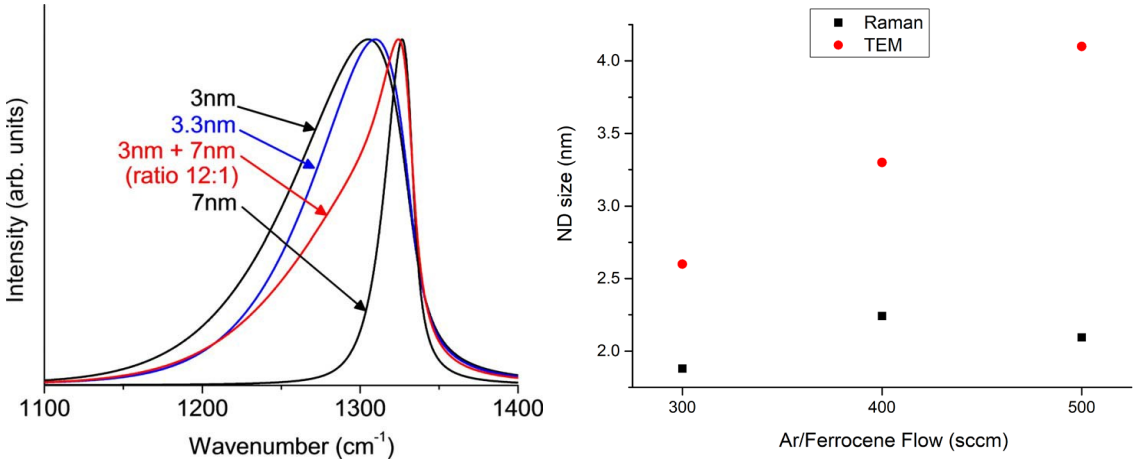

Figure 4.13 – (**a**) Simulated Raman peak for phonon confined NDs with different size and distribution. The peaks tend to become asymmetric, wider and with lower Raman shift maximum.[47] (**b**) Comparison of particles size obtained through eq. 4.2 and from TEM size distribution analysis.

Nevertheless, the Raman spectra show convincing evidence about the presence of nanodiamonds, more so in the ND400 and ND500 cases, where the diamond peak is at lower Raman shifts than the bulk value.

In order to show that the synthesis conditions can easily result in products with no nanodiamond, additional conditions were studied to explore the parameter space just around the sample that gave the best result. The experimental parameters used for sample ND400 have been repeated in two different variations:

1. Lower power (40 W) and same total flow (800 sccm)
2. Lower total flow (400 sccm) and same power setting (80 W)

In both cases the particles produced are not the same as in the conditions explored until now, both compositionally and structurally. In case-1, agglomerates of crystalline particles are found in TEM analysis, an example is shown in figure 4.14.

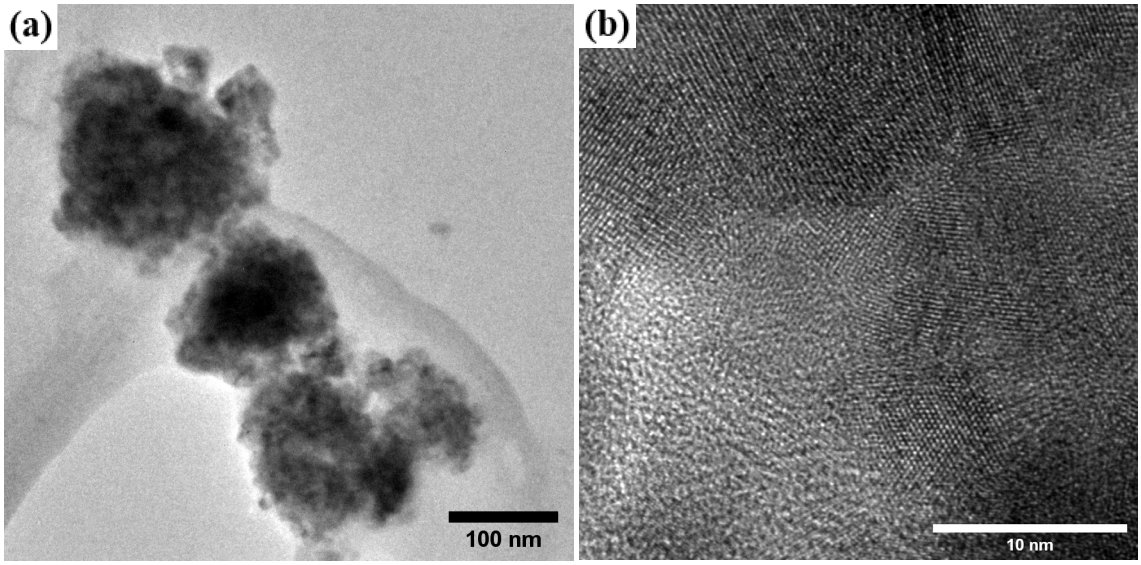

Figure 4.14 – (**a**) Low magnification image of agglomerated particles found on low power samples and (**b**) their high magnification detail showing their crystalline structure and morphology.

Further analysis of selected area diffraction pattern and EDX in one of these areas shows that the agglomerates are most probably composed by a mixture of iron oxides, hematite and magnetite (Figure 4.15).

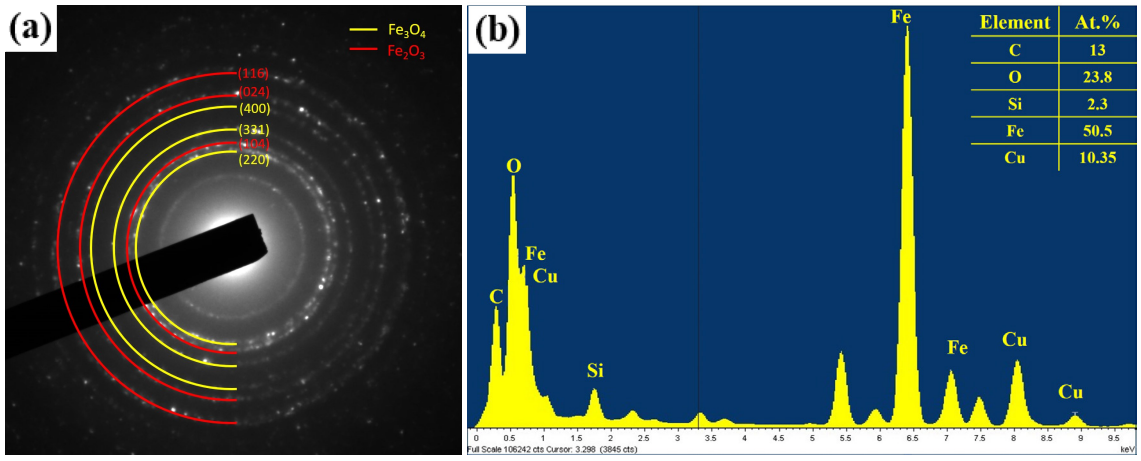

Figure 4.15 – (**a**) SAED pattern of an agglomerate of particles similar to the one pictured in figure 4.14, labelling the diffraction rings fits well with a mixture of hematite and magnetite, the two most common iron oxides. (**b**) EDX spectrum of the same area showing a prominent peak from iron species.

In case-2, when the product is directly collected in pure ethanol, the colloid turns light brown over time and after a few hours brown agglomerates precipitate. This is particularly different from the higher total flow conditions, for which the solution remains transparent after the deposition and no agglomeration or precipitation con be observed. TEM analysis shows very small particles, which are embedded in an amorphous matrix and do not show the same diffraction fringes of the ND ones (Figure 4.16). In this case EDX and SAED were not successful on identifying the chemical composition of the particles but from HRTEM diffraction fringes it is concluded that the particles are sub-stoichiometric iron oxide faces.

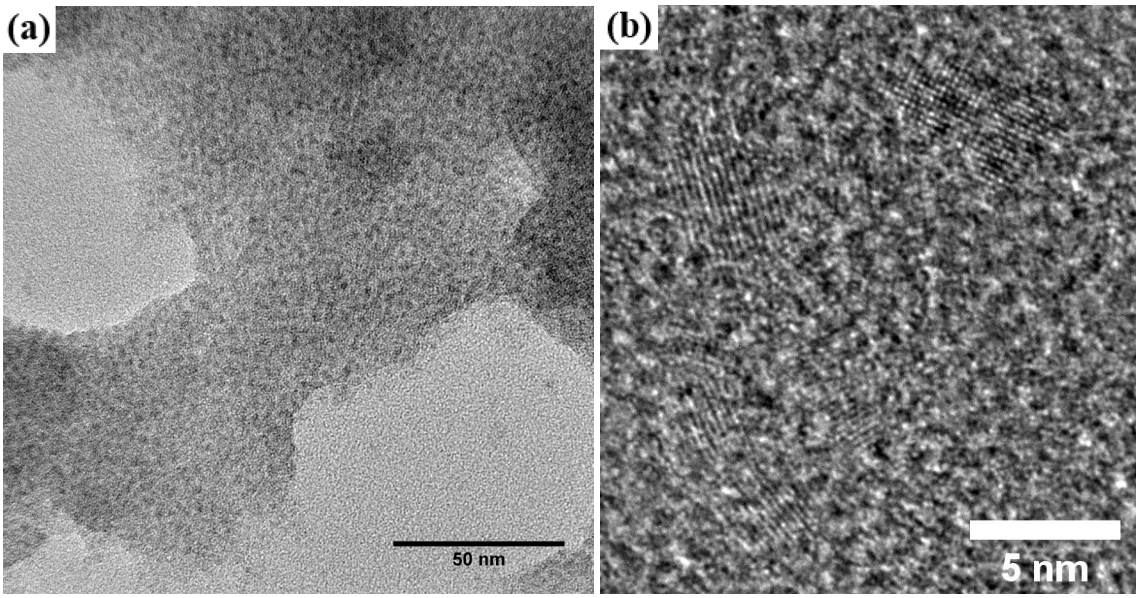

Figure 4.16 – Typical output of the process when ferrocene concentration is too high (for example with 400 sccm total flow without additional Ar diliution) or power is too high (120 W), (**a**) low magnification appearance and (**b**) close-up of one of these areas showing the composition of small crystalline particles which have been assigned to FeO_x through study of HRTEM images FFT and the structureless embedding matrix.

4.3.2 Addition of Hydrogen

The most common method to produce NDs has been the detonation of carbon containing explosives, a method that also results in mixture of different carbon polymorphs. For this reason, researchers have made efforts to purify the output from non-diamond species and a standard procedure has been put forward, the most successful relying on subordinating samples to multiple acid baths.[20] A method to phase-select the products within the synthesis process would be desirable for simplicity and cost effectiveness. In a study involving a DC micro-hollow cathode discharge that produced NDs from ethanol, hydrogen was introduced within the gas mixture and made possible to selectively etch the

non-diamond species.[32] In this study the same idea is tested considering the similarities between the two systems.

A Hydrogen mixture was introduced in the system from a premixed cylinder (2% in Ar) through a parallel gas input line. The concentration was varied by changing the flow against a fixed total flow of 800 sccm, the ND400 conditions were chosen as the best starting conditions as according to Raman (Figure 4.12b) and TEM analysis (Figure 4.9a) resulted in the most unambiguous presence of ultra-small NDs. At first it is noticed that a higher power of 100 W (from the supply, vs 80 W previously used) is needed to sustain the discharge reliably, and even in this case it is possible to sustain the discharge for no more than 15 minutes, after which the plasma becomes unstable and develops hotspots on the capillary walls which lead to the melting of capillary. The discharge changes appearance yet with the smallest amount of hydrogen mixture attainable with the mass flow controllers used for this study, turning whiter. Table 4.4 summarizes the synthesis parameters for samples which successfully output particles.

Label	ϕ_{H_2} (sccm)	$\phi_{bubbler}$ (sccm)	ϕ_{Ar} (sccm)	[H_2] (ppm)
NDH10	10	400	390	250
NDH20	20	400	380	500

Table 4.4 – Summary of the samples produce with H_2 admixture, labelling and experimental parameters.

TEM of the samples shows that very small particles (Figure 4.17) have been produced. For flows of H_2 mixture higher than 20 sccm, no particle is discernible in TEM.

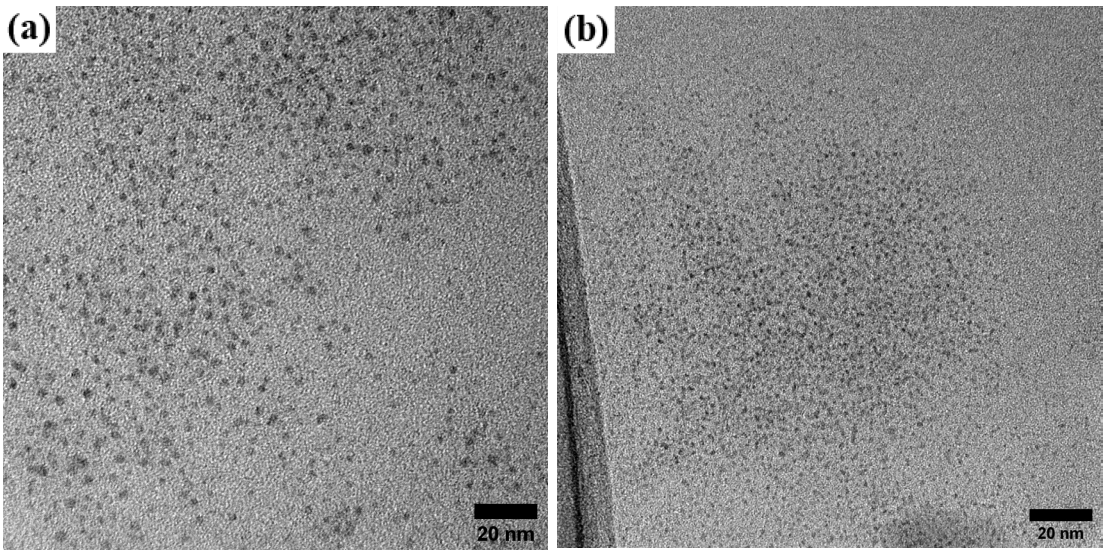

Figure 4.17 – Example of low resolution TEM images of the hydrogen process outcome showing very small dispersed particles. (**a**) NDH10 and (**b**) NDH20.

It was not possible to obtain a clear SAED pattern for any of the samples synthesized with hydrogen admixture. The intensity of the diffraction maxima depends on both the density (spatial) of diffracting elements in the scoped area and their size, with larger particles giving clearer diffraction peaks. It is believed in the present case that the smaller size of particles (with respect to the synthesis conditions without hydrogen) and greater spatial dispersion of particles throughout the grid hinders the formation of clear diffraction patterns. In other words, it is not possible for these samples to find an area in the grid which is populated enough for the smaller particles to generate a clear diffraction pattern. In fact, for the same grid preparation routine, the particles are more sparsely distributed on the grid. So, assuming that the colloid is well dispersed, and the drying process gives even distribution throughout the grid, the synthesis throughput as well as the concentration of the colloid are smaller. Another evidence supporting this statement is that the amount of product deposited on solid substrates is visibly less, the more hydrogen is included in the process.

The analysis of particles size distribution (Figure 4.18) was obtained by manually measuring single particles diameter in high resolution images and it is found that average particle diameter is reduced with respect to the hydrogen-less experiments (Figure 4.2). It is possible to notice from the histograms (Figure 4.18) that the difference between the size distributions is mainly due to a much smaller population of bigger particles. Also, there is a weak trend for the average particle diameter to be smaller for higher inputs of hydrogen.

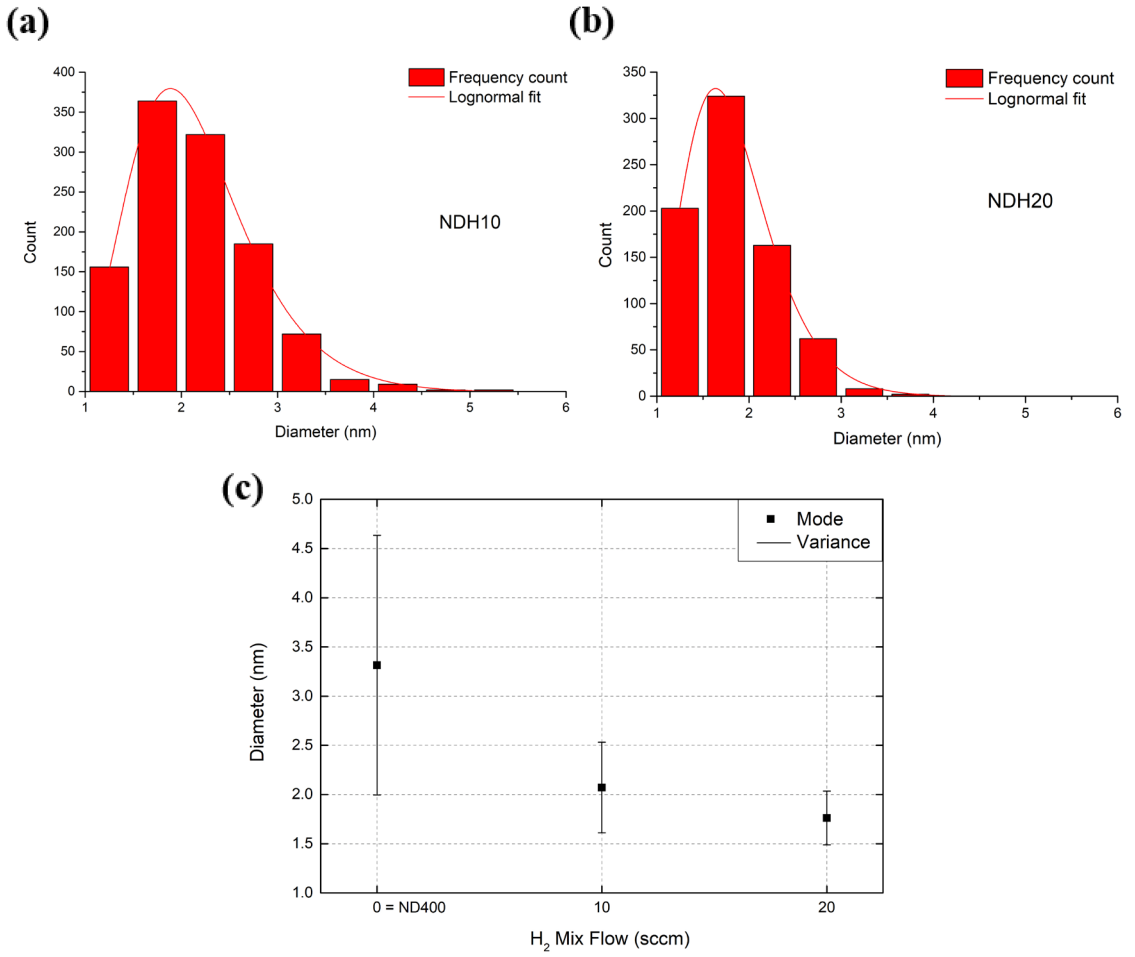

Figure 4.18 - Average diameter as a function of hydrogen mixture flow, obtained from HRTEM images and relative histograms for (**a**) 10 sccm H_2 and (**b**) 20 sccm H_2. The distributions were fitted with a log-normal function and the error bars in the data points indicate the geometric standard deviation relative to them. (**c**) The most frequent size of nanoparticles decreases upon introduction of hydrogen and the width of the distributions is also smaller, stating the particles are much more mono-sized.

The XPS spectra show that the C1s region is dominated by a double peak structure, with one of the peaks (284 eV) exhibiting asymmetry. A deconvolution results in a substantial contribution from sp^2 C-C bonds (Figure 4.19a-b), a minor sp^3 component and a prominent peak assignable to C=O bonds (288.2 eV), which could originate from

environmental contamination. The carbon spectra are lower in intensity than the samples produced without hydrogen and their structure suggests that is purely adventitious contamination. At the same time, increased amounts of Fe and Si are found throughout the samples in respect to the hydrogen-less experiments as can be observed by peak area analysis of the survey spectra (Figure 4.19c). Fe abundance is found to be on the order of 8.7-10 at.% and Si on the order of 10.6-15 at.%.

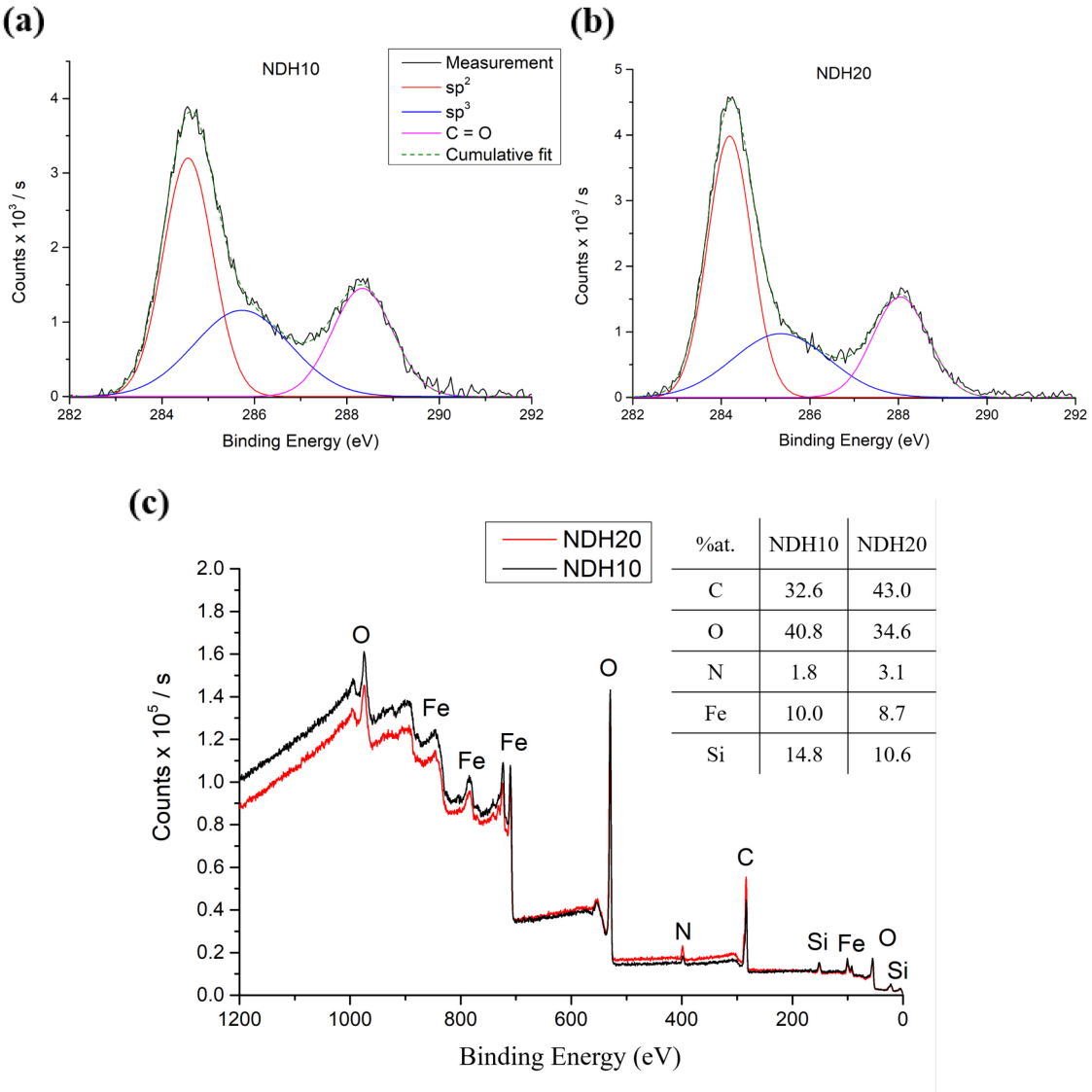

Figure 4.19 – (**a-b**) XPS C 1s and Fe 2p of the two samples produced with hydrogen admixture (**a**) NDH10 and (**b**) NDH20. (**c**) Survey spectra of the two samples and relative atomic fraction calculated from peak area analysis.

Remarkably, Raman spectra do not show any contribution from the G band (Figure 4.20), while having a pronounced peak at 1300 cm^{-1}. Austenitic iron and hematite Raman spectra also show a peak at 1300 cm^{-1}, so given the abundant presence of Iron testified by XPS, it is concluded then that the main product in this process is iron oxide nanoparticles.

In conclusion the addition of hydrogen within the process permits to obtain iron oxide nanoparticles of small diameter. The experimental results do not show any evident formation of NDs. Hydrogen may be responsible for the etching of particles or the suppression of their growth and at the same time the overheating of the capillary leads to poor sustainability of the process as well as contamination of the samples from its etching. A certain variability of the results for samples prepared under nominally same conditions is evidence also of a low reproducibility for this process. So, in the present case the purification scheme using admixture of hydrogen in the process gas is not a viable choice.

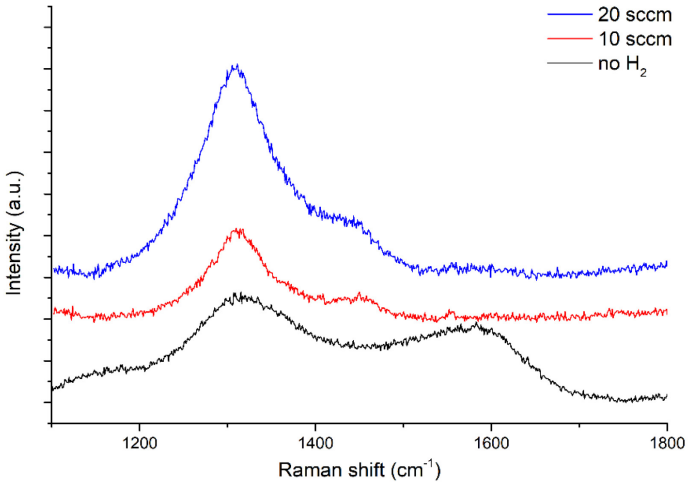

Figure 4.20 – Raman spectra of the same samples produced with hydrogen, showing a complete lack of a G band.

4.3.3 Benzene as precursor

To understand the role of precursor chemistry and on the formation process, we attempt to form NDs from benzene, a volatile liquid compound which has the same C:H ratio (1:1) as ferrocene but does not contain Iron.

Benzene is delivered to the process from a bubbler, similarly to the delivery of ferrocene. However, benzene is much more volatile than ferrocene at 25 °C (1.2 kPa at 25 °C), so that a considerably lower flow rate through the bubbler must be selected in order to have similar concentration of species delivered to the plasma. Later in this chapter, evidence is presented of substantial dissociation of ferrocene molecules within the first stage of the plasma process. Therefore, we expect that the precise molecular configuration has little or no effect on the formation of NDs. In order to tune the plasma parameters and achieve similar plasma conditions for both ferrocene- and benzene-based processes, we used

optical emission as a guiding diagnostic. In particular we varied the control parameters (e.g. applied power and flow) of the benzene-based plasma processes to produce optical emission spectra similar to those produced during the synthesis of NDs with ferrocene precursor; in particular peaks related to C_2- and CH- radicals (see also section 4.4) were considered and monitored.

A range of different conditions of power (from 60 W to 100 W) and bubbler flow (from 1 sccm to 5 sccm) have been explored with negligible qualitative differences in terms of the synthesized samples. Two representative synthesis condition with 90 W applied power at 1 sccm and 2 sccm Ar flowing through the bubbler diluted with Ar to reach 800 sccm total flow will be shown. The synthesis products appears mostly composed of structureless aggregates under the TEM electron beam (Figure 4.21a and 4.21b) in the case of 1 sccm, while at 2 sccm a structureless film coating appear on the TEM grid (Figure 4.21c and 4.21d).

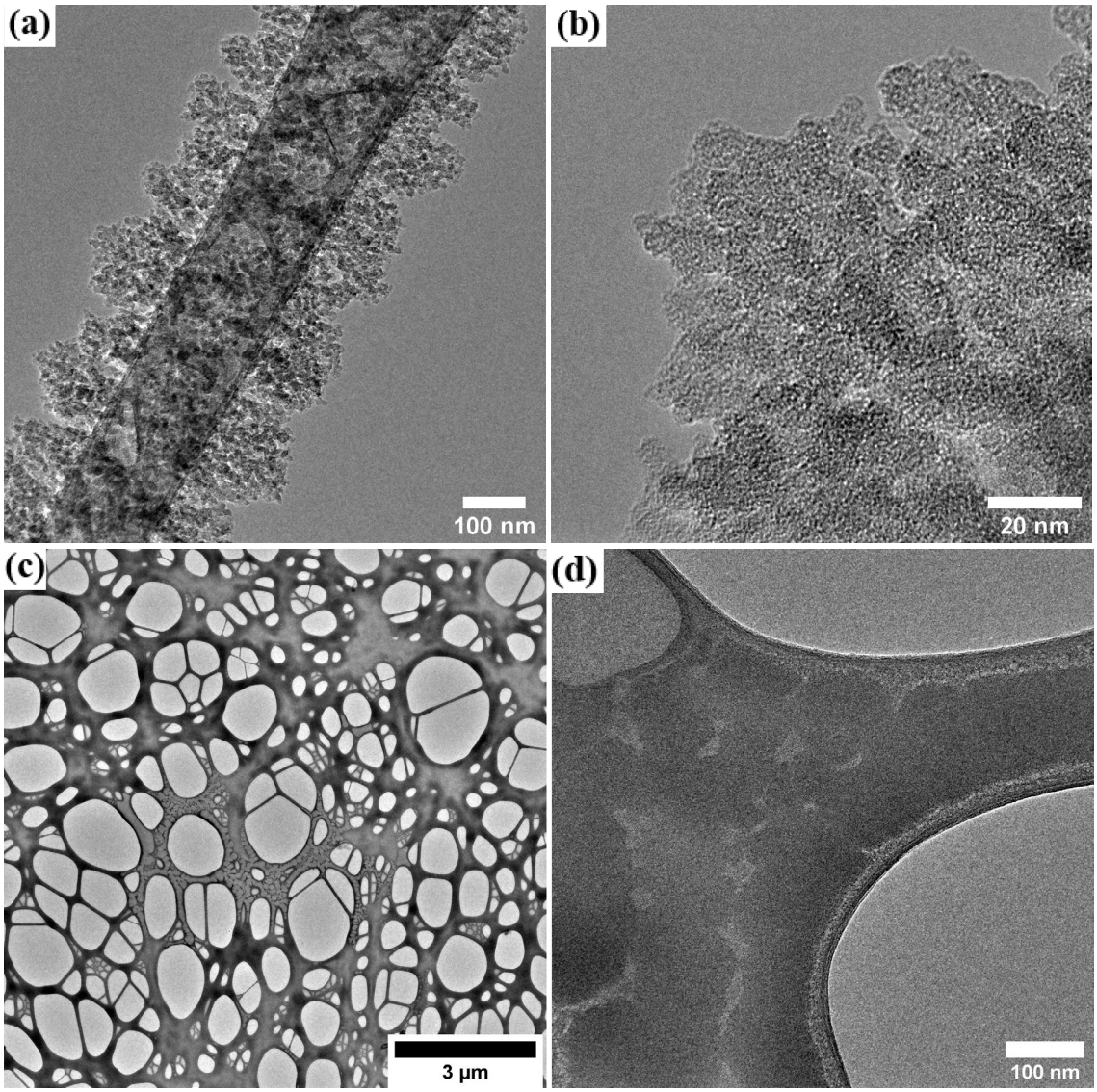

Figure 4.21 – TEM images of the benzene process for two different flows through the bubbler. (**a-b**) 1 sccm showing (**a**) low magnification and (**b**) high magnification images where no crystalline particles are distinguishable, , instead dendritic structures of amorphous material are found. (**c-d**) 2 sccm, showing a film coating the grid which appears structureless.

XPS spectra of the two samples are shown in Figure 4.22. The deconvolution of spectra shows a small amount of sp^3-bonded C.

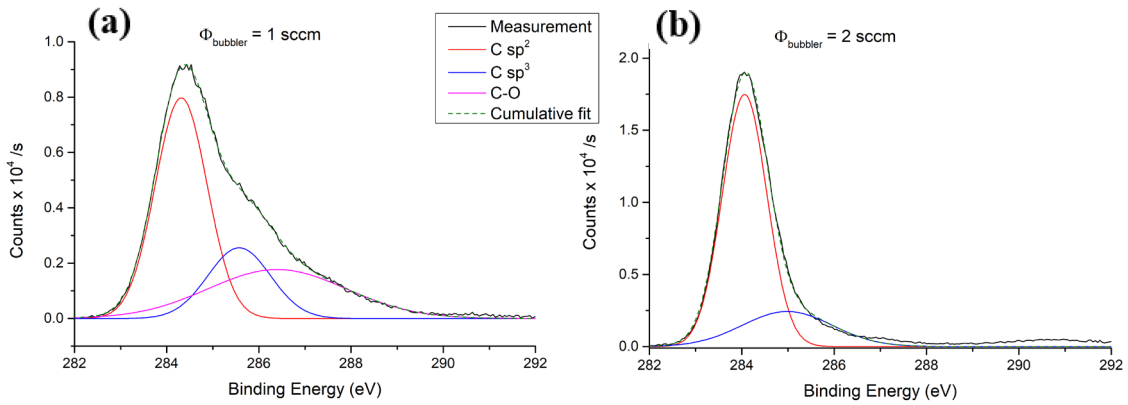

Figure 4.22 – XPS C1s spectra of the samples produced with different flows of Argon through the bubbler with benzene (**a**) 1 sccm and (**b**) 2 sccm. The deconvolution of spectra shows smaller contribution of sp^3 C bonding for the samples.

The lack of crystalline particles in the TEM images in these cases demonstrates that the products are different with respect to the ferrocene process. This would suggest that iron may play an important role in the formation of NDs and that the starting "building blocks" (i.e. fragmented precursor carbon species), which have produced similar OES spectra cannot alone explain the formation of NDs. However, using OES spectra to calibrate processes with two different precursors may not be sufficient to ensure similar plasma conditions as emission spectra represent only a limited snapshot of a vast number of underlying mechanisms. For instance, the distinct dissociation pathways for the two different molecules (ferrocene and benzene) that result in the same emission patterns for the carbon species could actually require different electron energy distribution in the plasma. Moreover, it is likely that the selected flow conditions for benzene are still yielding a higher concentration of precursor in respect to the ferrocene process. This highlights the need of finding better descriptors to compare discharges of different precursors and tune the process parameters accordingly to understand and predict the role of precursors chemistry in the formation of NDs.

4.3.4 Summary of materials characterization

In a fast one-step gas phase process, the atmospheric pressure microplasma with ferrocene vapour and argon is able to synthesize ultra-small diamond crystals with diameter modes ranging from 2.6 nm to 4.2 nm depending on the precursor concentration. The size

distribution is narrow (1-2 nm) and their shape is mostly spherical with some faceted and irregular particles. The structural analysis suggests a minor presence of diverse polymorphs of diamond, namely a hexagonal phase (h-diamond) and a face centred cubic phase (called n-diamond). The extreme conditions for ferrocene concentration in the process (ND100 and ND500) result also in small graphitic crystals and other non-diamond phases of carbon as tubular and onion-like structures. Varying the concentration of ferrocene leads to a limited control of particle size with a functional dependence that is non-linear, and a minimum for intermediate precursor flow conditions (ND300).

The compositional analysis (XPS and Raman) shows evidence of the co-presence of small size sp^3-bonded species assignable to NDs along with sp^2 bonded species with no clear trend in function of precursor concentration. TEM-EDX in highly populated areas and XPS survey spectra show traces of Fe in all samples (Fe <1.5 at.% EDX and XPS survey) produced with ferrocene. While based on XPS analysis, the ratio of sp^3 to sp^2 bonds is increasing, in favour of diamond-like species, by increasing the flow of ferrocene. Raman scattering analysis does not suggest a simple trend. Nevertheless, Raman measurements are compatible with phonon-confined nano-diamonds, in fact the diamond peak is shifted to lower values (1307-1320 cm^{-1}) and the peak width (100-150 cm^{-1}) is also increased when compared with the expected bulk value. An estimation of crystal size through a phonon-confinement model for the peak width (FWHM) estimates NDs of 1.9 nm to 2.2 nm within the tested samples. These values do not follow the same trend as the TEM size, but can be reasonably compatible with the values obtained, considering the presence of twinned particles and graphitic phases not accounted for in the TEM size distribution analysis.

The admixture of hydrogen in the plasma process which was envisioned as a possible purification scheme from non-diamond carbon yielded smaller iron oxide particles, with no evidence of presence of NDs. Moreover, the process is practically limited by thermal instabilities of the discharge.

Process variations with lower total flow (400 sccm instead of 800 sccm) and higher power setting (120 W vs 80 W) resulted in the formation of hematite and magnetite phases as testified by SAED patterns, EDX or HR-TEM. These materials were in the form of polycrystalline agglomerates in the case of lower total flow and in nanoparticles embedded in an amorphous matrix in the case of higher power. Using benzene as a precursor also did not result in the formation of NDs. Apparently similar discharges as in

the case of ferrocene were obtained, by choosing operative conditions which resulted in similar emission intensity from C_2 and CH species and a lower flow through the bubbler to account for the higher vapour pressure of benzene. The outcome of the process was mostly amorphous materials, as dendritic structures or films on the TEM grid. Hence, exploration of different conditions easily shows that the synthesis of NDs is limited with a relatively narrow range of parameters, and either Iron in ferrocene or the specific plasma dissociation pathways play an important role on the formation of NDs.

4.4 Process Characterization

4.4.1 OES elemental analysis

Optical emission spectroscopy (OES) of a plasma process can provide useful information on the physical phenomena happening within the plasma. OES has the advantage not to influence the plasma (unlike e.g. electrical probes) and can be adapted to reactors operating in restricted spaces if the emission is sufficiently intense for the light collection and the sensitivity of the detection system. The spectrometer can resolve the light into fine components that can be associated to different chemical species which emit light when de-exciting from excited states. The presence of emission peaks from certain species can give valuable information about the precursor's chemical dissociation pathway, while the relative intensity of peaks belonging to the same element transitions or between lines of different elements can be used to extract plasma parameters such as gas temperature, electron temperature and density. The knowledge of these plasma parameters is important to understand the environment in which particles form and grow during the synthesis process. In figure 4.23 an exemplary OES spectrum for the ferrocene

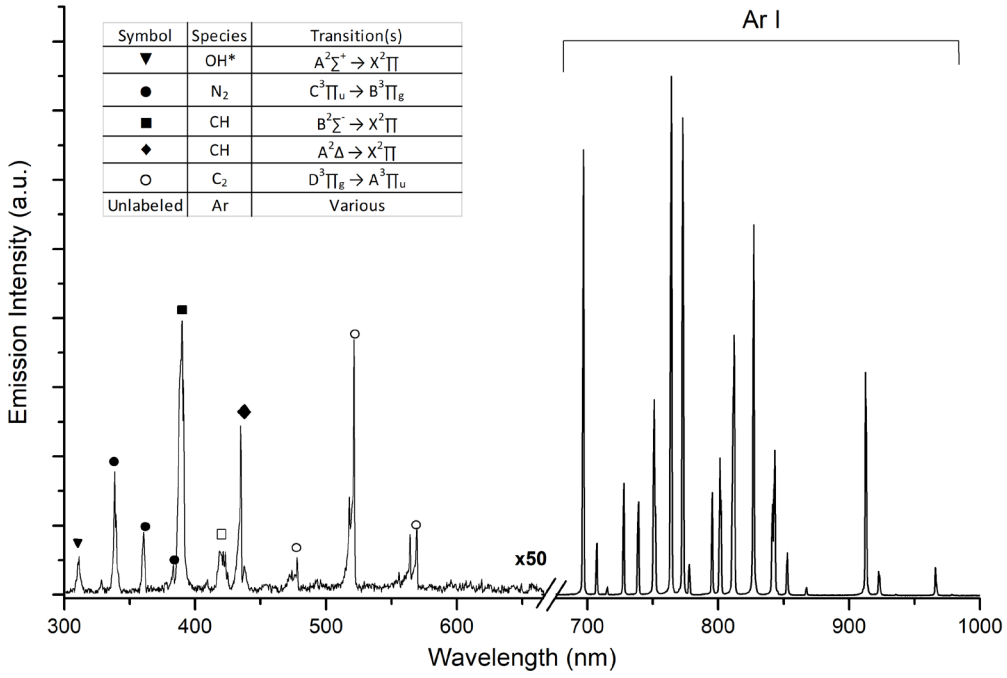

Figure 4.23 – OES spectrum of ND400 conditions acquired after opening the valve of the bubbler housing ferrocene. It shows a variety of different peaks pertaining to difference species in different regions. In the infrared part of the spectrum (> 680 nm) almost only emission from excited Ar atoms appear. The range below 680 nm (ultraviolet and visible) is almost completely populated with emission from molecular species. This region has been magnified for visual clarity, the difference in intensity between the two regions partially reflects the different concentrations of Ar (>99%) and molecular species.

process is shown. It is measured right after the addition of the ferrocene mixture and for an 80 W Ar-background plasma.

This typical spectrum for the ferrocene process shows several peaks, the strongest originating from the electronic transitions of Argon excited states, which sit in the infrared region. A small peak at 777 nm is associated with excited atomic oxygen. The presence of oxygen is likely due to a small leak in the gas mixing circuit. In the ultraviolet (UV) and visible part of the spectrum, several weaker features can be distinguished that can be associated to environmental gases and precursor dissociation products. It is possible to distinguish light-emitting species assignable to OH radicals, molecular nitrogen (N_2), hydrocarbon-related peaks (CH) and the C_2 swan band. Table 4.5 summarizes the associated transitions and wavelength ranges of the most prominent peaks.

Wavelength (nm)	Species	Transition(s)
306	OH*	$A^2\sum^+ \rightarrow X^2\prod$
320 - 380	N_2	2^{nd} positive $C^3\prod_u \rightarrow B^3\prod_g$
386-390	CH	$B^2\sum^- \rightarrow X^2\prod$
430-435	CH	$A^2\Delta \rightarrow X^2\prod$
450 - 600	C_2	$D^3\prod_g \rightarrow A^3\prod_u$

Table 4.5 – Identification and labelling of the OES peaks of interest and relative transitions, lines relative to Ar I transitions have been intentionally omitted

Surprisingly, it is not possible to find any of the hydrogen Balmer lines, which are commonly present in plasmas involving hydrocarbons.

The time evolution of the intensities of these major peaks permits also to distinguish between species which pertain to the precursor chemistry and others identifiable as residual gases coming from the gas lines and the background nitrogen inside chamber (Figure 4.24). In fact, it is observed that OH radicals and N_2 related peaks are quenched after 10 minutes that the plasma is on. When the residual gases are depleted, CH-related peaks and C_2 swan band grow in intensity (pink “warm-up” region in Figure 4.24). While

the formers have a steady increase and then a slow decrease, the latter reach a stationary value after 15 minutes. Even though the discharge seems to be stable even after 1 hour of processing, after 30 minutes all peaks intensities decrease due to accumulation of black deposit on the capillary walls, which partially blocks light from escaping. It is generally observed that a better quality and reproducibility of the products is achieved if samples were collected after 15 minutes of plasma on-time (green "collection" region in Figure 4.24), which suggests that the plasma process is not stationary until then.

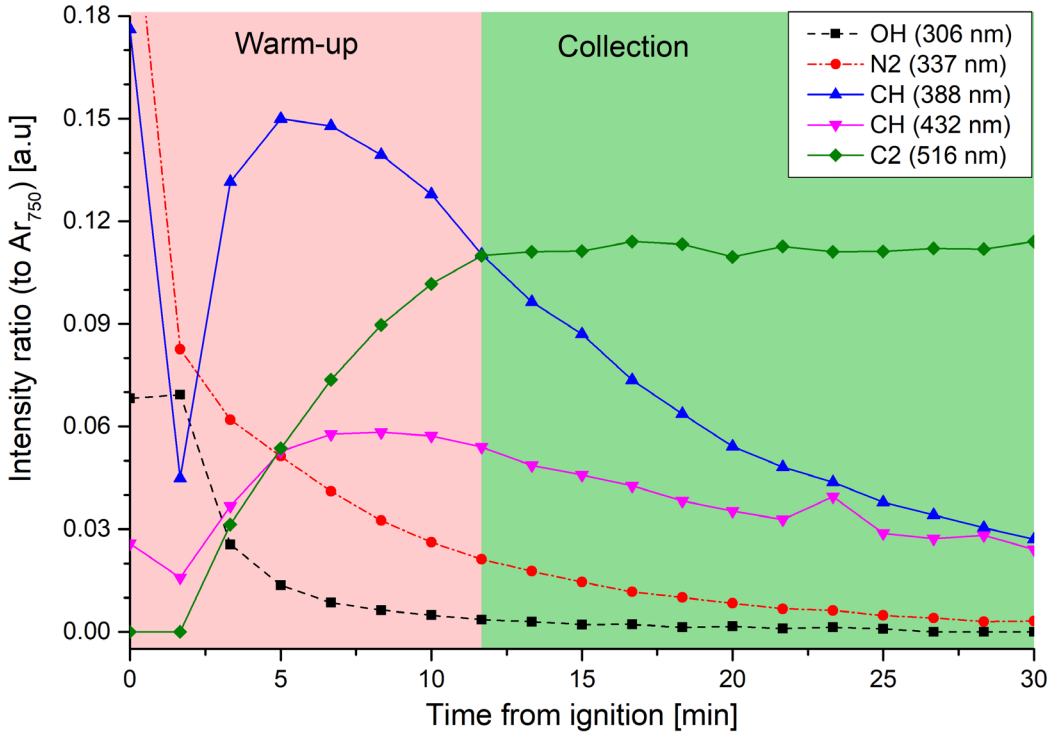

Figure 4.24 – Peaks intensity in function of processing time, normalized to each spectrum's Argon line at 750 nm. The legend identifies the species involved. After a 5 mins transient during which OH and N_2 are depleted, the CH-related peaks spike and then start to decay. After 10-12 minutes the C_2 swan band peaks settle at a constant value.

Comparing spectra from different ferrocene flow conditions acquired after 10-15 minutes from ignition, in what has been denoted "collection" time (Figure 4.25), it is observed that the overall intensity of light emitted by precursor-related species increases almost monotonously while the Argon lines remain constant (Figure 4.25a). The only exception is the 400 sccm conditions (ND400), for which emission from CH- and C_2- related species is stronger than others. Instead, upon introducing hydrogen or using benzene as a precursor, new lines are observable (Figure 4.25c and 4.25d) when compared to the ferrocene-based process (Figure 4.25a). The spectrum in 4.25c is measured for a plasma starting in the ND400 conditions, hence a 80 W Ar plasma with 400 sccm flow through

the bubbler housing ferrocene and right after introducing 10 sccm of H_2/Ar mixture as in conditions for synthesis of sample NDH10 in the material characterization section. Upon introducing hydrogen, the H_α line at 656 nm along with an additional line from Ar(I) transition appears and the discharge is visibly quenched in brightness. This fact demonstrates that hydrogen molecules are dissociated in atomic hydrogen for this plasma conditions. By increasing the input of hydrogen (for example in NDH20 conditions, 20 sccm of H_2/Ar), the strength of the Balmer line increases and the C_2 swan band peaks decrease. Moreover OH (310 nm) and N_2 peaks are constantly present throughout the plasma process with hydrogen admixture, which suggests that these species come from the hydrogen/argon premixed cylinder. The continuous background in these spectra (baseline in Figure 4.21c) is the signature of capillary heating under such conditions.

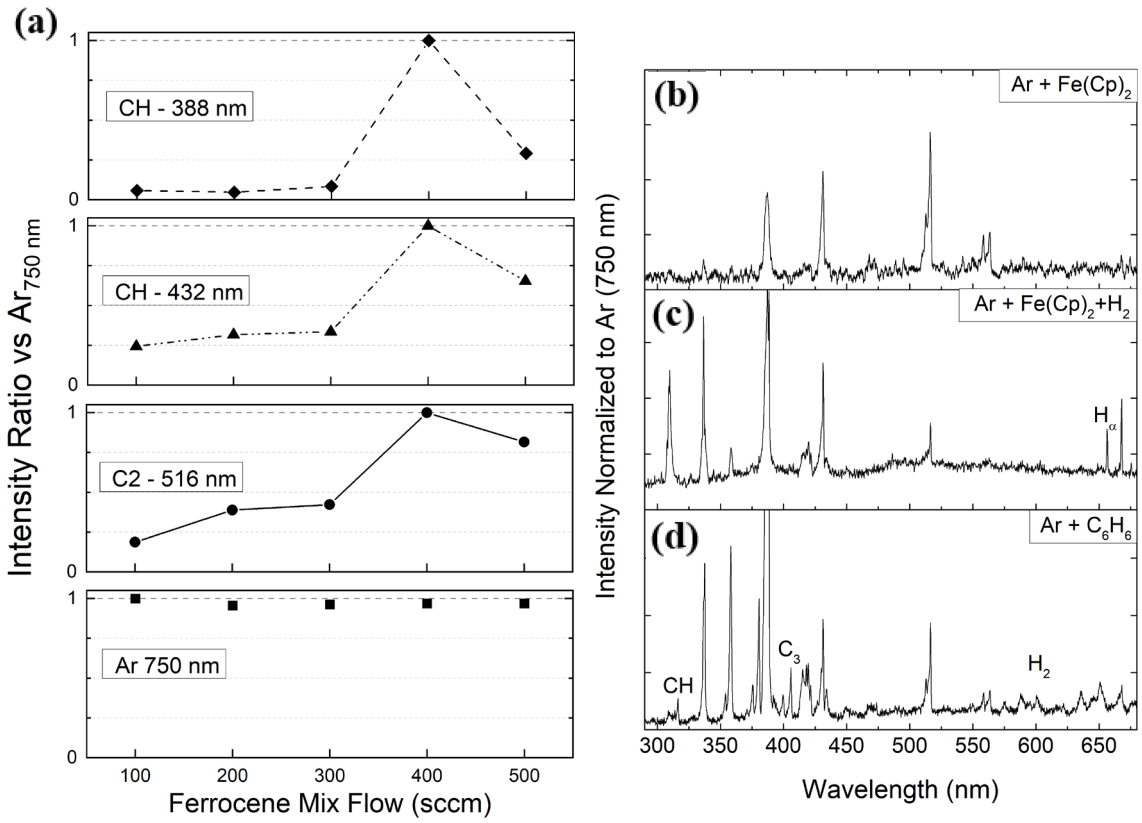

Figure 4.25 – (**a**) Evolution of CH- and C_2- related species emission as a function of precursor flow ratioed to Ar 750 nm intensity for each precursor flow condition, showing a weak increase with increasing precursor flow; Ordinate values are normalized to the maximum emission ratio in the set, which shows that in the ND400 conditions the relative proportion of emission from molecular species is higher in respect to Ar @ 750 nm. In most precursor flow cases the emission ratio of molecular species is less than 50% than in the ND400 case. (**b**) Spectrum acquired in the ND400 conditions at the beginning of products collection. (**c**) Spectrum of plasma in the same conditions as in (**b**) upon introducing 10 sccm of hydrogen/Ar mixture, which results in the same synthesis parameters for NDH10 sample. Atomic H_α Balmer line at 656 nm is observed as well as N_2 and OH peaks which are imputable to impurities in the cylinder, while (**d**) the process with 1 sccm flow through the bubbler housing benzene. This spectrum shows additional peaks from the C-X transitions of CH at 316 nm and a set of peaks around 405 nm assigned to C_3 radical species.

OES from the process with benzene shows additional CH peaks at 316 nm and the signature of C_3 radical species near 405 nm, as well as a series of peaks around 650 nm which are assignable to the H_2 Fulcher band.

The conclusions that can be drawn from the chemical analysis of OES spectra for the process plasma are that there may be only a narrow time window of process which may be responsible for the optimal synthesis conditions to obtain NDs. This could be related to the presence of impurities in the process, for which a too long process would be impacted by wall deposition and a too short one would be affected by residual impurities in the gas lines and the capillary. Alternatively, the existence of an optimal ratio of species related to the ferrocene dissociation chemistry could be at the foundation of the formation of NDs where deposition of materials on the capillary walls could contribute to reach suitable plasma conditions. In all cases, the plasma chemistry involved proved to be non-linear with time. Another important conclusion which can be understood from the presence of C_2, CH and atomic H is that the present plasma conditions are able to dissociate considerably all the precursors introduced.

4.4.2 Estimation of process gas temperature

Gas temperature is an important plasma parameter that reflects the energy stored by the process gas and the dissociation products of molecular precursors in internal degrees of freedom. The temperature associated to the distribution of rotational levels of emitting molecular excited states can be used to probe the gas temperature within the plasma, as described in chapter 2. In this study, species relative to ferrocene dissociation are used to understand the plasma environment in which NDs are formed. Specifically, C_2 swan band main peaks around 516 nm are used to extract values for the gas temperature during the process. The spectra analysed are measured at the beginning of the collection time, hence 10 to 15 minutes after ignition, for all the different samples obtained by varying ferrocene concentration (section 4.3.1). The spectra used are shown in Figure 4.26a. The relative height and the presence of some specific features in the spectra permits to have an approximate estimation of the gas temperatures involved in the process. In fact, there is a

distinguishable variation of C_2 Swan band spectra shape and intensity among the samples synthesized with different precursor flow.

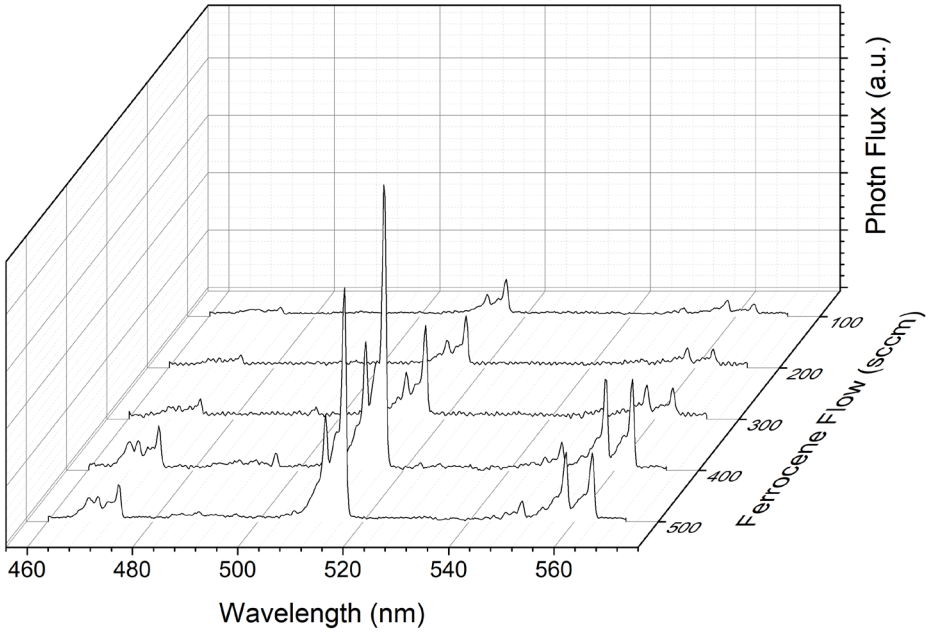

Figure 4.26 – Close-up of the region pertaining to the C_2 swan bands and their variation with ferrocene input in the reactor. the variation in relative intensities of different peaks is due to a different gas temperature.

As described in chapter 2, the emission spectra of molecular species is characterized by bands relative to vibrational transitions with a fine structure of peaks due to rotational sublevels. The extraction of gas temperatures is carried out with two different methods as described in Chapter 2. In the first one, which will be called “global” in this context, the experimental spectra are fitted with a simulated rotational and vibrational spectrum by assuming a single-temperature Maxwell-Boltzmann (MB) distribution of energy levels (e.g. Figure 4.27a). The second method, which will be called “partial”, simulates each vibrational band with a separate MB distribution for the rotational states. A difference between the values obtained with the two methods may signify a departure of rotational excited states from a single-temperature MB distribution (see Chapter 3). The temperatures estimated with the partial method will be considered for further analysis. The temperatures extracted from the measured spectra varies between 600 K and 900 K with the “partial” method and between 800 K and 1100 K with the “global” method (Figure 4.22b). Also, the two methods result similar trends but different values for lower ferrocene input values. Instead, there is a better agreement even in the values estimated for the ND400 and ND500 cases. In both cases the 400 sccm conditions show lower gas temperatures compared to the other synthesis conditions. There is also a tendency for the

difference between the temperatures obtained with the two methods for each experimental condition to become smaller at higher ferrocene content. This latter fact indicates that the distribution of rotational-vibrational levels in the excited C_2 species is more fitting a single-temperature distribution for higher precursor content.

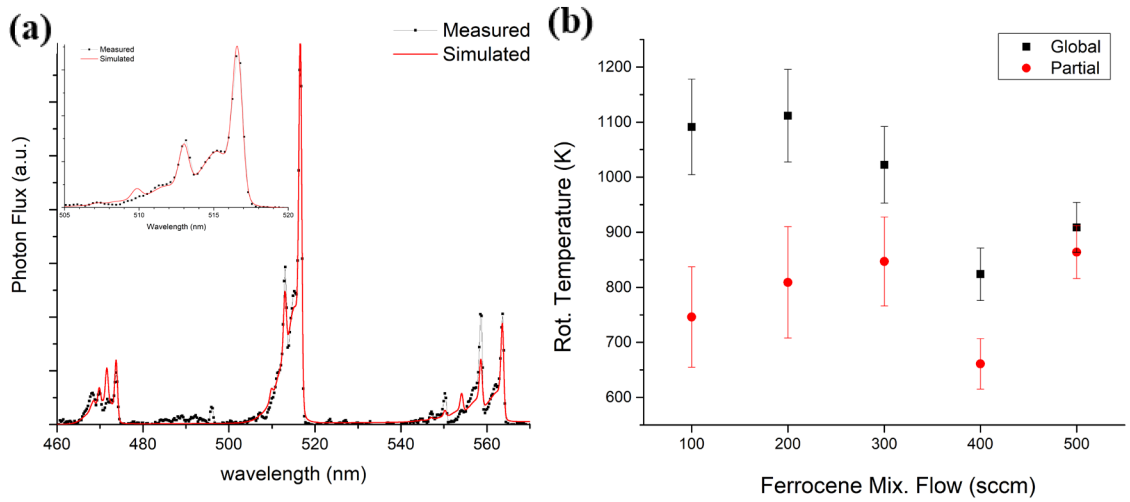

Figure 4.27 – (**a**) Example of simulated spectrum of C_2 swan band fitted to the ND400 OES spectrum. The fit gives 800 K rotational temperature, the inset shows a close-up of the main peak, showing a good matching between simulated and measured spectra. (**b**) Rotational temperatures in function of precursor flow obtained with two methods described in the text. Error bars are uncertainties of the fitted spectra.

4.4.3 Effective Electron Temperature

Another important parameter that can contribute to understand plasma processes is the effective electron temperature. As described in chapter 2, it can be derived by analysing the relative intensity of selected lines in the Ar part of the spectrum through Boltzmann plots to extract a distribution-related temperature (*excitation temperature* T_{exc}) that can be

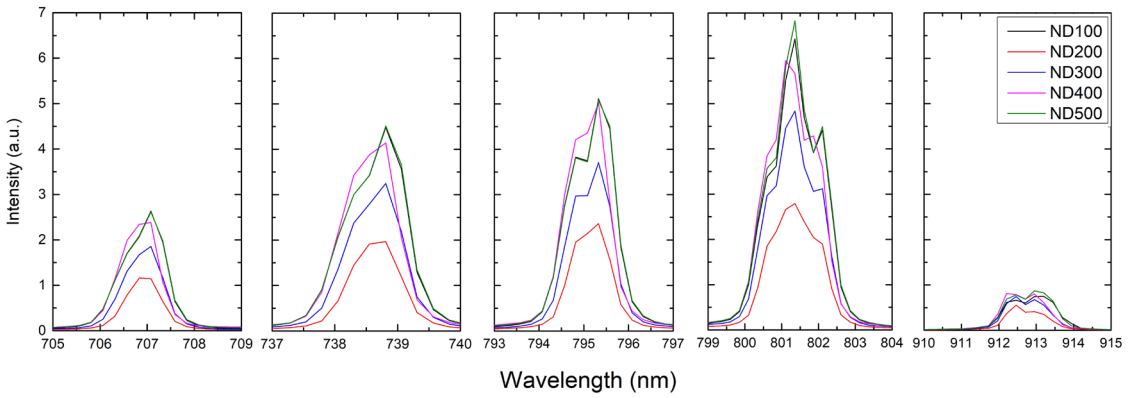

Figure 4.28 –Peaks relative to excited Ar transitions which have been used for Boltzmann plots, for the different synthesis conditions that resulted in the formation of NDs.

converted into an effective electron temperature (T_e) through a collisional-radiative model. In Figure 4.28, the variation of selected Ar peaks with NDs synthesis conditions used for Boltzmann plots are shown. These spectra are acquired during the first minute of the collection time, hence in the conditions under which synthesis products are collected. The peaks are then analysed with Voigt distributions (convoluted Lorentzian and Gaussian distributions), deconvoluting in the cases where more than one peak is expected in that range from database values (NIST) to extract the peak height.

Effective electron temperatures extracted from the analysis are between 1 eV and 2 eV for all the precursor flows (Figure 4.29). The figures obtained are in the same order of magnitude (1-3 eV) with experiments made previously with the same plasma reactor,[48] and in general expected for non-equilibrium atmospheric pressure discharges.[49] The estimated values tend to decrease weakly with increasing precursor concentration, except for the 400 sccm conditions (Figure 4.29).

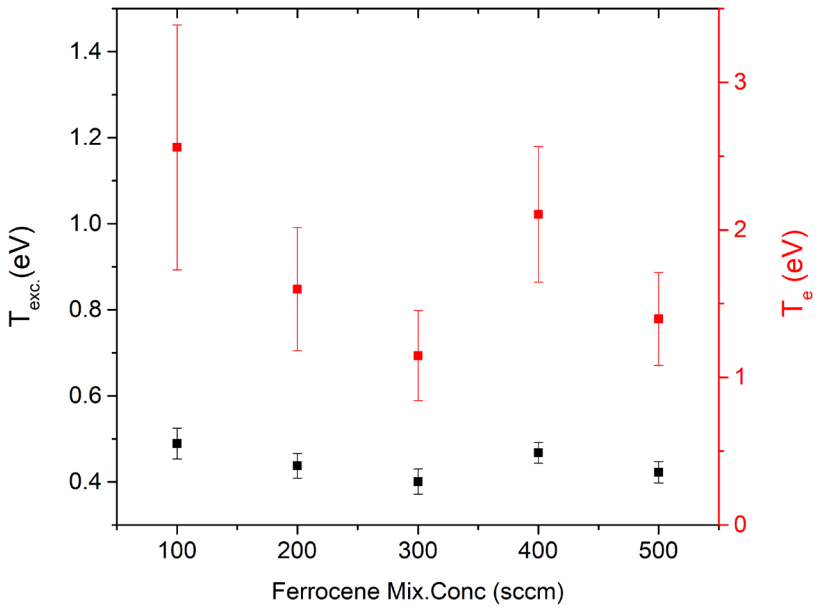

Figure 4.29 – Excitation temperature extrapolated from Boltzmann plot linear fits and estimated effective electron temperature as a function of ferrocene concentration. A general tendency to decrease values of T_e with increasing precursor input can be noticed, except for the ND400 case. Error bars in $T_{exc.}$ are uncertainties in the fit, while for T_e are the propagated errors from the equation connecting the two quantities (see Chapter 3).

In order to understand the dependence of T_e on the operation parameters and the time evolution of the process, some additional T_e measurements were carried out from:

1. The sequence of spectra relative to ND400 as a function of processing time (Figure 4.30), which was used to extract the time evolution of single emitting species in Figure 4.24.

2. A sequence of spectra acquired as a function of applied power (Figure 4.31a), for two different total flows (400 sccm and 800 sccm) and constant ferrocene input (400 sccm).

3. A sequence of spectra acquired as a function of applied power (Figure 4.31b), for two different ferrocene inputs (200 and 400 sccm) and constant total flow (800 sccm), i.e.: comparing ND200 and ND400 conditions as a function of applied power.

Figure 4.30 which is relative to the set of experiments 1) above shows that the value of the effective electron temperature is constant and approximately 2.4 eV as long as initial impurities are present in the gas lines (see Figure 4.24). Then, T_e is monotonously decreasing after 10-15 min from ignition, hence when emission from C_2 swan bands becomes constant over time and products are collected. As mentioned in Chapter 3 the absolute values of the effective electron temperatures are only indicative of the order of magnitude, as there can be sources of systematic errors which cannot be account by the collisional radiative model employed (e.g.: effect of water vapour on electron impact

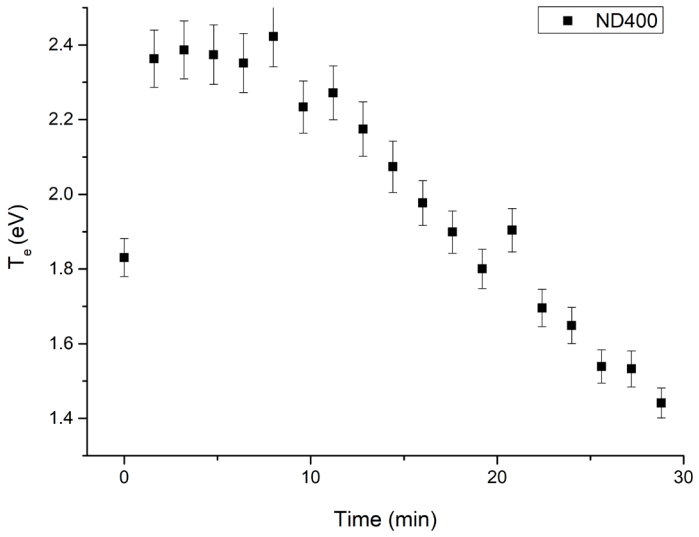

Figure 4.30 – Evolution of effective electron temperature as a function of processing time for the conditions of ND400 sample. The trend shows a constant value region for the first 10 minutes (which coincides with the presence of impurities as can be seen in Figure 4.24) and a progressive linear decrease in value after 10 minutes from ignition (t = 0).

rates). However, the measurements are taken successively within the same experiment and with no variations in the environmental conditions or the position of the optics, hence the trends in effective electron temperature values reflect changes within the plasma. The time dependence of effective electron temperature found is suggesting that assuming the discharge to be stable/or in a steady state because of a constant emission from C_2 species proved to be misleading, while probably one of the reactants involved in the formation chemistry is being consumed over time. This fact supports the statement made in the previous section 4.4.2 for which the formation of particles may happen only in a particular time window of the process.

Figures 4.31a and 4.31b show the results relative to the sets of experiments 2) and 3) respectively. The acquisition of these spectra was performed by first keeping the Ar plasma with 400 sccm ferrocene (ND400) ignited at 80 W for 15 minutes, in order to get rid of impurities, then changing power or flow to the needed values and waiting approximately 1 minute for the OES peaks to reach steady values. After each spectrum is acquired, the parameters are changed to the next values. The position of the fiber optic was changed in respect to the previous measurements (i.e.: figure 4.30) and the measurements were taken in another day. This is reflected by estimated absolute values which are systematically lower of roughly 1 eV in respect to nominally analogous conditions. This fact corroborates the idea that within these experimental conditions and this analysis, only relative values make sense and show trends in the plasma dynamics.

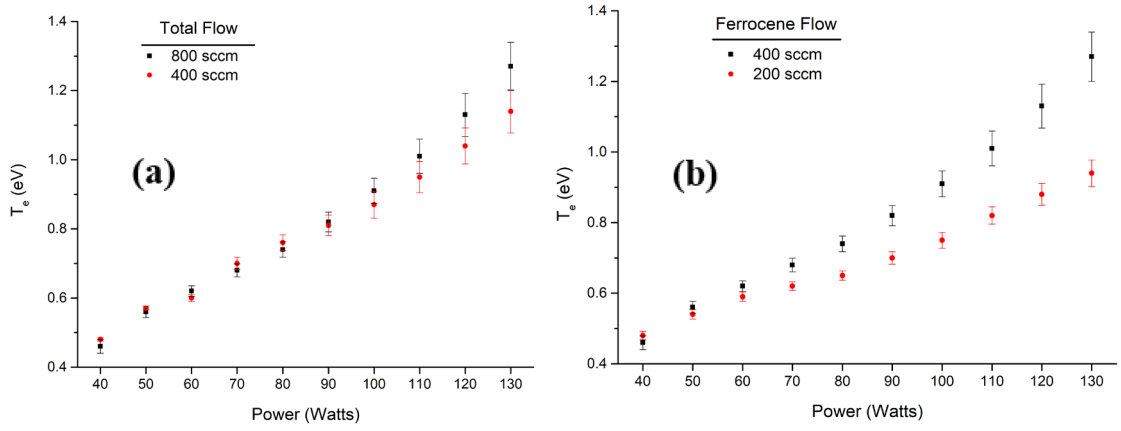

Figure 4.31 – Measured dependence of electron temperature as a function of power for (**a**) two different values of total flow for fixed 400 sccm of ferrocene/Ar and (**b**) for fixed total flow of 800 sccm and two different flows of precursor, matching ND200 and ND400 conditions. A transition between two regimes is observed at around 60 W, below which the T_e seems independent of the flow conditions, and above which it varies as a function of ferrocene concentration and total flow. A stronger dependence is observed as a function of ferrocene concentration than as a function of total flow.

From both results it is possible to observe that effective electron temperatures increase with power, but with a different slope depending on total flow and ferrocene concentration. The effect of input precursor flow seems also to have a stronger effect on T_e as doubling the ferrocene input from 200 to 400 sccm results in a larger difference in the measured effective electron temperature with respect to doubling the total flow.

It is apparent also from Figure 4.31b, that there may be two different regimes for the discharges, in terms of the ferrocene dissociation chemistry or the plasma chemistry at the capillary walls. In fact, below 60 W, T_e does not vary with applied power. This fact could explain why for the additional experiments at lower power conditions (40 W), the TEM analysis of products (bottom of section 4.3.1) showed the synthesis of iron oxide as hematite and magnetite, while in the conditions for which NDs were obtained, small amounts of iron are present in the samples.

4.4.4 Particle Temperature

Nanoparticles surface temperature can be higher than the background gas temperature in an atmospheric pressure plasma as described in chapter 2. Understanding the magnitude of these phenomena is particularly important for small particles within a plasma and have been proved important to understand the formation of various nanocrystalline phases with crystallization temperature higher than gas background temperature.[48,50]

Particle temperature is estimated using effective electron temperature and gas temperature (partial method) obtained from OES data as input values in a non-material specific collisional model (collision corrected model, CCM) described in Chapter 2. Also, another input in the model is the size of particles obtained from TEM analysis and values for electron density which are typical for this type of plasma reactor, between 10^{19} m^{-3} and 10^{21} m^{-3}. Table 4.6 reports the estimated physical parameters of interest to the model for the NDs synthesis process.

$n_e = 10^{20}$ [m^{-3}]	Size [nm]	Debye Length [nm]	Mean Free Path* [nm]	Kn [AD]	NP Potential ($-eV_p/k_bT_e$) [AD]
ND100	4.2	302	1190	36	1.00
ND200	3.3	333	941	50	1.39
ND300	2.6	352	797	68	1.71
ND400	3.3	261	1078	40	1.02
ND500	4	361	880	45	1.57

Table 4.6 – Parameters calculated from experimental data to validate the applicability of the CCM. The OML theory would require the ion mean free path to be much bigger than Debye length; in this case it is larger, but of the same order of magnitude. The Knudsen number (*Kn*) is within the transition region between free molecular regime and hydrodynamic regime. V_p is the floating potential and k_b is the Boltzmann constant. AD means "adimensional". See Chapter 3 for further explanation.

For all the conditions the ion mean free path is bigger than the screening length, but in the same order of magnitude. This means that the CCM model must be used to obtain the charge balance on the particles surface. The plot in figure 4.32 shows the calculated particles temperature for the different NDs samples, with the indication of the relative background gas temperatures as a function of different values of the electron density. In the specific case a significant deviation of at least 100 K from the gas temperature is found, if $n_e > 10^{20}$ cm^{-3}. This value of electron density, even if it is not directly measured for the NDs process, is typical of the discharge used (see for example the values measured from H_α broadening in chapter 5 on Si QDs).

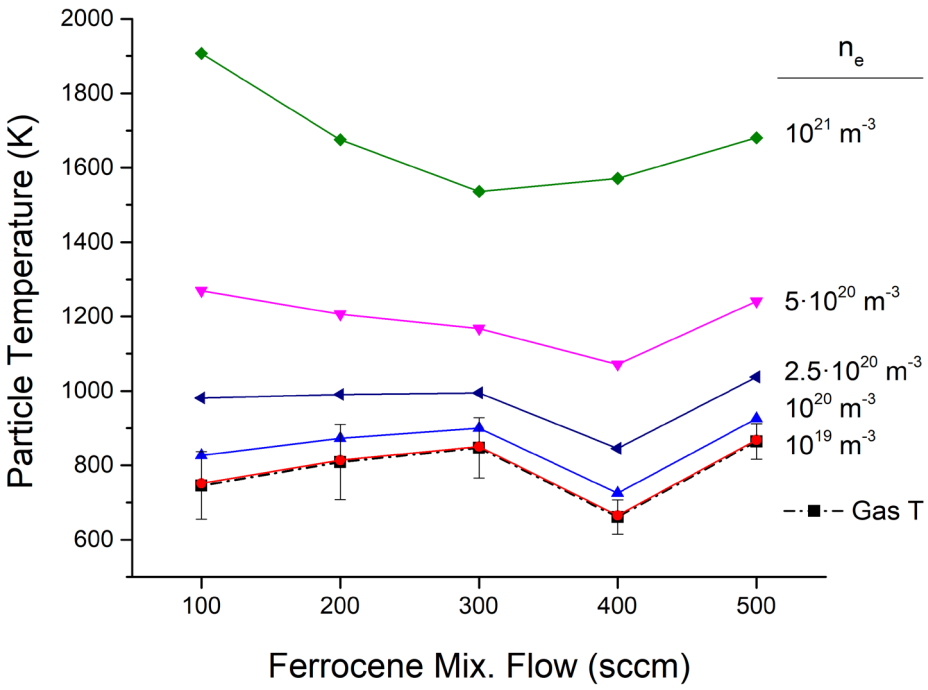

Figure 4.32 – Particles surface temperature obtained through the CCM model. A significant deviation (>100 K) is observed for electron densities above 10^{20} m^{-3}. The present estimation inputs TEM size as the particle size in the model, the measured T_e and T_g. Electron densities were not measured, hence typical values for this kind of discharge are explored.

4.5 Discussion of results

4.5.1 On plasma dissociation of ferrocene and CVD synthesis of NDs

Understanding the NDs formation mechanism is of enormous scientific importance for both the optimization of the synthesis and physics of planetary formation. Despite ferrocene has been widely used as a precursor to produce iron particles for catalysing the growth of carbon nanotubes,[51] there are no report of the formation of nanodiamonds from these processes. Ferrocene is characterized by a particularly weak bond between the iron atom and the cyclopentadienyl (Cp) groups. In conventional chemical vapor deposition (CVD) furnaces the substrate is kept at a temperature such that Fe atoms resulting from the dissociation of the parent ferrocene molecule form iron nanoparticles or iron carbides depending on the molar ratio of iron with respect to carbon. Both can catalyse the formation of carbon nanotubes. In the case of iron particles, a graphitic cap around the particles is being continuously lifted (or serve as the root) to form the nanotubes,[52,53] and there is substantial evidence that particles are in the austenitic γ-Fe phase when the substrate temperature is over 750 K. Usually the γ-Fe phase is stable over 910 K, but when Carbon is dissolved in small quantities in iron the stability can be reached even at lower temperatures.[53] Other studies on ferrocene dissociation in microplasmas[54,55] show that high purity iron/iron oxide nanoparticles particle are obtained only at low applied power. These authors showed that high power, for which fast electrons gain enough energy to break the aromatic rings, bring to the formation of a hydrocarbon contamination on the surface of particles, eventually leading to an embedding of particles in an amorphous H:C matrix, the evidence of dissociation of the aromatic rings consisted in the detection of optical emission from CH, C_2 and C_3 only at higher power. Lin et al.[55] studied also the energetics of plasma chemistry routes to the dissociation of ferrocene, they found that there are two possible pathways to break the bonds between iron and cyclopentadienyl groups, a ionic and a neutral one, both needing a modest energy (respectively 3.9 eV and 6.9 eV to break the first bond) compared to the first ionization energy of Argon. Given the higher proportion of energetic electrons, it was concluded that the preferential dissociation pathway would be the neutral dissociation by direct electron impact. Moreover, they inferred the faith of aromatic rings from OES results and previous mass spectrometry studies[56] that showed the production of higher carbon content hydrocarbons. The aromatic rings can be opened in linear C_5H_5 radicals, which can later be fragmented by electron impact and the smaller fragments can undergo radical

recombination reaction as in the case of methane and acetylene plasma enhanced CVDs. A schematic diagram of the process is reproduced from the paper (figure 4.33).

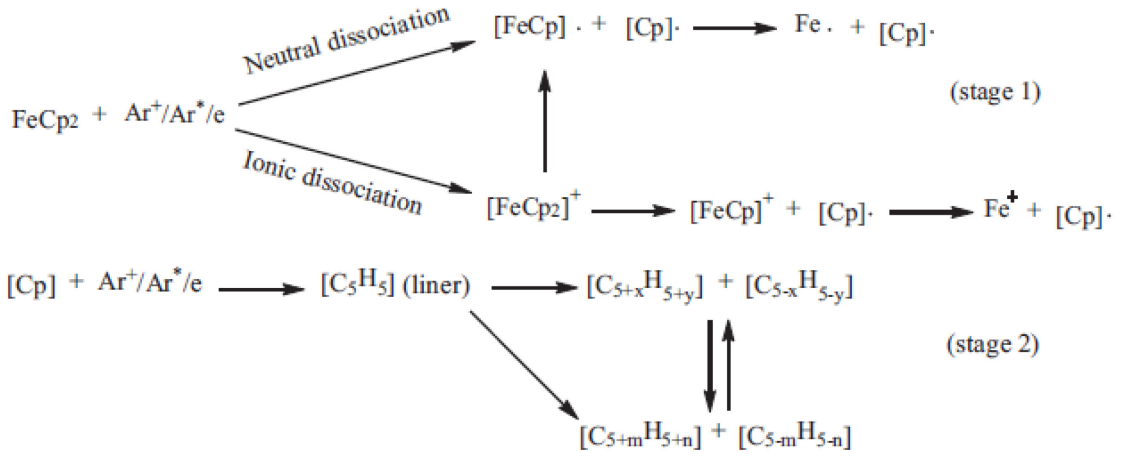

Figure 4.33 – Ar plasma dissociation mechanism of Ferrocene proposed by *Lin et al.*,[57] the diagram labelled as *stage 1* showing two possible pathways to break the Fe bond, one ionic and one neutral both initiated by energetic species within the plasma. The energy balance favours the less energy expensive neutral pathway. The diagram labelled as *stage 2* describes the possible evolution of cyclopentadienyl group, whose ring can be easily opened to create linear radicals. Then various dissociation and recombination reactions between hydrocarbon radicals can happen at the same time, and the balance depends specifically on the temperature and the distribution of energetic species in the plasma.

In experiments presented the content of iron is negligible within the experimental conditions that resulted in the synthesis of nanodiamonds. Only at low power (40 W vs 80 W of NDs forming conditions) the results of the process is iron oxide particles, either agglomerated or embedded in an amorphous matrix. The effective electron temperature measured as a function of power setting and total flow (figure 4.31) suggests also that the process has two different regimes from the point of view of ferrocene dissociation chemistry. In fact, the effective electron temperature is expected to vary significantly for different dissociation pathways, as electrons with different energies will participate to different processes. The same process using benzene does not show any evidence of formation of diamond or other sp^3 bonded species. Consequently, the conditions for the formation of NDs from ferrocene are met in a narrow parameter window and may be allowed by some peculiar mechanism related to the plasma chemistry of ferrocene dissociation or the effect of iron atoms within the plasma. Optical emission spectroscopy shows that various optically active species are involved in the process; C_2 and CH related species show the most important variations among different synthesis conditions, both varying with time and precursor flow, and can be conjectured to have a dominant role in

the dynamics of the process. Moreover, any atomic hydrogen or metal peaks could not be detected, without the explicit addition of molecular hydrogen in the process.[12]

It has been 30 years since the first plasma-enhanced CVD synthesis (PE-CVD) of nanocrystalline diamond films from a fullerene (C_{60}) vapour source,[57] and since then a lot has been understood about the growth of nanodiamond films. The most common precursors are methane (CH_4) or Acetylene (C_2H_2) admixtures in hydrogen or argon plasmas. This has been done almost exclusively on non-diamond substrates seeding in different ways, on silicon wafers, silicon carbides, nitrides metals, polishing substrates with diamond powders or coating with other carbon materials.[58–60] It is a general consensus that in microwave-plasma enhanced CVD in the presence of atomic hydrogen the most important growth factors are the concentration of CH_3 radicals and the ratio between atomic and molecular hydrogen. In general hydrogen-rich discharges produce more C_2H_2 in the discharge region, while argon-rich ones produce more C_2 species,[15] but in both cases CH_3 is the highest concentration radical on the surface during growth. CH_3 radicals can attach to open carbon sites on the growth surface and can further react with atomic hydrogen, which abstracts a hydrogen atom to form molecular hydrogen that leaves the surface or attach to another carbon poor radical. Instead it is believed that carbon rich C_xH_y radicals cannot participate to the growth in the presence of atomic hydrogen, because they are short-lived being quickly attacked by atomic hydrogen. Hydrocarbon molecules can undergo different types of chemical reactions within the discharge region:

1. Hydrogen abstraction, reducing the ratio of hydrogen in hydrocarbons, more efficient in high temperature regions (1400 K to 2500 K)

$$CH_n + H \rightarrow CH_{n-1} + H_2$$

2. Hydrogen addition, increasing the ratio of hydrogen in hydrocarbons, more efficient in low temperature regions (900 K to 1400 K), M is any molecule in the reaction zone

$$CH_{n-1} + H + M \rightarrow CH_n + M$$

3. Radical recombination reaction which tend to increase the proportion of single-carbon radicals for high temperatures and the opposite for lower temperatures

a) $CH_n + CH_m + M \leftrightarrow C_2H_{n+m} + M$

b) $CH_n + CH_m \leftrightarrow C_2H_{n+m-l} + H_l \quad (l = 1,2)$

Still some controversy remains about synthesis in argon plasmas and the discharges with no intentional addition of hydrogen (like the first reports based on fullerene), where the dominant species is C_2. In fact, the reported concentration of dicarbon cannot account for the high deposition rate in these cases.[61] A second mechanism for diamond growth has been proposed then, and it relies on the fact that C_2 species have been calculated to have a very low activation barrier (less than 5 kcal/mol) for insertion in a C-H terminated diamond surface and that C-C bonds can be exothermically formed on a surface between two adsorbed dicarbon species.[62] This latter mechanism does not require atomic hydrogen to participate to the growth, and the high C_2 concentration is obtained via fragmentation due to ion collision in the case of C_{60}, or the reactions $2CH_4 \rightarrow C_2H_2 + 3H_2 \ \ and \ C_2H_2 \rightarrow C_2 + H_2$ in the case of methane. Another theory which has been put forward explains the high growth rate as an effect of soot particles which are formed in the cooler parts of the reactors where recombination reactions from hydrocarbons radicals tend to produce higher carbon content species.[63] These particles may equally act as diamondoid seeds or as nucleation centres.

Three methods have been employed to directly synthesize unsupported ultra-small NDs, all three characterized by fast dynamics and extreme temperature quenching rates: detonation of carbon-containing explosives, laser ablation of graphite targets and a microplasma process with a hollow cathode DC discharge and an ethanol vapour as precursor.[20,31,32] Detonation NDs has been by far the most successful process, even though it needs different purification steps in order to remove all non-diamond soot which is formed alongside, and usually results in agglomerates of particles. Laser ablation of graphite targets has the advantage of being a single step process, although it is not easily scalable, and the particle size distribution is broader. The microplasma process has been successful on purifying the process on flight thanks to the selective etching behaviour of hydrogen added to the discharge, but the authors report very low deposition rates. The authors also observed a strong OES signal from C_2 and CH radical species to which they attributed respectively the initial nuclei and the formation of growing hydrocarbon layer,

accounting for the growth of NDs. They ultimately judged the synthesis happening via a homogeneous nucleation process, with a critical role of the C:H:O ratio of ethanol precursor, that would be ideal to the purpose.[33] They also compared their synthesis conditions to previous attempts on nucleating NDs from the gas phase, which were unsuccessful and produced graphene or much larger NDs and assigned the difference to the peculiar quenching rates of microplasmas.

4.5.2 On the formation of nanodiamonds from ferrocene

In the present study, the presence of dicarbon and hydrocarbon optical emission peaks in ND forming conditions demonstrates that the process is operating in high-power conditions, that allow electrons to have enough energy to dissociate also the aromatic rings of ferrocene molecule. Even though C_2 and CH species are detected in OES, no atomic hydrogen can be observed. It follows that in the conditions of the plasma reactor used, aromatic rings are easily dissociated due to energetic electrons or Ar metastables and little or no recombination between light hydrocarbon radicals. As a consequence, the formation of "soot" from carbon species is very unlikely and for this reason it is also unlikely that diamonds are formed in this way, also given the highly collisional environment in an atmospheric pressure plasma and the energetics involved.

Instead the particles temperature is high enough for iron to form nanoparticles in the γ-fcc crystalline phase. In fact, considering nuclei up to 1 nm (smaller cluster would give even higher temperatures), the temperature reached is systematically within the γ phase thermodynamic stability region (Figure 4.34), which is above 910 K for an atmospheric pressure process. γ-Fe nanoparticles have very similar lattice constant as diamond, so they would be ideal seeds for nucleation of nanodiamond. Moreover, Wen et al.[37] showed from first principles calculation how, a γ-Fe seed could bring the formation of n-diamond from a sp^2 bonded carbon precursor. Then, assuming n-diamond as a metastable phase, part of the particles may be able to revert to the cubic phase. A possible mechanism is proposed and considers different steps that help explaining the experimental observations.

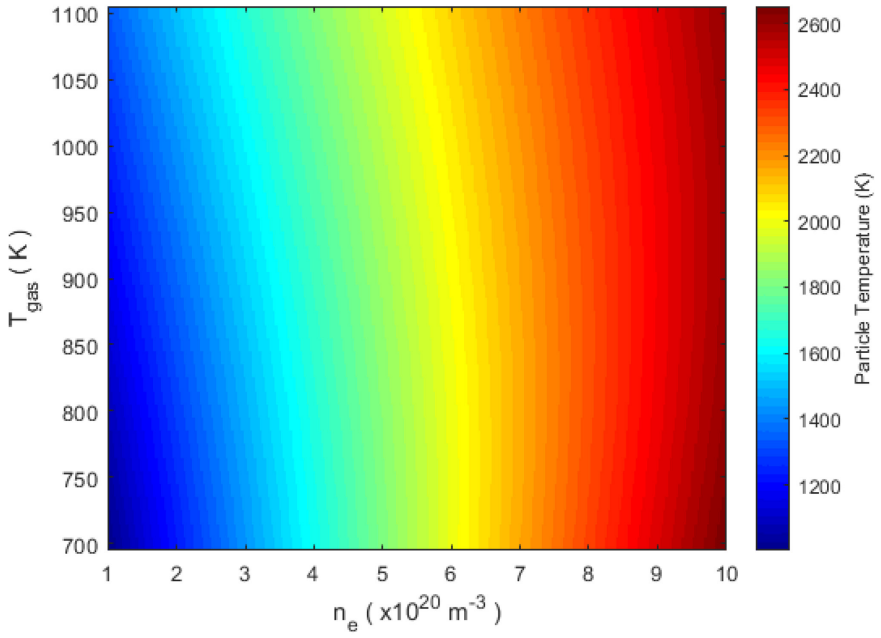

Figure 4.34 – Chart showing the different particles temperatures for a 1 nm particle obtained from the CCM model previously described. The calculated temperatures show how a small crystalline nucleus may reach very high temperatures, in this case compatible with the stable formation of iron γ phase.

The diagram of figure 4.35 depicts schematically the mentioned steps.

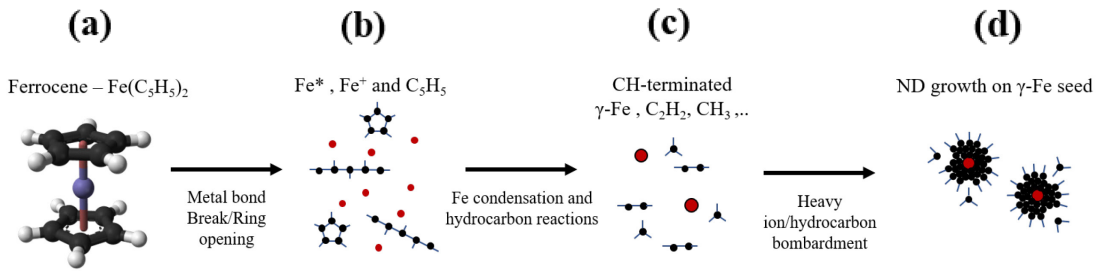

Figure 4.35 – Diagram showing the different steps of the proposed diamond formation mechanism starting from ferrocene.

(a) *Breaking of the Fe bonds*

Both ionic and neutral pathways for breaking the iron bonding require low energy, respectively 3.9 eV and 6.9 eV, which can be either supplied from Ar metastables and hot electrons. This could happen right when the gas flow enters the plasma region.

(b) *Formation of carbon capped γ-Fe seed*

The fast breaking of Fe bonds may be favourable to the formation of iron clusters, whose stable phase is the γ-face centered cubic phase, which is stable in the temperature range in which small particles should be within the atmospheric pressure collisional plasma. In analogy to CVD processes for carbon nanotubes, the iron cluster may be capped with a carbonaceous cap, which in the present case would be amorphous or particularly defective, given the high rate of collisions in this pressure range. This would differentiate the process with benzene as there would not be any particle formed in the discharge. So, it is proposed that these iron clusters would act as seeds for the growth of nanodiamonds.

(c) *Opening of the aromatic rings and dissociation in simpler hydrocarbons*

The measured electron temperatures show two different regimes, a high-power regime which is dependent on the total flow and concentration of precursor, and a low power which is independent. At the threshold (~ 60 W) electrons have enough energy to open aromatic rings and further dissociate linear hydrocarbon radicals in simpler hydrocarbon, when this happens an increased flow of precursor or total flow influences the dissociation/recombination reactions between hydrocarbons, as testified by the presence of C_2 and CH in the optical emission spectrum of the plasma and their variation with flow. This hypothesis could explain the presence of pure iron oxide particles at lower power and the presence of iron oxide particles embedded in amorphous carbonaceous material at higher power (with respect to NDs forming conditions). In addition, the presence of atomic hydrogen when hydrogen is introduced in the plasma may prevent the formation of diamond around the Fe clusters or etch them, resulting in iron oxide nanoparticles when exposed to atmosphere. The particle size dependence on flow can also be explained by such a mechanism, a trade-off between nucleation density and supply of growth species. Lower concentration of ferrocene would result in a smaller density of formed iron clusters which can then have more chance to grow bigger. At higher concentrations particles would have a chance to grow bigger due to attachment of C_2 species.

(d) *Growth of n-diamond phase on γ-Fe seeds*

The bombardment from C_2 and CH species of a γ-Fe cluster would initiate the growth of n-diamond phase, which has similar structure (fcc) and lattice parameter (3.56 Å) as the particles. The surface reactions involved could be the insertion of C_2 in the CH terminated surface, which has a low activation barrier of less than 5 kcal/mol and successive formation of C-C bonds from adsorbed C_2 species which is exothermic. The relative fluxes of these two species may determine whether crystalline diamond or amorphous hydrocarbon layers are formed. It has been noticed that in section 4.4.1 that the emission spectra relative to benzene process shows a dominant contribution from CH species with respect to C_2 and the additional presence of C_3 species. This latter fact would fit this view, as the synthesized products in this case were amorphous materials.

4.5.3 Stability of the nanodiamond phase

The plasma conditions (e.g. gas temperature, particle temperature and flow) play important roles after particle growth, before they can be collected. Theoretical calculations and computations[15,16] show that the phase stability of carbon allotropes is size-dependent and favours cubic diamond over graphite at the nanoscale. Specifically, the cubic diamond phase is thermodynamically more stable then graphite for hydrogenated carbon particles smaller than 3-5 nm even at atmospheric pressure. This has been explained as the effect of strain induced by surface curvature when particles are small enough, imposing an additional pressure which favours the formation of cubic diamond to hexagonal graphite. Also, various studies on carbon clusters suggest that other polymorphs like fullerenes and nano-onions usually co-exist at this smaller size (≈ 2 nm). This implies that entalphies of formation of such phases have similar values in that size range and are sensible to external factors like the presence of impurity atoms or particular synthesis conditions.[64] Even though diamond nanoparticles in the cubic diamond phase are expected to be more stable than other phases below 3 nm, most of the synthesis methods require fast quenching. In fact, the close energetics of formation of various carbon phases at the nanoscale easily drive phase transformations among them. For example, a 5 nm nanodiamond would exothermally transform into a graphitic particle by

growing 1 nm in diameter. This is also testified by the fact that no experimental study which does not involve epitaxial growth or seeding on diamondoid substrates ever resulted in nanodiamonds bigger than a limiting size (3-5 nm depending on the experiment).

In the present case, irrespective of the formation mechanism, the NDs formed are likely to be stabilized due to the reduced residence time of particles in the plasma region which is typical of the microplasma reactors. In fact, in the current reactor, the residence time for particles inside the active plasma region is calculated to be on the order of few milliseconds and cooling rates can be as high as 10^4-10^5 K/s (estimated considering conductive heat losses from particles temperature calculated in 4.4.4 to room temperature). The co-presence of multiply twinned crystals nano-onions and n-diamonds, which can be thought as metastable phases,[39,41,43,65] is also compatible with the same mechanism of kinetical stabilization by fast temperature quenching.

Yang and Li [66] built a T-P phase diagram for nano-sized carbon phases, by modifying a previous bulk model developed by *Bundy et al*.[67] This was done considering the single phase boundaries *T(P)* for transitions between pair of phases: 1) graphite and diamond (GD), graphite and liquid (GL), diamond and liquid (DL) to obtain the position of the GDL triple point. The modifications introduced by *Yang and Li* are based on semiempirical relations and are at the present time the best ones matching various experimental results throughout the literature. They assume the total pressure P_t acting on the particles as the sum of an external (P) and an internal pressure (P_{in}), where the latter originates from the curvature of the surface and is calculated from Laplace-Young equation. For a spherical nanocrystal it reads:

$$P_{in} = \frac{4f}{d} \qquad \text{Eq. 4.3}$$

where f denotes the stress induced by the curvature of the surface. Atmospheric pressure conditions are characterized by almost zero external pressure (with respect to internal pressure ≈ GPa), so that $P_t \approx P_{in}$ and at the equilibrium between phases f can be taken as the average between the values for graphite (f_G = 1.1 J/m^2) and diamond (f_D = 6.1 J/m^2).[68] Bundy's G-D first order phase transition temperature as a function of pressure is described by the equation:

$$T_{bulk}^{GD}(P_t) = -825.243 + 485.437P_t \qquad \text{Eq. 4.4}$$

Inserting the expression of P_t (=Eq. 4.3 at atmospheric pressure) the size-dependent G-D transition is obtained:

$$T_{nano}^{GD}(d) = -825.243 + 485.437\left(\frac{4f}{d}\right) \qquad \text{Eq. 4.5}$$

The equation shows that the phase boundary between nano-graphite and nanodiamond is a decreasing function of temperature and equilibrium sizes range between more than 8 nm at 0 K and 2.4 nm at 2000 K. If particles temperatures calculated in section 4.4.4 and TEM sizes measured for the NDs sample are plotted in the size-dependent GD T(P) phase diagram at P_{atm} the diagram in Figure 4.36 is obtained.

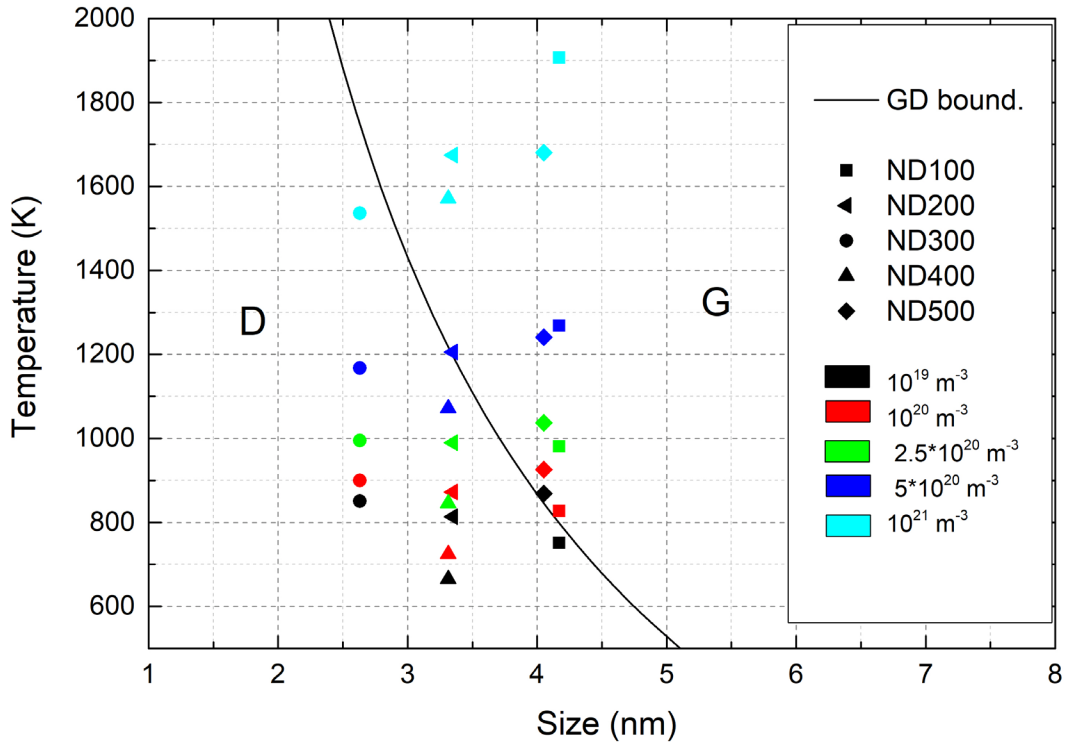

Figure 4.36 – Experimental data plotted in the D/G size-dependent phase transition diagram obtained from Yang and Li.[68] NDs samples obtained from the same ferrocene input are pictured with the same symbol (or constant value of particle size). In colors the different values of electron densities are distinguishe, giving different particle temperature for the same particle size. *D* and *G* denote regions of temperature in function of size of stability for diamond and graphite phases, respectively.

A good consistency with the experimental observations is found for certain electron density values. In fact, as long as $n_e < 10^{21}$ m^{-3} the extreme ferrocene concentration conditions (ND100 and ND500, square and diamond symbols in the diagram in figure 4.36) lie in the graphite stability region, and the other conditions mostly in the diamond

stability region or across the G-D phase boundary. This could explain why particles which form or grow to a bigger size tend to be in a graphitic phase. However, the material characterization of sample ND300 (circles in figure 4.36) is inconsistent with this simple picture, as it should then be the sample in the purest diamond phase, given the smaller size with respect to other samples.

However, this simplistic picture only considers one phase boundary between diamond-like and graphitic phases, while a realistic determination of phase stabilities is expected to be complicated by the plethora of different nanocarbon phases with close energetics.[68] Nevertheless, this analysis on the stability of nanodiamonds after the formation, helps explain some experimental observations made in the present study. The small size and the small size dispersion are due to the small residence times and fast quenching rates of the used reactor, able to avoid the growth of NDs that would promote the formation of graphitic particle and able to kinetically stabilize n-diamond, multiple twinned particles and carbon onion phases. For the extreme conditions of lowest and highest flow of precursor the particles are slightly bigger due to the initial formation dynamics, and the calculated particles temperatures place them across the phase transition boundary with graphite, with the result of having a partial population of particles in the graphitic phase.

4.6 Conclusions and outlook

A gas phase atmospheric pressure microplasma reactor has been used to synthesize ultra-small NDs from a ferrocene vapour in an argon background gas. The particles produced are spatially dispersed and of various morphologies, from spherical to faceted, 2.5 nm to 4.2 nm small with a 1-2 nm small size dispersion. They show different crystalline phases of diamond, also graphite and carbon onions are present in some cases. In this process, the ability to control size and the phase produced are limited by the size-dependent thermodynamic stability of carbon nanoscopic allotropes.

The analysis of plasma optical emission and the estimation of particle's surface temperature through a heating model identified a possible formation mechanism, based on the seeding from γ-Fe clusters nucleated within the early stages of the plasma itself, and the growth through bombardment of CH and C_2 species, without the contribution of atomic hydrogen. Comparing to other studies with microwave-enhanced CVDs which operate at higher gas temperatures (3000 K), the relatively cold process (600 K to 1000 K) may favour this growth mechanism in the absence of atomic hydrogen even irrespectively of the presence of iron cluster seeds.

The process is fast and done in one-step, so it has the potential advantage to be simpler and more efficient compared to other methods used in the literature. The ability to synthesize small nanodiamonds is intimately connected to the small residence time of particles in the plasma region and the fast cooling typical of this plasma reactor, able to quench the growth of particles and stabilize otherwise metastable phases.

A clear comprehension of the formation mechanism is still lacking. Relatively to the process presented in this experimental study, the understanding of their formation in conjunction with a fine tuning of plasma parameters such as gas temperature and effective electron temperature would allow synthesizing a selected crystalline phase with better purity and control over the particles size in a wider range. It would be either important for purely scientific reasons, because of the interest in understanding of interstellar formation of nano-diamonds, or technologically, to allow a more efficient and controlled synthesis for new relevant applications of nanodiamonds as biomarkers, drug delivery systems and quantum optics, where the control of particle size and phase purity is critical.

References

1. Hirsch, A. The era of carbon allotropes. *Nat. Mater.* **9**, 868–871 (2010).

2. Novoselov, K. S. *et al.* A roadmap for graphene. *Nature* **490**, 192–200 (2012).

3. Baughman, R. H. Carbon Nanotubes — the Route Toward. *Science (80-.).* **297**, 787–792 (2002).

4. Bosi, S., Da Ros, T., Spalluto, G. & Prato, M. Fullerene derivatives: An attractive tool for biological applications. *Eur. J. Med. Chem.* **38**, 913–923 (2003).

5. Fu, C.-C. *et al.* Characterization and application of single fluorescent nanodiamonds as cellular biomarkers. *Proc. Natl. Acad. Sci.* **104**, 727–732 (2007).

6. Prabhakar, N. *et al.* Core–shell designs of photoluminescent nanodiamonds with porous silica coatings for bioimaging and drug delivery II: application. *Nanoscale* **5**, 3713–3722 (2013).

7. Neumann, P. *et al.* Quantum register based on coupled electron spins in a room-temperature solid. *Nat. Phys.* **6**, 249–253 (2010).

8. Babinec, T. M. *et al.* A diamond nanowire single-photon source. *Nat. Nanotechnol.* **5**, 195–199 (2010).

9. Dolde, F. *et al.* Electric-field sensing using single diamond spins. *Nat. Phys.* **7**, 459–463 (2011).

10. Balasubramanian, G. *et al.* Nanoscale imaging magnetometry with diamond spins under ambient conditions. *Nature* **455**, 648–651 (2008).

11. Mochalin, V. N., Shenderova, O., Ho, D. & Gogotsi, Y. The properties and applications of nanodiamonds. *Nat. Nanotechnol.* **7**, 11–23 (2012).

12. Hill, H. G. M., Jones, A. P. & Hendecourt, L. B. Diamonds in carbon-rich proto-planetary nebulae. *Astron. Astrophys.* **44**, 41–44 (1998).

13. Dai, Z. R. *et al.* Possible in situ formation of meteoritic nanodiamonds in the early Solar System. *Nature* **418**, 157–159 (2002).

14. Greaves, J. S. S. *et al.* Anomalous microwave emission from spinning nanodiamonds around stars. *Nat. Astron.* **2**, 662–667 (2018).

15. Barnard, A. S. *Stability of Diamond at the Nanoscale*. *Ultrananocrystalline Diamond: Synthesis, Properties and Applications: Second Edition* (2012). doi:10.1016/B978-1-4377-3465-2.00001-3.

16. Badziag, P., Verwoerd, W. S., Ellis, W. P. & Greiner, N. R. Nanometre-sized diamonds are more stable than graphite. *Nature* **343**, 244–245 (1990).

17. Raty, J. Y. & Galli, G. Ultradispersity of diamond at the nanoscale. *Nat. Mater.* **2**, 792–795 (2003).

18. Bradac, C. & Osswald, S. Effect of structure and composition of nanodiamond powders on thermal stability and oxidation kinetics. *Carbon N. Y.* **132**, 616–622 (2018).

19. Osswald, S., Yushin, G., Mochalin, V., Kucheyev, S. O. & Gogotsi, Y. Control of sp2/sp3 carbon ratio and surface chemistry of nanodiamond powders by selective oxidation in air. *J. Am. Chem. Soc.* **128**, 11635–11642 (2006).

20. Danilenko, V. V. On the history of the discovery of nanodiamond synthesis. *Phys. Solid State* **46**, 595–599 (2004).

21. Guglielmotti, V. *et al.* CVD-based techniques for the synthesis of nanographites and nanodiamonds. *Nuovo Cim. della Soc. Ital. di Fis. C* **36**, 3–9 (2013).

22. Basso, L. *et al.* All-optical single-step process for production of nanometric-sized fluorescent diamonds. *Nanoscale* (2018) doi:10.1039/C7NR08791H.

23. Galimov, É. M. *et al.* Experimental corroboration of the synthesis of diamond in the cavitation process. *Dokl. Phys.* **49**, 150–153 (2004).

24. Banhart, F. & Ajayan, P. M. Carbon onions as nanoscopic pressure cells for diamond formation. *Nature* **382**, 433–435 (1996).

25. Daulton, T. L., Kirk, M. A., Lewis, R. S. & Rehn, L. E. Production of nanodiamonds by high-energy ion irradiation of graphite at room temperature. *Nucl. Instruments Methods Phys. Res. Sect. B Beam Interact. with Mater. Atoms* **175**–**177**, 12–20 (2001).

26. Wang, J. B., Zhang, C. Y., Zhong, X. L. & Yang, G. W. Cubic and hexagonal structures of diamond nanocrystals formed upon pulsed laser induced liquid – solid

interfacial reaction. *Chem. Phys. Lett.* **361**, 86–90 (2002).

27. Lin, I.-N., Chen, H.-C., Wang, C.-S., Lee, Y.-R. & Lee, C.-Y. Nanocrystalline diamond microstructures from Ar/H2/CH4-plasma chemical vapour deposition. *CrystEngComm* **13**, 6082 (2011).

28. Chen, Z. . *et al.* Growth of nano-crystalline diamond by pulsed laser deposition in oxygen atmosphere. *J. Cryst. Growth* **226**, 62–66 (2001).

29. Huang, Q. *et al.* Nanotwinned diamond with unprecedented hardness and stability. *Nature* **510**, 250–253 (2014).

30. Hu, S., Sun, J., Du, X., Tian, F. & Jiang, L. The formation of multiply twinning structure and photoluminescence of well-dispersed nanodiamonds produced by pulsed-laser irradiation. *Diam. Relat. Mater.* **17**, 142–146 (2008).

31. Nee, C. H., Yap, S. L., Tou, T. Y., Chang, H. C. & Yap, S. S. Direct synthesis of nanodiamonds by femtosecond laser irradiation of ethanol. *Sci. Rep.* **6**, 1–8 (2016).

32. Kumar, A. *et al.* Formation of nanodiamonds at near-ambient conditions via microplasma dissociation of ethanol vapour. *Nat. Commun.* **4**, 1–8 (2013).

33. Bachmann, P. K., Leers, D. & Lydtin, H. Towards a General Concept of Diamond Chemical Vapor-Deposition. *Diam. Relat. Mater.* **1**, 1–12 (1991).

34. Torres-Gómez, L. A., Barreiro-Rodríguez, G. & Méndez-Ruíz, F. Vapour pressures and enthalpies of sublimation of ferrocene, cobaltocene and nickelocene. *Thermochim. Acta* **124**, 179–183 (1988).

35. Djerdj, I. *et al.* Transmission electron microscopy study of carbon nanophases produced by ion beam implantation. *Mater. Sci. Eng. C* **26**, 1202–1206 (2006).

36. Wen, B., Zhao, J. J. & Li, T. J. Synthesis and crystal structure of n-diamond. *Int. Mater. Rev.* **52**, 131–151 (2007).

37. Wen, B., Zhao, J., Li, T. & Dong, C. N-diamond: An intermediate state between rhombohedral graphite and diamond? *New J. Phys.* **8**, (2006).

38. Peng, J. L., Bursill, L. A., Jiang, B., Orwa, J. O. & Prawer, S. Growth of c-diamond, n-diamond and i-carbon nanophases in carbon-ion-implanted fused quartz. *Philos. Mag. B Phys. Condens. Matter; Stat. Mech. Electron. Opt. Magn. Prop.* **81**, 2071–

2087 (2001).

39. Peng, J. L., Orwa, J. O., Jiang, B., Prawer, S. & Bursill, L. A. Nano-crystals of c-diamond, n-diamond and i-carbon grown in carbon-ion implanted fused quartz. *Int. J. Mod. Phys. B* **15**, 3107–3123 (2001).

40. Kittel, C. *Introduction to Solid State Physics*. *Solid-State Physics (Fourth Extensively Updated and Enlarged Edition): An Introduction to Principles of Materials Science* (2010). doi:10.1007/978-3-540-93804-0.

41. Xiao, J., Li, J. L., Liu, P. & Yang, G. W. A new phase transformation path from nanodiamond to new-diamond via an intermediate carbon onion. *Nanoscale* **6**, 15098–15106 (2014).

42. Hirai, H. & Kondo, K. 1991 Science Modified Phases of Diamond Formed Under Shock Compression and Rapid Quenching.pdf. **253**, 65–68.

43. Prawer, S. *et al.* Size dependence of structural stability in nanocrystalline diamond. *Phys. Rev. B* **62**, R16360–R16363 (2000).

44. Nemeth, P. *et al.* Lonsdaleite is faulted and twinned cubic diamond and does not exist as a discrete material. *Nat. Commun.* **5**, (2014).

45. Németh, P., Garvie, L. A. J. & Buseck, P. R. Twinning of cubic diamond explains reported nanodiamond polymorphs. *Sci. Rep.* **5**, 0–6 (2015).

46. Osswald, S., Mochalin, V. N., Havel, M., Yushin, G. & Gogotsi, Y. Phonon confinement effects in the Raman spectrum of nanodiamond. *Phys. Rev. B - Condens. Matter Mater. Phys.* **80**, (2009).

47. Ferrari, A. C. & Robertson, J. Raman spectroscopy of amorphous, nanostructured, diamond-like carbon, and nanodiamond. *Philos. Trans. R. Soc. A Math. Phys. Eng. Sci.* **362**, 2477–2512 (2004).

48. Askari, S., Levchenko, I., Ostrikov, K., Maguire, P. & Mariotti, D. Crystalline Si nanoparticles below crystallization threshold: Effects of collisional heating in non-thermal atmospheric-pressure microplasmas. *Appl. Phys. Lett.* **104**, (2014).

49. Bruggeman, P. J., Iza, F. & Brandenburg, R. Foundations of atmospheric pressure non- equilibrium plasmas. *Plasma Sources Sci. Technol* **26**, (2017).

50. Gatti, M. & Kortshagen, U. Analytical model of particle charging in plasmas over a wide range of collisionality. *Phys. Rev. E - Stat. Nonlinear, Soft Matter Phys.* **78**, 1–6 (2008).

51. Conroy, D., Moisala, A., Cardoso, S., Windle, A. & Davidson, J. Carbon nanotube reactor: Ferrocene decomposition, iron particle growth, nanotube aggregation and scale-up. *Chem. Eng. Sci.* **65**, 2965–2977 (2010).

52. Kuwana, K. & Saito, K. Modeling ferrocene reactions and iron nanoparticle formation: Application to CVD synthesis of carbon nanotubes. *Proc. Combust. Inst.* **31 II**, 1857–1864 (2007).

53. Wirth, C. T. *et al.* The phase of iron catalyst nanoparticles during carbon nanotube growth. *Chem. Mater.* **24**, 4633–4640 (2012).

54. Lin, P. A., Kumar, A. & Mohan Sankaran, R. New insights into plasma-assisted dissociation of organometallic vapors for gas-phase synthesis of metal nanoparticles. *Plasma Process. Polym.* **9**, 1184–1193 (2012).

55. Lin, L., Starostin, S. A., Hessel, V. & Wang, Q. Synthesis of iron oxide nanoparticles in microplasma under atmospheric pressure. *Chem. Eng. Sci.* **168**, 360–371 (2017).

56. Zakurin, V., Gubin, S. P. & Bochin, V. P. Fragmentation of metallocenes in the low-temperature plasma I. comparative study of the arc discharge plasma ion composition and the mass spectra obtained under the electron impact. *J. Organomet. Chem.* **23**, 535–544 (1970).

57. Gruen, D. M. Conversion of fullerenes to diamond.

58. Liu, H. & Dandy, D. S. *Diamond Chemical Vapor Deposition - Nucleation and Early Growth Stages*. (Noyes Publications, 1995).

59. Pehrsson, P. E. & Butler, J. E. Diamond Films and Coatings. in (ed. Davis, R.) 68 (Noyes Publications, 1993).

60. Das, D. & Singh, R. N. A review of nucleation, growth and low temperature synthesis of diamond thin films. *Int. Mater. Rev.* **52**, 29 (2007).

61. Rabeau, J. R., John, P., Wilson, J. I. B. & Y. Fan, J. No Title. *J. Appl. Phys.* **96**,

6724 (2004).

62. Gruen, D. M., Redfern, P. C., Horner, D. A., Zapol, P. & Curtiss, L. A. Theoretical Studies on Nanocrystalline Diamond: Nucleation by Dicarbon and Electronic Structure of Planar Defects. *J. Phys. Chem. B* **103**, 5459–5467 (1999).

63. May, P. W., Harvey, J. N., Allan, N. L., Richley, J. C. & Mankelevich, Y. A. Simulations of chemical vapor deposition diamond film growth using a kinetic Monte Carlo model and two-dimensional models of microwave plasma and hot filament chemical vapor deposition reactors. *J. Appl. Phys.* **108**, (2010).

64. Barnard, A. S., Russo, S. P. & Snook, I. K. Coexistence of bucky diamond with nanodiamond and fullerene carbon phases. *Phys. Rev. B* **68**, 73406 (2003).

65. Mykhaylyk, O. O., Solonin, Y. M., Batchelder, D. N. & Brydson, R. Transformation of nanodiamond into carbon onions: A comparative study by high-resolution transmission electron microscopy, electron energy-loss spectroscopy, x-ray diffraction, small-angle x-ray scattering, and ultraviolet Raman spectroscopy. *J. Appl. Phys.* **97**, (2005).

66. Yang, C. C. & Li, S. Size-Dependent Temperature - Pressure Phase Diagram of Carbon. 1423–1426 (2008).

67. Bundy, F. P. *et al.* The pressure–temperature phase and transformation diagram for carbon. *Carbon N. Y.* **34**, (1996).

68. Jiang, Q. & Chen, Z. P. *Thermodynamic phase stabilities of nanocarbon*. *Carbon* (Elsevier, 2006).

Chapter 5 - Energy Band Diagrams

5.1 Introduction

5.1.1 Plasma synthesis and optoelectronic properties of nanoparticles

A plasma process used to synthesize solid materials must attain a certain degree of control over their optical and electronic properties, in order to use them for applications. When the dimensions of a solid system approach the nanometer range (< 20-40 nm) most of the material properties, and especially optoelectronic ones, become strongly size-dependent due to the quantum confinement of carriers wavefunction. Hence, the control of nanoparticles size at the synthesis stage has a direct effect on their optoelectronic properties. This chapter introduces a description of the most important electronic states of a solid through the description of energy band diagrams (EBDs) and the experimental determination of their key parameters. Also, two case studies will be presented to show more practically the experimental methods used throughout this study to estimate the EBDs.

5.1.2 Electron states in solids and EBDs

The EBD is a diagram composed of the key electron energy states near the Fermi level. They are usually depicted as a function of a spatial dimension because they are most useful when comparing the electron energy states at the interface between two materials, and the relative position determines the transport processes at the interface. In fact, these states describe the least bound electrons in a solid (e.g.: valence band states in semiconductors) and the nearest empty electron states (e.g.: conduction band states in semiconductors) which are the most important ones for low energy transitions and transport phenomena. Their relative position in respect to the Fermi level and their density per unit energy interval (i.e.: density of states, DOS) determine the main characteristics of a material at the macroscopic level, whether metallic, semiconducting or insulating (see Figure 5.1).[1] Instead, core electrons are strongly bound to the nuclear Coulomb potential and do not participate to most of the physical and chemical interactions, except when dealing with high energy excitations (e.g. excitation by X-rays).

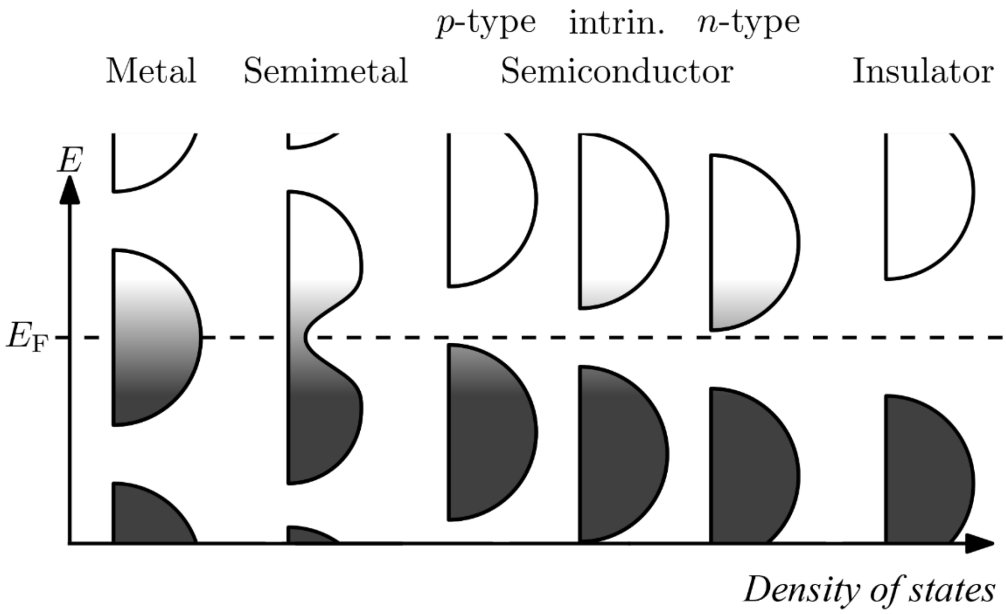

Figure 5.1 - Schematic representation of energy band diagrams for materials distinguished for electrical conduction properties, with indication of density of states in the abscissa and statistical population of levels as a color shade (black means completely filled, white completely empty). If the Fermi level falls within an energy band, as in metals and semimetals, the electrons/holes can acquire arbitrarily small amounts of energy from external stimuli. In semiconductors and insulators instead, there is an energy gap for which no electron state exist and whatever perturbation must have at least that amount of energy to cause a transition. Semiconductors are insulators in which the Fermi level is near enough to the band edges (small gap) that the thermal energy (26 meV @ RT) is able to partially populate the conduction (valence) band with electrons (holes). Doping of a semiconductor can move the energy bands relative to the Fermi level and populate preferentially one kind of charge carrier, conduction electrons in n-type, valence holes in p-type.[1]

There is an infinite number of energy states in a solid material, distributed in energy bands. These bands are composed of closely spaced energy levels which can be seen as originating from the intermixing of the discrete atomic levels as they approach to distances where electrons start to interact (see Figure 5.2a). The way in which electrons interact is such there will be some forbidden regions of energy (Energy bandgap) for which no electron states are possible, and the specific way depends on the symmetry of the atomic arrangement in the material. For crystalline materials, the energy bands depend on the crystal symmetry. They are described as energy band structures $E(\vec{k})$ (figure 5.2b), which are periodic functions of the crystal momentum $\vec{k}$ (a quantity that describes the propagation of electron "waves" in a crystalline lattice) with the same periodicity of the crystalline lattice $E(\vec{k}) = E(\vec{k} + \vec{G})$, where $\vec{G}$ is a vector of the reciprocal lattice associated to the crystal. As a result, the macroscopic physical properties (electrical resistivity, heat conduction, propagation of light etc.) of a crystalline material are generally anisotropic and follow the symmetry of the crystal. For most of the practical

applications though, the full description of the symmetry properties of electron states in not needed.[2] Hence, EBDs are built to show only the minimum number of parameters for

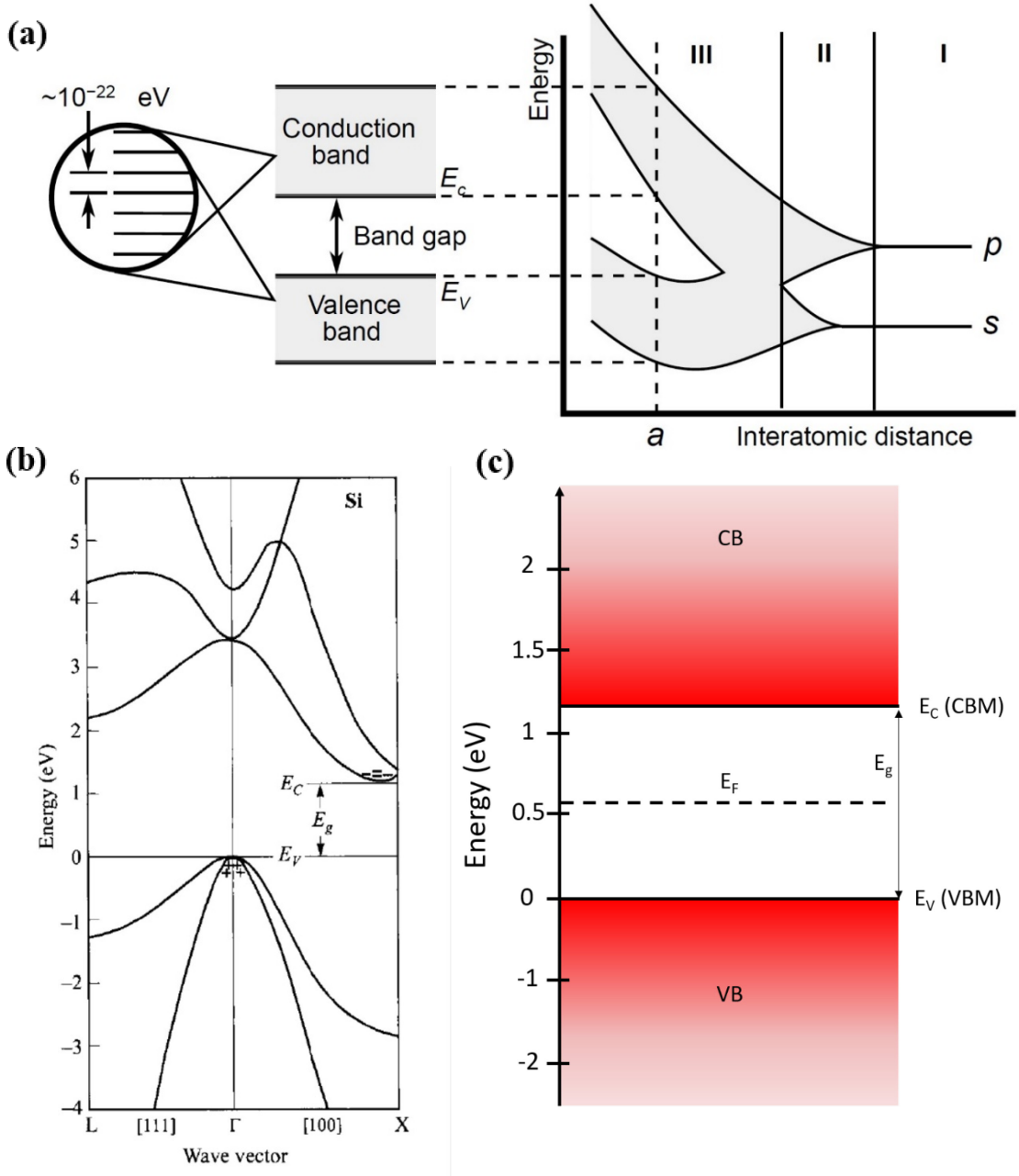

Figure 5.2 - (**a**) Schematic diagram representing the formation of extended energy bands of a solid material with N atoms from N discrete atomic/molecular levels as a result of intermixing between electron levels by shrinking the interatomic distance. Roman numbers distinguish regimes in which electron levels have a distinct character; I) atomic -like discrete levels (in energy), II) a molecular-like region III) full band-like extended states. These regions can be also interpreted in terms of the Heisenberg indetermination principle for electron wavefunctions, atomic discrete levels are localized in atoms (well-determined position) and are less-determinate in momentum. The character of band-like states in region III is opposite, electrons are delocalized throughout the solid (extended) and are more-defined in momentum. (**b**) Calculated band-structure of bulk crystalline Silicon in the reduced zone. The lines are the energy-momentum relations of electron states along particular symmetry directions of the crystal. The indicated quantities (E_C, E_V, E_g) together with the Fermi level are the energy levels of interest to build EBDs. (**c**) Energy band diagram of intrinsic bulk Silicon relative to the band structure in (**a**) and referenced to the valence band maximum.[2]

the electron states of interest, and as stated earlier these are usually the energy of electron states near the Fermi level (valence band maximum VBM or E_V and conduction band minimum CBM or E_C), the Fermi level itself and the bandgap E_g (Figure 5.2c). These quantities will be introduced better in section 5.2.1.

It is important to remember though, that EBDs inherit the limits of applicability of the band structure picture, in addition to the lack of information about the symmetry of electron states. It can only accurately describe the behavior on the long range, as the resolution (in space) of the band diagram is subject to the Heisenberg uncertainty principle. Electron levels in bands are delocalized in all the crystal and well defined in the momentum space, so the band structure picture is precisely defined only over long length scales. By shrinking the size of a crystal, the quantum confinement of electron wavefunction turns the character of electron states towards a molecular-like description, hence localized in space with less defined momentum (in a analogous way as passing from region III to region II in Figure 5.2a, but in function of particle size and with different dynamics). Hence, for nanoparticles (1 nm < size < 40 nm) and clusters (< 1nm), which lie in this transition region (*mesoscopic scale*), the band-like description of electron levels is not always meaningful. Thus, some authors use the molecular orbital terminology nanoparticle EBDs, and the valence band maximum is called the highest occupied molecular orbital (HOMO) and the conduction band minimum is the lowest unoccupied molecular orbital (LUMO). In addition, the band structure picture is accurate only for weakly correlated materials, where the one-electron picture is valid.[1] For these reasons, care must be taken when interpreting the values in EBDs as described by the energy band theory. Even with these complications, the energy band diagrams for nanoparticles proved useful for implementing nanostructured materials in devices.

5.2 Anatomy of an EBD

5.2.1 Definition of parameters of an EBD

Figure 5.2c showed an example of a relative EBD diagram, composed from the parameters which are intrinsic of the material. In Figure 5.3 an energy band diagram for an interface between a semiconductor and vacuum is shown. This version is more complete because it includes physical quantities of interest for interfacing different kind of materials (metals and semiconductors, or metals and oxides…) and which are experimentally accessible.

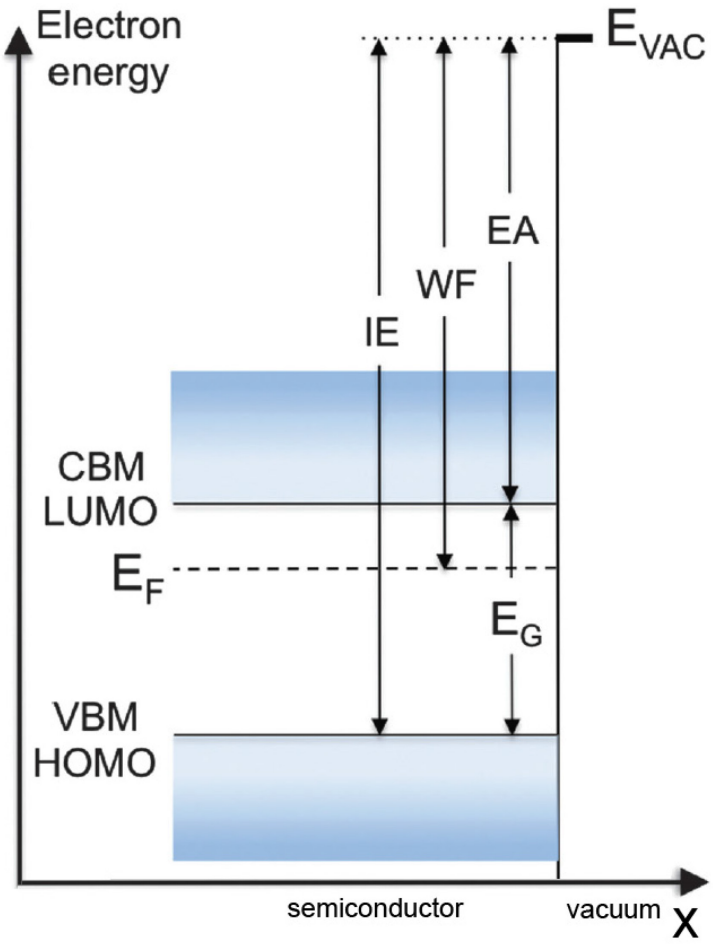

Figure 5.3 - Energy band diagram of a semiconductor/vacuum interface with flat bands. CBM/LUMO and VBM/HOMO are the band edges, E_F the Fermi level, E_{VAC} vacuum level, WF work function, E_G the energy gap, IE ionization energy and EA electron affinity, adapted from [2].

The most important electron energy bands are called the *conduction band* and the *valence band* and are the lowest energy unoccupied band and the highest energy occupied band respectively. The *valence band maximum* (VBM) or valence band edge (E_V) and the

conduction band minimum (CBM) or conduction band edge (E_C) are the highest lying and lowest lying electron energy levels in the respective bands, which matter as threshold energies for transport phenomena within the same band (intra-band transitions). These correspond to the highest occupied molecular orbital (HOMO) and lowest unoccupied molecular orbital (LUMO) respectively in the molecular orbital picture.

The *energy bandgap* E_G (or HOMO/LUMO gap) is the energy difference between the band edges E_C - E_V and represents an energy threshold value for interactions that promote electrons across bands (inter-band transitions). It is the main factor distinguishing materials for electrical conductivity and optical response in the visible range. Wide bandgap materials have negligible concentration of electrons in the conduction band (see Figure 5.1 comparing shaded areas for different gap materials) hence there are no free carriers to conduct electricity resulting in an electrical insulator. Also, the bandgap serves as an energy threshold for absorption of light. In fact, semiconductors/insulators with bandgap values bigger than 3.26 eV are transparent to visible light. When considering the interacting nature of charge carriers, especially in semiconductive nanoparticles, it is important to distinguish between an *optical bandgap* (E_{OPT}) and an *electronic bandgap* (or transport gap, E_{TRA}). The transition of an electron to the conduction band leaves an electron-hole in the valence band, which is bound to the parent electron via Coulomb interactions (= *exciton*). A process that must separate the two, for example in order to have charge transport, needs an extra energy (hence $E_{OPT} < E_{TRA}$). Whenever is not explicitly stated, for "energy bandgap" is meant the lower energy one (E_{OPT}). Regarding optical phenomena we also temporarily restore the symmetry features of band structure to distinguish two kinds of bandgaps. For some materials (e.g.: Si in figure 5.2b) the lowest energy gap happens at different values of crystal momentum $\vec{k}$ (*indirect bandgap*). Inter-band transitions then must involve a change in crystal momentum through the emission or absorption of a phonon (quanta of lattice vibrations). The optical absorption (and emission) in this case is less efficient, as opposed to the efficient inter-band transitions across a *direct bandgap*.

The Fermi level E_F is a thermodynamic quantity which is a crucial factor determining the electrical properties of a semiconductor and does not depend on the band structure of a material. It can be defined as *the thermodynamic work required to add an electron to the material* or *the hypothetical energy level of electron which would have a 50% probability to be occupied at thermodynamic equilibrium*. It does not necessarily correspond to an

actual energy level, but its relative position with respect to available energy states determines the probability of occupation of a certain state with energy ε at equilibrium. Its position relative to the band edges, which can be modulated by doping with a foreign element, determines the type of charge carrier (*majority carriers*) conducting in the metal/semiconductor (see Figure 5.1 how the shaded area changes among different types of semiconductors). The Fermi level is a conserved quantity in thermodynamic equilibrium, hence when contacting different materials stays constant. Measurements of the work function relative to a known reference permits to estimate its value against a well-defined vacuum level.

VBM, CBM, E_G and E_F are intrinsic parameters of materials and electrons and their values vary only with internal changes to the material or the addition of electrons to the system. Energy scales though are always defined up to an additive constant, and practically speaking, a reference value for energy must be chosen when interfacing different materials. This includes practically all the experimental conditions for measurements as the sample materials will be interfaced to electrical contacts or other materials.

Instead (Figure 5.3) work function (WF), ionization energy (IE) and electron affinity (EA) specifically depend on the interface with another material or "vacuum" and are usually the experimentally accessible quantities. E_{VAC} is called the *local vacuum level* and is the energy level of an electron just outside the influence of the surface, with no kinetic energy. The vacuum level is an ideal reference level, while experimentally it can change significantly between different measurements methods. For this reason, throughout this chapter it will be called interchangeably as a reference level or vacuum level. Ionization Energy is the minimum energy needed to extract an electron from the VBM, $IE = E_{VAC} - E_V$. Conversely Electron Affinity (also denoted with the "χ" symbol) is the energy obtained by moving an electron from the vacuum just outside the semiconductor to the bottom of the conduction band $EA = E_{VAC} - E_C$. The WF (also denoted with the "φ" symbol) is the minimum energy needed to remove an electron from a solid to a point in the vacuum immediately outside the solid surface $WF = E_{VAC} - E_F$ and coincides with IE and EA in the case of metals. The work function takes values between IE and EA for semiconductors, for which the Fermi Level falls in the middle of the energy gap where there are no electron levels. WF, IE and EA are defined in function of a reference level, and thus are quantities which vary depending on the state of the surface of a material. The surface variability may be due to surface dipoles or the influence of adsorbates on electron

states, and usually this contribution cannot be distinguished experimentally from the bulk one.[3]

5.2.2 Importance of EBDs: Junctions

The practical importance of EBDs can be appreciated when describing how the electron energy levels behave upon joining two different materials. A detailed description of all the possibilities is outside the scope of this work, however a brief explanation of most common junctions will be given.

The first example is a *p-n homojunction*, which is the junction created by two differently doped version of the same semiconductor. The two semiconductors individually have different Fermi levels, when joined together electrons flow from the n-type to the p-type and a holes diffuse from the p-type to the n-type, due to the different densities of such species at the same energy in the two cases. This in turns, leaves behind a space charge region of opposite sign in the interface region and a resulting built-in electric field. At thermal equilibrium the Fermi level is equilibrated, hence the bands bend due to the built-in potential (V_{bi}) created in the space charge region. The equilibrium energy band diagram of the junction is shown in Figure 5.4a. After the junction is made, the majority carriers in the respective side of the junction see an additional energy barrier equal to the built-in

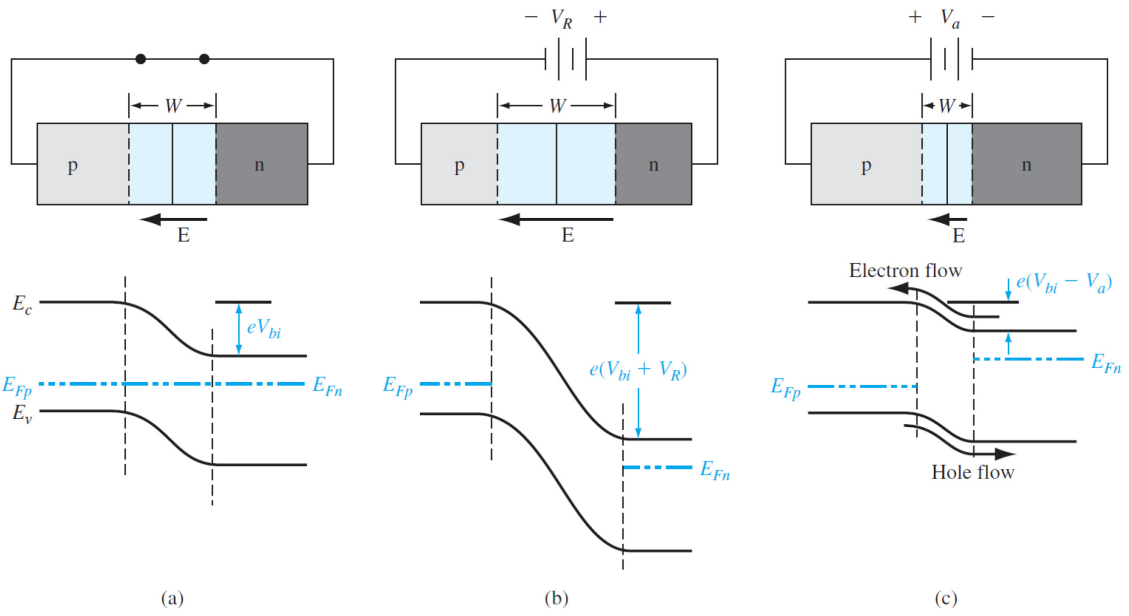

Figure 5.4 - Band diagrams of a junction between a p-type and a n-type version of the same semiconductor (**a**) at thermal equilibrium, (**b**) applying a reverse bias and (**c**) a direct bias.[4]

potential for diffusing to the other side.[4] If a bias is applied, thermal equilibrium is broken, the Fermi level is not conserved anymore and the situation can be further stressed (higher barriers, figure 5.4b) with a reverse bias or relieved (lower barriers and flow of majority carriers, figure 5.4c) with a direct bias. These principles have an enormous practical value for the fabrication of light-emitting diodes and radiation detectors, transistors and many more devices.

The junction between a metal and a semiconductor is analogous, but with the space charge region developing only on the side of the semiconductor. Also, the sign of the space charge depends on how the work function of the two materials compare. In figure 5.5a the EBDs for an n-type semiconductors with lower work function than the metal ($\varphi_m > \varphi_s$) is shown. Electrons flowing from the metal to the semiconductor experience a barrier (*Schottky barrier* φ_{B0}) whose magnitude depends on the difference between metal work function and semiconductors electron affinity. This barrier does not change (ideally) upon applying a bias to the junction (Figures 5.5b and 5.5c) while the one felt by electrons flowing from the semiconductor to the metal can be strongly modulated by the bias. The conduction through a junction of this kind is bidirectional but only due to one type of charge carrier and its behavior can be tailored by selecting appropriate combinations of metals and semiconductors with the right work function and electron affinity. This has enormous impact on the engineering of all the semiconductor-based devices (photovoltaic cells, transistors, diodes, …) for the design of the metallic contacts.

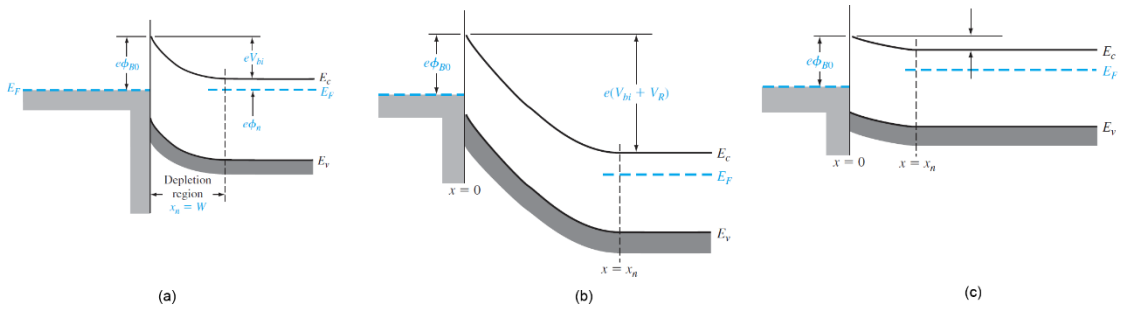

Figure 5.5 - Band diagrams of a junction between a metal and n-type semiconductor with lower work function (**a**) at thermal equilibrium, (**b**) applying a reverse bias and (**c**) a direct bias[3]

An analogous situation happens in a *semiconductor-electrolyte interface*, for which there will be charge transfer between the liquid and the solid if the redox potentials of the electrolyte fall inside the semiconductor's bandgap. In this context, band diagrams are

vital to design photoelectrochemical cells that catalyze redox reactions of interest to environmental sciences.

The junctions between different bandgap semiconductors are called *heterojunctions*, and are distinguished in three types, depending on the dopant type of each semiconductor. In figure 5.6 the band diagrams of a junction between a small-gap n-type (n) semiconductor and a wide-gap p-type semiconductor (P) are shown. Band discontinuities exist before and after the junction is made (ΔE_C and ΔE_V in figure 5.6) and can be estimated following the *Anderson rule*. This rule, states that the vacuum levels of the two semiconductors should be aligned, hence the mismatch between band edges can be related to the electron affinities of each semiconductor according to: $\Delta E_c = e(\chi_n - \chi_p)$ and $\Delta E_c + \Delta E_V = \Delta E_G$.

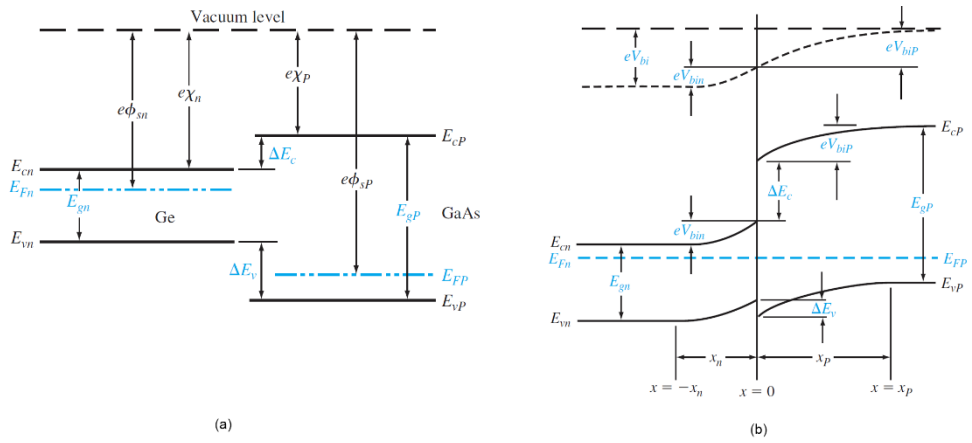

Figure 5.6 - Band diagrams of a junction between a n-type small gap semiconductor and a p-type wide gap semiconductor, (**a**) before the junction is made (non-equilibrated) and (**b**) band bending and discontinuities after the junction is made.

As in the case of a single semiconductor p-n junction, in order for Fermi Levels to equilibrate, the majority carriers flow from across the interface and create space charges. This time though the band discontinuities can create potential wells for charge carriers, and peculiar transport properties in those regions.

These examples showed that the EBD is a powerful tool to understand the potential landscape seen by charge carriers when a junction between materials is made, and how a composite system is going to behave upon external perturbation. It was also mentioned that most of the phenomena describing junctions will be determined once Fermi Levels, bandgaps and values of band edges is known. Then, during the design of a device

composed of different interfaces, the estimation of EBDs of materials involved is crucial and very often a sufficient condition to choose the right materials for a given application.

5.3 Experimental determination of parameters

5.3.1 Measurement of parameters

In this section the techniques used for the experimental determination of the minimum set parameters to build the EBD will be described. In this perspective, the knowledge of Fermi level, bandgap and valence band edge against a determined reference level is sufficient to build an EBD. The techniques described in this section will be used in the determination of EBDs in the two case studies presented in section 5.4 and for the plasma-synthesized nanoparticles throughout this work:

1. **Fermi level**: from photoemission techniques (PES) (section 5.3.2) and Kelvin probes (KP) (section 5.3.3).

2. **Optical bandgap**: through ultraviolet-visible (UV-Vis) spectrophotometry and fluorescence measurements (section 5.3.5) and surface photovoltage spectroscopy with the Kelvin Probe (section 5.3.3).

3. **Valence band edge**: from photoemission techniques in ultra-high vacuum (UHV) (section 5.3.2) and with an air-photoemission system (APS) attached to the Kelvin probe (section 5.3.3).

5.3.2 UHV Photoelectron Spectroscopy

Photoemission spectroscopy experiments are based on the electrons emitted by a solid in vacuum (10^{-9} torr) after the absorption of high energy photons. With deep UV sources (hv < 100 eV) the technique is called ultraviolet photoemission spectroscopy (UPS) and scopes the energy and yield of electrons coming from the valence band region of a solid material. The UV sources used for these measurements are typically gas discharge lamps, and an electrostatic analyzer is used to count the emitted electrons, resolved in energy. However only electrons at the topmost surface (2-3 nm) can escape the material, hence UPS measurement probe only properties at this depth.

The kinetic energy of the photoemitted electrons depends on the difference in energy between the radiation source and the ionization energy of electrons in the solid as expressed in eq. 5.1.[5] The samples are grounded in the measurement setup, hence in electrical contact with the spectrometer. In this case the Fermi level of the sample is equalized to the spectrometer Fermi level, and the ionization energy is relative to the spectrometer reference level. Figure 5.6a shows the energy diagram relative to the sample-spectrometer system in a UPS measurement. IE can be expressed in terms of the known work function of the spectrometer ϕ_{sp} and the energy separation between the electrons excited in the valence band states and the fermi level of the material (binding energy ϵ_B). In this frame the Fermi edge is a reference point of energy scale ($\epsilon_B = 0$) in photoelectron spectroscopy, given the electrical contact with the spectrometer and should not change from sample to sample as long as they are grounded.[6,7]

$$\epsilon_{kin} = h\upsilon - IE = h\upsilon - (\epsilon_B + \phi_{sp}) \qquad \text{Eq. 5.1}$$

After being photoexcited, electrons must travel to the surface and escape it (Figure 5.6b). In doing so, they undergo inelastic scattering with other electrons in the material (secondary electrons), a portion of which have enough energy to escape the surface. The

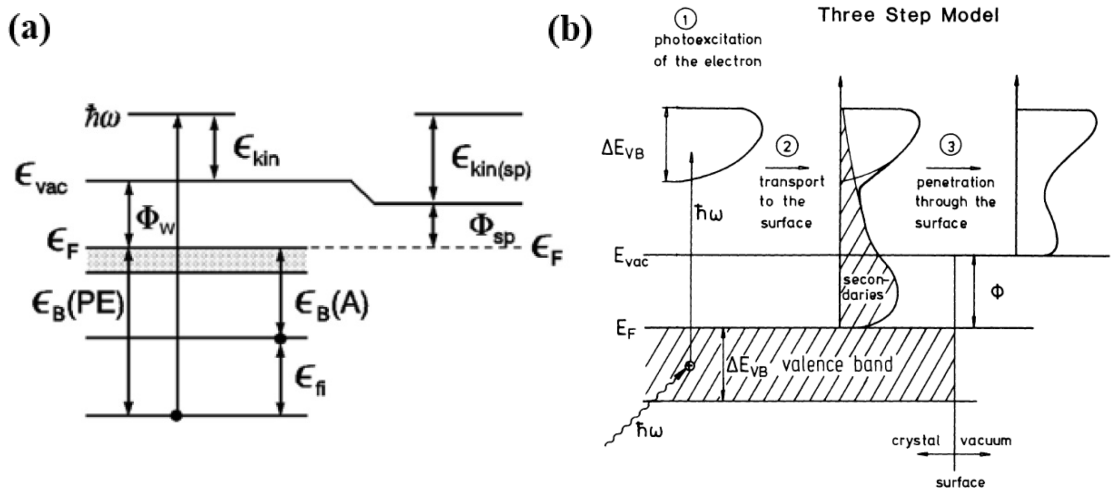

Figure 5.6 - (**a**) Energy band diagram illustrating the photoexcitation process for a grounded metallic sample in PES measurements. $\epsilon_B(PE)$ is the binding energy appearing in eq. 5.1, ϕ_W is the sample work function, other quantities not mentioned in the text are of interest to Auger spectroscopy.(**b**) Simplified model that explains the phenomena happening to photoexcited electrons exiting the surface, the features profiled can be observed in Figure 5.7.[5]

cutoff energy below which secondary electrons cannot escape the surface is depends on the work function of the material and the energy of incoming photons.

A typical spectrum is presented in Figure 5.7, showing the basic photoemission features for a nanostructure Si film surface.[8] Three common features can be observed in ideal UPS spectrum:

1. A threshold at low binding energies (high kinetic energies) at which a significant photoemission signal starts (VB edge in Figure 5.7).

2. A structure of peaks which pertain to valence electrons emitted from the valence band, whose intensity depend on the density of states at a given energy (The example in Figure 5.7 is relatively structureless, only a peak at 12.5 eV may be assigned to VB states).

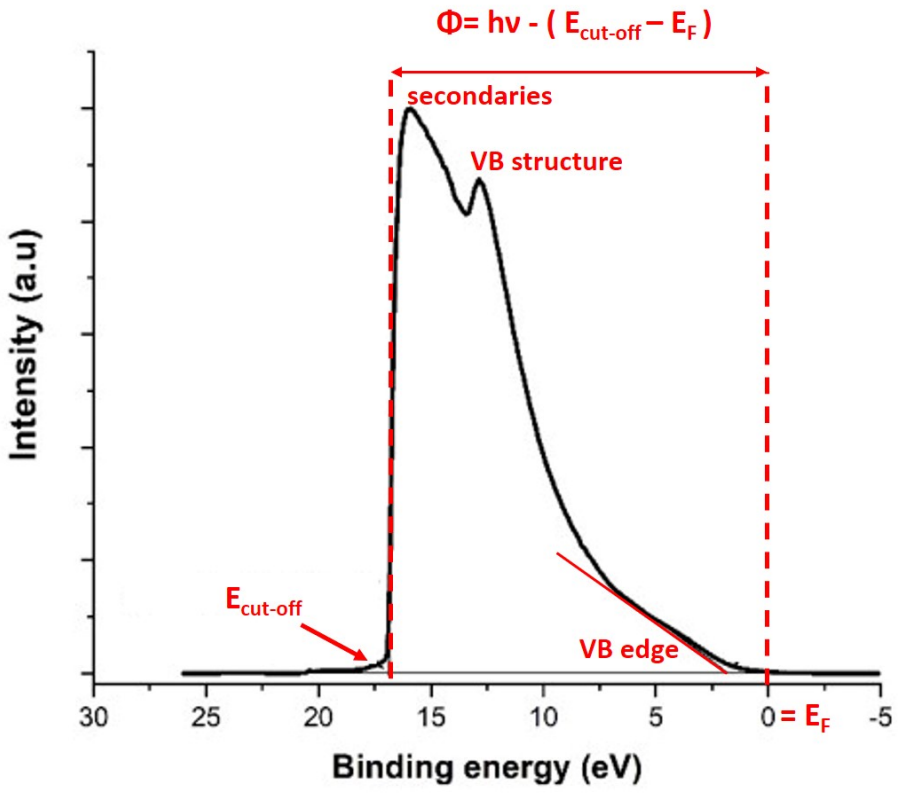

Cut off (eV)	Work function (eV)	VB (eV)
16.8	4.4 ± 0.2	5.9 ± 0.1

Figure 5.7 - UPS spectrum of a nanostructured Si surface and calculated values, showing the various features listed in the text, based on the model in figure 5.6b. The excitation source is a He(I) discharge with energy hν=21.22 eV [5]

3. A broad asymmetric peak caused by secondary electrons (Figure 5.6b, "secondaries" peak in Figure 5.7) with a sharp cutoff ($E_{cut\text{-}off}$ in figure 5.7) at high binding energies (low kinetic energies), generally also the spectrometer has a contribution to this peak.

From the above models, a direct interpretation of the spectral features is possible in function of the materials parameters. When a sharp edge in the photoemission (feature 1) is distinguished at low binding energies its threshold energy is an estimation of the ionization energy. If the cutoff energy for secondary emission is detectable (feature 2), the work function of the material is represented by the difference between the energy of the photon source (usually He(I) at 21.22 eV) and full breadth of the photoemission spectrum.[6] Experimentally, it is usually needed to apply a bias (<10 V) to see an additional emission cut-off due to secondary electrons emitted by the spectrometer. If samples are correctly grounded and the work function of the spectrometer is known or else measuring the work function of a reference material (as Au or Cu) along with the sample permits to estimate Fermi Level and VBM of the sample material from the measured Work Function and Ionization energy. UPS measurements are implicitly limited by the general mechanism involved in the photoemission as the light interacting with the sample induces a surface dipole which complicates the evaluation of the Fermi level and VBM values, especially in conductive or highly doped samples.[9] In addition direct (i.e., k-conserving) transitions influence the UPS spectra heavily, so some information about the valence band states may be missing because of transitions forbidden by the k-conservation selection rule.[8] However, the UPS strength rely on the high photoemission yield, and the narrow energy resolution achievable (30 meV commonly).

Photoemission experiments with X-rays (XPS) can be also used to estimate the valence band edge of a semiconductor, with similar considerations from the point of view of energetics as UPS (Figure 5.6a). XPS measurements are not affected by k-selection rules and measures essentially a density of valence-band states. However, only the difference E_V - E_F can be assessed as no secondary electrons' cutoff is present, and the energy resolution is much lower than UPS, typical values are 0.3-0.5 eV.[8]

Both techniques though are operated in high vacuum though, which can help preserving the state of surfaces.

5.3.3 Kelvin Probe

The Kelvin probe is non-contact, non-destructive scanning probe microscopy technique used to measure the work function of the sample under study. It is based on a parallel plate capacitor experiments performed by Lord Kelvin in 1898,[10] which has later been used to measure the contact potential difference between dissimilar metals. This technique measures the work function of a material relative to a metallic tip with known work function Φ_{KP}. If two non-insulating materials with different work functions are placed in the vicinity of each other, opposite surface charges develop and a potential called contact potential difference (CPD) (Figure 5.8) equal to the difference of work functions $eV_{CPD} = e(\Phi_{KP} - \Phi_M)$. If the two are electrically contacted, a current flows from the lower work function material to the higher work function one. If a bias V_b is applied between the two in a way that $V_b = - V_{CPD}$, then the levels equilibrate, and no charge is accumulated on the surfaces and no current flows in the circuit.

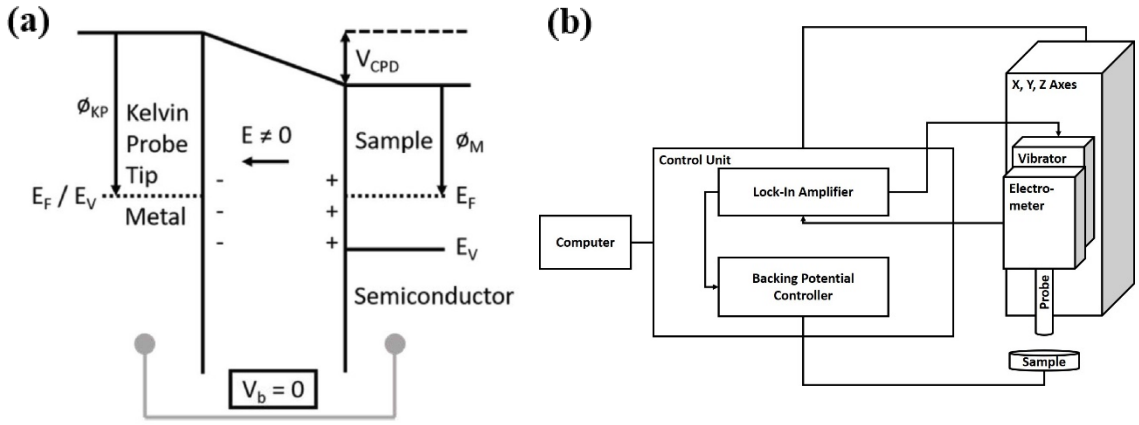

Figure 5.8 - (**a**) Energy band diagram of a metal and a semiconductor in electrical contact, a CPD forms charging negatively the higher Φ material's surface and positively the lower Φ conductor's surface. A backing bias V_b can be applied to equilibrate the level. (**b**) Schematics of the components of a modern scanning Kelvin probe, with a vibrating tip.

The modern Kelvin probe instruments use a conductive tip of calibrated work function (Φ_{KP}) vibrating orthogonally to the plane of the sample, in close proximity of it (0.2 - 2 mm). The vibrating tip induces an oscillating flow of current in the backing circuit, which is then modulated to a DC signal by a lock-in amplifier (Figure 5.8b). Then the CPD is measured either by nullifying the current applying the backing potential $V_b = - V_{CPD}$ or by sweeping the bias across the null current conditions, it turns out a way to measure the difference in work function for the first 2-3 atomic monolayers. The vibration of tip is

intended to avoid the contribution of buried charges accumulating in a fixed probe configuration. The modern setups comprise also a scanning stage to average over a certain area of the sample, this is because work functions are sensitive to crystal facets, roughness and adsorbates. For the same reason it is better to calibrate the tip work function every time that a sample must be measured, as the effects of ambient temperature and humidity can influence the values of work function substantially. In that case, the CPD of a reference material V_{CPD}^{ref} with known and reliable work function ϕ_{ref} (usually noble metals as Au or Pt) is measured. The Fermi level of a semiconductive sample in these conditions is estimated through the eq. 5.2.

$$E_F = \phi_{KP} + V_{CPD}^{Sample} = (\phi_{ref} - V_{CPD}^{ref}) + V_{CPD}^{Sample} \qquad \text{Eq. 5.2}$$

An example of point measurement for a nanostructured CuO sample on Silicon is shown in figure 5.9. A value of the CPD in the bare Silicon substrate is also checked, to measure an effective variation of the CPD in the area of the sample. The resulting Fermi level is also indicated as 4.90 ± 0.02 eV, following the calibration of the tip work function against a sputtered Au-on-Si reference sample.

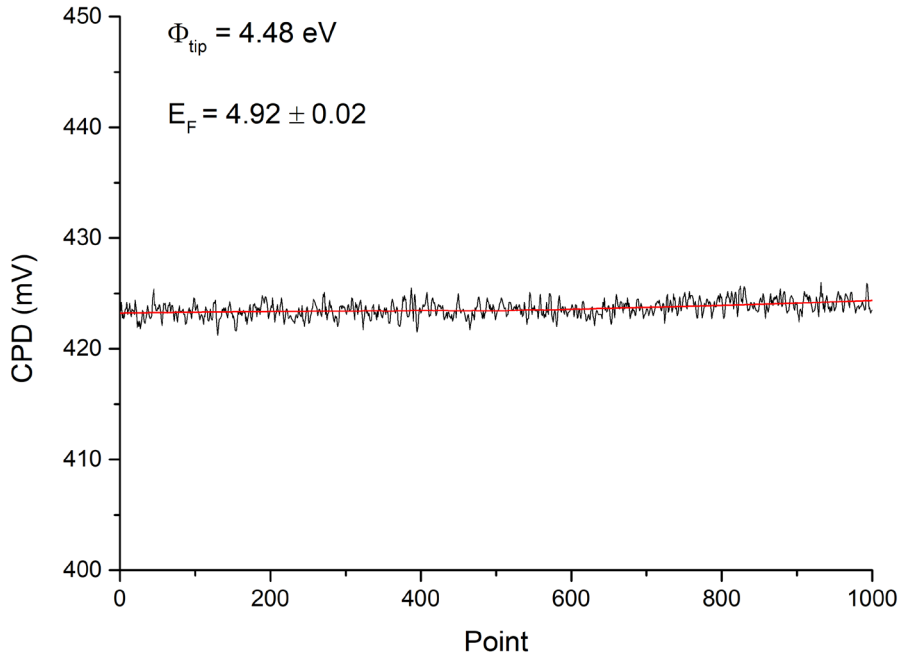

Figure 5.9 - Example of point measurements of the CPD for a nanostructured CuO sample. Point in the x axis refers to consecutive measurements from the KP system. Indicated the calibration values for the tip work function, obtained by measuring an Au- coated Si substrate, and the estimated Fermi level for the sample.

However, the KP has some intrinsic limitations for the estimation of Fermi levels from work functions of materials. As already mentioned, the work function of material can vary with crystal orientation and the presence of surface states. The macroscopic Kelvin Probe has a 2-mm large tip, hence any feature smaller than this size will be smoothed by neighboring contributions. In addition, care must be taken for samples that absorb the ambient light, as an induced photovoltage may affect the values from measurements. Moreover, the values of work functions are referenced to a "vacuum" level in atmosphere, which may change even of 1 eV with different atmospheric conditions.

The surface photovoltage spectroscopy (SPS) technique can also be used in a Kelvin Probe setup to have a qualitative assessment of the energy bandgap. SPS measurements are based on monitoring the illumination-induced changes in the surface potential, as a function of incident photon energy. The ability to build charge on the surface depends both on the light-induced bending of energy levels, that results either in charge accumulation or depletion, and charge carriers mobilities.[11,12] For semiconductor nanoparticles the mechanism is described as the trapping of photo-induced charges at surface defects, modifying the surface potential (hence the band bending, see figure 5.10).[13] A significant rise in the SPV signal is expected at photon energies exceeding the semiconductor band gap. Therefore, an estimation of the bandgap is obtained by detecting the onset of significant SPV signal varying the wavelength of exciting illumination.

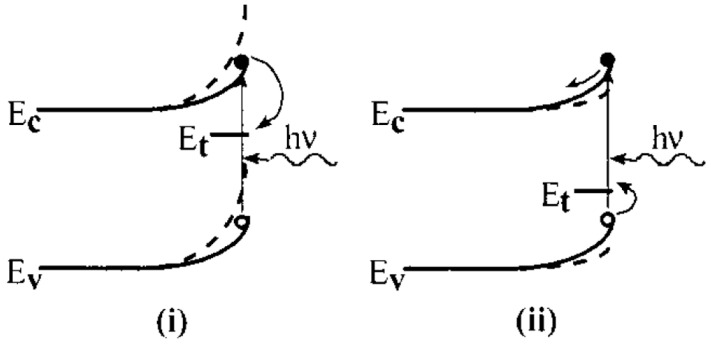

Figure 5.10 - Energy band diagram in proximity of a semiconductors surface, where bands are bent due to surface states. The photoexcitation process further bends the bands at the surface and provokes the migration of (i) electrons and (ii) holes to mid-gap trap states with energy E_t. The accumulation of these charges determines the arousal of a SPV. [13]

The experimental setup used for SPS measurements is the same as a Kelvin probe with the addition of a halogen lamp, and a diffraction grating to select the exciting light

wavelength. The experimental procedure is based on measuring the initial CPD without illumination, and then measuring the CPD under illumination the difference is the SPV (Figure 5.11a). The SPS spectra are then obtained by measuring the CPD in function of the excitation wavelength (resolution $\Delta\lambda\sim1$ nm) (Figure 5.11a). The dependence of the SPV on the photon energy and bandgap mimics that of the absorption spectrum when SPV signal is due to interband transitions, thus it follows a power law $\propto (h\nu - E_g)^n$ whose coefficient n changes with the kind of transition involve (n=1/2 for direct transitions, n=2 for indirect transitions, see section 5.3.5 for further details). By plotting $(SPV)^{1/n}$ against photon energy, the bandgap is evaluated through a linear fit, in analogy to Tauc plots. An example of bandgap extraction for a nanostructured Si film is shown in (Figure 5.11b)

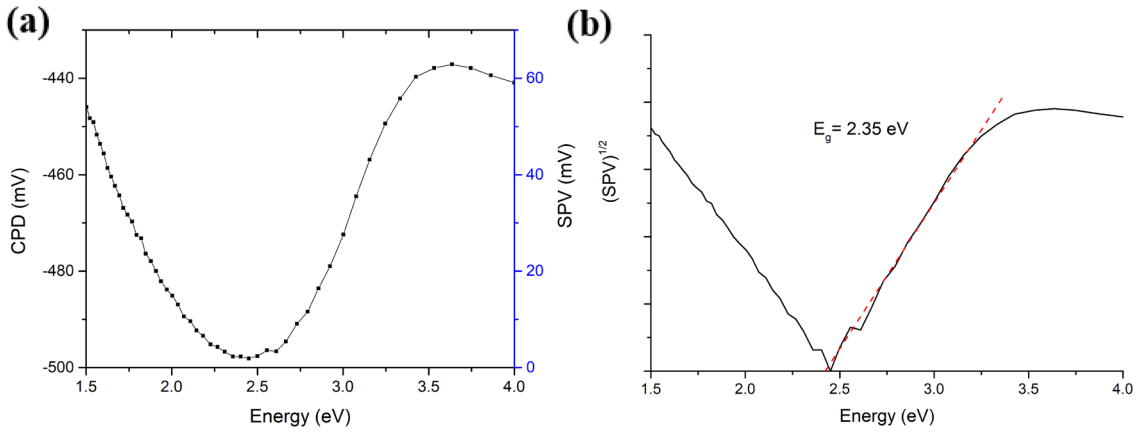

Figure 5.11 - Example of SPS measurement and analysis for a nanostructured Si sample. (**a**) CPD measurements (left scale) in function of light wavelength and evaluation of SPV (right scale) taking the difference with the CPD value in the dark (-500 mV). (**b**) Estimation of the bandgap by assuming an indirect transition, the onset was confirmed to be due to interband transitions by cross-checking with optical absorption data.

SPS has the advantage of not depending on scattering/reflection contributions as optical methods and only senses light that is absorbed, without requirements on the thickness of the sample, nor the use of reflectance standards.[13] However, there are mechanisms which can give rise to an SPV from sub-bandgap illumination, the most common ones involving the direct modification of the surface charge by excitation of trapped carriers, and the formation of electron hole pairs via photo-assisted tunneling. Thus, the interpretation of SPV spectra in terms of transitions is not always straightforward.

Another technique which has been used in this work to evaluate the position of Valence Band edge (semiconductors) or work function (metals) is air photoemission spectroscopy (APS). This method uses a system attached to the Kelvin probe equipment and is a form of UPS in atmospheric conditions. The setup (Figure 5.12a) uses a deep UV photon source (DUV) to stimulate the photoemission of electrons and a positively biased Kelvin probe's tip as a collector.[14,15] The source is a deuterium lamp which supplies photons with energy between 3 eV and 7 eV, a smaller range when compared to that available through UPS. However, the work function and valence band maximum of most of the metals and semiconductors lie in this range, and the lower energy source is better to avoid surface charging effects [15]. The working mechanism was proposed by *Baikie et al* [15] and is schematically shown in figure 5.12b. The photoemitted electrons are subject to an image force upon exiting the surface, after which they suffer scattering with environmental molecules as O_2 and N_2. Eventually they can attach to them and the negative ions drift to the tip in proximity if a positive bias is applied. Electrons in APS have a larger escape depth compared to UPS (>10 nm vs. 2-3 nm) but the information about their kinetic energy is lost as they are subject to the image force. The technique is measuring the ion currents as a function of photon energy and gives information about the local density of states (LDOS) at 1-3 eV near the Fermi Level [15].

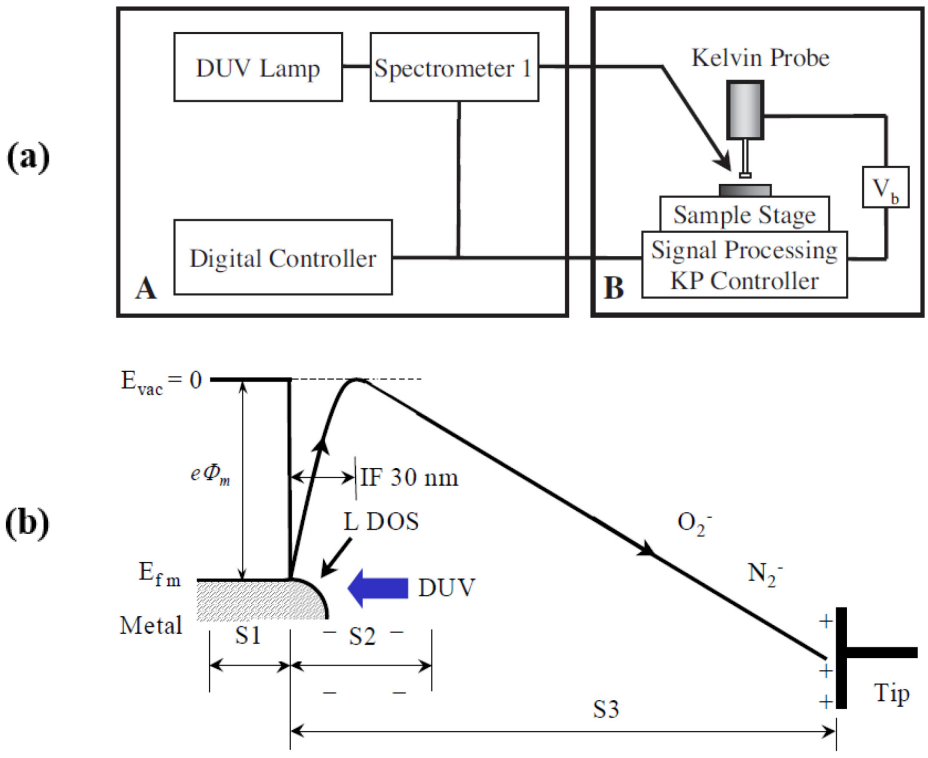

Figure 5.12 - (**a**) Diagram showing the experimental setup for APS measurement in a Kelvin Probe. (**b**) Energy diagram showing the process of UV-induced photoemission in air.[14]

The resulting photocurrent per absorbed photon is related to the square of the work function for metals and the cube power of ionization energy for semiconductors, following Fowler's theory.[16] This method has been successful for the estimation of work functions of various metals and valence band edge if different semiconductors by comparing with known values.[14,17] An example of measured APS spectrum for a nanostructured CuO film and relative analysis is shown in Figure 5.13. Data are subtracted by a baseline, defined by the low energy part of the spectrum where flat signal is present (continuous red line). Then the cube root of the PE signal is calculated (blue squares) and a linear fit is performed in the first significant slope of the signal. The value of VBM is then extrapolated from the intersection between the best fit line with the energy axis.

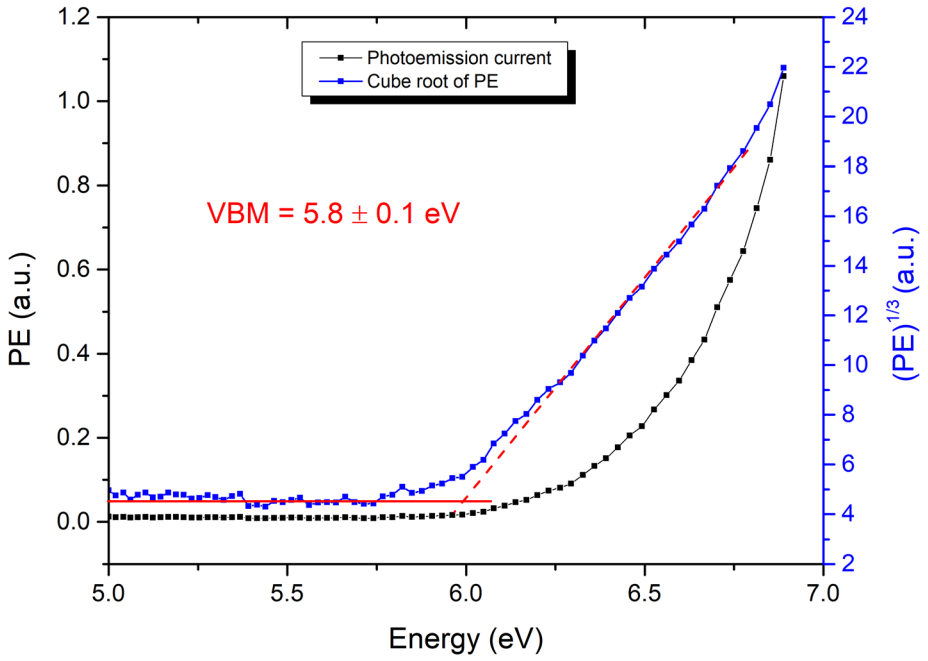

Figure 5.13 - Example of analysis of a measured APS spectrum (black squares, photoemission current) for a film composed of CuO nanoparticles. The VBM is obtained by first subtracting a constant baseline in the flat low energy part of the spectrum (red continuous line), then by extrapolation of the intersection to the energy axis with the linear fit (red dashed line) of the cube root of the PE spectrum (blue squares).

This technique suffers most of the limitation that the Kelvin Probe has. In fact, KP and associated APS are operated in atmosphere and subject to surface dipoles and surface chemistry induced by environmental adsorbates which can easily shift the values up to few eV raising or lowering the barriers felt by electrons escaping the material or even

induce completely new energy levels, especially in the valence band states. These may be considered as systematic errors in the values, which cannot be accounted for if there is not a rigorous knowledge of the surface chemistry. Nevertheless, these techniques are mostly useful for characterizing surfaces which will be exposed to atmosphere (e.g. for corrosion studies) and they also have advantages of being cheap, easy and fast techniques.

5.3.4 Optical methods

The most common way to measure the optical bandgap is by measuring the light absorption and photoluminescence properties of a material. There are different mechanisms by which solids can absorb (and emit) light. To mention few in order of photon energy needed: phonons and free carriers (intraband) absorb infrared light, interband transitions are stimulated by visible and UV light, then electron plasma and inner interband transitions by higher energy UV photons.[5] By measuring the wavelength-dependent absorption (or emission) in the UV and visible range, it is possible to estimate the bandgap of a semiconductor. Two examples of interband transitions are shown in figure 5.14 in a simplified band structure for direct (panel **a**) and indirect semiconductors (panel **b**).

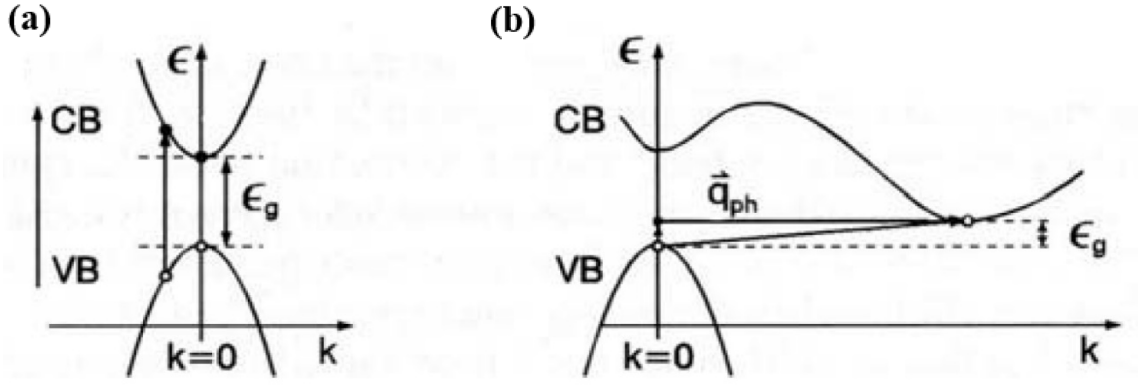

Figure 5.14 - Optical interband transitions in relation to the band structure of different kinds of semiconductors. The vertical single headed arrow represents a photon with energy hν bigger than the bandgap εg, promoting an electron (full circle) in the conduction band (CB) and leaving an electron-hole (empty circle) in the valence band (VB). In direct semiconductor (a) the transition is vertical ($\Delta\vec{k} = 0$), resulting in efficient absorption (b) in indirect semiconductors in order to absorb light the transition must involve the emission or absorption of a phonon with enough momentum to supply the change in crystal momentum needed ($\vec{q}_{ph} = \Delta\vec{k}$), this three-body process makes light absorption less efficient. The emission of light (for example with photoluminescence) is a process specular to absorption.5

The absorption of light from a material in a semiconductor is permitted if the light has an energy ($h\nu$) larger than the bandgap (E_g) and, at the same time, there are occupied electron states which can absorb the photons and available final states to populate. The eq. 5.3 describes in general the dependency of absorption of a material in function of incident photon energy ($h\nu$), bandgap (E_g) and the *optical joint density of states* $\rho(h\nu - E_g)$, which counts the number of combined states in the valence and conduction bands available for transitions.[18]:

$$\alpha(h\nu) \propto A \cdot \rho(E - E_g) \rightarrow A \cdot (h\nu - E_g)^n \qquad \text{Eq. 5.3}$$

where $\alpha(h\nu)$ is the absorption coefficient in function of photon energy, A is a factor that accounts for the probability of dipolar transition between states and the coefficient *n* depends on the type of transition involved. It changes in value whether the transition is direct allowed (*n*=1/2) or forbidden (*n*=3/2), indirect allowed (*n*=2) or forbidden (*n*=3).[19,20]

The experimental equipment to estimate the bandgap from absorption measurements is an ultraviolet-visible (UV-Vis) spectrophotometer. It is an instrument equipped with broadband lamps which emit light in the UV and visible range, collimates it to obtain a parallel beam and monochromators to select wavelengths. The monochromatic light is shone onto the sample, which has to be mostly transparent. A detector measures than the intensity of light which has passed through the sample in function of wavelength (*Transmittance*) (Figure 5.15a). If an integrating sphere is attached to the beam line, it is possible also to estimate the integrated reflection and scattering contribution, by for example placing the transparent sample in the center of the sphere (see Figure 5.15b), in

this case the measured value is a combination of the transmitted light and the scattered one (T+S).

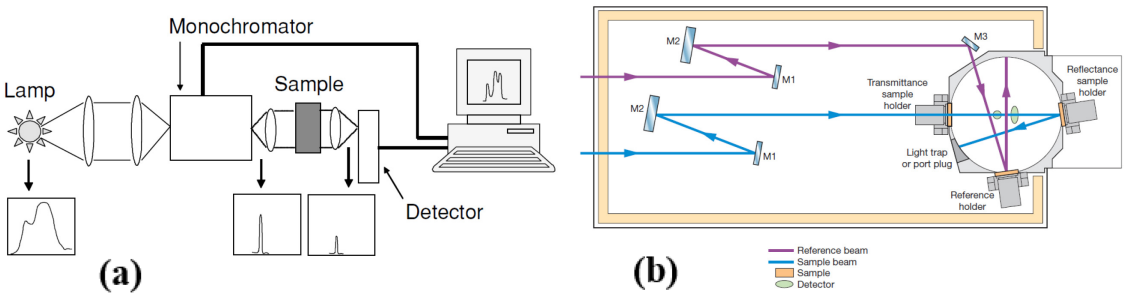

Figure 5.15 - (**a**) Schematic diagram of the spectrophotometer equipment. The light from a broadband lamp is shaped into a parallel beam by the optics, then wavelength selected by a monochromator. The monochromatic light is then passed through the transparent sample, and the transmitted light is collected by a detector. (**b**) Detail of the sample compartment and measuring ports for a spectrophotometer equipped with an integrating sphere. The sphere's inner walls are coated with a reflective white coating. All the light which is reflected and scattered from the sample in all other directions (in respect to the direction of the incident beam) is collected by the detector after being reflected on the sphere's walls. The measurements in all cases are normalized to a reference sample with the substrate only.

In general, when light is shone on a solid material it can be either absorbed, reflected, scattered or transmitted through. The intensity *I(x+dx)* passing through a thickness *dx* of the material will be attenuated of a quantity proportional to the incident light intensity *I(x)* as in eq. 5.4:

$$I(x) - I(x + dx) = -I(x)\mu dx \qquad \text{Eq. 5.4}$$

The proportionality constant μ is called the *extinction coefficient*. By integrating the contribution of a layer of thickness *L*, the result is the *Beer-Lambert Law* (Eq. 5.5):

$$I(L) = I_0 e^{-\mu L} \qquad \text{Eq. 5.5}$$

Where I_0 is the light beam intensity incident on the sample. When the samples do not reflect or scatter light appreciably and are mostly transparent, the detection of light transmitted through the sample (*transmittance* $T = I/I_0$) in function of light wavelength is sufficient to estimate the absorption properties of the material, as the extinction coefficient can be directly interpreted as the absorption coefficient (α) of the material:[5]

$$\alpha = -\frac{1}{L}\ln\left(\frac{I}{I_0}\right) = -\frac{1}{L}\ln(T) \qquad \text{Eq. 5.6}$$

When it is not possible or not obvious if the scattering and reflection contributions are negligible and the instrument can give access to an angle-integrated measurement of these (e.g.: with an integrating sphere) it is still possible to estimate the absorption coefficient. If a negligible contribution from system losses and specular reflection is assumed (purely diffuse reflecting surface) then an equation similar to the Beer-Lambert law can be obtained to estimate the value of the absorption coefficient. The portion of absorbed light can be expressed as in Eq. 5.4, but with the proportionality constant equal to the absorption coefficient. Integrating on a path length L, using eq. 5.5 for an arbitrary L=x and integrating one obtains eq. 5.7:

$$I_A(L) = \int_0^L I(x)\alpha dx = \alpha I(0)\frac{(1-e^{-\mu L})}{\mu} \qquad \text{Eq. 5.7}$$

Considering the absorbance as the ratio of light absorbed at a particular wavelength in respect to the incident intensity as $A = I_A(L)/I_0$, and that for each wavelength the energy conservation implies that A+T+S=1 (same integrated light intensity in and out of the sample), then the chain of relations in eq. 5.8 follows:

$$A = \frac{I_A(L)}{I(0)} = \alpha\frac{(1-e^{-\mu L})}{\mu} = 1-(T+S) \qquad \text{Eq. 5.8}$$

By inserting the value of μ obtained inverting eq. 5.5 and rearranging the last equation in eq. 5.8 to express it in function of the measured quantities (T and T+S), an expression for α is found (eq. 5.9):

$$\alpha = -\frac{1}{z}\ln(\mathrm{T})\left[\frac{1-(T+S)}{1-T}\right] \qquad \text{Eq. 5.9}$$

In Figure 5.16 an example of the measurement (panel **a**) and calculated absorption coefficient (panel **b**) is shown for a nanostructured ZnO film on a quartz substrate. The increase in value of absorption is associate with the onset of interband transitions through the ZnO bandgap.

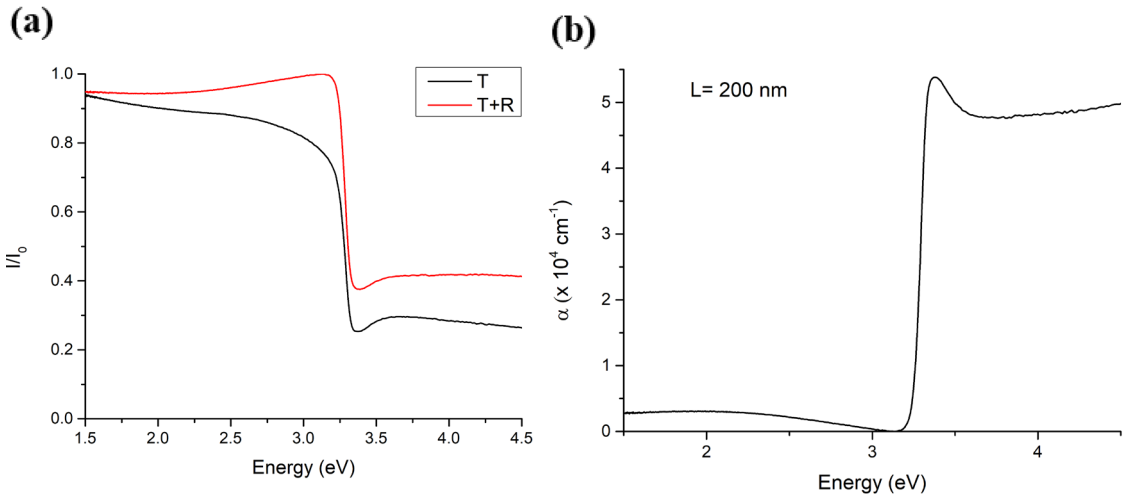

Figure 5.16 - (**a**) Measured T and T+R for a nanostructured ZnO sample on quartz substrate, each measurement has been normalized to a black quartz substrate measured in the respective configuration (I_0). (**b**) absorption coefficient calculated from equation 4.9, with indication on the film thickness.

To extract the value of bandgap, it is possible use eq. 5.3 by assuming a certain value of the coefficient n. With the Tauc plot method, the energy bandgap is estimated by using Eq. 5.3. In particular plotting $(\alpha h\nu)^{1/n}$ with the chosen value of n against the photon energy $h\nu$, one can fit a line in the higher energy part of the absorption edge and the extrapolated intersection with the energy axis is then an estimation of the bandgap.[20] The figure 5.17 shows a Tauc plot for the ZnO samples, by assuming a direct allowed interband transition (n=1/2).

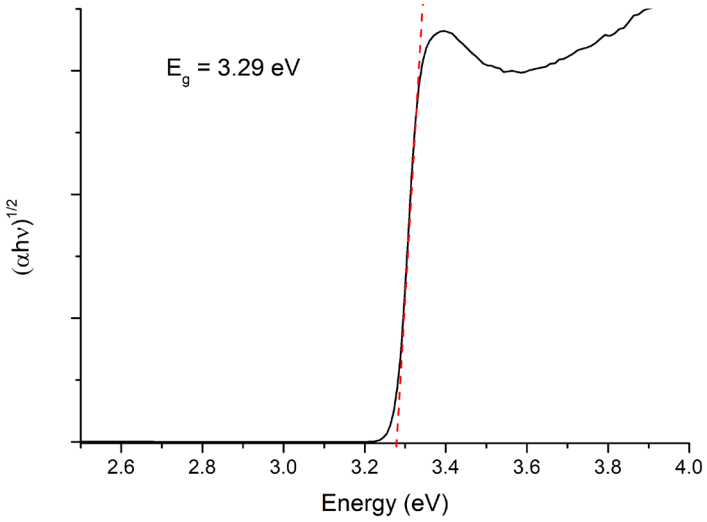

Figure 5.17 - Tauc plot, fitting of the absorption edge and estimated bandgap for the ZnO nanostructured sample, assuming a direct allowed transition.

Alternatively, if in eq. 5.3 the logarithm ln(α) is taken, it becomes:

$$\ln(\alpha) = \ln(A) + n\ln(h\nu - E_g) \qquad \text{Eq. 5.10}$$

then taking the first derivative as a function of photon energy it is found that the resulting function has a discontinuity at the value of the bandgap:

$$\frac{d\ln(\alpha)}{d(h\nu)} = \frac{n}{h\nu - E_g} \xrightarrow{h\nu = E_g} +\infty \qquad \text{Eq. 5.11}$$

In addition, the slope of the linear part of ln(α) as a function of ln($h\nu$ - E_g) in eq. 5.10 permits to evaluate the coefficient *n*. It follows that the two equations eq. 5.10 and eq 5.11 can be used to estimate the bandgap and the type of transition involved without any prior assumption on the kind of transition involved.

Alternatively, the optical bandgap, under given assumptions, can be measured with photoluminescence measurements, the inverse process of absorption. In this physical phenomenon, light with energy higher than the bandgap (usually in the UV) creates electron-hole pairs and these can recombine via the emission of light. The emission of light is generally at lower energies than the bandgap estimated using absorption measurements, the difference (*Stokes shift*) being due to non-radiative de-excitation channels.[21] As an inverse process to absorption, it is more efficient for direct bandgap materials, however these kind of measurements can be problematic with nanoparticulate samples, as surface states and impurity states in the middle of the gap are usually good

recombination centers for electrons and holes. Hence, it is not always straightforward to associate the emission of light to an interband transition.[22]

5.3.5 Comparison of different techniques for the same parameter

It was shown that various techniques can be used for the determination of VBM and Fermi level and bandgap. However, care should be taken when combining the results from different techniques in building the full EBD. Two matters are particularly important:

1. Region probed by the technique: each technique has a certain dependency of the depth from which the information arrives, for XPS near 10 nm, for UPS 2-3 nm, Kelvin Probe from 2-3 monolayers, UV-Vis absorption and APS depend strongly on the absorption coefficient, but they commonly probe a much deeper region than the other techniques (100-1000 nm). Hence, if the samples are not homogeneous in this region or not thick enough, then an EBD built combining different techniques may not be realistic.

2. The reference level chosen for the determination of EBD parameters: differences above 0.1 eV can be critical for the correct alignment of energy levels between different material. It has been shown in the previous sections that the experimental accessible quantities are work function and ionization energy and the definition of Fermi level and VBM (which relate to the electrons potential energy within the material) depend on the reference ("vacuum") level; UPS and XPS *relate to a potential energy of the ultra-high vacuum* in the XPS chamber and represent more realistically the intrinsic properties of the materials if the samples are well grounded, not charging under the radiation and the spectrometer is correctly maintained. The APS and KP values instead *relate to the electrostatic potential at the particular atmospheric conditions at the time of the experiment* [3], which depends on the atmospheric condition and have deviations on the order of 1 eV. However, this might not be a problem if the sample materials are to be exposed to atmosphere without further treatment to their surfaces or if the interactions with the atmosphere must be studied.

The presented arguments imply that accurate EBDs should be built from values measured in the same experimental setup, whenever possible, and try to understand the analyze critically the combinability of the parameters measured with different methods.

5.4 Full EBD of case studies

5.4.1 Case studies

In this section two cases studies will be presented to exemplify the measurements benefits and challenges, which are part of the experimental work for the determination of EBDs. The majority of these works (published) were done by collaborators and the contribution of the present author was to estimate the EBD of the samples they produced. A brief description of the works follows:

1. Gasparotto, A. et al. - Surface Functionalization of Grown-on-Tip ZnO Nanopyramids: From Fabrication to Light-Triggered Applications. - ACS Appl. Mater. Interfaces **11**, 15881–15890 (2019)

   Influence of Ti-related species on the surface of ITO-supported ZnO nanopyramids on the photochemical properties: UV-induced hydrophobicity and catalysis of degradation of organic molecules. Performance is compared between an untreated sample and two samples produced with different Ti sputtering times (2 and 4 hours).

2. Barreca, D. *et al.* Multi-functional MnO2 nanomaterials for photo-activated applications by a plasma-assisted fabrication route. *Nanoscale* **11**, 98–108 (2019):

   Influence of substrate temperatures (100, 200, 300 and 400 °C) of a plasma enhanced chemical vapor deposition (PE-CVD) growth process on the morphology, composition and photochemical performance of MnO_2 nanomaterials on FTO.

Each subsection will be organized in the following way; I) a brief introduction on the work of collaborators in terms of material characterization and other results; II) a description of the experimental routines for estimating each parameter of the EBD and the presentation of the relative results; III) a short discussion on the significance of the

estimated EBDs in terms of electron states and their variation with the experimental parameters and their role within the interpretation of collaborators results.

5.4.2 Ti - functionalized ZnO nanopyramids

ZnO is a n-type semiconductor which has appealing optoelectronic and structural properties for light-triggered applications like photocatalysis, dye-sensitized solar-cells or self-cleaning surfaces. Ti-doped ZnO and ZnO-TiO_2 composites are of interest to the mentioned application fields, because they combine the exceptional reactivity and anti-corrosion properties of TiO_2 and the high electron mobility of ZnO. A combined chemical vapor deposition (CVD) and Radio Frequency (RF) sputtering system was used to produce surface-modified ZnO nanopyramids introducing a small amount of dispersed Ti-containing species.[23]

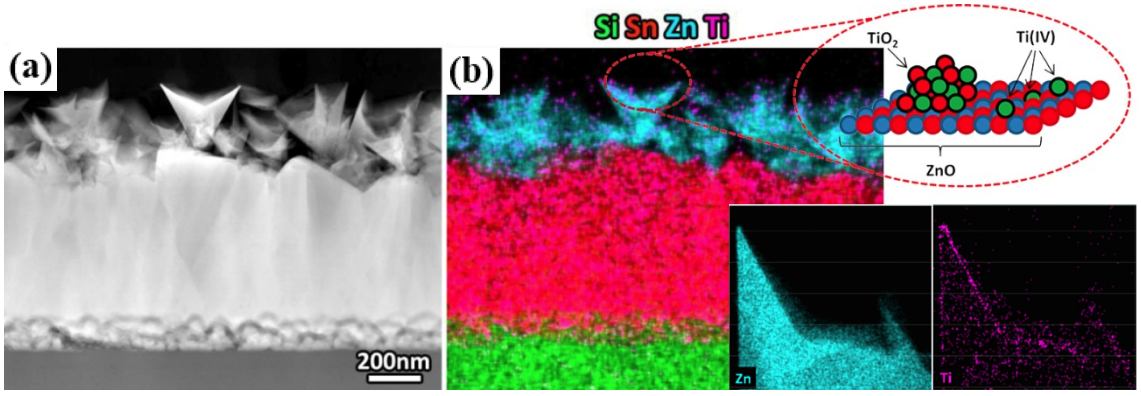

Figure 5.18 - (**a**) FE-SEM cross-view image showing the morphology of the deposited sample. (**b**) EDX mapping in the same area showing a feeble signal from Ti atoms coming from the surface of the nanopyraminds. The inset at the bottom is HAADF-STEM close-up showing that Ti atoms are effectively on the surface of the nanopyramids.

The ZnO nanopyramids grown on FTO substrates with a CVD process appear as arrays of pyramids with mean base size of 220 nm and with a downward pointing tip (Figure 5.18a). An RF sputtering method has been applied to functionalize their surface with Ti, for two different process duration (2 h or 4 h) in order to tailor the total content of Ti-containing species. X-ray diffraction (XRD), Field emission scanning electron microscopy (FE-SEM) and atomic force microscopy (AFM) studies observed no difference in the morphology and structure after the deposition of Ti. Secondary ion mass spectroscopy (SIMS) profiling, energy dispersive x-ray (EDX) mapping and high angle

annular dark field in a scanning transmission electron microscope (HAADF-STEM) (Figure 5.18b) showed Ti-containing species dispersed on the pyramids surface. Both HAADF-STEM and XPS where used to characterize the deposits as crystalline and amorphous TiO_2 and isolated Ti(IV) species on the surface, with the 4h-sputtered sample showing a higher proportion of TiO_2 species. Water contact angle (WCA) measurements and the photoinduced degradation of an organic dye of the produced samples indicate that the 2h-sputtered Ti:ZnO nanopyramids have superior properties as faster hydrophobic-to-hydrophilic conversion upon UV irradiation, self-cleaning properties, and photocatalytic performance in respect to bare ZnO nanopyramid samples or reference TiO_2 films. Interestingly, the 2h-sputtered overperformed the 4h-sputtered samples, which suggested the existence of an ideal Zn/Ti ratio driving a better performance for these applications. Their analysis found that the first stages of deposition involve the functionalization of ZnO nanopyramids with dispersed Ti(IV) ions which act as surface dopants. Longer deposition promotes the nucleation and growth of TiO_2 particles by plasma activated surface diffusion. The photoinduced hydrophilic properties, self-cleaning ability and photocatalytic performance were then be ascribed to the combined effect of dispersed Ti(IV) centers and TiO_2 agglomerates on the oxidative power of photogenerated carries in an optimal ratio. Above this optimal value an excessive coverage of surface sites by TiO_2 decreases the performance as in the 4h-sputtered sample.

The valence band edges of the samples were estimated for XPS experiments in the valence band region. Spectra were recorded with a Kratos Axis Ultra DLD spectrometer equipped with an Al Kα X-ray source (1486.6 eV), using an analyzer pass energy of 20 eV. For each sample, three measurement spots were taken (spot size = 400 μm^2). In figure 5.19a, the XPS valence band spectra of the samples are shown, along with the best fit lines of the valence band edge. A shift of the photoemission edge to higher binding energies (+0.4 eV) is observed for the samples containing Ti, likely the result of the surface modification of valence band states. The calculated values of E_F-VBM obtained from extrapolation of the intersection between energy axis and fit lines are shown in Figure 5.19b. Along with it, the valence band spectra have been divided in regions pertaining to different bands, O2p, Zn3d and hybridized Zn-O bonds.[24] It is possible to observe that the structure of peaks changes slightly in the case of the 2h-sputtered sample, a difference which is better appreciated by normalizing the spectra to the Zn3d peak (inset

in figure 5.19a). In conjunction with the XPS core level spectra analysis, this difference has been associated to the possible presence of Ti(IV) species on the surface.

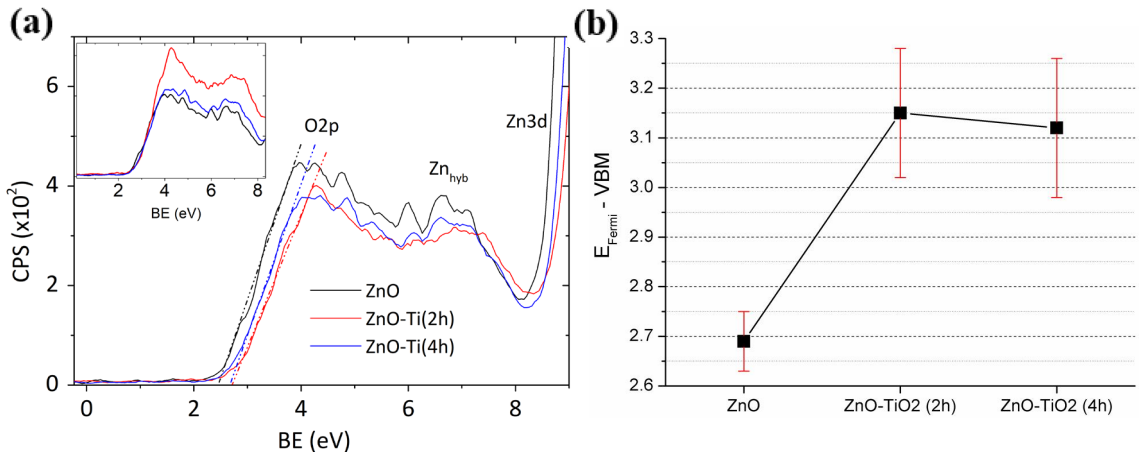

Figure 5.19 - (**a**) XPS spectra in the valence region for the functionalized ZnO nanopyramids, including the linear fitting to evaluate the valence band maximum. Also, the regions pertaining to Zn and O bonding in ZnO are indicated. (**b**) Results of the fitting of valence XPS spectra for multifunctional MnO_2 nanomaterials. The inset shows an example of spectrum used for fitting.

The absolute Fermi energy was evaluated by Kelvin probe (KP) measurements in air (KP Technologies APS04) with a 2 mm gold plated tip. A sputtered Au-on-Si reference was adopted to calibrate the tip work function ($\Phi_{tip} = 4.48\ eV$). The estimated uncertainties on the CPD measurements is 20 meV. The samples showed a variation of CPD of about 250-300 meV when exposed to ambient light in respect to the values measured at dark, with recovery times longer than 10 hours. Hence, measurements were protracted for 20

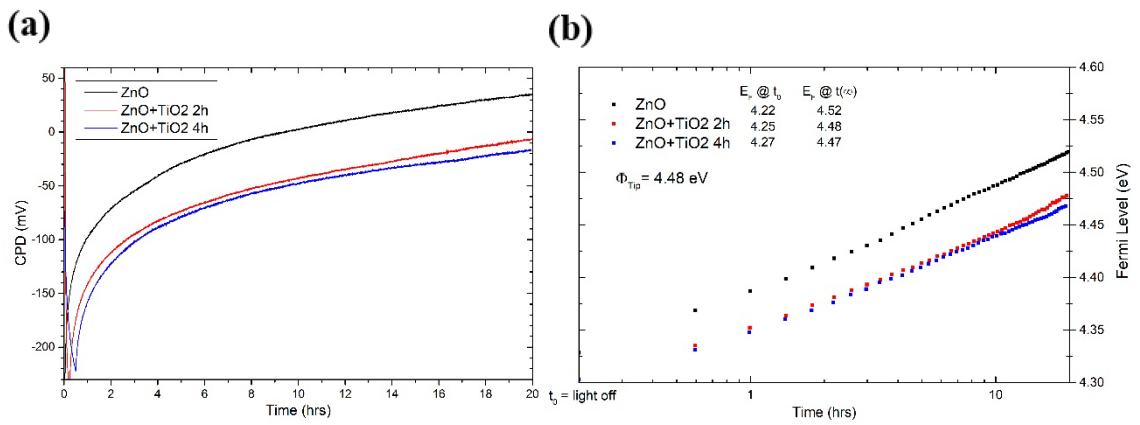

Figure 5.20 - (**a**) CPD measurements over 20 hours of measurement in dark and (**b**) semilogarithmic plot of calculated Fermi levels for the three ZnO nanopyramids samples. At t_0 the KP enclosure is shut, and the measurement starts in the dark. After 18-20 hours (t(∞)) the measurements converge to fixed values which are taken as the equilibrium ones, thus considered for the EBDs.

hours inside the dark box enclosing the kelvin probe until the data points showed and accumulation point (Figure 5.20a). The Fermi levels (Figure 5.20b) for Ti-containing samples are slightly lower than the bare ZnO nanopyramids, however the difference is comparable to uncertainty in the measurement, so it is concluded that the presence of Ti and different sputtering times have little or no effect on the Fermi level position.

UV−vis absorption spectra (resolution = 1 nm) were used to estimate the absorption coefficient and the energy bandgap of samples. The instrument is a PerkinElmer Lambda 650S spectrophotometer equipped with a halogen lamp and a 150 mm integrating sphere. The measurements recorded are: (i) combined transmittance and reflectance by placing the sample at the center of the integrating sphere (T+S in section 5.3.4) and (ii) transmittance only by placing the sample at the entrance of the sphere (T in section 5.3.4); a quartz sample was used as reference. This allowed to determine the absorption coefficient taking into account any possible effect due to reflectance changes (L=200 nm film thickness from FE-SEM). The measured spectra are shown in Figure 5.21a and 5.21b, while the absorption coefficient calculated through eq. 5.9 is presented in Figure 5.21c. It is easily observed that spectra have similar features, a sharp drop in signal intensity at equal values of energy, a small valley and then a monotonic region of low intensity transmitted. The shape of the spectra near the absorption edge, demonstrates that the content of Zn and O vacancies is not varying among the samples, as for ZnO they usually introduce modifications of the absorption edge. Figure 5.17c, however, shows that Ti-containing samples have systematically higher absorption coefficient.

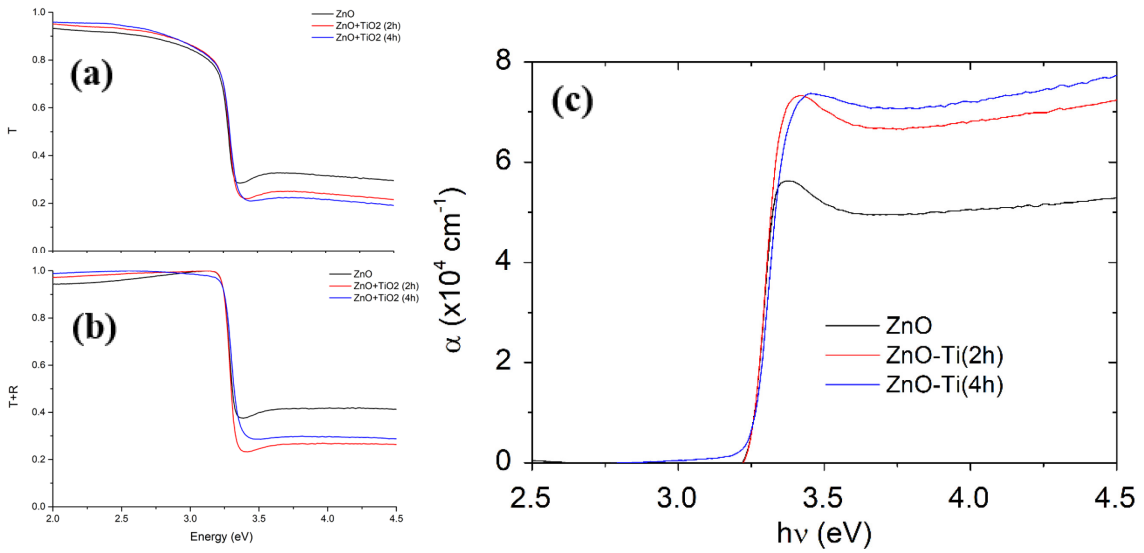

Figure 5.21 - (**a**) T and (**b**) T+S measurements for the three samples in the study, showing similar characteristics but lower intensity at the detector for Ti-containing species at higher energy. (**c**) Absorption coefficient calculated through eq. 4.9 and assuming an optical path length of 200 nm.

For estimating the bandgap, the second method described in section 5.3.4 was used, which does not rely on any assumption on the kind transitions involved in the optical absorption. Figures 5.22a, 5.22b and 5.22c show the result of the analysis. The main plots shown are the functions calculated with eq. 5.10, while each inset is a plot of the functions described in eq. 5.11. Peaks can be noticed, for which the value of the derivative function tend to diverge, the x values relative to the maximum of the peak are considered as estimations of the bandgaps. Then by inserting the E_g obtained in eq. 5.10 and fitting the linear part near the zero of the abscissae, a value for *n* is estimated. In all the three cases a value of *n* very near to 0.5 is found (0.42, 0.45, and 0.45 for the three samples), hence it is very likely that the optical transitions involved are of direct type. For comparison, in Figure 5.22d the Tauc plots are build, by assuming a direct type transition (*n*=1/2).

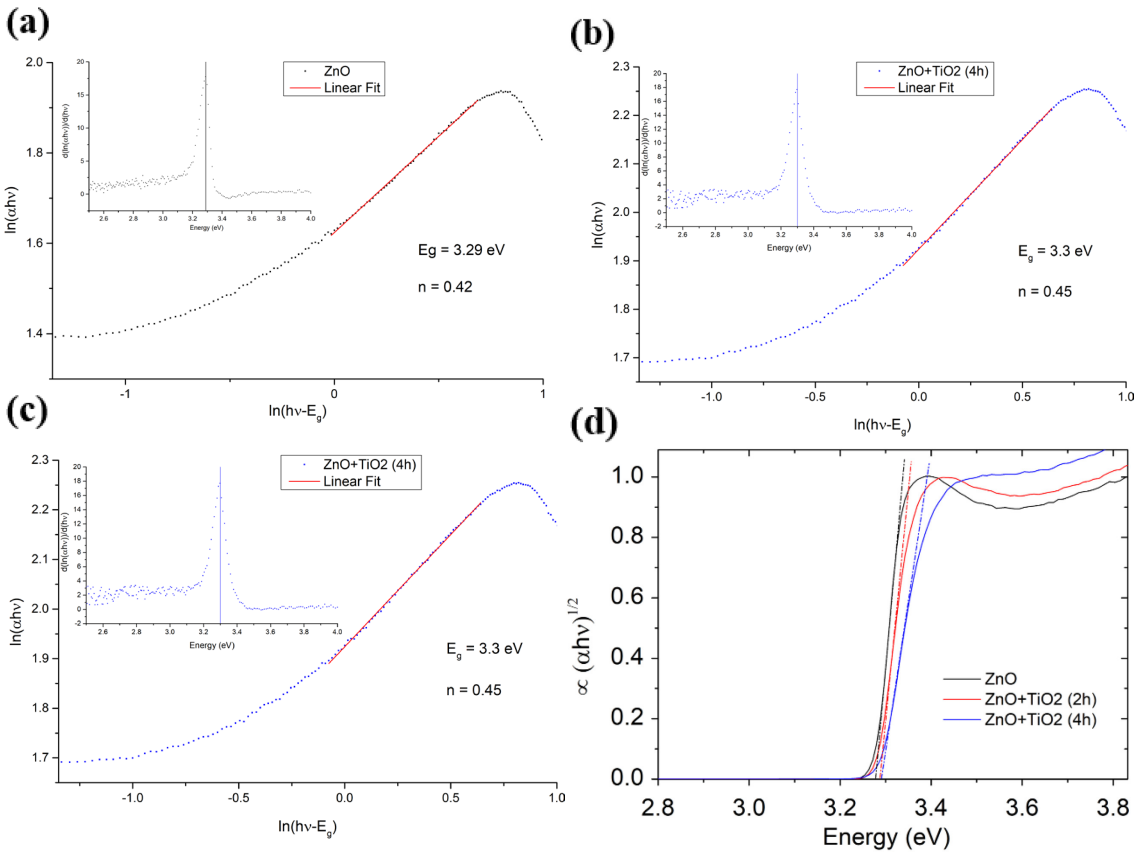

Figure 5.22 - Assessment of the bandgap of the three samples studied for surface functionalized ZnO nanopyramids (**a**) untreated ZnO pyramids (**b**) Ti (2h) and (**c**) Ti (4h). The main plots show the linear fitting of ln(α) in function of ln(hν-E_g) for extracting the value of n. The insets show a clear peak (divergence) of the first derivative of ln(α) in respect to the photon energy. (**d**) Tauc plots obtained by assuming direct transitions, showing a very good correlation between the two methods.

The coincidence of the results further confirms the previous statements. For all the three samples similar values of bandgap of 3.3 eV are found. Moreover, the samples had the

same sample thickness, hence lower transmittance at higher energies ($E > E_g$) is indicative of a higher light absorption efficiency for samples containing Ti. The fact that the bandgap does not change with the content of Ti implies that bulk doping of Ti is not happening.

These measurements than permitted to build a partial EBD the samples. In fact, it has been decided to not include bandgap values in the EBD. The underlying reason is that the XPS and Kelvin Probe values are probing the topmost surface of the samples, hence where the sputtered deposit of Ti species is found, while the UV-Vis probes a much deeper region. This means that EBDs build using the values of E_g obtained from UV-Vis spectroscopy would not represent the electron states of the composite Ti-ZnO system. The partial EBDs are shown in figure 5.23.

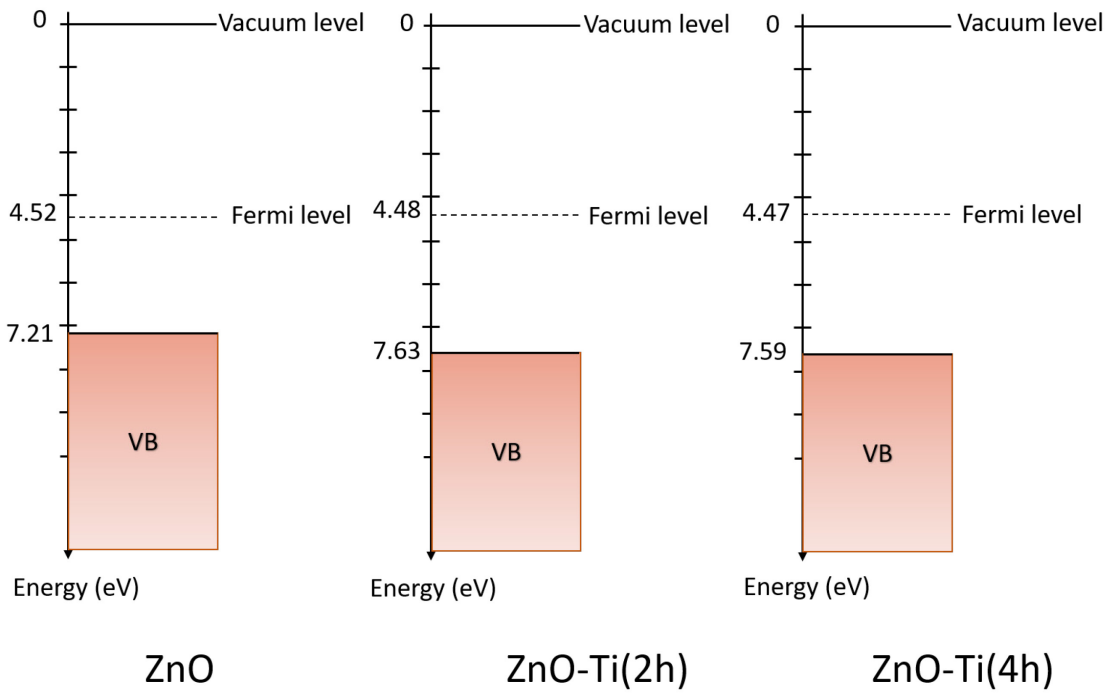

Figure 5.23 - EBDs of ZnO nanopyramid samples built by combining XPS (VBM), UV-vis absorption (Bandgap) and Kelvin Probe data (E_F). While maintaining a similar bandgap and absolute position of the Fermi level, the valence band maxima shift towards more negative values for Ti-containing species, hence stressing the n-type behavior.

The EBDs in Figure 5.23 were built using the (E_F-VBM) values from the XPS measurements in the valence region and the absolute E_F measured with the Kelvin Probe. Even though it may appear contradictory in light of the discussions in section 5.3.5, it is not expected for ZnO to have strong contribution to the surface potential due to surface dipoles, as it is a wide-bandgap semiconductor with low conductivity. In any case, XPS

measurements are relative measurements of the separation of valence band edge and Fermi level, thus as long as no comparison is made in terms of absolute values of other materials, the EBDs estimated are a good representation of the internal changes to the electron states near the Fermi level due to the surface modifications introduced by Ti species. The results indicate that the valence band maxima shift to lower values relative to the Fermi levels (more positive potentials for holes in the valence band) for the samples modified by Ti-species, while the Fermi levels stay constant. This is an indication of the fact that Ti-related species modify the valence band states at the edge or the density of states at those energies. This can either happen by introducing dopant states near the valence band edge (shallow acceptors) depleting the electron states which are within 0.4 eV from the bare ZnO VBM edge, or by chemical bonding at the surface that would rearrange the electron levels in the valence band. As the XPS in the valence band region is reflecting the DOS at the VBM and states in the VBM of ZnO are assigned to O2p energy bands, considering that the formation of TiO_2 happens mostly in the 4h sputtered samples and no significant change is observed for VBM between the 2h and 4h-sputtered sample, it is more likely that Ti species are acting as dopant states to the effects of electron energies. If in addition a negligible effect of Ti species on the value of bandgap is assumed, then the n-type behavior of bare ZnO would be enhanced by the surface modification introduced by sputtered Ti. The above observations were in part used to understand the increased perfomance of Ti-containing species in the photochemical properties. By assuming the redox semipotentials being at fixed values within the bandgap of ZnO (that is what happens for wide-gap semiconductors of interest for photocatalysis) the oxidative power of photoexcited holes depends on the position of the valence band maximum in respect to the redox semipotentials. In this frame, a more positive valence band edge (from the point of view of carrier potential) implies that photogenerated holes would have a stronger oxidative power at the surface of ZnO nanopyramids.

5.4.3 Multifunctional MnO_2 nanomaterials

MnO_2 is a transition metal oxide possessing various crystalline polymorphs of interest to a big variety of application fields, such as Li-ion batteries, supercapacitors, gas sensors because of the variety of chemical and physical properties. In particular for photocatalysis, the bandgaps of these polymorphs lie in a range where solar radiation can

be used (1.5-2.7 eV) to activate the catalytic processes. The study presented involves the plasma-enhanced CVD growth of nanostructured β-MnO_2 on a FTO substrate in function of the substrate temperature in the furnace. It is found that varying the growth temperature from 100 °C to 400 °C the sample are always phase pure but show different morphologies and degrees of fluorine doping (Figure 5.24).[25] At low temperatures FE-SEM analysis show hierarchical dendritic structures at low temperatures (100 °C and 200 °C, Figure 5.24a and 5.24b) and thorns-like structures at higher temperatures (300 °C and 400 °C, Figure 5.24c and 5.24d). The dendritic structures at low temperature become bigger at 200 °C (mean size 200 vs 230 nm) and more compact as seen in the cross-sectional views, while at high temperatures the thorns tend to become thinner with increasing temperature (80 nm vs 50 nm) despite the same elongation (900 nm mean length). In addition, the surface RMS roughness increased with higher growth temperatures.

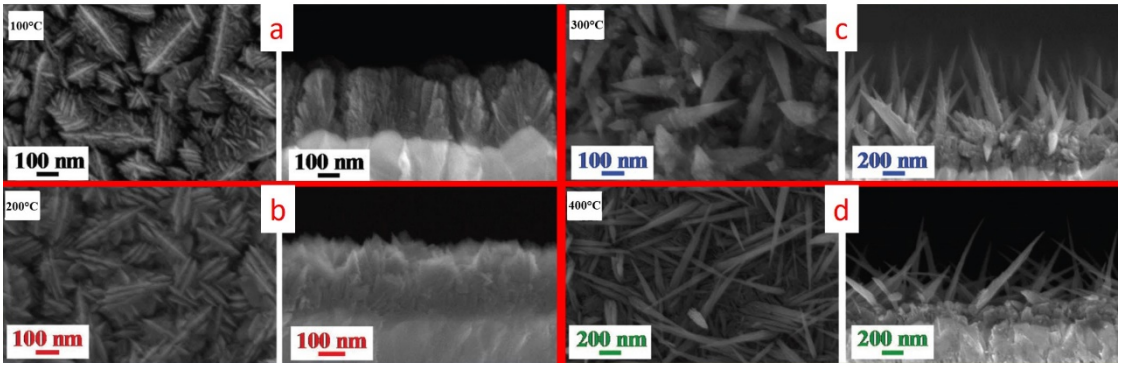

Figure 5.24 - FE-SEM micrographs in plain- and cross- view showing the different morphologies of nanostructured β-MnO_2 in function of growth temperature in the PE-CVD furnace. (**a**) 100 °C and (**b**) 200 °C present dendritic lamellar structures that increase in size and compactness with higher temperatures. (**c**) 300 °C and (**d**) 400 °C show thorns-like structures that become thinner at higher temperatures.

XRD of the samples determined that samples are in the β-MnO_2 phase with a co-presence of Mn_2O_3 at 400 °C. The XPS core spectra instead showed that the surface Mn/O ratio varies between 1.7 to 1.5 from 100 °C to 400 °C growth temperature which has been assigned to an oxygen-vacancy rich surface. Moreover, the incorporation of fluorine in the surface lattice was found with depth profiling, along with CF_x species. The amount of fluorine varied through the samples synthesized at different temperatures, from 7% to 2% upon increasing the growth temperature.

WCA measurements show a different initial degree of hydrophobicity of samples and upon illuminating the samples with UV lamps, the lower temperature samples (100 °C

and 200 °C) were able to change to a hydrophilic behavior considerably in respect to higher temperature samples (300 °C and 400 °C). The UV-induced self-cleaning properties were also estimated, through WCA measurements of samples with a film of methyl stearate on top, upon illumination the lower temperature samples were performing better changing to hydrophilic surfaces. The photocatalytic properties were tested by monitoring the degradation of an aqueous solution of a dye (Plasmocorinth B) in contact with the samples through UV-VIS absorption, in function of the exposure time to UV. The β-MnO_2 samples were able to visibly decompose the dye solution even under the illumination of visible light with comparable efficiency. The comparison of the kinetic rates of photodegradation show that samples grown with intermediate temperatures (200 °C and 300 °C) had the best performances. Reported higher photocatalytic performances for the samples grown at intermediate temperatures were justified as an interplay the high contents of Fluorine at lower growth temperatures which result in higher effective bandgaps and a lower number of active surface sites. Moreover, the co-presence of Mn_2O_3 has been judged detrimental. In this respect, the samples grown at 200 °C and 300 °C represent a favorable balance among these factors.

Valence band XPS measurements were carried out in a Kratos Axis Ultra DLD X-ray photoelectron spectrometer at ≈10^{-9} mbar base pressure using an Al Kα (1486.6 eV) X-ray source operated at 15 kV and 10 mA, with an analyser pass energy of 20 eV. For each sample, three measurement spots were taken with a spot size of 400 μm^2. For the MnO_2 samples the valence band edges were at a very small separation to the fermi level and

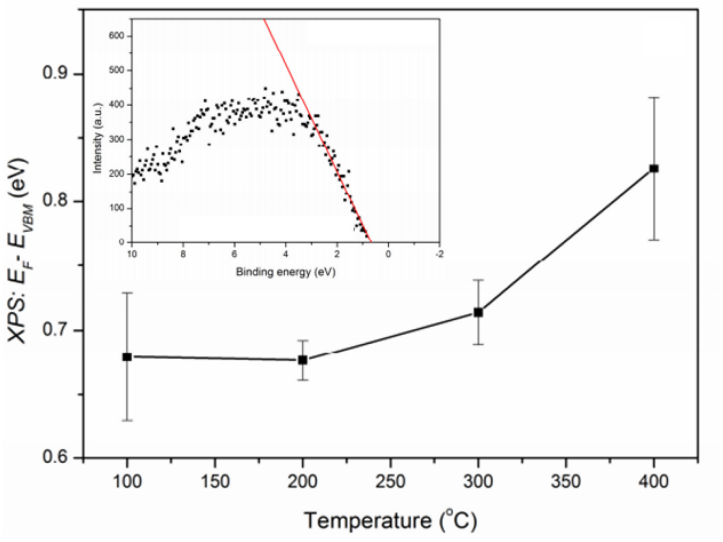

Figure 5.25 - Results of the fitting of valence XPS spectra for multifunctional MnO_2 nanomaterials. The inset shows an example of spectrum used for fitting.

changing slightly with higher deposition temperature in the CVD process. The results of the fits, along with an example spectrum is shown in Figure 5.25.

Given the small values obtained, it was decided to support the measurements with additional photoemission measurements with the Air photoemission system attached to the Kelvin probe. The analysis of photocurrents measured for the multifunctional MnO_2 nanomaterials is shown in figure 5.26a. The linear fit of higher energy parts of the cube root of photocurrent signal resulted in the values of valence band edge presented in the Figure 5.26b.

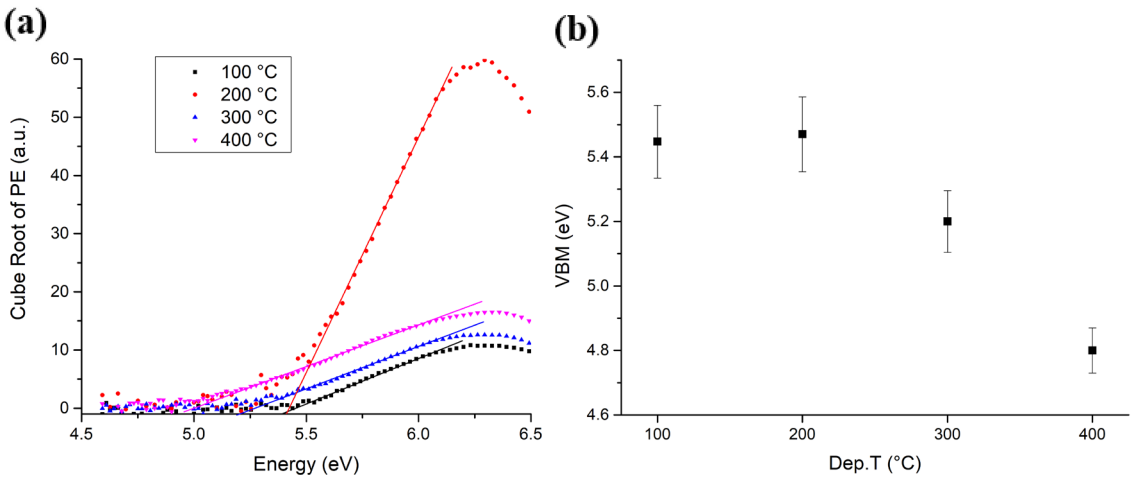

Figure 5.26 - (**a**) Cube root of photocurrent measured with the APS system and linear fits for MnO_2 nanomaterials in function of CVD deposition temperature. (**b**) Relative values of VBM extracted from the linear fit.

Indeed, the photoemission onsets vary from sample to sample, going to lower values with the deposition temperature. Comparing the XPS values and the APS values a similar trend, leading to a stronger separation in respect to the fermi level (hence lower absolute values) with increasing temperature. The mentioned variations are believe to be due to oxygen vacancies, which introduce acceptor dopant states inside the bandgap of MnO_2, near the valence band maximum.

The absolute Fermi energy was determined by Kelvin probe (KP) measurements (KP Technologies APS04) with a 2 mm gold plated tip. A sputtered Au-on-Si reference was used for the calibration of the tip work function. The tip is scanned over a 2 mm x 2 mm area across the border with an exposed part of the Si substrate, to measure a difference in

the CPD due to the sample (example for the 200°C grown sample in Figure 5.27a) and to take into account the variations of CPD within the deposited area. The V_{CPD}^{ref} is then obtained by averaging the values measured only in the sample area (shaded area in Figure 5.27a). The resulting Fermi level were then estimated as using equation 5.2. The results of the of the calculations are shown in Figure 5.27b for all the samples under study. The estimated absolute Fermi levels are between 5.35 eV and 5.40 eV for the three samples at 100 °C 200 °C and 300 °C and show a significant variation only for the sample grown at 400 °C (5.12 eV).

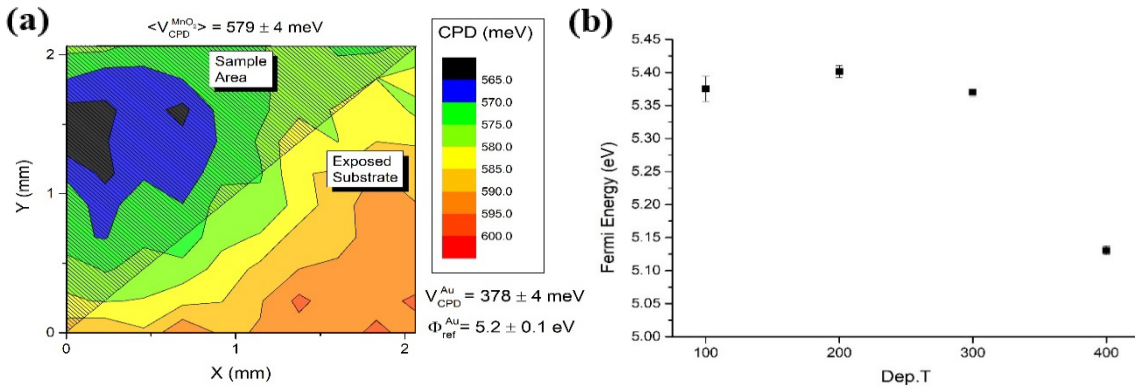

Figure 5.27 - (**a**) Example of scanning KP measurement for a nanostructured MnO_2 sample grown at 200 °C. The shaded area is where the deposited film is, the rest is substrate deposited. The value printed on top is an average measurement over the sample are. Also indicated the calibration values of work function and CPD for the Au reference work function used to calibrate the tip work function, obtained by measuring an Au- coated Si substrate. (**b**) Estimated Fermi levels as a function of MnO_2 nanomaterials deposition temperature in the CVD process.

The collaborators measured the UV-vis absorption properties from transmittance measurements. Herein are reported because they have been used for building the EBDs. They reported that the spectra show more pronounced absorption edges at lower wavelength, the higher the deposition temperature (Figure 5.28a). The estimated bandgaps via Tauc plot assuming direct transitions is decreasing in magnitude with higher

temperatures (Figure 5.28b). In addition, the values are larger than the reported values for the β-MnO_2 in literature (typically 1.6-1.7 eV).

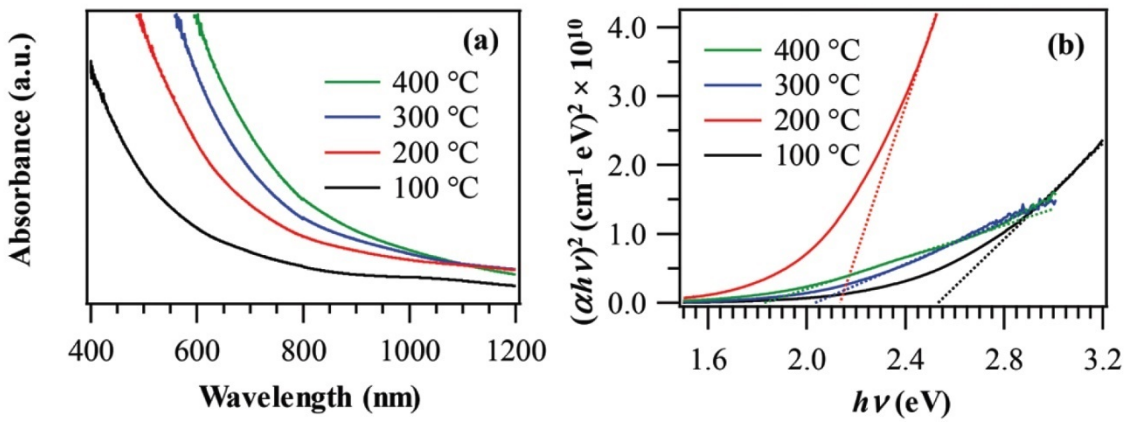

Figure 5.28 - **(a)** Absorbance obtained from transmittance measurements for the samples synthesized at different temperatures, showing a more pronounced absorption tail for higher temperature grown samples. **(b)** Tauc plots used to estimate the bandgaps assuming direct transitions.

The EBDs were then built to support the understanding of the different performances for photoactivated processes between samples (Figure 5.29).

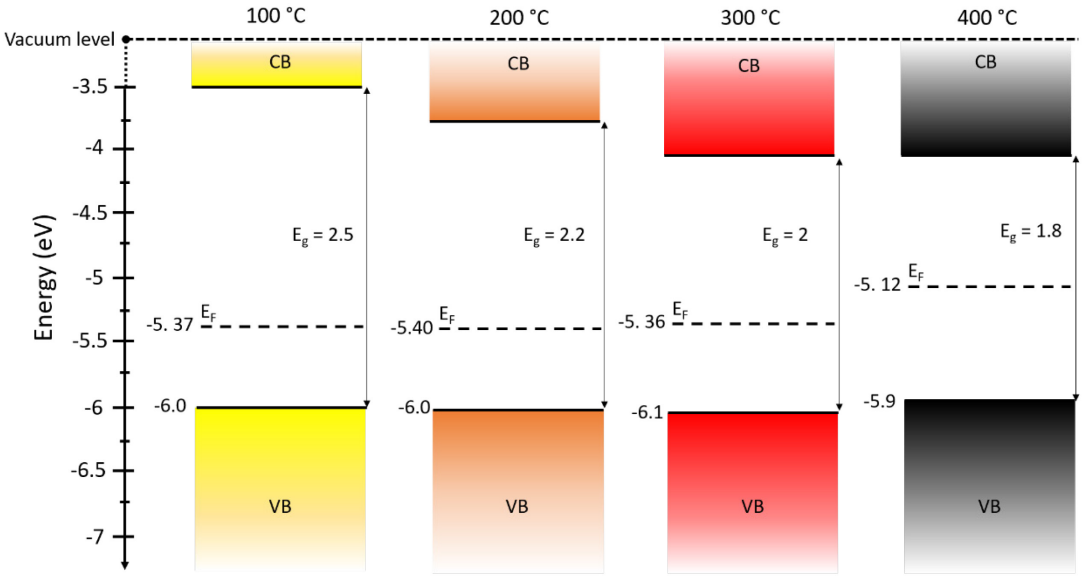

Figure 5.29 - EBDs of the nanostructured β-MnO_2 samples synthesized at different temperature, starting from XPS measurements for the VBM, Kelvin Probe measurements for the Fermi level and UV-VIS absorbance for the bandgaps.

The EBDs in Figure 5.29 have been built from XPS in the valence band region for the separation of VBM with Fermi level, the absolute Fermi levels estimated with the Kelvin Probe method and bandgaps estimated from absorption UV-Vis spectrophotometry. Even though the XPS values are small, they were assumed as more reliable values, as XPS is not affected by the k-selection rules as the air-photoemission system does (similarly to UPS) and the state of surfaces in UHV is preserved. As in the case of ZnO, the variation of reference level for UHV-PES measurements and KP ones is not expected to be important as MnO_2 nanomaterials are not expected to be highly conductive. In any case, both UV-Vis and XPS are relative measurements, thus as long as absolute values are not of interest (to compare with interface materials) these EBDs have unambiguous significance in respect to intrinsic variations of electron states between samples synthesized at different temperature. The samples show a rather constant absolute value of valence band maximum in function of the CVD growth temperature. The absolute values of Fermi level are near 5.40 eV and do not change significantly (within the experimental uncertainty ±0.02 eV) among samples except for the sample grown at the highest temperature (400 °C) for which a variation of -0.2 eV is reported. Optical bandgaps instead, decrease from 2.5 eV to 1.8 eV with increasing growth temperature. The results imply a more p-type character for samples grown at lower temperatures, and this behavior is more stressed the lower the temperature. The 400 °C sample instead has a more "compensated" semiconductive behavior with the Fermi level in the middle of the optical gap. In MnO_2 materials Fluorine is known to impact the carrier concentration by passivating the oxygen vacancies, and in the samples higher fluorine concentrations are found for lower growth temperature. In this respect, a constant separation between E_F and VBM for samples with different concentrations of Fluorine, may be the result of the "pinning" of Fermi levels to Fluorine-related surface states. With this assumption, the higher bandgaps against a constant E_F-VBM would imply that Fluorine surface states act as donor states, thereby increasing the effective bandgap by affecting the DOS near the Conduction band edge. In the last sample at 400 °C the co-presence of Mn_2O_3 phases are indicative that the estimated EBD is an estimation of the "effective" electron states of a junction between MnO_2 and Mn_2O_3 phases, hence the bigger variations in Fermi level, VBM and bandgap. These results were also useful in the interpretation of the performance of photochemistry effects, as higher effective bandgap values decrease the photocarrier losses by recombination, giving an increased proportion of photocarriers available for surface chemistry.

5.5 Conclusions

In this chapter a general description of energy band diagrams has been given, along with a set of experimental tools and methods to measure the absolute energy values. It has been stressed how significant are the EBDs in order to design real-world devices which are in general comprising interfaces between different materials, and tailor their overall optoelectronic properties for applications.

A set of experimental techniques which are usually available in materials science laboratories have been introduced theoretically and experimentally showing the pros and cons of each one on the determination of the VBM, Fermi Level and energy bandgap, which are the most relevant quantities needed to build the EBD of a solid material. The comparison between different techniques highlighted also the problems of comparing values across different techniques, as the definition of a reference level can change depending on the state of sample surfaces and the measuring environment. As a result, it is suggested to use ultra-high vacuum techniques for probing the intrinsic properties of a surface, while near-ambient techniques are better suited for materials which will be exposed to atmospheric conditions.

In conclusion, two case studies were presented to show the experimental challenges of measuring each parameter of the EBD and to show how the determination of the EBDs was beneficial to the understanding of photocatalytic behavior of two nanostructured semiconductive materials.

References

1. Kittel, C. *Introduction to Solid State Physics*. *Solid-State Physics (Fourth Edition): An Introduction to Principles of Materials Science* (2010).

2. Sze. *Physics of Semiconductor Devices Physics of Semiconductor Devices*. *America* vol. 10 (1995).

3. Kahn, A. Fermi level, work function and vacuum level. *Mater. Horizons* **3**, 7–10 (2016).

4. Neamen, D. A. *Semiconductor Physics and Devices Basic Principles*. *Materials Today* vol. 9 (2006).

5. Kuzmany, H. *Solid state spectroscopy, an introduction, second edition, cap-9 (185-200)*. (2009). doi:10.1007/978-3-642-01479-6.

6. Park, Y., Choong, V., Gao, Y., Hsieh, B. R. & Tang, C. W. Work function of indium tin oxide transparent conductor measured by photoelectron spectroscopy. *Appl. Phys. Lett.* **68**, 2699–2701 (1996).

7. Ley, L. & Cardona, M. *Photoemission in Solids II (Case Studies)*. *Springer* vol. 27 (1979).

8. Hufner, S. *Photoelectron Spectroscopy: Principles and Applications*. (Springer-Verlag Berlin, 2003).

9. Beerbom, M. M., Lägel, B., Cascio, A. J., Doran, B. V. & Schlaf, R. Direct comparison of photoemission spectroscopy and in situ Kelvin probe work function measurements on indium tin oxide films. *J. Electron Spectros. Relat. Phenomena* **152**, 12–17 (2006).

10. Kelvin, Lord. V. Contact electricity of metals . *London, Edinburgh, Dublin Philos. Mag. J. Sci.* **46**, 82–120 (1898).

11. Kronik, L. & Shapira, Y. Surface photovoltage spectroscopy of semiconductor structures: At the crossroads of physics, chemistry and electrical engineering. *Surf. Interface Anal.* **31**, 954–965 (2001).

12. Kronik, L. & Shapira, Y. Surface photovoltage phenomena: Theory, experiment, and applications. *Surf. Sci. Rep.* **37**, 1–206 (1999).

13. Gal, G., Mastai, Y., Hodes, G. & Kronik, L. Band gap determination of semiconductor powders via surface photovoltage spectroscopy. *J. Appl. Phys.* **86**, 5573–5577 (1999).

14. Baikie, I. D., Grain, A., Sutherland, J. & Law, J. Near ambient pressure photoemission spectroscopy of metal and semiconductor surfaces. *Phys. Status Solidi Curr. Top. Solid State Phys.* **12**, 259–262 (2015).

15. Baikie, I. D., Grain, A. C., Sutherland, J. & Law, J. Ambient pressure photoemission spectroscopy of metal surfaces. *Appl. Surf. Sci.* **323**, 45–53 (2014).

16. Fowler, R. H. The Analysis of Photoelectric Sensitivity Curves for Clean Metals at Various Temperatures. *Phys. Rev.* **38**, 45–56 (1931).

17. Challinger, S., Baikie, I., Birdwell, A. G. & Strehle, S. Construction of the Energy Band Diagram of Hydrogen Terminated Diamond and Silicon Nanowires. *Phys. Status Solidi Curr. Top. Solid State Phys.* **14**, 1–5 (2017).

18. Solé, J., Bausa, L. & Jaque, D. *An introduction to the optical spectroscopy of inorganic solids*. (John Wiley & Sons, 2005).

19. Mott, N. F. & Davis, E. A. *Electronic Processes in Noncrystalline Materials*. *Physics Bulletin* vol. 24 (Oxford University Press, 1979).

20. Tauc, J. Optical properties and electronic structure of amorphous Ge and Si. *Mater. Res. Bull.* **3**, 37–46 (1968).

21. Lakowicz, J. *Principles of fluorescence spectroscopy*. (Springer Science, 2013).

22. Fojtik, A. & Henglein, A. Luminescent colloidal silicon particles. *Chem. Phys. Lett.* **221**, 363–367 (1994).

23. Gasparotto, A. *et al.* Surface Functionalization of Grown-on-Tip ZnO Nanopyramids: From Fabrication to Light-Triggered Applications. *ACS Appl. Mater. Interfaces* **11**, 15881–15890 (2019).

24. Ivanov, I. & Pollmann, J. Electronic structure of ideal and relaxed surfaces of ZnO: A prototype ionic wurtzite semiconductor and its surface properties. *Phys. Rev. B* **24**, 7275–7296 (1981).

25. Barreca, D. *et al.* Multi-functional MnO2 nanomaterials for photo-activated applications by a plasma-assisted fabrication route. *Nanoscale* **11**, 98–108 (2019).

Chapter 6 - Silicon QDs and their films

6.1 Introduction

Silicon is an environmentally friendly, earth-abundant material that has been studied for the past 80 years as a prototype semiconductor material and enabled the revolution of computers and electronics including the invention of transistors. In its bulk form, though, it has shown to have some limitations such as poor intrinsic electrical conductivity and the inefficiency for light absorption and emission, qualities of interest for electronics, photovoltaics and photonics. Despite this, its abundance and existing industrial infrastructure has pushed research efforts in order to modify its basic material properties in many different ways: doping, alloying, defects and strain engineering or shrinking the grain or particles size to the quantum regime.

More particular, silicon quantum dots (QDs) have attracted great attention in numerous fields of science such as photonics, photovoltaics, electronics or biomedicine[1–5] for the unique interplay between quantum effects, surface states and direct/indirect transition dynamics and their biocompatibility.[6–8] When the size of a particle approaches the Bohr exciton radius, the confinement of the electron wavefunction determines a size-dependent redistribution of electron energy levels. This can result in the increase of light absorption and emission efficiency, a shift in the absorption edge to higher energy photons and different charge transport mechanisms. For example, Si crystalline QDs can show higher efficiency in absorbing and emitting light, because of the relaxation of the crystal momentum selection rule for light absorption, paving the way to silicon-based lasers[9] and low cost photovoltaic cells with theoretical efficiency beyond the single-junction limit [10].

Over the last decade, the focus has been on crystalline Si QDs,[11–14] and the efforts made on the study of amorphous Si QDs have been very limited[14–16] due to the difficulty of preserving the individual character of the QDs. Nonetheless, both phases present distinguished and remarkable features. Amorphous silicon thin films often offer better transport properties due to enhanced structural disorder preventing radiative recombination[17] and tunability of their optical absorption edge by controlling hydrogen content.[18] At the nanoscale, QDs can provide added functionalities not available from bulk silicon for amorphous and crystalline Si, in combination with other nanoscale properties (surface-to-volume ratio, surface chemistries, etc.). The synthesis of Si QDs

by low-pressure plasma has been the focus of extended research work that has revealed the benefits of plasma processes for nanomaterials synthesis,[19–23] while the investigation on the synthesis with high pressure discharges is relatively young.[15,24,25]

The work presented in this chapter is an experimental and theoretical investigation of the Si QDs produced with an atmospheric pressure microplasma reactor. Several parts of this work have been already published.[14,26,27] The first part is a review of the collaborative work, which relate to the experimental aspects of the synthesis process, the structural characterization of both crystalline and amorphous silicon QDs and the process characterization through optical emission spectroscopy and a particle heating model. Then, the morphology, chemical composition, oxidation behavior and optoelectronic properties of Si QDs in the form of films are studied through various measurements, to derive the relationships between structural features and opto-electronic properties of the films as a function of synthesis conditions. The ultimate goal is to produce energy band diagrams of the films for direct integration in devices. Finally, the applicability of the Si QDs films is tested integrating them as active layers in all-inorganic solar cells.

6.2 Experimental Setup

6.2.1 Reactor design and OES

The plasma reactor used for the synthesis of Si QDs operates in a parallel electrode configuration at atmospheric pressure (760 Torr). A schematic diagram of the system is depicted in Figure 6.1. The plasma is generated inside a rectangular glass tube with a 0.5 mm gap and 0.3 mm of wall thickness (Figure 6.1) where the precursors flow in the perpendicular direction with respect to the applied field (cross-flow). The reactor is contained in a stainless-steel chamber with a continuous flow of N_2 filtered from residual oxygen and water moisture and an oil-free mechanical pump, dynamically keeping atmospheric pressure. Radio frequency (RF) power at 13.56 MHz and 120 W is applied through a matching unit and to two rectangular copper electrodes with a section of 20 mm x 5 mm.

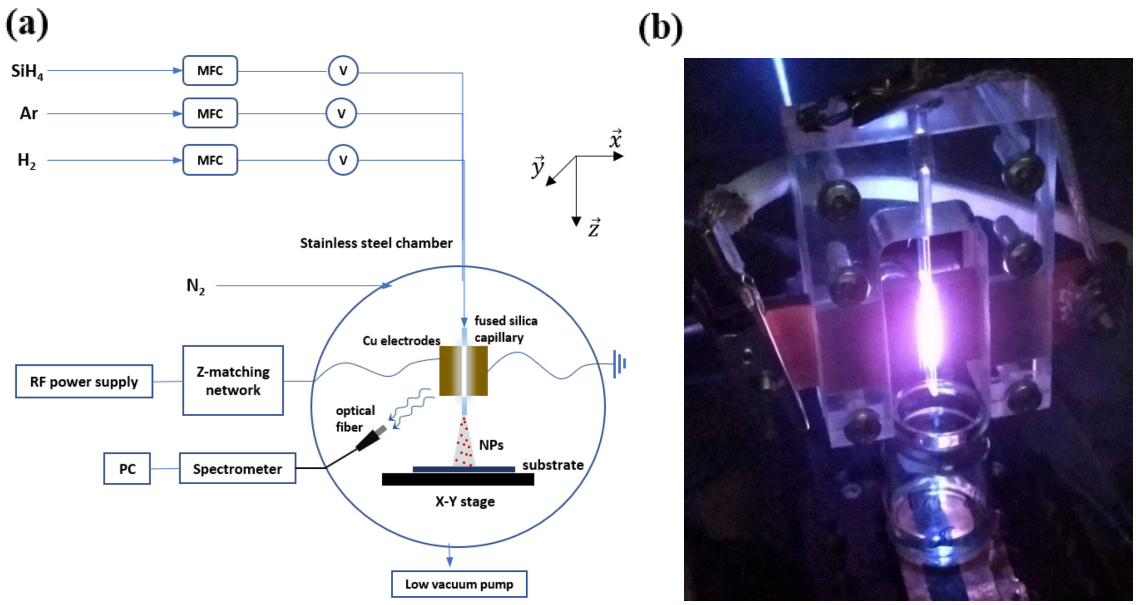

Figure 6.1 - (**a**) Schematics of the experimental setup: gas mixing circuit, reactor chamber and setup for OES. The optical fiber is pointing perpendicularly to the capillary in the middle of the visible discharge to capture a horizontal line of sight. (**b**) Picture of the micro-plasma reactor operating an 80 W Ar plasma with an ethanol vial placed directly below the capillary exit to obtain a colloid.

Argon and hydrogen are supplied as background gases, while silane (SiH_4, premixed cylinder 5600 ppm in Ar) is used as Si precursor varying its concentration between 50 ppm and 200 ppm. The flows of Ar and H_2 are set to 810-840 sccm and 150 sccm

respectively, in order to keep concentrations of 99.7% and 0.3% approximately at a fixed total flow of 1 sLm. Table 6.1 summarizes the actual values of partial flow settings in the mass flow controllers (MFC) and concentrations used in each experimental condition.

Flow through the MFCs			Actual concentrations		
SiH_4 (sccm)	H_2 (sccm)	Ar (sccm)	SiH_4 (ppm)	H_2 (%)	Ar (%)
9	150	841	50	0.3	99.7
19	150	831	100	0.3	99.69
28	150	822	150	0.3	99.69
37	150	813	200	0.3	99.68

Table 6.1 - Summary of gas flow settings in the mass flow controllers and actual concentrations in the gas mixture against a fixed total flow of 1sLm = 1000 sccm. The samples throughout the study are labeled by the SiH_4 concentration.

The plasma setup is accessorized with a two-axis stage and it is possible to directly deposit Si QDs on a substrate and form homogeneous films. The plasma conditions are characterized using optical emission spectroscopy. The equipment used to acquire the emission spectra is an Ocean Optics HR4000CG UV-NIR spectrometer (range 194-1122 nm) coupled with a 50 µm optic fiber. These measurements are carried out locating one end of the optic fiber perpendicular to the plasma 10 mm away.

6.2.2 Characterization methods

Silicon QDs are characterized using transmission electron microscopy (TEM) with a JEOL JEM-2100F microscope. The TEM analysis includes bright-field imaging to observe the morphology of the QDs and selected area electron diffraction (SAED) to characterize their crystallinity. Chemical analysis is performed using Fourier transform infrared spectroscopy (FTIR) and X-ray photoelectron spectroscopy (XPS) core levels measurements. The FTIR is a Nicolet iS5 from Thermo Scientific equipped with an attenuated total reflectance (ATR) iD5 accessory. XPS and ultraviolet photoelectron

spectroscopy (UPS) measurements were performed using an ESCALAB 250 Xi microprobe spectrometer (Thermo Fisher Scientific, UK), equipped with an X-ray and UV source. XPS analysis was carried out with a focused XR6 monochromatic, micro-focused AlK$_\alpha$ ($h\nu$ = 1486.6 eV, < 900 μm spot sizes) radiation source with a hemispherical energy analyzer. The binding energy was calibrated against the Pt_{4f} peak taken to be located at 72.1 eV with a pass energy of 20 eV. XPS measurements were carried at a pressure 1-5 $\times 10^{-9}$ mbar. Depth profiling is performed with the same instrument, cycling 20 times between sputtering from an Ar^+ beam (<10 μm wide) accelerated at 2 kV for 5 seconds and measuring the XPS spectra. The valence band spectra were collected with a 20 eV pass energy. The films morphology is assessed with a Hitachi SU5000 scanning electron microscope with a field emission gun source (10 kV acceleration voltage, ~5 mm working distance) and equipped with an X-ray detector for energy dispersive x-ray (EDX) spectroscopy, cross-view images are taken with a 45° to 90° tilted sample holder. Optical absorption is obtained using a Perkin-Elmer 650S ultraviolet-visible (UV-Vis) spectrometer equipped with a 150 mm integrating sphere. For valence electron analysis XPS in the valence region, UPS and a Kelvin probe were used. UPS spectra were collected with a UV source energy He(I) ($h\nu$ = 21.22 eV) at a pressure of approximately 5.5 × 10^{-8} mbar, with 2 eV pass energy. A negative bias of 10 V was applied to the sample to shift the spectra from the spectrometer threshold. The energy resolution was around ~100 meV. The Kelvin probe (KP technologies APS04) is operated in atmosphere with a 2 mm gold alloy tip, after calibrating the tip work function against a sputtered Au thin film (W_{Au} = 4.69 ± 0.05 eV, W_{tip} = 4.4 ± 0.1 eV). Additionally, the Kelvin probe (KP) setup is equipped with a surface photovoltage module which measures the surface contact potential difference (CPD) induced by a monochromated white light source and an air photoemission module (APS), which uses a deuterium lamp source ($\Delta\lambda$=1 nm) to induce photoemission of electrons from the samples.

6.2.3 Experimental procedures

After evacuation of the chamber, few sccm of silane mixture are flowed inside the chamber, in order to burn residual oxygen present, then N_2 is introduced until reaching atmospheric pressure. The plasma is ignited using He gas and then switched to an Ar and hydrogen mixture and kept on for fifteen minutes, in order to evacuate gas lines and the capillary from residual atmospheric gases. Then SiH_4 is introduced and a blue coloring

of the plasma is observed. The samples are collected either directly on a vial placed 0.5 cm below the exit nozzle for 10 minutes to produce colloids or collected directly from the plasma on a substrate placed on top of the scanning stage for 20 min to 30 min resulting in a homogeneous film of yellowish/whiteish color (depending on the synthesis conditions). The colloids are stable without turbidity or precipitations even years after the synthesis.

For TEM imaging, the QDs are collected directly in vials containing ethanol, then drop casted onto an ultrathin carbon grid (Agar Scientific) and dried. For SEM, FTIR, XPS, UPS and KP samples are directly deposited to form a film of QDs on ITO-coated glass substrates (150 nm, 15 Ω/sq. VisionTek) or on thin Mo foils in order to have good electrical contact with the stubs. All the characterizations were carried out within 1 hour after the synthesis to limit the effect oxidation, unless otherwise specified. For the ATR-FTIR, powder samples were produced by scratching the solid film with a clean spatula. For SEM cross-view the deposition is performed across the border of a Mo foil in order to avoid the artifacts from cutting the foil. Oxidation studies are performed by exposing the films to atmosphere and by XPS depth profiling in different spots on the same sample, for each experimental point. For UV-Vis characterization, Si QDs were deposited on a quartz substrate and measured at different ports of the spectrophotometer integrating sphere, in order to discriminate the contribution of transmission, reflection and scattering for the evaluation of optical absorption.

6.3 Characterization of QDs - Collaborative work

6.3.1 Structural

TEM results show that well-separated Si particles are produced for all values of SiH_4 concentrations (50 ppm, 100 ppm, 150 ppm and 200 ppm) introduced into the plasma (Figures 6.2, 6.3 and 6.4). However, high resolution TEM (HR-TEM) images reveal major differences between the particles depending on the precursor concentration. In particular, high silane concentrations (150-200 ppm) lead to the production of exclusively amorphous particles, while with low concentrations (50 ppm) crystalline particles are obtained (Figure 6.2). As an example, figures 6.2a-b display HR-TEM of a crystalline QD synthesized using a SiH_4 concentration of 50 ppm and an amorphous QD produced with 200 ppm of the precursor, respectively. In Figure 6.2a, the particle exhibits fringes with spacing of 0.17 nm that corresponds to the (311) plane of the silicon crystalline lattice.

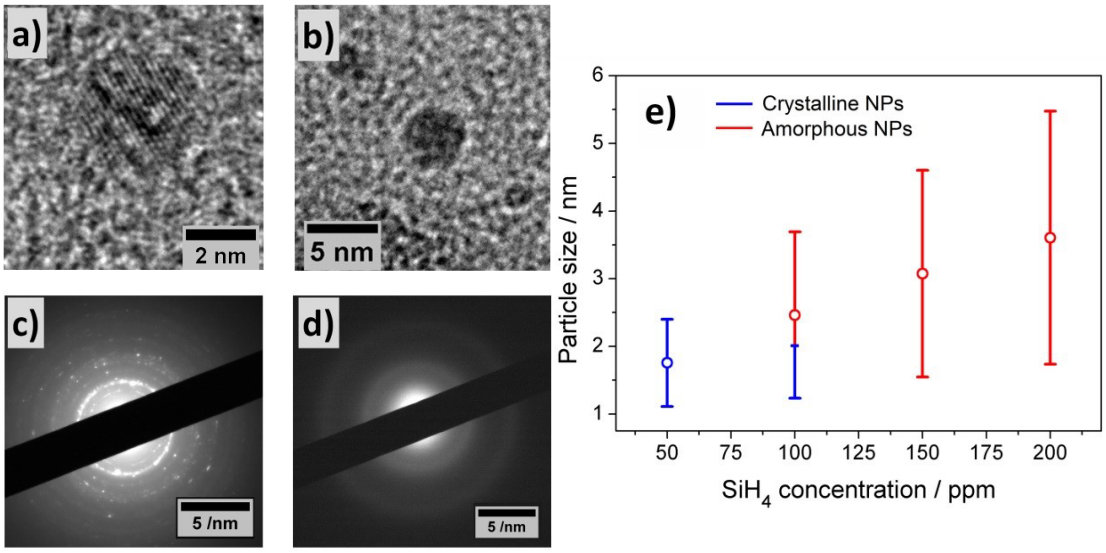

Figure 6.2 - Transmission electron microscopy (TEM) characterization of the Si quantum dots (QDs). High resolution TEM of (**a**) a crystalline and (**b**) amorphous Si QD. (**c-d**) Selected area electron diffraction (SAED) pattern of (**c**) crystalline and (**d**) amorphous Si QDs. (**e**) Mean particle size (dots) and standard deviation (bars) of the Si QDs as a function of the precursor concentration used; blue and red lines denote respectively the crystalline or amorphous character of the QDs within the size distribution.

More detailed evidence of the crystalline or amorphous character of the Si QDs is obtained using selected area electron diffraction (SAED) patterns. Figures 6.2c-d show SAED patterns for the two extreme conditions of precursor concentration considered (50 ppm and 200 ppm). The crystallinity of the Si QDs produced using low SiH_4 concentration, results in the observation of sharp spots that together form well-defined rings in the SAED pattern (figure 6.2c). The spots detected in the diffractogram match well with crystalline planes corresponding to the diamond lattice of silicon (see Figure 6.3). On the other hand, a high concentration of precursor (150-200 ppm) results in faded diffuse rings in the SAED pattern that can be attributed to their amorphous character (Figure 6.2d).

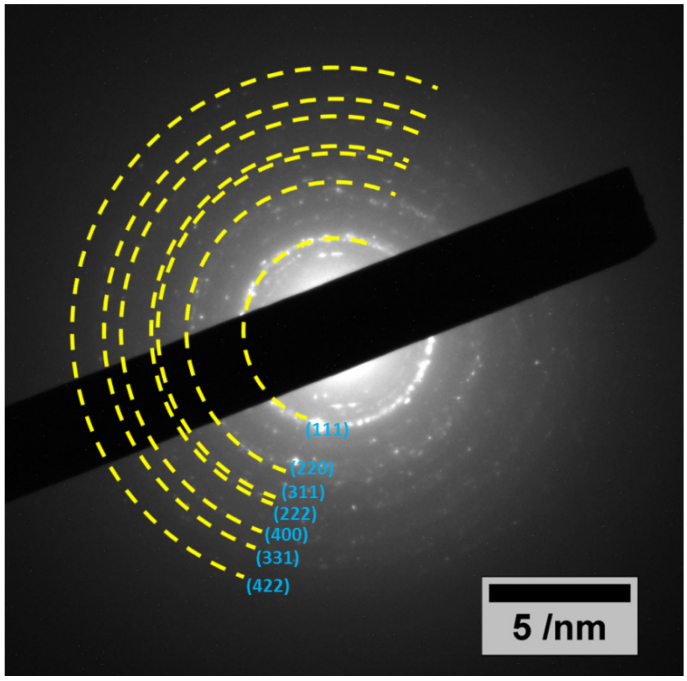

Figure 6.3 - Selected area electron diffraction of crystalline Si quantum dots. Crystalline planes labeled with Miller indices pertaining to the diamond lattice of Silicon are indicated in the diffractogram.

The conditions described above illustrate how the reactor system used is capable of producing highly crystalline QDs or purely amorphous QDs by controlling, in this case, the silicon precursor concentration. These results are in agreement with results published elsewhere.[14,15] Hence, it is possible to adjust from crystalline Si QDs production with low precursor concentration in the plasma ($\leq$ 50 ppm), to amorphous Si QDs with high concentrations ($\geq$ 150 ppm). For the 100 ppm SiH_4 conditions the situation exhibits intermediate characteristics. TEM analysis of samples prepared using 100 ppm of SiH_4 concentration showed that within the particle size distribution, only the smallest (< 2 nm) particles exhibited crystalline character, while larger particles were amorphous. Thus, at these conditions both crystalline and amorphous particles can be generated

simultaneously, or there must be a size-dependent crystallization process happening

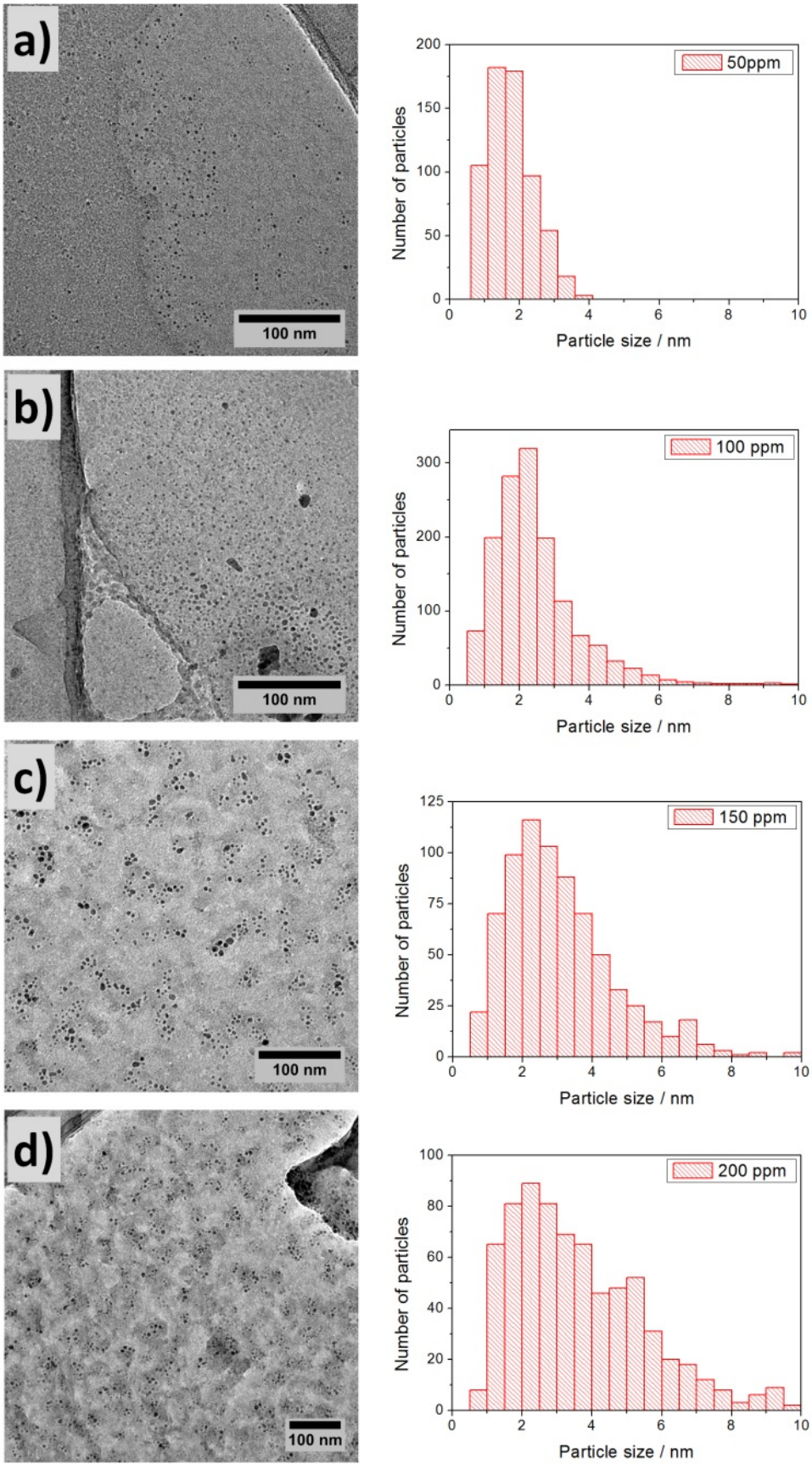

Figure 6.4 - Transmission electron microscopy images and particle size histogram obtained for different precursor concentrations in the plasma: (**a**) 50 ppm, (**b**) 100 ppm, (**c**) 150 ppm and (**d**) 200 ppm.

during the synthesis, alongside a limited particle growth. Regarding the particle size analysis, low magnification TEM images have been used, counting at least 500 particles for each of the conditions (Figure 6.4). The overall results are presented in figure 1e, showing the mean value and the standard deviation (these were obtained by fitting a log-normal distribution) of the particle's size for various precursor concentrations, indicating the crystalline or amorphous character with red and blue color respectively. In the graph it is possible to observe that increasing the concentration of precursor in the plasma leads to the production of NPs with larger size, with mean diameters varying from 1.7 nm to 3.6 nm. At the same time, the size dispersion also increases starting with a value of 0.6 nm for 50 ppm of SiH_4 and reaching a value of 1.8 nm for 200 ppm of SiH_4.

6.3.2 Characterization of the process plasma

To fully understand the formation process of the Si QDs it is necessary to characterize the plasma parameters of the system for the different experimental conditions under study. In order to characterize the formation mechanism and the successive conditions of formed particles in the plasma, OES has been used to derive gas temperature (T_g), electron temperature (T_e) and electron density (n_e) as described in Chapter 3. In figure 6.5, an OES spectrum for the 50 ppm SiH_4 sample synthesis condition upon introduction of silane in an 80 W Ar/H_2 discharge is shown. As soon as the Si precursor is introduced in the

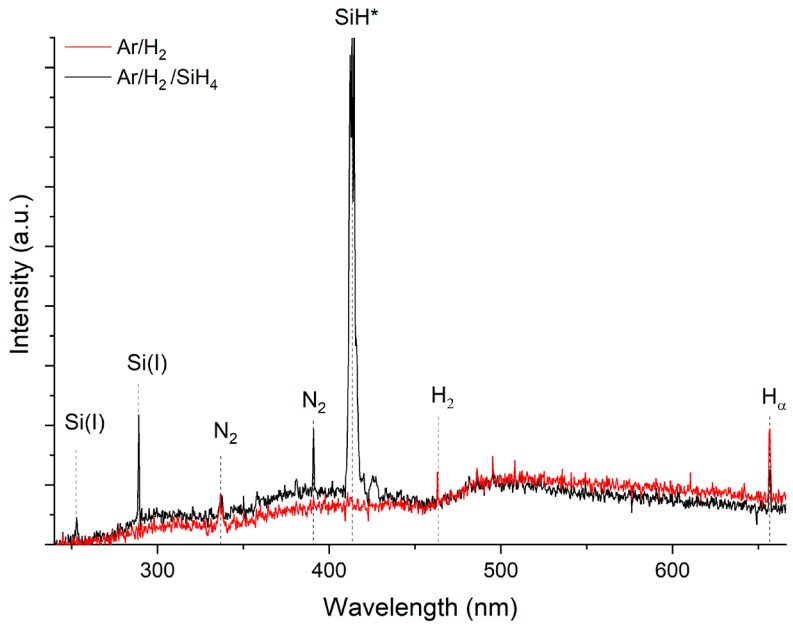

Figure 6.5 - Example OES spectrum in the region of interest to molecular species for an 80 W Ar/H_2 plasma (*black*) and upon introduction of silane (*red*). The silicon and silyl radical- related peaks appear upon introducing few ppm of Silane gas in the reactor and give the typical blue shade to the plasma.

reactor, the Ar/H_2 plasma turns from white to blueish, maintaining a homogeneous diffuse discharge over the space between electrodes. The process is stable for the first 15-20 minutes after which the plasma tends to shorten in length and red deposits pile up from the top part of the capillary side walls. Besides, thermal instabilities start to build up turning the discharge partially unstable and composed by small micro-discharges instead of a diffused one, and the development of these features is faster for higher concentrations of SiH_4. The OES spectra are dominated by sharp Ar(I) lines in the region between 670 nm to 1000 nm (not shown), few weak lines between 250 nm and 660 nm and a continuous background. The lines pertaining to molecular species which have been identified are summarized in Table 6.2.

Wavelength (nm)	Species	Transition(s)
251	Si(I)	$4s\ ^3P_2^0 \rightarrow 3P^2$
288	Si(I)	$4s\ ^1P_1^0 \rightarrow\ ^1D_2$
340-360	N_2	2nd positive $C^3\prod_u \rightarrow B^3\prod_g$
414.2	SiH^*	$A^2\Delta \rightarrow X^2\prod$
460	H_2	G0B0
656.4	H_α	$3\ ^2D \rightarrow 2\ ^1P^0$

Table 6.2 - Identification of discernible peaks for the spectra of Silane discharges and notation of the involved transition.

The dominant peak in this range (250 nm to 660 nm) is the 414.2 nm emission associated with SiH^* radicals and is giving the characteristic blue color to the discharge. It is also observed ionized atomic Si and weak emissions from molecular hydrogen (G0B0 system) and atomic hydrogen (Balmer series α) along Nitrogen-related peaks. Si(I) and SiH radical emission is usually observed in diffused Ar/SiH_4 discharges with efficient dissociation of silane,[28] while no emission from the Fulcher system (~600 nm) of molecular hydrogen or the H_β is observed. Moreover, the introduction of SiH_4 changes

the intensity distribution of Ar lines and in general the absolute brightness of the discharge is reduced, the more Silane is introduced.

In the specific case of the $SiH_4/H_2/Ar$ process for synthesizing the Si particles, the gas temperature is estimated from the rotational levels of OH radicals.[29,30] OH radicals come from the residual water vapor in gas lines and is generally unwanted for the synthesis of Silicon, as it easily brings to the early oxidation of particles. Usually it is completely depleted during the first 10/15 minutes after igniting the plasma and it may affect the plasma profoundly as water is electronegative and can stimulate electron attachment. Nevertheless, a change on the other OES lines intensity when the OH signal goes down is not observed, so it is assumed that in this case has a negligible effect on the plasma. The rotational emission spectrum of OH was then measured operating the reactor in atmosphere, right after the $SiH_4/H_2/Ar$ plasma has visually stabilized, 2-3 minutes after the introduction of Silane. Then, the rotational spectrum has been simulated with algorithms in software LIFBASE and the estimated rotational temperature obtained is approximately constant for all the conditions under consideration with a value of 490 ± 50 K.

The effective electron temperature is calculated using argon emission lines. The intensity of optical emission lines pertaining to 4p and 5p levels of argon vary upon introduction of different precursor concentrations (Figure 6.6c). The Boltzmann plots build for these lines are used to estimate the effective electron temperature in function of SiH_4 concentration through a collisional-radiative modeling of argon lines, as described thoroughly in chapter 3.[31–33] The effective T_e estimated decrease from 1.2 eV to 0.9 eV with increasing plasma SiH_4 concentration from 50 ppm to 150 ppm (see blue triangles in Figure 6.6b). However, at the highest precursor concentration (200 ppm) effective T_e increases back to 1.2 eV. The electron density was instead estimated by analyzing the variation of the full width at half maximum (FWHM) of H_α emission line with precursor concentration (Figure 6.6a). These can be deconvoluted in different contributions as detailed in chapter 3, with the broadening contribution due to the Stark effect enabling the estimation of n_e. The red circles in figure 6.6b display the results in function of the different experimental conditions. The results show that the electron density gradually decreases from $1.8 \cdot 10^{14}$ cm^{-3} to $0.8 \cdot 10^{14}$ cm^{-3} when the SiH_4 concentration is increased from 50 ppm to 200 ppm. The density of emitting species usually depends on the plasma electron density as electron impact excitation is the main excitation mechanism in these

plasmas, the overall drop in brightness of the discharge observed with precursor concentration is compatible with the trend observed.

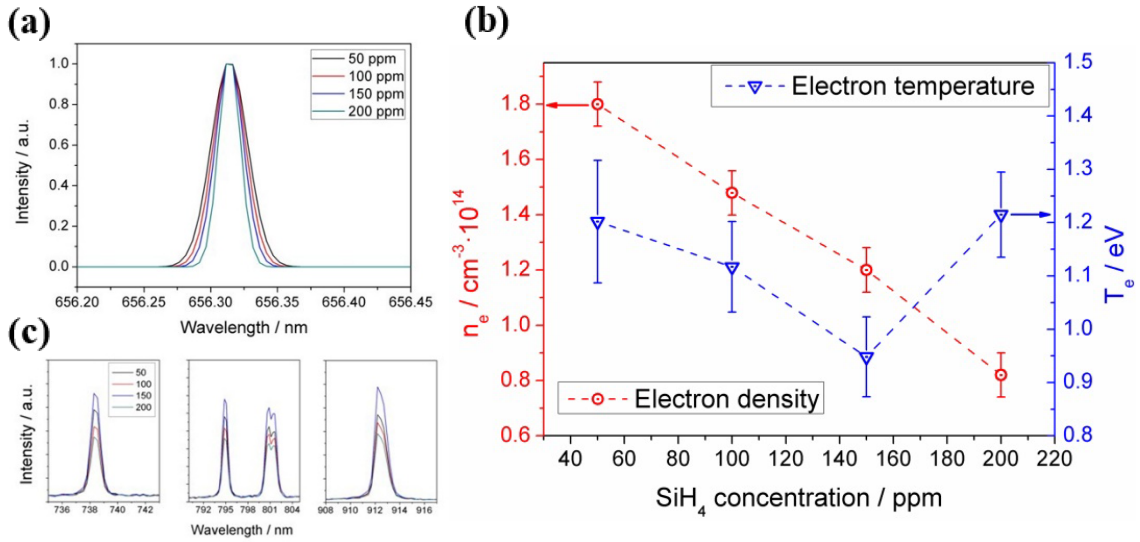

Figure 6.6 - Variation of (**a**) the FMWH of H_α emission line for the different synthesis conditions , the deconvolution of the contribution of various components (described in Chapter 3) permits to estimate the electron density and (**c**) the intensity variation of selected Ar emission lines from which the effective electron temperature is estimated. (**b**) Electron density and electron temperature calculated for different silane precursor concentration introduced in the plasma.

6.3.3 Particle heating and size-dependent crystallization

The particle heating model described in chapter 3 was used to calculate the temperature at the surface of the Si QDs (T_p) during the synthesis process within the APP, using OES-derived parameters as input values. Figure 6.7 presents the estimated values of T_p corresponding to the synthesis conditions explored herein (black, red, green and blue squares); in the same graph the experimental crystallization temperature is also plotted (CT, grey points in figure 6.7) of Si QDs as reported in literature.[34] The CT divides the graph in two regions: particles with a temperature below the CT are expected to be amorphous (blue region in figure 6.7) while particles with a temperature above the CT are expected to present a crystalline character (orange region in Figure 6.7). Due to the intrinsic difficulty for measuring these values, it is not possible to define a sharp CT line to separate the two states.[34] Instead, a transition region represented by a white band can be defined (see Figure 6.7). It is possible to observe that for low SiH_4 concentrations (50

ppm, black squares in figure 6.7) the data points are all located entirely on the crystalline side of the graph. This result clearly agrees with the experimental evidence reported in figures 6.2, 6.3 and 6.4, that is, the formation of purely crystalline Si QDs. For high precursor concentrations (> 100 ppm) the opposite situation is observed. In this case, T_p is mainly located in the amorphous region with only the smallest, and less numerous, particles near the crystallization band. This is again in agreement with experimental data of Figure 6.2e, where amorphous particles were observed for these conditions.

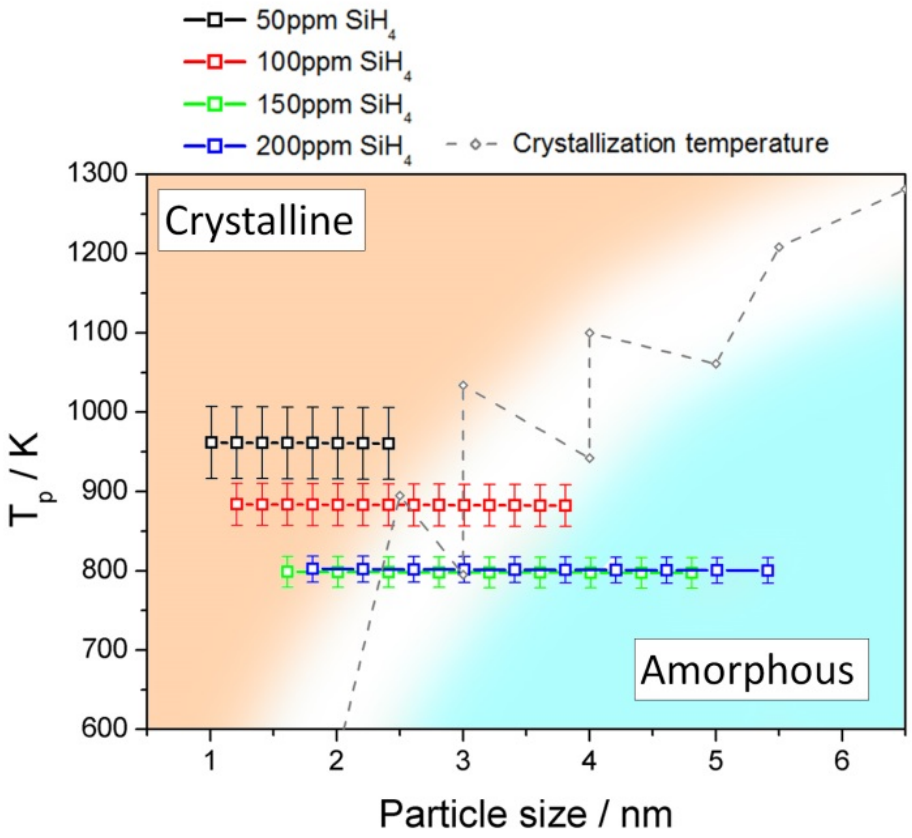

Figure 6.7 - Particle temperature calculated using the collision-corrected model (CCM) for the different concentration of precursor introduced in the plasma and experimental crystallization temperature from reference [53]. The temperature has been calculated for the particle size distribution obtained for each condition. The crystallization temperature divides the graph in crystalline (orange) and amorphous (blue) regions.

The inability to produce a sufficiently high QD temperature for the crystallization of the Si QDs under these conditions can be partly attributed to the lower energetic plasma conditions (see Figure 6.6) but also to the larger particle size produced. At intermediate SiH_4 flow (100 ppm), only the smallest particles are located on the crystalline side and the rest lay on the crystallization band as indeed confirmed in the QDs characterization.

The observations of OES are not enough to distinguishing a particular nucleation mechanism. For low-pressure plasmas (as described in chapter 2), it has been described as the nucleation by initial clustering of electronegative silyl and silylene anions and subsequent growth by polymerization.[35,36] The cross-flow field configuration from this point of view could help the formation by trapping the negatively charged particles within the plasma, increasing the lifetime of the mentioned anions hence increasing the chance of interaction between them,[28] and the small reactor volumes would be responsible for the uniquely small size of the particles. However, these mechanisms have been criticized as less-probable at atmospheric pressure. In fact, the ionization degree is generally lower than the low-pressure counterparts[19,36] and the oscillating nature of the plasma bulk would prevent the trapping of anions for confined discharges.[37] A more probable mechanism would be based on polymerization reactions due to neutral and radical species, whose collisional rates are enhanced at atmospheric pressure.[38] In this respect, the hydrogen abstraction, addition and exchange reactions are the most important reactions involved in the nucleation and growth, and the presence of atomic and molecular hydrogen would a strong effect on the reaction balances. Irrespectively of the nucleation mechanisms, the results obtained in this study agree well with the fact that crystallization is a separate process from the nucleation stage and happens as particles grow,[39] and provide theoretical justification to the experimental observations since only particles smaller than 2 nm were found to be crystalline for this intermediate condition. More experiments are needed in order to clarify these mechanisms, especially involving mass spectroscopy of intermediate stages in the formation and growth of particles.

6.4 Characterization of QDs Films

6.4.1 Morphology of Si QDs films

Morphological properties of deposited films are important for the transport properties of a layered material and for their integration in application devices. This is especially true for nanoparticles, for which the conduction of electrical charges must happen across interfaces between particles, and surface states may act as efficient trap states making conduction inefficient. A desirable synthesis apparatus must be able to have good control over the thickness and morphology of deposited layers.

In this work, the thickness and morphology of NPs films are studied as a function of stage scanning speed, bias of the substrate and deposition time. Here, only the deposition conditions have been changed while only the synthesis conditions leading to crystalline particles (50 ppm SiH_4) have been used, as crystalline Si QDs have a direct application of interest in photovoltaics (see section 6.4.7). The two-axis stage is scanning in a raster fashion following a snake-like pattern (in Figure 6.8 shows one repetition of the process) and can be set at different scanning speeds, extension of the deposition in the two directions, the number of passes *N* and number of repetitions or total duration of the scan. The raster size (*r* in figure 6.8a) depends on the extension in the rastering direction (Δy in figure 6.8a) and N, as $r = \Delta y/N$. To avoid inhomogeneities, the raster size has to be smaller than the physical width of the spray from the reactor (~0.5 mm diameter at a 1 cm height from the substrate in the present case). The figures 6.8a shows an example in which the raster size is bigger than the diameter of the sprayed deposit, some parts of the supporting substrate will remain exposed and the deposition is inhomogeneous. In figure 6.8b the opposite situations result in a homogeneous deposition. In the present case then a raster size of ~1/8 cm has been chosen.

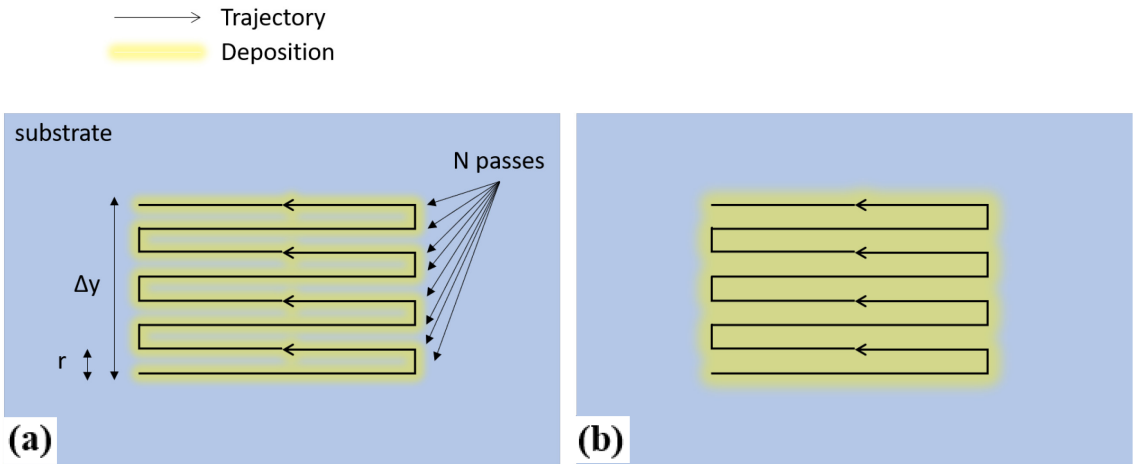

Figure 6.8 - Trajectories of relative motion between the scanning stage and the reactor capillary with indication of the track left by the deposition (yellow) and indication of the quantities of interest. (**a**) Inhomogeneous deposition for a raster size bigger than the size of the deposition track. (**b**) Homogeneous deposition resulting from a raster size smaller than the size of the sprayed track.

The effect of positive bias of the substrate has been explored (as particles are supposed to be negatively charged) to understand if an electric field at the surface of the substrate can affect the morphology of the resulting films. For each condition explored three samples at different deposition times have been explored (5, 10 and 20 minutes). Table 6.3 summarizes the combinations explored.

Substrate bias	Slow scanning (1.2 mm/s)	Fast scanning (13.2 mm/s)
GND	3 samples	3 samples
+ 350 V	3 samples	3 samples
+ 1 kV	None	3 samples

Table 6.3 - Summary of the combinations of sample bias, scanning speed and deposition duration explored. GND is grounded condition for the substrate. The three samples refer to samples produced for different deposition duration, 5 10 and 20 minutes.

The samples produced have been analyzed in an FE-SEM both in top view and in cross-sectional view, to characterize the morphology of films (e.g.: Figure 6.9). The deposited particles form tree-like dendritic structures that can vary in height from 4 µm to 45 µm depending on the deposition parameters. Also, the size and distribution density changes with the deposition parameters. The morphology is therefore far from that of a compact

film and they will be referred as Si QDs films with the understanding that these are highly micro-/nano-structured films. Figure 6.9 compares two extreme cases, a film deposited at slow scanning speed and grounded substrate (left) and a film deposited at fast scanning speed with +1 kV positive bias, both for a 20 minutes long deposition. It is possible to observe that the dendritic formations are smaller and sparser (in-plane view in Figure 6.9a) and finely branched for the former conditions (Figure 6.9a cross-sectional view), while they grow in bigger (in-plane view in Figure 6.9b) more compact clusters in the latter case (Figure 6.9b cross-sectional view).

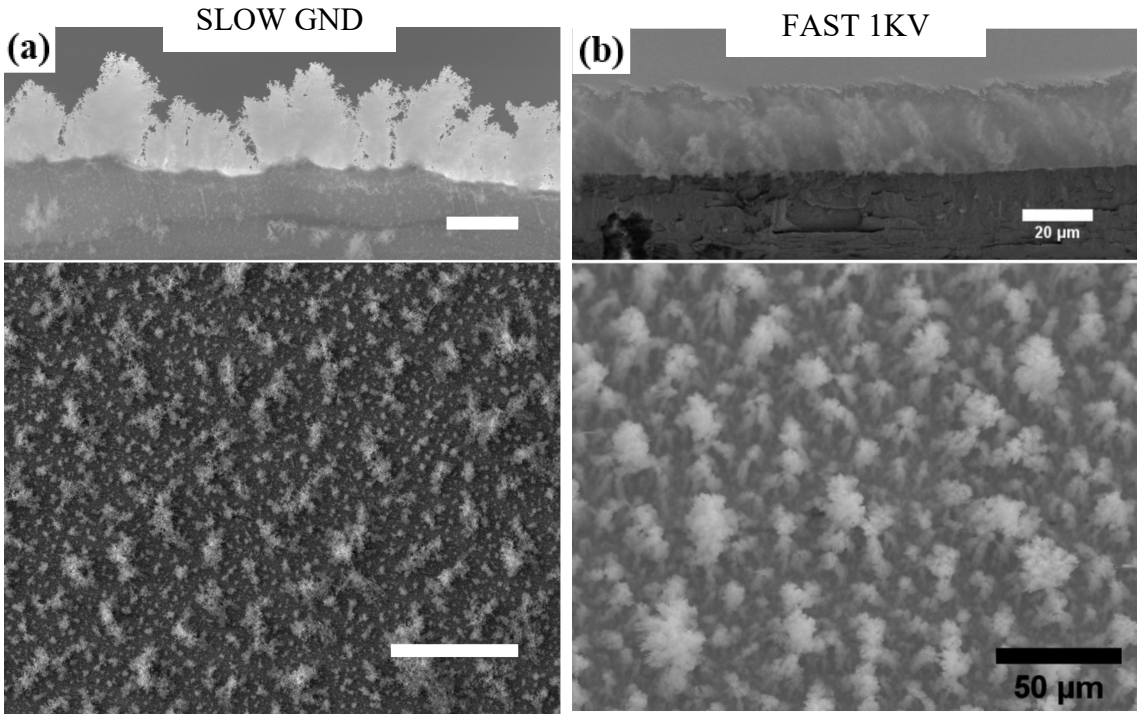

Figure 6.9 - SEM micrographs of the deposition in the two extreme cases (**a**) slow scanning and grounded substrate and (**b***)* fast scanning and +1 kV bias. At the top of each in-plane image there is the relative cross-view. The images evidence different structures formed in the two conditions, in the slow case sparse dendritic formation with very fine branches and in the fast case a more homogenous film of bigger structures.

In order to provide a parameter that could describe the film thickness, A comparison of the cross-sectional micrographs and the deposition parameters is shown for fast scanning speed in Figures 6.11a-i and slow scanning speed in Figures 6.12a-f. In the cross-sectional images, the borders of the deposition are not always clear. In those cases, EDX mapping has been used to identify the border between deposited material and the substrate, an example of which is shown in Figure 6.10.

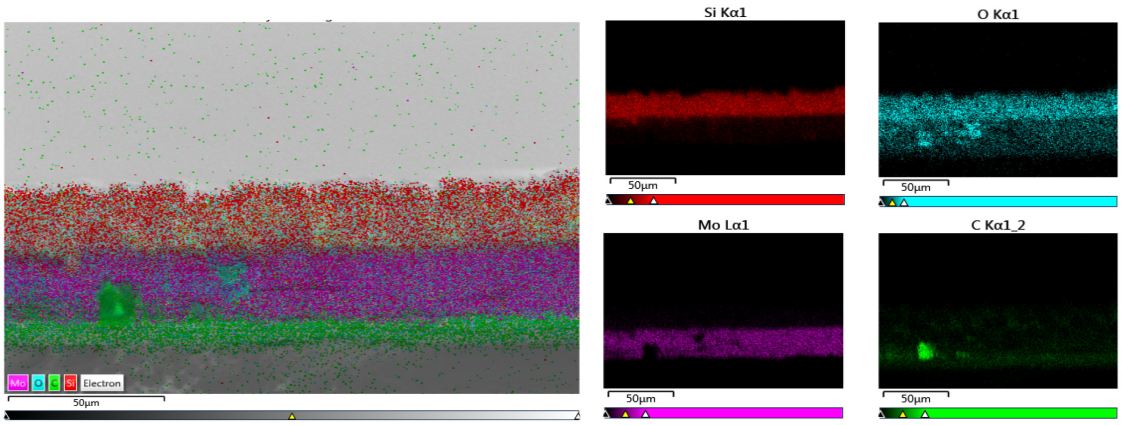

Fig. 6.10 – Example EDX mapping of a cross-view SEM micrograph, clearly showing the boundary between the Mo foil substrate, and the layer of Si particles deposited. This mapping has been used to estimate the film thickness in the cases where the boundary is not clearly visible in electron images.

The comparison qualitatively shows that in general faster scanning speeds and biasing result in progressively more compact films, both in the in-plain dimensions and in height. In particular, regarding the single features of the depositions, the dendritic formations are shorter and denser for higher scanning speeds irrespectively of the biasing (e.g.: comparing Figures 6.11c and 6.12c), while a stronger biasing voltage seems to make the structures more homogeneous in height throughout the sample (e.g.: comparing Figures 6.11c, 6.11f and 6.11i, or Figures 6.12c and 6.12f).

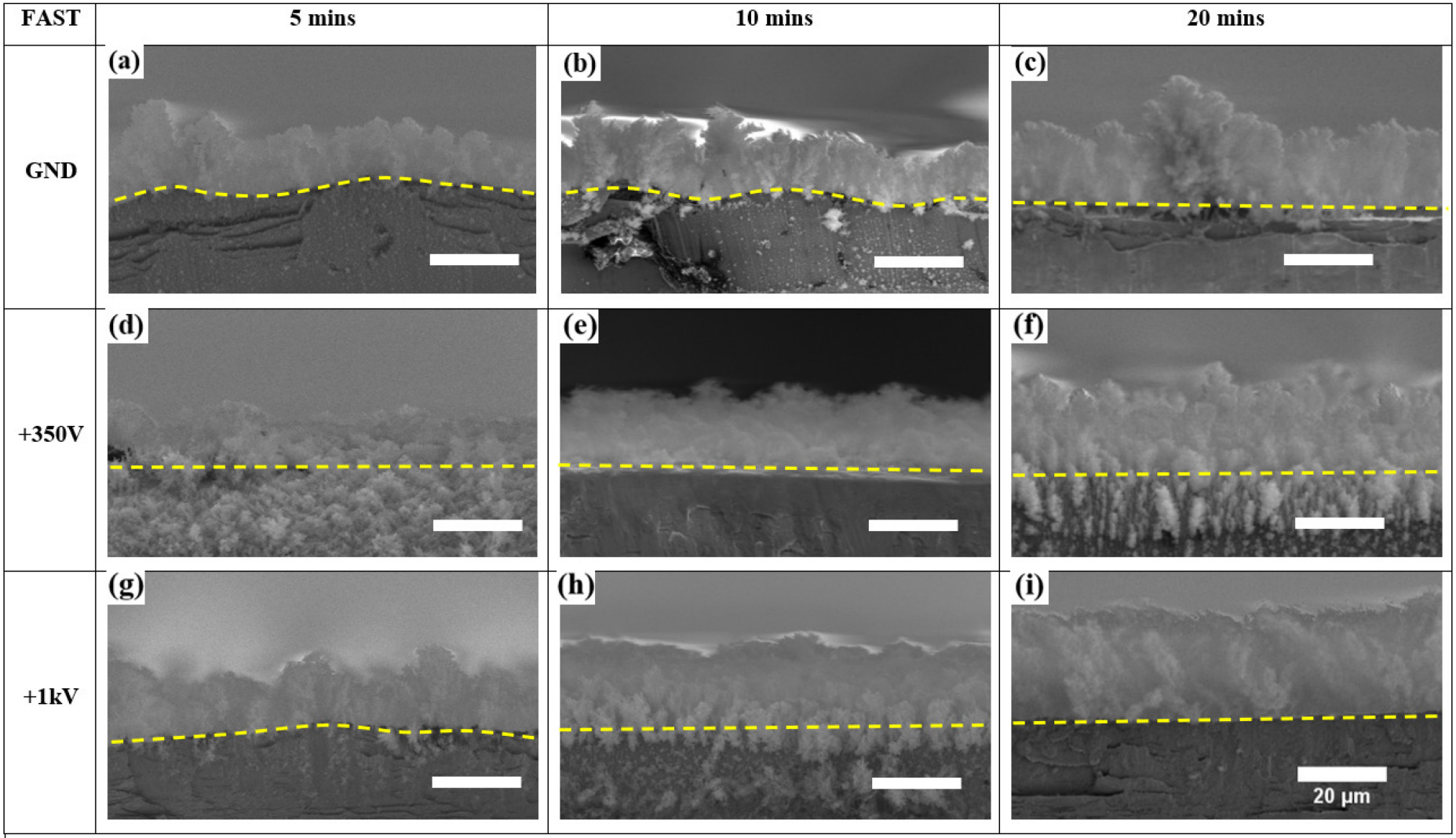

Figure 6.11 - Chart showing SEM Cross-views of all the different samples produced with fast scanning speed, as a function of deposition time and biasing voltage.

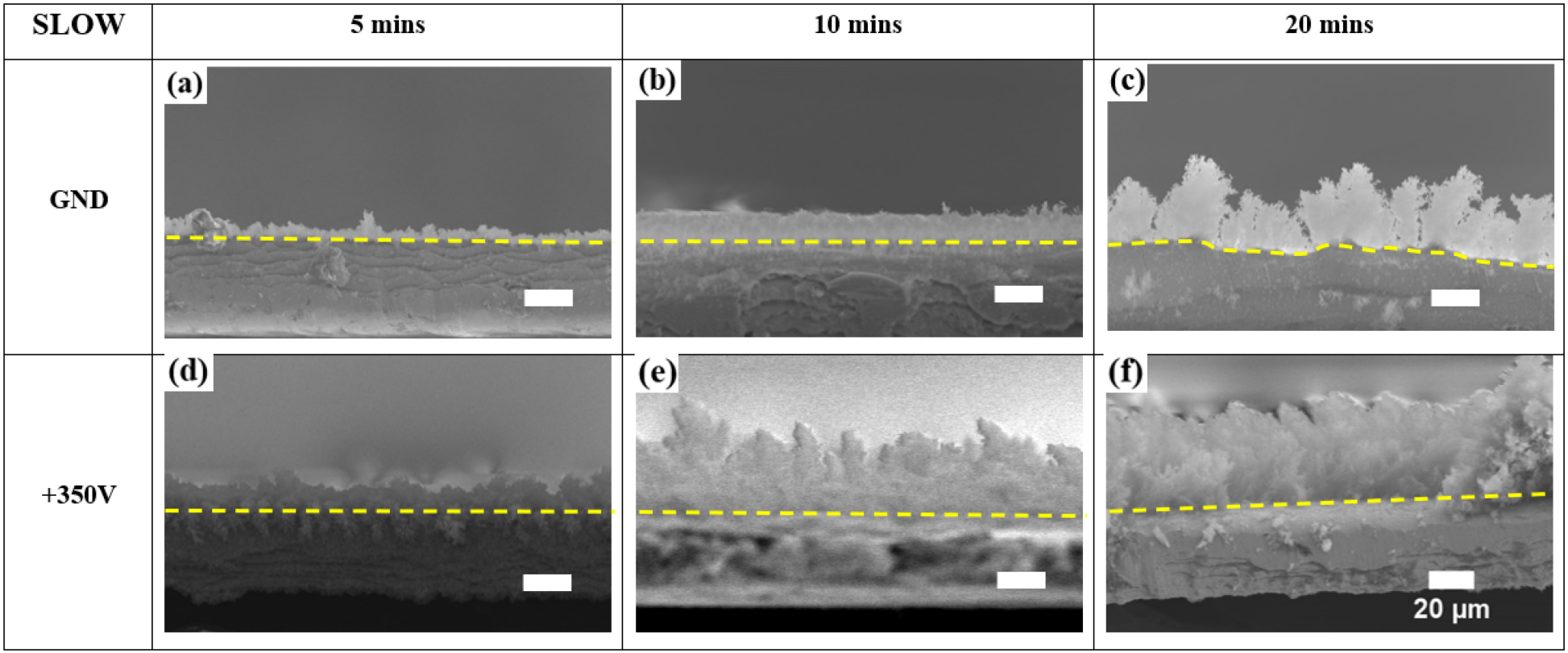

Figure 6.12 - Chart showing SEM Cross-views of all the different samples produced with slow scanning speed, in function of deposition time and biasing voltage.

In order to describe the variations with scanning parameters more quantitatively, the height of the deposition was sampled and measured at regular intervals of 5 µm in the SEM cross sectional pictures. These measurements were then counted in frequency per height interval and fitted with a Gaussian distribution to estimate the mean height of the films and corresponding standard deviation. The standard deviation is then used as a representation of the RMS roughness of the films. The resulting thickness and RMS roughness as a function of deposition time (Figures 6.13a-b and Figures 6.14a-b) show different dynamics.

The mean film thickness (t) increases in function of deposition times in all cases (Figure 6.13a). In slow scanning mode (plots with square symbols in Figure 6.13) after 5 minutes the mean thickness is below 10 µm no matter the biasing voltage and at later times the film growth is strongly affected by the biasing conditions. Grounded substrate conditions result in slow increase in thickness, practically unvaried at 10 minutes (5 µm) and a final 20 µm thick deposit after 20 minutes of processing. A +350 V bias instead provokes a steady increase in thickness which passes for the 8 µm at 5 minutes to 30 µm in additional 5 minutes, after 20 minutes of deposition a 45 µm thick layer is found. The rate of increase of the thickness appears the same in slow scanning mode samples the last 10 minutes of deposition. Fast scanning mode (plots with circles in Figure 6.13) instead gives a 15 µm thick films after 5 minutes of depositing, irrespectively of the biasing voltage. Then the

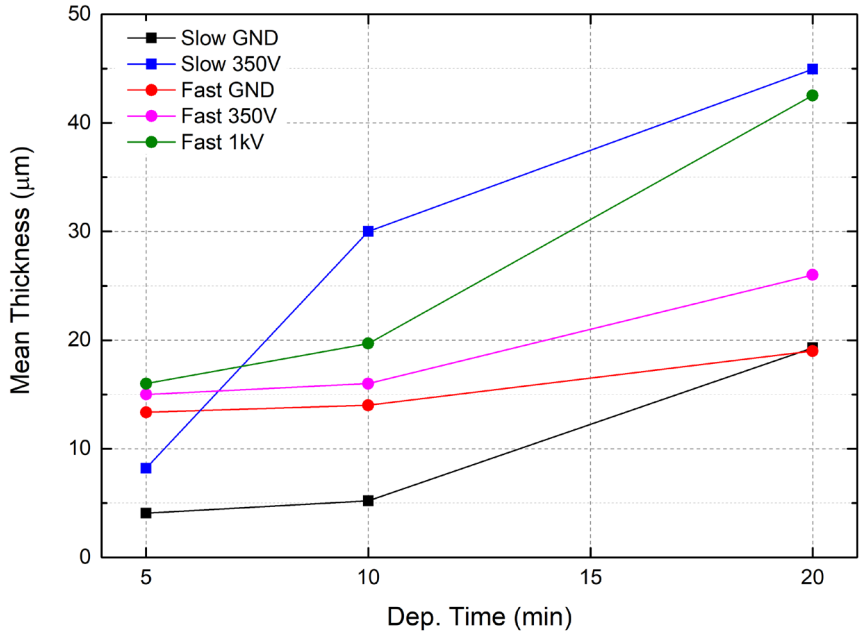

Figure 6.13 – Plots of film mean thickness as a function of deposition time for all the samples produced. Plots with square symbols are all related to films deposited at slow scanning speed, while circles refer to fast scanning speeds. Lines are guides for the eye.

rate of increase of film thickness is increasing in function of the bias. In fact, after 20 minutes of deposition the grounded sample has reached 18 µm, the biased at 350 V 26 µm and the 1 kV biased one 43 µm.

RMS roughness (σ) of films tends to increase at longer deposition times for all the samples, even though with different dynamics depending on the parameters (Figure 6.14). After 5 minutes of deposition almost all the samples have an RMS roughness around 2 µm. In the slow scanning mode (plots with square symbols in Figure 6.14) again the bias has a strong effect at different deposition times. While after 10 minutes there is an apparent decrease in RMS roughness for the grounded samples, for the 350 V biased there is an almost monotonic increase. After 20 minutes they reach respectively 5 µm and 10 µm respectively. For the fast scanning mode (plots with circle symbols in Figure 6.14) the grounded and 350 V biased sample have an apparent decrease in RMS roughness after 10 minutes of processing to increase again at later stages. For the 1 kV biased sample, the RMS roughness always increases and particularly faster in the last 10 minutes of deposition. The final RMS roughness of the samples deposited in the fast scanning mode after 20 minutes of deposition increases with increasing positive biasing voltage, reaching 3 µm, 6 µm and 14 µm at 0, +350V and +1 kV respectively.

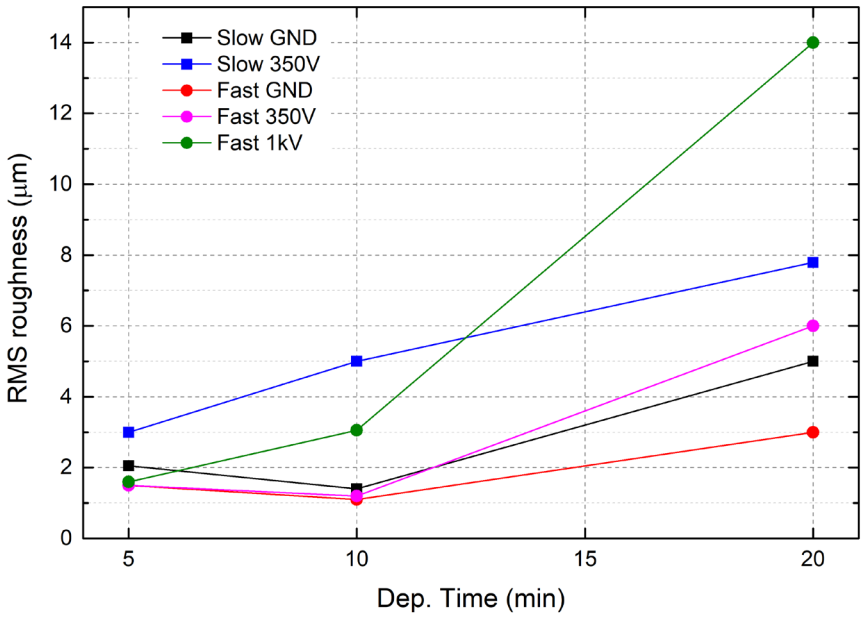

Figure 6.14 – Plots of film RMS roughness as a function of deposition times. Plots with square symbols are all related to films deposited at slow scanning speed, while circles refer to fast scanning speeds. Lines are guides for the eye.

The plot of RMS roughness normalized to each sample mean thickness (σ/t) is shown in Figure 6.15 and summarizes the dynamics of deposition in function of the parameters. Considering that film thickness is increasing in all conditions, a decreasing relative RMS roughness means that the films are growing more in the in-plane direction, as is the case of slow scanned depositions (squares in figure 6.15). Then, applying a positive bias of 350 kV reduces the relative roughness of 10 % to 12 %. Conversely, an increasing relative RMS roughness means that the films are growing more vertically, as is the case of fast scanned depositions (squares in figure 6.15). In this regime the highest bias tested (1 kV) resulted in the monotonic increase of relative RMS roughness, while for the grounded sample and the lower biased one (350 V), it first decreases and then increases. The relative RMS roughness after 20 minutes of processing is higher for higher biases.

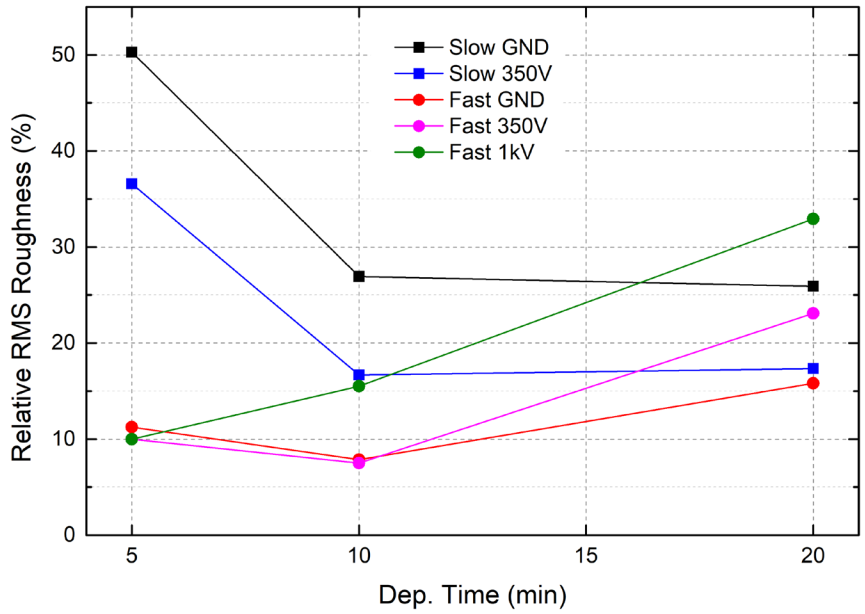

Figure 6.15 – Plots of film RMS roughness as a function of deposition times in terms of fraction of the total film thickness. Plots with square symbols are all related to films deposited at slow scanning speed, while circles refer to fast scanning speeds. Lines are guides for the eye.

Generally compact films are needed to have better interfaces with other materials, as well as a reasonable ability to control the film thickness. This implies that small RMS roughness are wanted, and possibly slowly monotonic increases in thickness as this determines a better controllability of final film thickness. Thus, as a result of this analysis, the best conditions are found to be by fast scanning without applying any voltage (red line with circles in Figures 6.13, 6.14 and 6.15).

6.4.2 Composition and surface

XPS and ATR-FTIR techniques have been used to characterize chemically films of the Si QDs produced for two distinct experimental conditions, labeled according to the SiH_4 concentration 50 ppm and 200 ppm, that correspond to samples with fully crystalline and fully amorphous nanoparticles respectively. In general, both techniques are sensitive to the surface of materials and a typical escape depth of photoelectrons is in the order of 10 nm while the evanescent waves of attenuated total reflectance FTIR penetrate for 1 μm in the sample materials. In this case, though, the size of particles is much smaller than the region scoped by the techniques and the results represent an average over the volume of many nanoparticles, hence their average chemical composition and surface groups respectively.

The photoelectron spectra in the Si 2p region are shown in Figures 6.16a-b, along with a deconvolution of the peaks in the different oxidation states of Si. The non-zero oxidation states (1+ to 4+) are associated with the different forms of Si-O bonds (4+ is the stoichiometric SiO_2), and their binding energy has been set at a fixed binding energy shift (ΔE_B) shift of 0.95 eV, 1.57 eV, 2.56 eV and 3.82 eV from the elemental peak at 99.4 eV associated to Si-Si bonds. It is observed that the amorphous sample (Figure 6.16b) shows a small shift of the curve peak to higher binding energies (100.3 eV vs 99.8 eV) in respect to crystalline Si (Figure 6.16a), which can be readily associated with a higher initial degree of oxidation. The deconvolution of peaks though, estimates a more significant contribution of higher oxidation states in the crystalline samples. The quantification of relative amounts of species through peak area analysis (Figure 6.16c) estimates respectively 50 $\%_{at.}$ and 35 $\%_{at.}$ of elemental Si for 50 ppm and 200 ppm SiH_4 samples respectively. It is likely that the most part of the oxidation comes from the exposure of samples to atmosphere and not from the synthesis process, as supported by TEM analysis of colloids (section 6.3.1) and other experiments presented further.

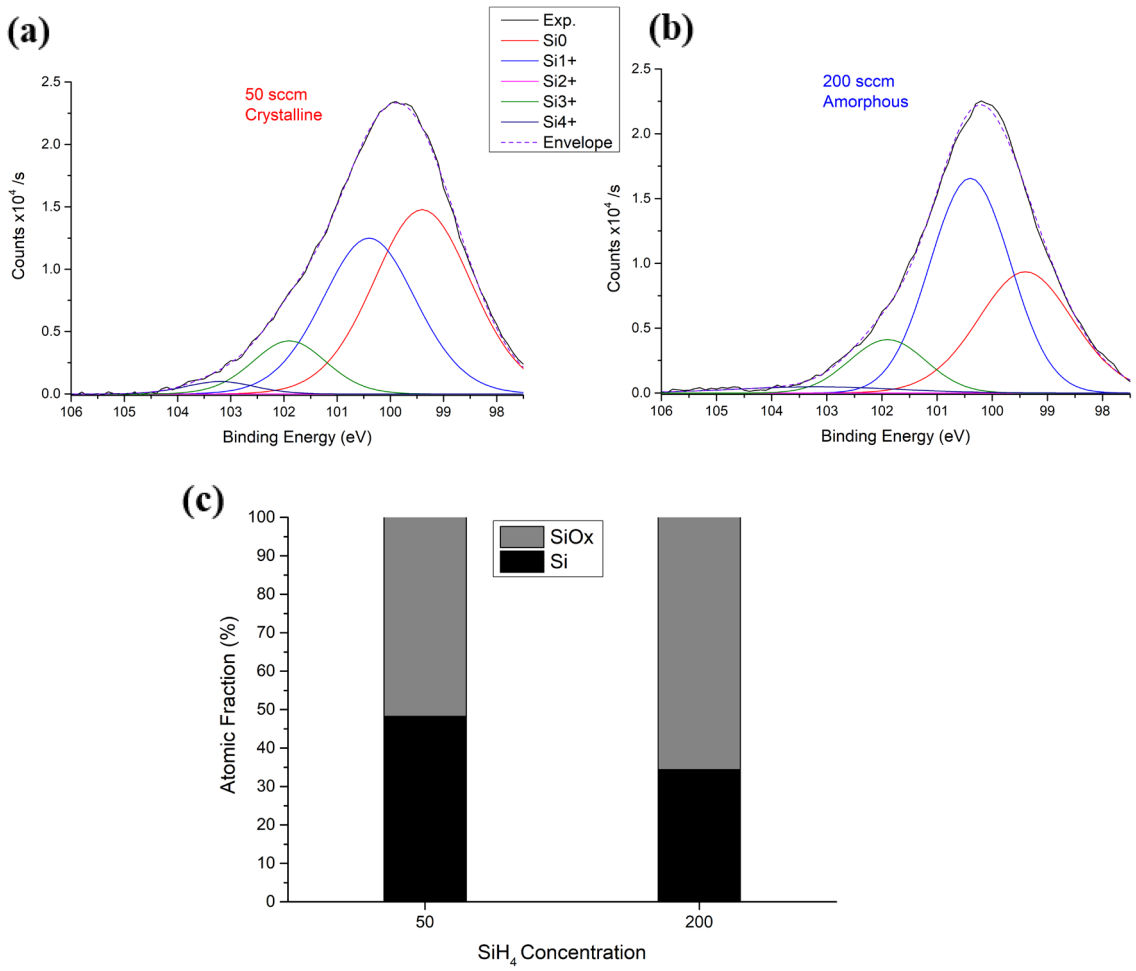

Figure 6.16 - Deconvolution of XPS Si 2p signal into components relative to the different oxidation states of Si atoms for the samples (**a**) crystalline, 50 ppm SiH_4 and (**a**) amorphous, 200 ppm SiH_4. (**c**) Estimated atomic percent of Si and O from peak area ratios for the two samples.

Further details on the chemical composition of the Si QDs were produced by FTIR analysis. Figure 6.17 displays the FTIR spectra of Si QDs produced using the indicated SiH_4 concentration in the plasma. In the two selected regions of the infrared spectrum shown in figure 6.17, it is possible to observe the vibrations that correspond to Si-O and various Si-H_x bonds. In particular, the region near 900 cm^{-1} is associated with bending and wagging modes of Si-H bonds and the absorption band at ~1075 cm^{-1} is typical of Si-O-Si stretching mode (figure 6.17a). The latter peak has very strong absorption cross section and therefore the low absorbance (lower than the Si-H_x peaks) is evidence of a small level of oxidation in the region probed by ATR-FTIR. The peaks at 783 cm^{-1}, 862 cm^{-1}, 902 cm^{-1} have been identified respectively with the bending, symmetric deformation, degenerate deformation of Silicon trihydride bonds (SiH_3) and stretching mode. The shoulders at 845 cm^{-1} and 890 cm^{-1} with the Silicon dihydride (SiH_2) wagging

and scissoring modes [40,41]. The region between 2000 cm^{-1} and 2300 cm^{-1} is instead the locus where SiH_x stretching modes are found (figure 6.17b), here some peaks and shoulders can be identified, especially for the fully amorphous sample (200 ppm) which show a stronger absorbance. The peak at 2136 cm^{-1} is commonly associated with SiH_3 stretching mode, while the shoulders at 2080 and 2110 cm^{-1} can be identified with the modes of SiH and SiH_2 [42]. Shoulders at 2180 cm^{-1} and 2250 cm^{-1} can be identified with O_xSi-H species. These are usually present in hydrogen-terminated silicon as the back-bond oxidation mechanism is the most common pathway to oxidation against the stronger Si-H bonds;[41] this will be discussed in more details in the next section devoted to the study of oxidation kinetics.

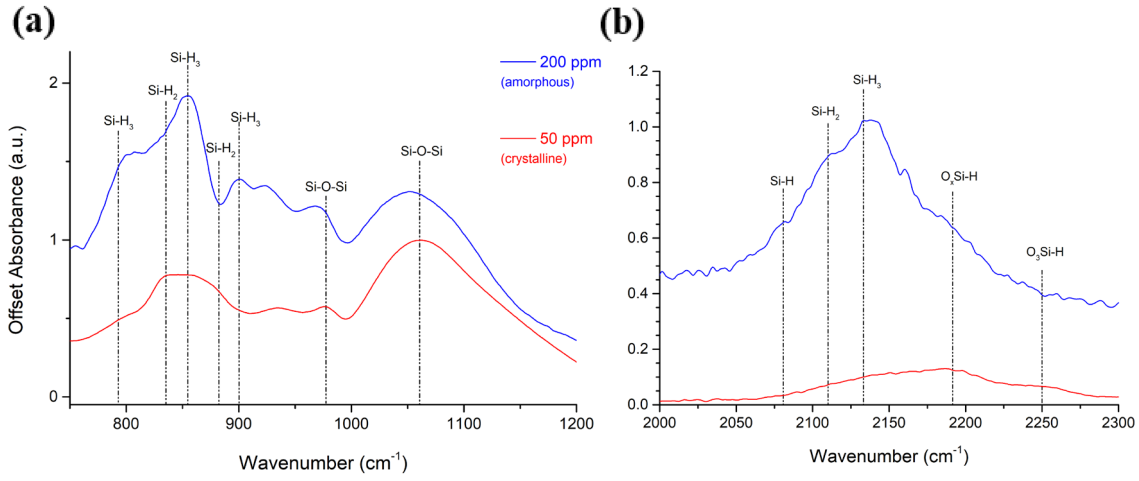

Figure 6.17 - Fourier transform infrared (FTIR) spectra of Si QDs for the different precursor concentrations in the two regions of interest for Si-related species (**a**) bending and wagging vibrations region for Si-H_x bonds and (**b**) stretching vibrations region. The dashed lines indicate the identified vibrational transitions pertaining to Si-H_x varieties and oxygen-bonded species described in the text. While the analysis of these spectra has been done in the context of this study, the measurements on ATR-FTIR were performed by a collaborator in relation to a previous study.[26] The samples were produced in the same conditions, and the resulting QDs were identical according to TEM.

In general, comparing the FTIR absorbance spectra it is possible to note that the intensity of SiH_3 peaks becomes significant for Si QDs synthesized using high precursor concentration (200 ppm) which corresponds to amorphous samples, while it is negligible for lower concentrations when particles are crystalline. This suggests that whenever some amorphous material is present, particles become partially hydrogenated due to hydrogen incorporation within the QDs.[18] Alternatively, different ratios of SiH_4/H_2 during the plasma synthesis process may influence the balance of hydride bonds on the particles surface. This is because desorption of di- and tri- hydride species or the abstraction of H

from the surface Si-H_x bonds can be promoted by atomic hydrogen in the plasma or higher particle temperatures.[43] This comes in favour of the more stable monohydride bonds. In the present case this could happen for the synthesis conditions that produced crystalline particles, as the concentration of H_2 in the plasma is the same and the concentration of SiH_4 is lower (in respect to the conditions to obtain amorphous particles), hence a higher H_2/SiH_4 proportion.

6.4.3 Oxidation behavior of Si QDs films

When QDs are deposited in films, the oxidation process can also be affected by the film morphology whereby buried particles may be less exposed to environmental factors such as humidity. To get a deeper understanding of the oxidation process, a depth-resolved oxidation study of the particles films has been conducted. The experiment consists in acquiring successive high-resolution XPS spectra of the Si 2p region over different days during which the samples are exposed to atmosphere, thus allowing them to oxidize spontaneously. Depth analysis is being accomplished sputtering the film surface with an energetic Ar^+ beam (2 kV) and probing the photoelectron spectra at successive steps. A rigorous determination of the sputter rate would require accurate information on the film morphology and density of the area being sputtered, which are not available. An approximate figure has been estimated through geometrical considerations and the calibrated sputtering rate of the instrument. The instrument estimates for the Argon beam to sputter 1 nm/s on a calibrated tantalum oxide target (Ta_2O_5, density 8.2 g/cm^3). Ignoring the effects of roughness and ion channeling in crystals, sputtering rates depend on beam energy, angle of incidence of ions and mass of the target. In the same beam conditions in respect to the calibration value (in terms of energy, angle of incidence and size of the spot) the sputtering rates scale with the ratio of densities of the material in respect to the calibration material. In the present case particles are imagined as a random packing of spheres, for which the volume fraction is 64% (for a regular close-packed lattice would be 74%).[44] Hence, an average density for the film of Si QDs is estimated as 64% of the Silicon density (2.329 g/cm^3), equal to 1.49 g/cm^3. The approximate value of sputtering rate is then obtained by multiplying the calibration value for the ratio of densities $1 \cdot (8.2/1.49)$ nm/s, thus estimated to be 5.5 nm/s. Each sputtering step in the present experiments last for 5 seconds, and the total number of steps is 15. Hence, in the following spectra the “below surface” conditions will refer to a layer at approximately

400 nm below the topmost unsputtered surface. The spectra obtained for the fully crystalline and fully amorphous samples as a function of time are shown in figures 6.18a-d, where the different oxidation states are indicated.

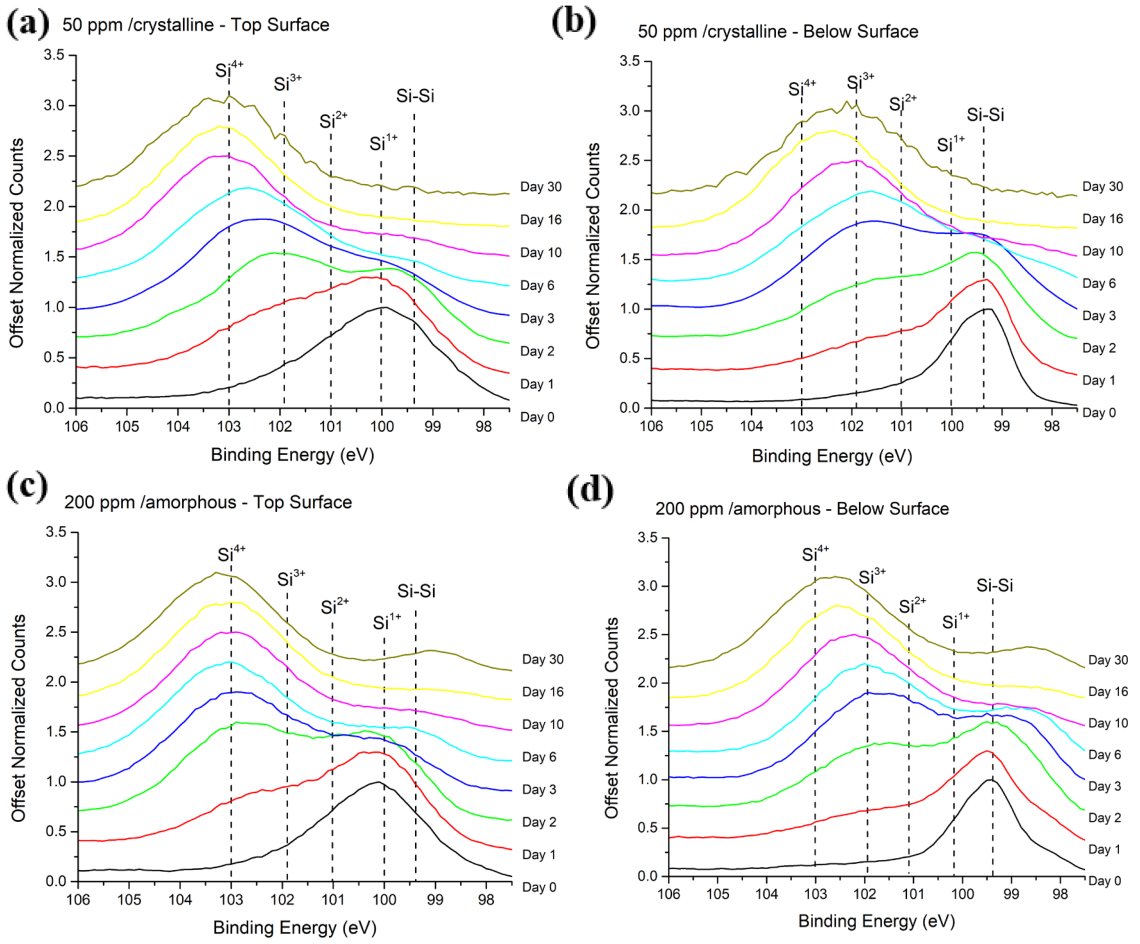

Figure 6.18 – High resolution XPS spectra in the Si 2p region for the top surface (**a**) and (**c**) below the surface (**b**) and (**d**) as a function of the days passed from the synthesis (day 0), to study oxidation as a result of exposure to ambient air. (**a**) and (**b**) refer to the experimental conditions that produced fully crystalline particles (50 ppm SiH_4) while the (**c**) and (**d**) correspond to the conditions for fully amorphous particles (200 ppm SiH_4). The dashed vertical lines correspond to the binding energies assigned to various oxidation states of Si 2p photoelectrons.

Spectra below the surface acquired the same day of the synthesis (day 0 in Figures 6.18a-d) show the center of the Si 2p peak shifted to lower binding energies and a smaller width of the peak in respect to the surface layer, for both crystalline and amorphous films. This is a clear indication that the particles on the surface layers are more oxidized, as a result of exposure to atmosphere. In addition, the amorphous samples in the spectrum below the surface (Figure 6.18d) has an additional tail at lower binding energy. With passing days of exposure to atmosphere all the spectra in Figure 6.18 show a modification of the peaks in shape and intensity. It is generally understood, by comparing the spectra with the

tabulated values of binding energies for different oxidation states of silicon (dashed lines in Figures 6.18a-d), that oxidation of the films is proceeding by progressively increasing the number of oxygen bonded silicon atoms, in respect to the ones bonded to other silicon atoms. By the 30th day of exposure the Si 2p peaks maxima in the surface layer (Figures 6.18a and 6.18c) coincide with the binding energy assigned to stoichiometric SiO_2. The spectra below the surface (Figures 6.18b and 6.18d) at the same 30th day after the synthesis show maxima at lower binding energy in respect to the surface ones. This is probably the result of incomplete oxidation. Moreover, at this stage the amorphous samples both in the top surface and below (Figures 6.18c and 6.18d) show a residual peak at 98.5/99 eV, which is in correspondence with the additional tail observed in the amorphous spectrum the same day of the synthesis below the surface (day 0 spectrum in Figure 6.18d). By a qualitative study of the spectra in Figure 6.18 it is possible to conclude that as the top layers have a bigger proportion of particles exposed to air, there is an increased chance for particles to interact with water vapors hence, in the short term, oxidize faster than the layers below the surface, irrespectively of the atomic structure of particles.

To understand if there is any quantitative difference in the oxidation dynamics between amorphous and crystalline films, a deconvolution of surface spectra in terms of the assigned peaks and in function of days of exposure to atmosphere has been performed. The result in shown in Figures 6.19a-b. This analysis has been done by deconvoluting each spectrum at different days in the various components, and then calculating the area below each components curve. The atomic fraction of silicon and silicon oxides (Figure 6.19) is obtained by summing all the areas relative to oxides and taking the ratio with the area of the elemental silicon peak. Even if starting with an already higher degree of oxidation at day 0, the fraction of oxides for the amorphous samples are above 90% already at the third day of exposure, while the crystalline one is approaching 90% of oxides at the 6th day of exposure. To show more clearly the different in kinetics, an additional curve obtained by delaying the abscissas of the 200 ppm curve by 0.7 days is presented in figure 6.19 (dashed line). This is done to cope with the different initial oxidation degree of the crystalline and the amorphous sample, as if they started with the same oxidation degree at the same time. It clearly shows that amorphous samples are oxidizing faster for the same exposure time to atmosphere. However, after a month of exposure to air, the oxidation for amorphous particles seems to have stopped at 95% oxides, as the relative curve in Figure 6.19 is flattened and keeps a constant value for the

last 15 days of the experiment. The curve relative to crystalline samples instead still shows a slow increasing trend after a month.

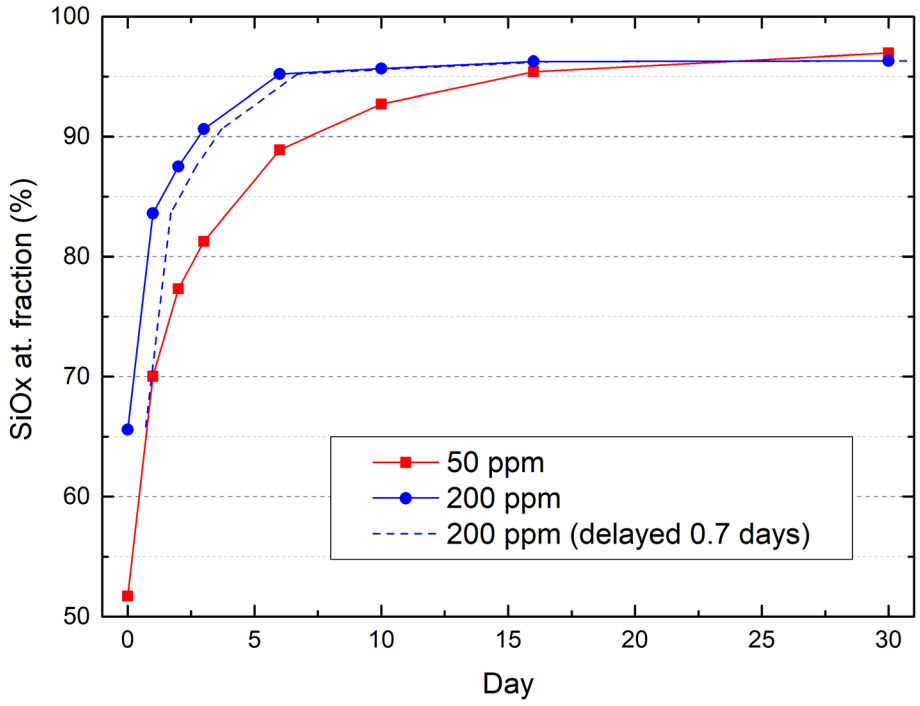

Figure 6.19 – Atomic percent of all the oxides in respect to elemental silicon for the crystalline and amorphous samples at the surface, as a function of the days passed from the synthesis. The data points are obtained by taking the ratio between the cumulative areas of peaks pertaining to oxides and the area under the elemental Si peak. Lines are guides for the eye. The dashed line represents a delay applied to the amorphous sample to show the different kinetics despite the different initial oxidation.

In the collaborative study[26] the stability of crystalline Si QDs was also studied over a period of 30 days through FTIR measurements. The study observed that Si-H_x bonds, evaluated in the FTIR region of stretching modes (region in figure 6.17b) are replaced over time by oxygen back-bonds (O_xSi-H in in figure 6.17b) and concluded that these nanocrystals, while being H-terminated, tend to oxidize slowly through the insertion of oxygen and the reaction with water vapour (e.g. from humidity in air). In fact, the Si-H bond is stable up to 500 °C in atmosphere and the oxidation process is mediated by the formation of Si-OH bonds, either back-bonds or from the reaction of water vapor with Si-H bonds on the surface.[26,41,45] Further surface reactions with water vapor and condensation among surface OH species eventually bring full oxidation of the surface, via the formation and desorption of water, finally leaving a network of Si-O-Si bonds.

In this study it was found that films of amorphous particles have shown to have a higher content of hydrogen bonded to Si atoms as trihydride and di-hydride species (Figure 6.17), a slightly higher degree of oxidation at the beginning of the XPS measurements (Figure 6.16) and tend to oxidize faster (6.19) than crystalline particles. In addition, the oxidation seems to be saturated at 95% after a month of exposure to air. Conversely, films of crystalline particles show a lower content of trihydride and di-hydride species as to FTIR (Figure 6.17), have a slightly lower degree of oxidation at the beginning of the XPS measurements (Figure 6.16) and tend to oxidize slower in respect to amorphous samples. Though they are still slowly oxidizing after a month of exposure to air over the oxidation degree attained by the amorphous particles at that stage.

The different oxidation kinetics have many possible explanations which are now discussed in light of some notable experimental studies.[42,43,46] The assumption made at this point is that the synthesis process produce mostly non-oxidized hydride-terminated particles both in the crystalline and amorphous case. This assumption is supported by the weak Si-O-Si vibrations (Figure 6.17a) in ATR-FTIR (which is a more bulk technique than XPS) and the XPS spectra below the surface (Figures 6.18b and 6.18d).

It has been speculated that a higher global H-coverage on the surface protect the material from oxidation, as it is more effective in preventing oxygen insertion in the lattice, slowing down the oxidation process.[42] In the present study, even though there is an initial higher IR absorbance and different varieties of Si-H bonds are present for the amorphous samples (Figures 6.17a-b), the amorphous samples show a higher initial degree of oxidation and faster oxidation kinetics. Hence, this explanation can be excluded.

Other studies indicated that the optimum conditions to protect particles from oxidation are not to have an higher absolute coverage of Hydrogen, but different species of SiH_x bonds (whether mono-, di- or tri- hydrides) have a different impact on oxidation kinetics; [43] the authors claim that mono-hydride species are supposed to be more resistant to oxidation given their higher binding energy, hence slowing down the oxidation process. This explanation is compatible with the experimental results in this study.

Hydrogen incorporation in amorphous particles can have two effects which result in the same faster kinetics: i) introduce stress in the Si lattice, in this context oxidation reactions are energetically convenient to release the stress[46] and should set in faster than the crystalline case; ii) an oxidation process from surface inward towards the core always finds the same bonds that need to be oxidized, i.e. some Si-Si and some Si-H bonds that

appears to be distributed equally throughout. In the crystalline particles, the process is different because there are two phases, the first that relate to surface and therefore Si-H and Si-Si bonds and the second where it would find only Si-Si bonds. Hence, hydrogen incorporation in amorphous particles can either both the higher initial oxidation degree and the faster kinetics in respect to crystalline ones.

The experimental results presented in this study do not permit to distinguish if the faster kinetics of the amorphous particles are due to different hydride species or the hydrogenation in the core of the particles. However, in a previous study which used a similar process,[18] the shift of bandgap for amorphous QDs of different size was explained by a different degree of hydrogenation in line with modeling results. Thus, it is likely that higher degree of hydrogenation of amorphous particles is responsible for the different oxidation kinetics also in this case, given the similitude between the reactors and the processes involved.

6.4.4 Estimation of near-E_f electron levels

In order to build the energy band diagrams of the Si QDs films which are important for integration of films in devices, the valence band maximum (*VBM*), fermi level (E_f) and bandgap (E_g) of the samples are estimated through different measurements. Specifically, fermi levels are estimated through ultraviolet photoemission spectroscopy (UPS) and a Kelvin Probe (KP), valence band edge is estimated through UPS, x-ray photoemission spectroscopy (XPS) and air photoemission spectroscopy (APS), the energy bandgaps are estimated through ultraviolet-visible spectrophotometry (UV-Vis) and surface photovoltage spectroscopy (SPS). The experimental procedures and the relative analytic methods are described more in detail in chapter 5, thus herein the experimental results for Si QDs films are presented and discussed functionally to the estimation of energy band diagrams. In this context also a sample with 100 ppm SiH_4 which formed films of particles in mixed crystalline and amorphous phases is considered.

UPS have been used to obtain the absolute value of the Fermi Level and the VBM of the samples, the spectra acquired and the values of interest for the analysis are shown in Figure 6.20. The three spectra show an almost featureless photoemission onset, although the threshold binding energies (*BE*) for photoemission happen at slightly different values. However, the cutoff energy for secondary electrons are at different values and the overall

width of the photoemission spectra is increasing for samples with increasing Silane concentration. The Fermi level can be extracted from the difference between the cut-off *BE* ($E_{cut\text{-}off}$) and the energy of the exciting photons, i.e. $E_F^{UPS} = E_{cut\text{-}off} - 21.22\ eV$. Decreasing values of E_f in function of increasing SiH_4 concentrations are found, specifically 4.7 eV, 4.3 eV and 3.5 eV respectively for the 50 ppm, 100 ppm and 200 ppm samples. The *VBM*s are calculated from the *BE* values relative to the onset of photoemission and the estimated E_f, as $VBM^{UPS} = E_F^{UPS} - E_{on\text{-}set}$. The estimated value of VBM are 5.9 eV, 6.2 eV and 5.7 eV respectively for the 50 ppm, 100 ppm and 200 ppm hence no clear trend with SiH_4 concentration.

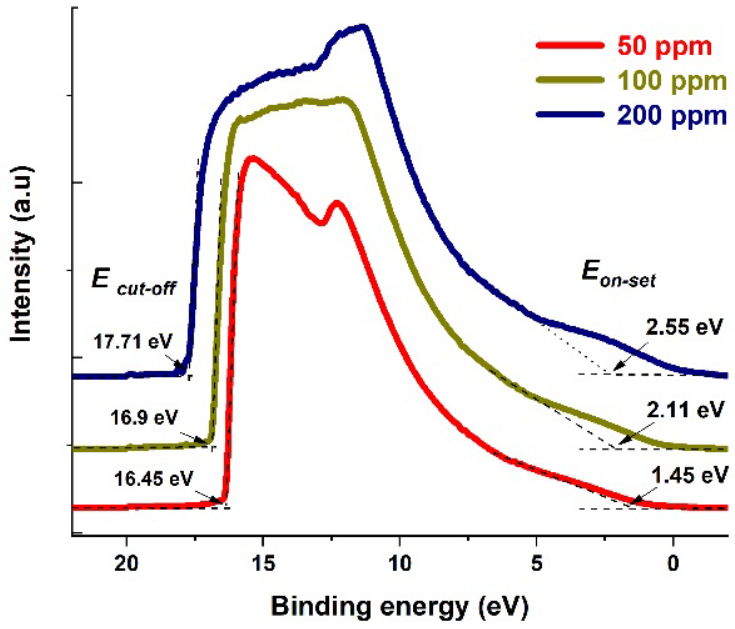

Figure 6.20 - UPS spectra of the three samples for different SiH_4 concentrations under study, the 50-ppm resulted in films of crystalline particles, 100 ppm mixed crystalline and amorphous particles and 200 fully amorphous particles. The UV source for this experiment is a He(I) emission at 21.22 eV. The dashed lines represent the baselines and fitting lines used for the extraction of parameters.

XPS in the valence region has been used to estimate the difference between the Fermi level and the VBM, even though with a worse energy resolution in respect to UPS. The spectra acquired with the relative analysis are shown in figure 6.21. The values of VBM-E_f are extrapolated by fitting lines in the higher BE part of the photoemission onset. Extracted values are 1.65 eV, 2.09 eV and 2.25 eV for the 50 ppm, 100 ppm and 200 ppm SiH_4 respectively. These values are different from the onset values measured for UPS but follow the same trend in function of SiH_4 concentration.

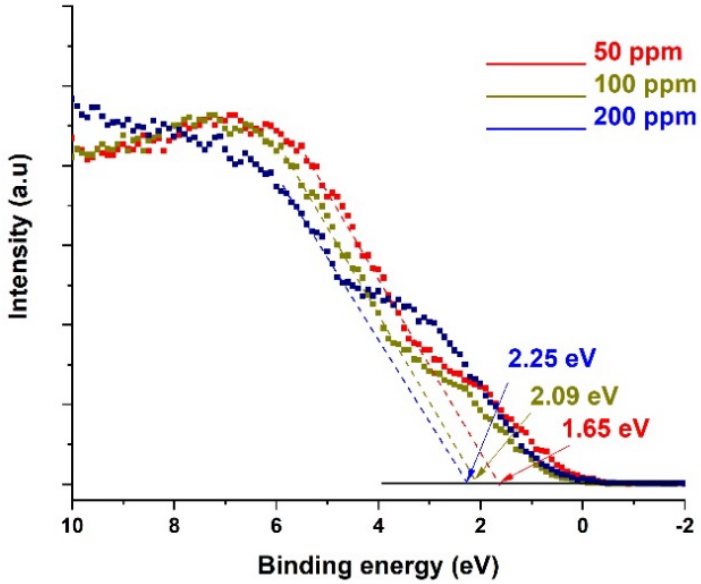

Figure 6.21 - XPS spectra in the valence band region for the three samples for different SiH_4 concentrations under study, the 50 ppm relate to films of crystalline particles, 100 ppm to mixed crystalline and amorphous particles and 200 to fully amorphous particles. The dashed lines are the linear fits used to extract VBM-E_f.

The air photoemission system (APS) is also used to extract the VBM edges, by measuring the photoemission current and extracting a linear fit of the onset from the cube root of the APS signal. In figure 6.22 the fitting of the analysis for these spectra is shown. The estimated values of VBM are 5.7 eV, 6.1 eV and 5.8 eV respectively for the 50 ppm, 100 ppm and 200 ppm SiH_4 samples. Values differ in magnitude in respect to UPS values but show the same trend for samples synthesized with different SiH_4 concentrations.

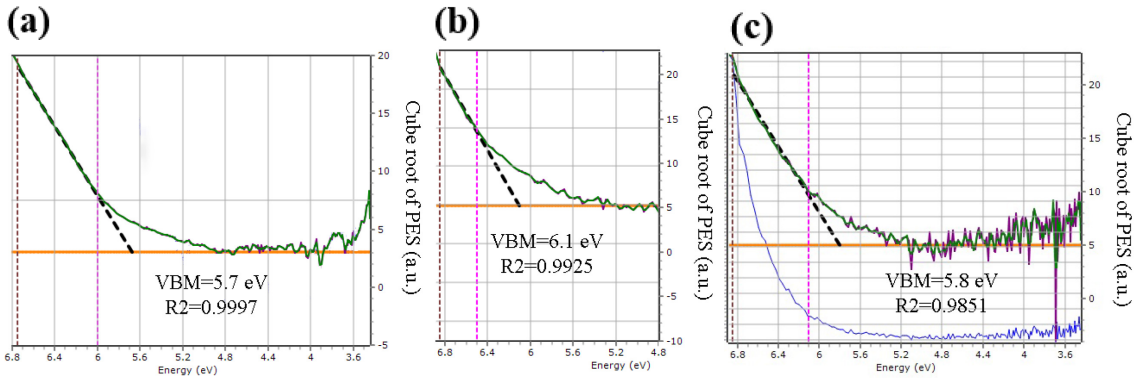

Figure 6.22 - Analysis of air photoemission spectra for the (**a**) 50 ppm (**b**) 100 ppm and (**c**) 200 ppm SiH_4 samples, the intercept of a best-fit of the higher energy part of the cube root of the PE signal permits to estimate the VBM. In the pictures, the baselines considered is shown (yellow line) as well as the fitting window (between the vertical dashed lines). In the spectrum (**c**) the blue curve is the measured photoemission signal relative to the same sample.

In the Kelvin Prove the contact potential difference (CPD) of the Si QDs films have been averaged over a scanned 1 cm^2 area and referenced to the calibrated tip work function (W_{tip} = 4.4 ± 0.1 eV) to extract the fermi levels, the values thus obtained are 6 eV, 4 eV and 3.9 eV respectively for the 50 ppm, 100 ppm and 200 ppm SiH_4 samples.

In order to cross-compare the values obtained by different techniques, values obtained from different techniques are plotted in Figure 6.23 and summarized in table 6.4. Figure 6.23a shows a comparison between the results obtained by KP and UPS for Si NPs films as a function of SiH_4 concentration for the estimated fermi levels. The values obtained from the two measurements show the same trend and similar values, except in one case (50 ppm) whose KP value is higher. The *VBM* estimated by UPS, APS and from XPS values by inserting the Fermi levels obtained with UPS in the measured *VBM-*E_f are shown Figure 6.23b.

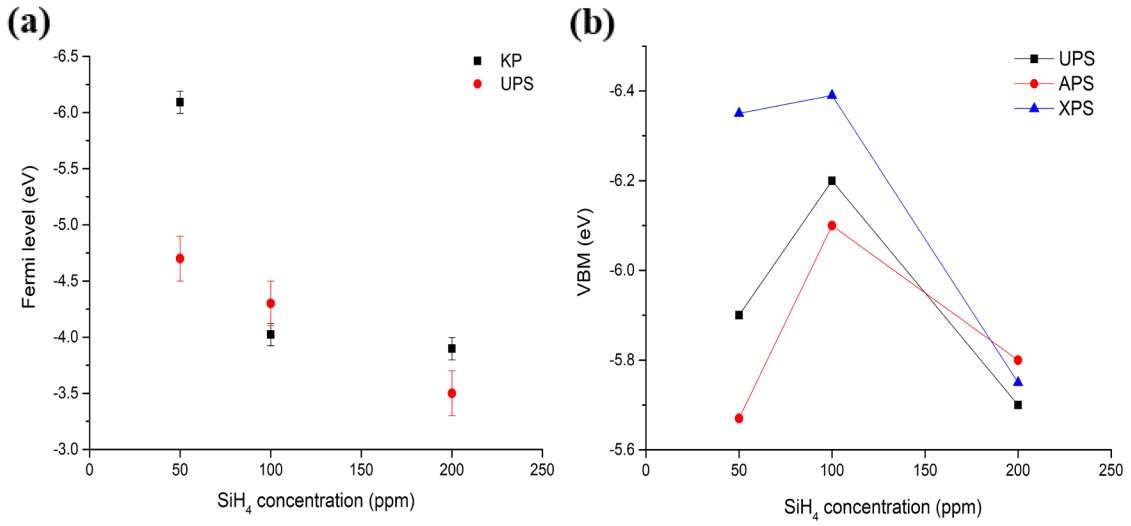

Figure 6.23 - (**a**) Comparison of Fermi level measured with Kelvin Probe and UPS. (**b**) Comparison of VBM values measured (UPS, APS) and calculated (XPS) with different techniques, uncertainties are omitted for clarity and can be found in table 6.4. In both cases the trends are generally conserved, but figures can be different.

[SiH_4] / ppm	Fermi Level / eV		VBM / eV		
	KP	UPS	UPS	XPS	APS
50	- 6.0 ±0.1	- 4.7 ±0.1	-5.9 ±0.1	-6.3 ±0.6	-5.7 ±0.2
100	- 4.0 ±0.1	- 4.3 ±0.1	-6.2 ±0.1	-6.4 ±0.6	-6.1 ±0.2
200	- 3.9 ±0.1	- 3.5 ±0.1	-5.7 ±0.1	-5.8 ±0.6	-5.8 ± 0.3

Table 6.4 - Fermi levels determined from Kelvin probe and UPS measurements with corresponding uncertainties. For the KP values, the uncertainty corresponds to std. deviation of measurements within the scoped area and for the UPS it is mostly due to the spectrometer energy resolution. VBM values determined from UPS and APS with corresponding uncertainties are also reported. VBM from XPS was calculated using the E_f estimated by UPS. Uncertainties correspond to energy resolution for UPS and XPS, and for APS a rms sum of std. deviation relative to the fit.

The comparison shows that discrepancies from different measurements do exist, which in most cases are within measurement uncertainties. Differences even above 0.1 eV can be significant for applications, however it should be noted that the literature seldomly reports a comparison of different measurement techniques and as such these results highlight and underline the difficulties and limitations of current and available measurement methods already discussed in Chapter 5. With the exception for one of the measurements, the Fermi levels show similar values and exhibit the same trend, i.e. the Fermi energy becoming smaller with the particles going from crystalline to amorphous (Figure 6.23a). The value of the Fermi level for the crystalline QDs (50 ppm) stands out and emphasizes the strong surface sensitivity of the KP technique (1-3 monolayers); while stray capacitance originating from inhomogeneities in the film can also impact the measurement, the very large value of the Fermi level is tentatively ascribed here to the impact of even minor surface oxidation. The VBM values also show similar trends (Figure 6.23b) with differences that can be justified by measurement uncertainties, with the exception of the VBM values of crystalline QDs (50 ppm) measured by XPS, which may be due to difficulties in extracting a good and reliable fit to the x-axis due to the limited resolution.

UV-Vis transmission and reflectance spectra were acquired for Si QDs films for the purpose of estimating the energy bandgap for the samples. In a previous study [18] it was already demonstrated that particles produced with this method show signs of quantum

confinement, as the photoluminescence (PL) emission wavelength changes with the particles size in accordance to the laws of quantum mechanics. In addition, in the conditions of fully amorphous particles (200 ppm) it was found that the hydrogen concentration in the admixture at the same time lowers the particles size and affects the bandgap value. Nevertheless, given the weak PL quantum yield for silicon, there is much more interest in the light absorption characteristics and their dependence on size and crystallinity of particles. In figure 6.24 the spectra acquired in the transmittance port of the spectrophotometer (T) and in the center of the integrating sphere (T+R) of the spectrophotometer are shown. For all the samples, the Si QDs exhibit continuous and relatively featureless optical characteristics with only a smooth decrease in the spectra for higher energy light, except the fully amorphous samples which show a longer tail at longer wavelengths.

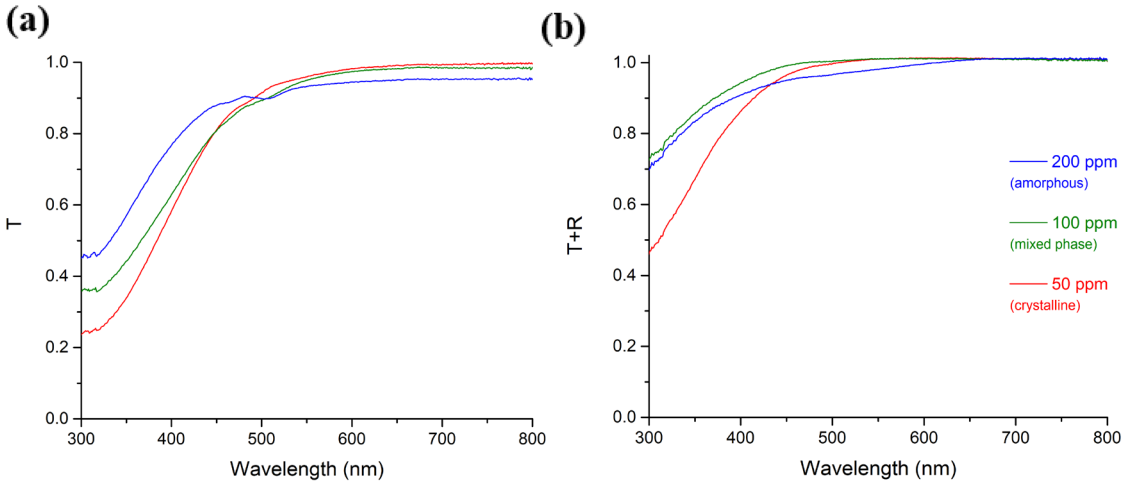

Figure 6.24 - (**a**) Transmission and (**b**) combined Transmission and Reflection spectra of the three samples under investigation, acquired respectively in the front port and in the middle of the spectrophotometers integrating sphere. The spectra are normalized to a quartz cuvette full of ethanol in each respective position.

Bandgap have been extrapolated from the spectra in Figure 6.24 by the Tauc plot method (see chapter 5) assuming an indirect character of the interband transition involved (Figure 6.25a). Films of Si QDs with crystalline particles (50 ppm SiH_4) present a bandgap of roughly 2.5 eV. For SiH_4 concentrations greater than 100 ppm, value at which samples start to have amorphous particles, the bandgap tends to a value of about 2.3-2.5 eV. The surface photovoltage spectroscopy (SPS) technique have been also used to have a qualitative assessment of the energy bandgap, if the mobility of carriers in the material is high enough for carriers to reach the surface of the material. In the present samples, it is observed a detectable surface photovoltage only in the samples with amorphous particles

(100 ppm and 200 ppm SiH_4, Figure 6.25b). This fact is suggesting that charge transport within the layer of amorphous particles is superior with respect to the films of crystalline nanoparticles.[47] The threshold in energy for the appearance of a photovoltage shows similar values as the UV-Vis estimated energy gaps (2.3 eV to 2.6 eV), and the sign of the shift indicates that samples have an n-type behavior.

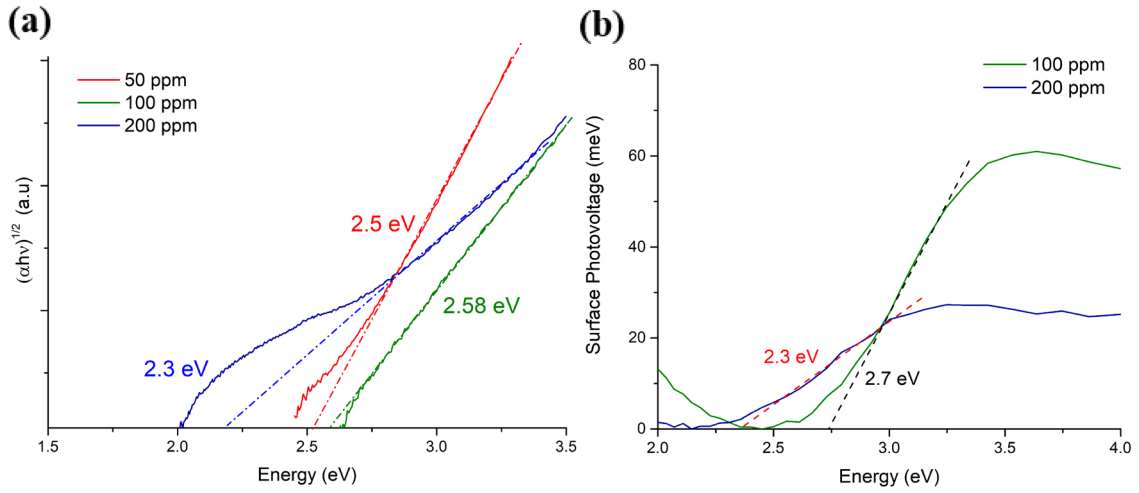

Figure 6.25 - (**a**) Tauc plots with relative best fit lines for the bandgap determination of Si QDs samples. (**b**) SPS spectrum of two amorphous particles-containing samples, showing a good match between the energy threshold to induce a photovoltage and the relative UV-VIS energy gaps obtained with Tauc Plots.

The energy bandgap values obtained for films of crystalline particles (50 ppm) are consistent with literature values of H-terminated Si-QDs in the size range reported (1.8 nm).[48] Instead the bandgaps obtained for films including amorphous particles (100 ppm and 200 ppm SiH_4) are consistent with values measured by other authors for hydrogenated amorphous Si QDS.[18,49]

6.4.5 Energy band diagrams

In this section the results from optical and electronic measurements presented in section 6.4.4 are combined to assess the Energy Band Diagrams (EBD) of the Si QDs films. Following the arguments put forward in the chapter 5, UPS-derived values are used as more reliable both for the determination of absolute Fermi level and for the VBM, under the only assumption of negligible light-induced surface dipole of the films. While the UV-Vis estimated values of bandgaps are used to the purpose. In this context, only the

results for samples with a definite crystalline phase are considered, unless the EBD would represent the junction between two different materials. Thus, only the films obtained for 50 ppm SiH_4 which resulted in only crystalline QDs and for 200 ppm of SiH_4 which resulted in fully amorphous QDs will be treated. The resulting EBDs are shown in Figure 6.26.

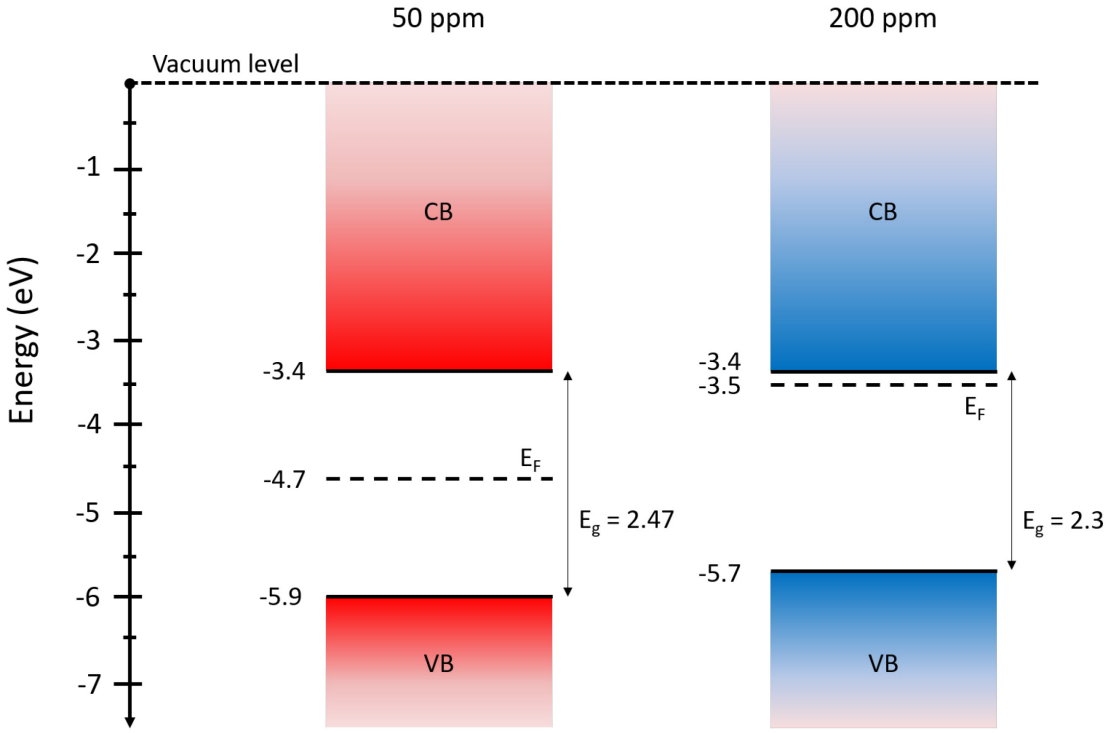

Figure 6.26 - Energy band diagrams obtained combining UPS values for Fermi level and VBM, and energy bandgaps obtained from Tauc plots of UV-Vis spectra for the samples under investigation.

The EBDs estimated show that valence band maxima vary slightly from the crystalline (-5.9 eV) to the amorphous (-5.7 eV) samples. Also, the bandgap has a small variation between the two films considered (2.47 eV vs 2.3 eV). The value of the Fermi level (with respect to band edges) instead has a more important variation between the two samples (+1.2 eV). Overall, the crystalline film as the EBD of a compensated semiconductor, where the E_f lies in the middles of the energy bandgap. Instead the film of amorphous particles shows a strong n-type character, as the E_f lies very near to the conduction band. For nanocrystalline sample the values of fermi level and valence band edge correlate very well with literature values. In fact the work function for intrinsic Silicon is reported between 4.6 eV and 4.8 eV.[50] The value of valence band is generally in agreement with most of the computational studies,[51,52] which report values between 6 eV and 6.4 eV and

the few experimental studies on Si QDs.[26,53] Regarding the amorphous samples, there is no theoretical or experimental study to the authors knowledge on the absolute values of electron levels for amorphous Si QDs to compare the values with. However, the bands of bulk hydrogenated amorphous silicon are expected to be modified substantially in respect to crystalline silicon only at the band edges, due to Si-H bonds and disorder.[54] In this picture, the estimated values of VBM and the derived CBM are very near to the values of crystalline samples. Instead, the value of Fermi level is particularly shifted, difference that could be due to a distinctive distribution of dopant levels in the middle of the bandgap. More investigations need to be done in order to understand the nature of this shift.

6.4.6 Si-QDs as active layer in solar cells

In this section a study mainly performed by collaborators[55] on the integration of Si QDs in photovoltaic (PV) devices is presented, to show the direct integrability of the presented films in working devices. The contribution of the present author was to deposit the film of crystalline particles from the 50 ppm SIH_4 process and estimate the EBD relative to this film in relation to the other materials of the all-inorganic photovoltaic device produced. The particles are directly deposited as a film with the help of the two-axis stage placed 1 cm below the exit orifice of the capillary. The Si QDs act as the active component for the photogeneration of electron-hole pairs. The device structure along with a cross-sectional SEM micrograph of the layered structure is shown in Figure 6.27.

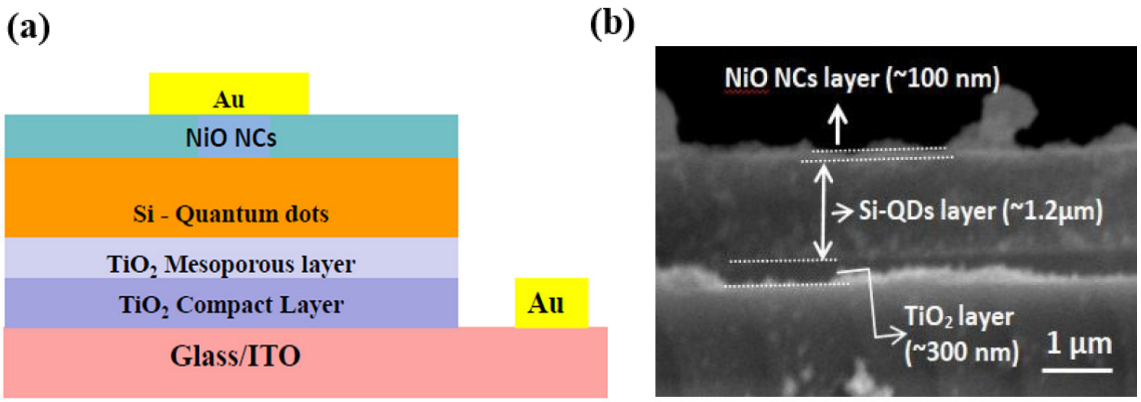

Figure 6.27 - (**a**) Diagram of the layered structure, showing a cross section of the device, the thickness of the real layer is represented in proportion in the drawing. (**b**) Cross sectional image of the device (glass/ITO/TiO2 compact layer/TiO2 mesoporous layer/Si-QDs/ NiO) without metal contact (Au) showing the thicknesses of TiO2, Si-QDs and NiO layers.

The device concept is based on a single active layer (Si QDs) absorbing light and generating electrons and electron-holes pairs, which can be drift to different contacts and sustain a current in an external load. The layers of NiO and TiO_2 serve as selective contacts respectively for electrons and holes blocking the other species. A mesoporous layer of TiO_2 is used also to facilitate the transport of carriers within the device, by increasing the contact area at the interface between the nanostructured Si layer and the TiO_2 film. Gold is used as a back contact while a transparent conductive oxide layer (ITO) is used as the front contact. This device concept is novel in that employs layers of unsupported nanoparticles synthesized with different microplasma techniques, both for the active layer (Si QDs) and the electron-blocking layer (NiO). The demonstration of a rectifying behaviour would be a notable achievement and would demonstrate promising carrier-generation abilities of the active layers and good energy alignment of the different layers. In fact, the bandgap of Si QDs is far from being ideal for the absorption of the full solar spectrum and it is generally understood that charge carrier transport across nanoparticles is limited for unembedded ones.

The following procedure has been followed to build the device:

1. **TiO_2 layers**: deposited on indium-doped tin oxide (ITO) coated glass through a sol-gel technique. A solution of TiO_2 was prepared by mixing Titanium (IV) isopropoxide (1.56 mL), ethanol (18 mL) and triethanolamine (0.39 g) on a hot plate at 40 °C for 2 h and constant stirring, then let rest overnight. Next, it was spin coated on the substrate at 5000 rpm for 30 seconds, followed by annealing at 350 °C for 4 h. The TiO_2 mesoporous layer was prepared by mixing TiO_2 Dyesol paste (18NR-T) and ethanol in a 1:4 weight ratio and followed by ultra-sonication for 2 h. The result is a stable anatase TiO_2 NCs colloid suitable for thin film deposition. The solution was later spin coated onto the TiO_2 compact layer coated ITO glass substrate at 2000 rpm for 60 s. After the spin coating, the substrate was heated at 100 °C for 10 min and then annealed at 400 °C for 2 h to obtain the sintering of the anatase particles. The result is a transparent TiO_2 mesoporous layer.
2. **Si NCs layer**: directly deposited on the TiO_2 on ITO substrate placed under the APP reactor as described for NPs films throughout the rest of the chapter. For better uniformity of the film, the two-axis stage was scanning at a high-speed

setting (13 mm/s). Also, to reduce inhomogeneities at the edges of the scanning area, the substrate was partially masked with Teflon and the size of the scanning area was set bigger than the designed deposited area.

3. **NiO NCs layer**: deposited on top of the active layer using an airbrush (Pro BD-132) spray coater. A 1 mL solution of NiO - ethanol was obtained with a liquid phase APP and spray coated via a nitrogen gas flow at 1 bar. Following, it was annealed for 10 min at 120 °C.

4. **Au metal contact:** deposited onto the NiO NCs layer using a magnetron sputtering technique (Moorfield minilab DC/RF magnetron box sputter system). Argon plasma at constant current of 0.15 A for 60 min with a working pressure of 1.5 x 10^{-2} mbar was used to sputter Au from a 99.99% pure Au target.

A diagram of the electron levels near the fermi level of the device shows the general functioning from the perspective of the potential felt by photogenerated charge carriers (see Figure 6.28a). For the device produced, the materials have been chosen such that charge carriers generated after the absorption of light are attracted by different contacts. In fact the NiO layer having a very strong p-type character and a higher energy conduction band minimum forms a barrier for electrons in the junction with the Si QDs active layer and acts as an electron blocking layer, while permitting (and even favoring) the transport of holes to the metallic gold contact. The TiO_2 layers are doing the opposite, acting as hole blocking layers and favoring the transport of electrons only to the transparent conductive oxide contact.

To characterize the efficiency of the solar cells, the current voltage characteristics of the device are measured while shining the light from a solar simulator. Current density–voltage (JV) curves were recorded using a Keithley 6430 sub-FA source meter unit under 1.5 AM illumination in air at ambient temperature. The applied bias varied from -1 V to 1 V in steps of 0.01 V at a scan rate 700 mV/s for all the measurements.

The results, shown in figure 6.28b, right, indicate a fill factor of 35% and an open circuit voltage V_{oc} of 0.64 V, however the current density is very poor and affecting the overall performance of the device. The reasonably high open-circuit voltage is likely a result of the suitable band alignment in the device architecture, while the poor current density can

be associated with a poor generation or extraction of carriers from the active layer. While the overall performance remains very low the device parameters are very encouraging and demonstrate the usefulness of a careful EBD parameters analysis for the engineering of real-world devices.

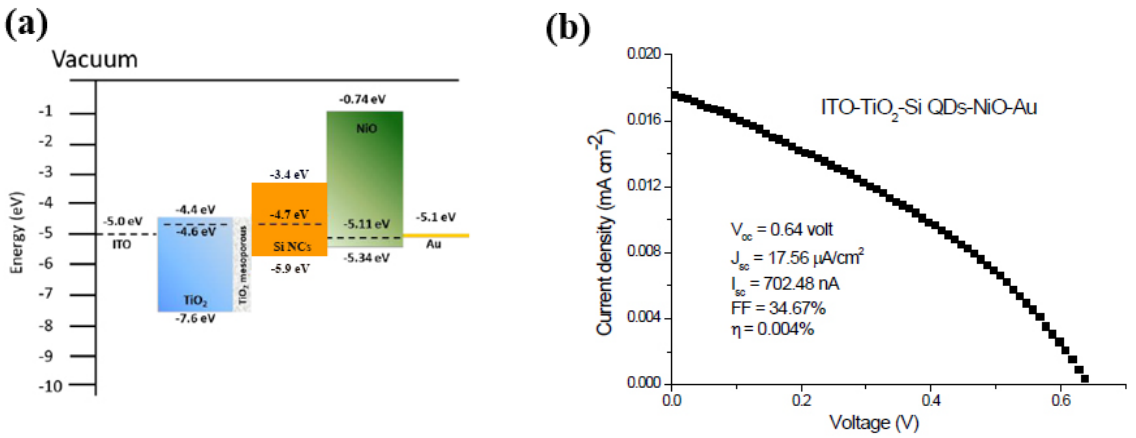

Figure 6.28 - (**a**) Unbalanced energy diagram of the layered device, showing the absolute values of CBM, VBM and E_F relative to the vacuum level. (**b**) Current density vs. voltage plot of the all-inorganic Si-QDs based device with NiO NCs hole transport layer under one sun condition (AM 1.5G) with indication of the resulting power conversion parameters.

6.5 Conclusions

Si QDs with small size and size dispersion that show tunable crystallinity can be grown in the present microplasma reactor. The study of a variety of experimental conditions has enabled to produce Si QDs exhibiting crystalline or amorphous characteristics by changing the SiH_4 precursor concentration in the gas phase.

The crystalline or amorphous character of the Si QDs was explained by the efficient heating of the particles in non-thermal APPs. The analysis of the energy balance on the surface of the particles shows that the plasma parameters can be tuned to control the temperature of the particles when immersed in the plasma and hence, their crystallinity.

The morphology of free-standing nanoparticle film directly deposited onto solid substrates was characterized and determined the best conditions to deposit compact films, which would ameliorate the interface transport properties. It is found that the scanning speed of an X-Y stage and applying a bias to the substrate influence the morphology of deposited particles, and fast scanning with no biasing result in the best controllability conditions for film thickness and low roughness.

The behavior of films exposed to atmosphere have been studied to understand the oxidation processes. It is found that the oxidation process is faster for films of amorphous QDs. Various considerations on the surface composition and the oxidation kinetics permitted to understand this phenomenon as the result of hydrogen incorporation in the core of amorphous particles.

Electron energy diagram of the electron states near the fermi level have been estimated , and, after a critical assessment of measurements from different instruments, found that films formed from these free-standing particles tend to develop a strong n-type character for amorphous QDs, despite similar values of valence band edge and optical bandgaps compared to the films of crystalline Si QDs.

In addition, the potential of the plasma process for crystalline Si QDs and the usefulness of energy band diagrams was demonstrated for the fabrication of an all-inorganic photovoltaic cell.

Overall, it is proved how the present microplasma process to synthesize Si QDs is convenient for the control of structural, optical and electronic properties of Si QDs through tailoring the parameters of plasma process.

References

1. Priolo, F., Gregorkiewicz, T., Galli, M. & Krauss, T. F. Silicon nanostructures for photonics and photovoltaics. *Nat. Nanotechnol.* **9**, 19–32 (2014).

2. Mastronardi, M. L., Henderson, E. J., Puzzo, D. P. & Ozin, G. A. Small silicon, big opportunities: The development and future of colloidally-stable monodisperse silicon nanocrystals. *Adv. Mater.* **24**, 5890–5898 (2012).

3. Kim, D. K., Lai, Y., Diroll, B. T., Murray, C. B. & Kagan, C. R. Flexible and low-voltage integrated circuits constructed from high-performance nanocrystal transistors. *Nat. Commun.* **3**, 1–6 (2012).

4. Park, J. H. *et al.* Biodegradable luminescent porous silicon nanoparticles for in vivo applications. *Nat. Mater.* **8**, 331–336 (2009).

5. Švrček, V., Mariotti, D., Shibata, Y. & Kondo, M. A hybrid heterojunction based on fullerenes and surfactant-free, self-assembled, closely packed silicon nanocrystals. *J. Phys. D. Appl. Phys.* **43**, (2010).

6. Mariotti, D., Mitra, S. & Švrček, V. Surface-engineered silicon nanocrystals. *Nanoscale* **5**, 1385–1398 (2013).

7. Švrček, V., Kondo, M., Kalia, K. & Mariotti, D. Photosensitive self-assembled nanoarchitectures containing surfactant-free Si nanocrystals produced by laser fragmentation in water. *Chem. Phys. Lett.* **478**, 224–229 (2009).

8. Švrček, V., Mariotti, D. & Kondo, M. Microplasma-induced surface engineering of silicon nanocrystals in colloidal dispersion. *Appl. Phys. Lett.* **97**, 1–4 (2010).

9. Pavesi, L., Dal Negro, L., Mazzoleni, C., Franzò, G. & Priolo, F. Optical gain in silicon nanocrystals. *Nature* **408**, 440–444 (2000).

10. Green, M. A. Third generation photovoltaics: Ultra-high conversion efficiency at low cost. *Prog. Photovoltaics Res. Appl.* **9**, 123–135 (2001).

11. Wolf, O. *et al.* Doping and quantum confinement effects in single Si nanocrystals observed by scanning tunneling spectroscopy. *Nano Lett.* **13**, 2516–2521 (2013).

12. Svrcek, V. *et al.* Dramatic enhancement of photoluminescence quantum yields for surface-engineered Si nanocrystals within the solar spectrum. *Adv. Funct. Mater.* **23**, 6051–6058 (2013).

13. Sagar, D. M. *et al.* Quantum confined electron-phonon interaction in silicon nanocrystals. *Nano Lett.* **15**, 1511–1516 (2015).

14. Askari, S., Levchenko, I., Ostrikov, K., Maguire, P. & Mariotti, D. Crystalline Si nanoparticles below crystallization threshold: Effects of collisional heating in non-thermal atmospheric-pressure microplasmas. *Appl. Phys. Lett.* **104**, (2014).

15. Askari, S. *et al.* Silicon-based quantum dots: Synthesis, surface and composition tuning with atmospheric pressure plasmas. *J. Phys. D. Appl. Phys.* **48**, 314002 (2015).

16. Anthony, R. & Kortshagen, U. Photoluminescence quantum yields of amorphous and crystalline silicon nanoparticles. *Phys. Rev. B - Condens. Matter Mater. Phys.* **80**, 1–6 (2009).

17. Street, R. A. Luminescence and recombination in hydrogenated amorphous silicon. *Adv. Phys.* 37–41 (2006).

18. Askari, S., Svrcek, V., Maguire, P. & Mariotti, D. The Interplay of Quantum Confinement and Hydrogenation in Amorphous Silicon Quantum Dots. *Adv. Mater.* **27**, 8011–8016 (2015).

19. Kortshagen, U. Nonthermal plasma synthesis of semiconductor nanocrystals. *J. Phys. D. Appl. Phys.* **42**, (2009).

20. Bapat, A., Gatti, M., Ding, Y.-P., Campbell, S. A. & Kortshagen, U. A plasma process for the synthesis of cubic-shaped silicon nanocrystals for nanoelectronic devices. *J. Phys. D. Appl. Phys.* **40**, 2247–2257 (2007).

21. Kortshagen, U., Mangolini, L. & Bapat, A. Plasma synthesis of semiconductor nanocrystals for nanoelectronics and luminescence applications. *J. Nanoparticle Res.* **9**, 39–52 (2007).

22. Mangolini, L., Thimsen, E. & Kortshagen, U. High-yield plasma synthesis of luminescent silicon nanocrystals. *Nano Lett.* **5**, 655–659 (2005).

23. Gresback, R., Holman, Z. & Kortshagen, U. Nonthermal plasma synthesis of size-controlled, monodisperse, freestanding germanium nanocrystals. *Appl. Phys. Lett.* **91**, (2007).

24. Nozaki, T., Sasaki, K., Ogino, T., Asahi, D. & Okazaki, K. Microplasma synthesis of tunable photoluminescent silicon nanocrystals. *Nanotechnology* **18**, (2007).

25. Sankaran, R. M., Holunga, D., Flagan, R. C. & Giapis, K. P. Synthesis of blue luminescent Si nanoparticles using atmospheric-pressure microdischarges. *Nano Lett.* **5**, 537–541 (2005).

26. Macias-Montero, M. *et al.* Energy band diagram of device-grade silicon nanocrystals. *Nanoscale* **8**, 6623–6628 (2016).

27. Alessi, B. *et al.* Bridging energy bands to the crystalline and amorphous states of Si QDs. *Faraday Discuss.* **222**, 390–404 (2020).

28. Barwe, B., Riedel, F., Cibulka, O. E., Pelant, I. & Benedikt, J. Silicon nanoparticle formation depending on the discharge conditions of an atmospheric radio-frequency driven microplasma with argon/silane/hydrogen gases. *J. Phys. D. Appl. Phys.* **48**, (2015).

29. Bruggeman, P. *et al.* Electronic quenching of OH(A) by water in atmospheric pressure plasmas and its influence on the gas temperature determination by OH(A-X) emission. *Plasma Sources Sci. Technol.* **19**, (2010).

30. Hofmann, S., Van Gessel, A. F. H., Verreycken, T. & Bruggeman, P. Power dissipation, gas temperatures and electron densities of cold atmospheric pressure helium and argon RF plasma jets. *Plasma Sources Sci. Technol.* **20**, (2011).

31. Yanguas-Gil, A., Cotrino, J. & González-Elipe, A. R. Measuring the electron temperature by optical emission spectroscopy in two temperature plasmas at atmospheric pressure: A critical approach. *J. Appl. Phys.* **99**, (2006).

32. Zhu, X.-M., Chen, W.-C. & Pu, Y.-K. Gas temperature, electron density and electron temperature measurement in a microwave excited microplasma. *J. Phys. D. Appl. Phys.* **41**, 105212 (2008).

33. Mariotti, D., Shimizu, Y., Sasaki, T. & Koshizaki, N. Gas temperature and electron temperature measurements by emission spectroscopy for an atmospheric microplasma. *J. Appl. Phys.* **101**, (2007).

34. Goldstein, A. N. The melting of silicon nanocrystals: Submicron thin-film structures derived from nanocrystal precursors. *Appl. Phys. A Mater. Sci. Process.* **62**, 33–37 (1996).

35. Fridman, A. A., Boufendi, L., Hbid, T., Potapkin, B. V. & Bouchoule, A. Dusty plasma formation: Physics and critical phenomena. Theoretical approach. *J. Appl. Phys.* **79**, 1303–1314 (1996).

36. Gallagher, A., Howling, A. A. & Hollenstein, C. Anion reactions in silane plasma. *J. Appl. Phys.* **91**, 5571–5580 (2002).

37. Wagner, A. J., Mariotti, D., Yurchenko, K. J. & Das, T. K. Experimental study of a planar atmospheric-pressure plasma operating in the microplasma regime. *Phys. Rev. E - Stat. Nonlinear, Soft Matter Phys.* **80**, 1–4 (2009).

38. Haq, A. U., Lucke, P., Benedikt, J., Maguire, P. & Mariotti, D. Dissociation of tetramethylsilane for the growth of SiC nanocrystals by atmospheric pressure microplasma. *Plasma Process. Polym.* 1–11 (2020) doi:10.1002/ppap.201900243.

39. Lopez, T. & Mangolini, L. On the nucleation and crystallization of nanoparticles in continuous-flow nonthermal plasma reactors. *J. Vac. Sci. Technol. B, Nanotechnol. Microelectron. Mater. Process. Meas. Phenom.* **32**, 061802 (2014).

40. Chabal, Y. J. Infrared spectroscopy of hydrogen on silicon surfaces. *Phys. B Phys. Condens. Matter* **170**, 447–456 (1991).

41. Xu, D. *et al.* Hydrolysis and silanization of the hydrosilicon surface of freshly prepared porous silicon by an amine catalytic reaction. *New J. Chem.* **27**, 300–306 (2003).

42. Marra, D. C., Edelberg, E. A., Naone, R. L. & Aydil, E. S. Silicon hydride composition of plasma-deposited hydrogenated amorphous and nanocrystalline silicon films and surfaces. *J. Vac. Sci. Technol. A Vacuum, Surfaces, Film.* **16**, 3199–3210 (1998).

43. Winters, B. J., Holm, J. & Roberts, J. T. Thermal processing and native oxidation

of silicon nanoparticles. *J. Nanoparticle Res.* **13**, 5473–5484 (2011).

44. Song, C., Wang, P. & Makse, H. A. A phase diagram for jammed matter. *Nature* **453**, 629–632 (2008).

45. Mariotti, D., Švrček, V., Hamilton, J. W. J., Schmidt, M. & Kondo, M. Silicon nanocrystals in liquid media: Optical properties and surface stabilization by microplasma-induced non-equilibrium liquid chemistry. *Adv. Funct. Mater.* **22**, 954–964 (2012).

46. Szekeres, A. & Danesh, P. Oxidation of amorphous and crystalline silicon. *J. Non. Cryst. Solids* **187**, 45–48 (1995).

47. Carolan, D. *et al.* Environmentally friendly nitrogen-doped carbon quantum dots for next generation solar cells. *Sustain. Energy Fuels* (2017).

48. Barbagiovanni, E. G., Lockwood, D. J., Filho, R. N. C., Goncharova, L. V. & Simpson, P. J. Quantum confinement in Si and Ge nanostructures: Effect of crystallinity. (2013) doi:10.1117/12.2036323.

49. Park, N. M., Kim, T. S. & Park, S. J. Band gap engineering of amorphous silicon quantum dots for light-emitting diodes. *Appl. Phys. Lett.* **78**, 2575–2577 (2001).

50. Allen, F. G. & Gobeli, G. W. Work function, photoelectric threshold, and surface states of atomically clean silicon. *Phys. Rev.* **127**, 150–158 (1962).

51. Kocevski, V., Eriksson, O. & Rusz, J. Transition between direct and indirect band gap in silicon nanocrystals. *Phys. Rev. B* **87**, 245401 (2013).

52. Ramos, E. *et al.* Theoretical study of the electronic properties of silicon nanocrystals partially passivated with Cl and F. *J. Phys. Chem. C* **116**, 3988–3994 (2012).

53. Botas, A. M. P. *et al.* High quantum yield dual emission from gas-phase grown crystalline Si nanoparticles. *J. Phys. Chem. C* **118**, 10375–10383 (2014).

54. Street, R. A. *Hydrogenated amorphous silicon*. (Cambridge University Press, 1991).

55. Chakrabarti, S., Carolan, D., Alessi, B. & Maguire, P. Supporting Information Microplasma-synthesized ultra-small NiO nanocrystals , an ubiquitous. (2019).

Chapter 7 – Wire Precursors

7.1 Introduction

The reactor design presented hitherto use gas-phase or liquid-phase precursors to achieve the formation of nanoparticles. The use of these precursors presents some intrinsic limitations connected to the achievable purity of products, environmental and economic sustainability. As an example, precursors used for gas phase synthesis of silicon nanoparticles are practically limited to silane gas (SiH_4) or the volatile liquid silicon tetrachloride ($SiCl_4$), while any non-toxic, versatile and oxygen-containing precursor, e.g. siloxane compounds $(OSiH_2)_n$, is not a good choice as it preferentially lead to oxide nanoparticles. Avoiding oxygen in the precursor or in the synthesis process is especially critical for pure metallic nanoparticles and, so far, most of the synthesis methods use metal-organic compounds as precursors. Most of these compounds are relatively expensive and are hazardous for the health and for the environment, thus needing extra care regarding the handling and the delivery of these precursors, whether in liquid or powder form. In addition, the synthesis processes rarely result in pure products (e.g. ferrocene for carbon nanotubes or for the nanodiamond synthesis process described in chapter 4), hence requiring extra purification steps. Wet chemistry methods instead, while being successful in controlling size dispersion and shape of nanoparticles, usually need capping agents in order to stabilize colloids of metal nanoparticles. Most of the complications of common synthesis processes for metal nanoparticles would be lifted by a synthesis process based on pure solid precursors.

Sputtering methods with low pressure non-thermal plasmas have already shown the advantages of pure solid precursors to produce nanometric or nanostructured films. The non-selectivity and non-equilibrium character of sputtering methods, for example, permit to deposit composite materials, non-stoichiometric compounds and alloys within the same plasma process starting from pure solid precursors.[1] Carefully controlling energy and the flux of sputtered species impinging on a heated substrate it is possible to control the stoichiometry of the growing material and the morphology of the formed films. At atmospheric pressure, solid precursors have been already used within thermal plasma processes. Direct-current (DC), radio-frequency (RF) or microwave thermal (arc) discharges, while mostly used for producing nanoparticles of refractory materials, have been also used or can be adapted for metallic NPs.[2] Two methodologies for using solid

precursors are common: use of sacrificial electrodes eroded by a plasma or injection of coarse microparticles in the plasma region.[3–8] In these thermal plasma processes, the mechanism that produces nanoparticles starts from the vaporization or sublimation of the target material due to very high gas temperatures followed by condensation of saturated vapors into nanoparticles. Quenching is then needed to prevent their growth. Also, laser ablation of solid targets can be classified in this category, as the particle nucleating mechanism is based on an expanding thermal plasma. These plasma-based methods are currently among the few able to produce pure metallic nanoparticles in large quantities and have some interesting qualities. For example, if the quenching is fast enough, it is possible to kinetically stabilize compounds or phases otherwise not thermodynamically stable, and the production rates are generally high. Yet, the high temperatures developed in these processes ipso facto limit the smallest nanoparticles size achievable to 20-30 nm diameter with large size dispersions of 20 nm to 50 nm, as particle growth, coalescence and Ostwald ripening are hard to control. Moreover, thermal instabilities and erosion of electrodes can limit the continuous operation.[2]

A non-thermal atmospheric pressure plasma (APP) that uses pure solid precursors would have a great potential. In fact, the precursors/chemistry related contamination would be reduced, stable colloids of small monodisperse particles could be obtained, and the process control could be much simpler than the established methods. In fact, it could be limited to the control of process parameters as gas flow and applied power, as it would not be needed to control the plasma chemical processes. These are usually complicated at atmospheric pressure and imply the knowledge of the energy distribution of the plasma electrons, which initiate dissociation of precursors and determine the relative kinetic rates of reactions involved. Unfortunately, the collisional character of non-equilibrium APPs result in limited energy transferred to the plasma ions, which in principle is not enough to provoke substantial physical sputtering at a solid surface.[9–11] Furthermore, frequent collisions at atmospheric pressure hinder the control of the ion fluxes, for instance via biasing. Nevertheless, sputtering phenomena at low energies have not been thoroughly studied and the high reduced electric fields in the sheath region of confined discharges may enable ion sputtering even at higher pressures than the pressure used in standard sputtering plasmas. The use of solid metallic precursors for APPs, that relies on sputtering or other mechanisms, could be very useful for a range of applications. In the context of nanoparticle synthesis, this type of concept would be particularly important for the delivery of metallic precursor, e.g. for the synthesis of nm-sized nanoparticles of metallic

elements. Small metallic particles are very prone to oxidization when high-temperature methods are used or require capping with chemical ligands when wet chemical methods are used. It is therefore still a challenge to produce bare or surfactant-free metallic nanoparticles. The ability to prevent oxidation or any form of ligands at the surface is particularly important for ultra-small nanoparticles, as some of their unique features (e.g. plasmonic response or transition to a semiconducting state [12–14]) are strongly dependent on the state of surfaces.

A few groups reported the successful synthesis of nanoparticles from solid precursors through non-thermal APPs, especially using a metallic precursor in the form of thin wires ($d < 0.3$ mm) inside a quartz or glass capillary as an electrode.[15–17] The formation of nanoparticles and the characteristic of these APP reactors have not yet been understood. In this chapter, the work on a similar reactor concept is presented (Figure 7.1), where the diameter of the sacrificial electrode wire is larger than what has been generally used in the work reported in the literature. The larger diameter (mm scale vs hundreds of μm) is here proposed to circumvent the difficulties of preceding designs in controlling the wire position (both vertically and radially) and allowing the use of more brittle materials as precursors, which cannot be conveniently produced into very thin wires. The use of larger diameter however required the re-design of the reactor dimensions with a range of implications on the plasma. The need to explore improvements in process control and study the underlying nanoparticle formation mechanisms were also driving principles for using larger diameters. In order to test these changes, the synthesis of nanoscopic bismuth (Bi) and antimony (Sb) particles starting from pure metal wires of 1 mm and 2 mm is demonstrated. These materials were selected because of their interesting properties from a materials perspective as they are expected to show a semi-metal to semiconductor transition at very small size.[18–21] Also, while Bi QDs have been already synthesized by wet chemistry methods and their optical and electronic studies are currently subject of scientific debate, exploring the synthesis of Sb QDs may give insight on the quantum confinement effects and the synthesis process itself. In fact, Antimony and Bismuth share very similar near-gap band structures in the bulk (and same semi-metallic behaviour) and crystal structures with the rhombohedral symmetry but are characterized by different bulk thermodynamic properties. In particular, different melting point (545 K and 903 K) and relative enthalpies of fusion (11 kJ/mol and 20 kJ/mol) with similar Boiling points (1837 K and 1908 K) and comparable enthalpies of vaporization (179 kJ/mol and 193 kJ/mol).

7.2 Experimental Setup

7.2.1 Reactor design

The reactor design used for the synthesis of both Bi and Sb nanoparticles is shown in Figure 7.1. A thin metal wire (1 mm diameter for Bi and 2 mm diameter for Sb), used as the ground electrode, is inserted into a hollow borosilicate glass capillary. Two parallel rectangular electrodes with a hole of the size of the capillary are placed outside 1 mm apart and are both powered with a 13.56 MHz power supply. The tip of the wire is initially aligned 2 mm below the beginning of the first electrode (Figure 7.1b). He gas is flown from the top end of the capillary and the synthesis products are collected at the capillary bottom end. The diameters of the capillaries (inner diameter ID and outer diameter OD) are changed according to the diameter of the wires (*D*), so to keep a fixed gap of 0.5 mm between the wire and the walls of the capillary and the same wall thickness.

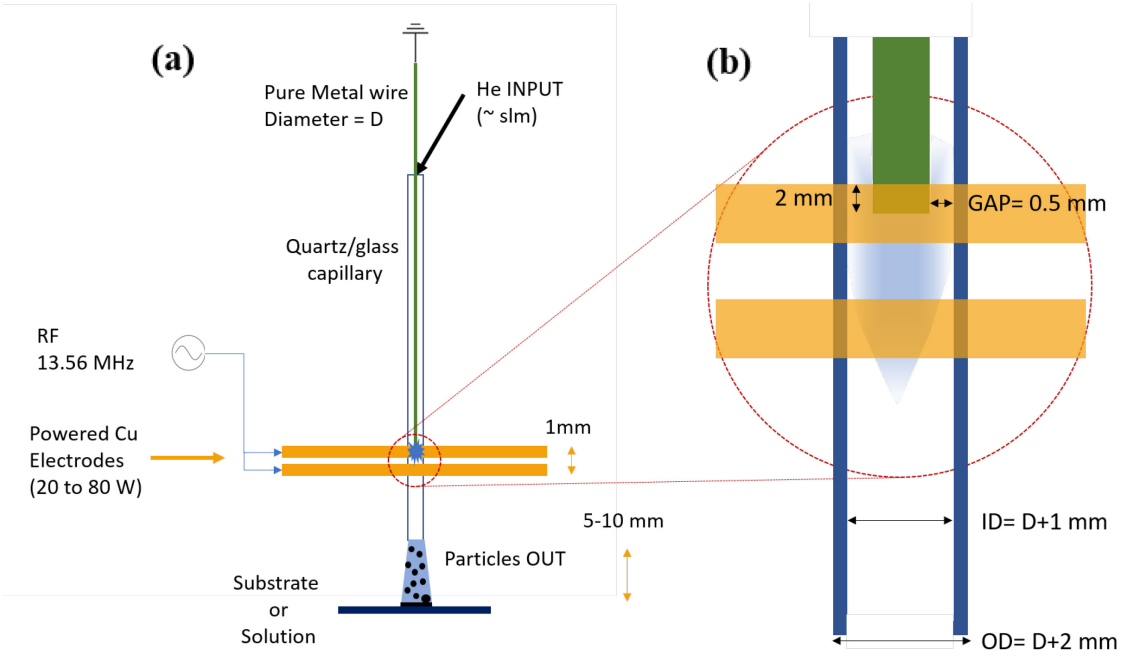

Figure 7.1 - (**a**) Schematic diagram of the experimental setup used in the context of this chapter. The geometrical characteristics of the capillaries are indicated by scaling relations, in order to keep a fixed gap between wire and capillary and the same capillary wall thickness. (**b**) Close-up of the electrodes region, showing the alignment of the wires and schematically the appearance of the plasma (light blue glow). Electrodes are colored in transparency to see through them.

This electrodes configuration has been suggested by the observation of a resulting higher throughput in other experiments. It is in the authors belief that while the top powered

electrode generates the plasma in the dielectric-wire gap (0.5 mm), the bottom powered electrode only helps the collection of particles through the formation of an extracting field. In fact, the discharge gap is much bigger than for the top electrode (~2.3 mm) and by removing it no material is collected on the substrate, instead a metallic deposit can be observed on the capillary right at the bottom of the top powered electrode. Further experiments are needed in order to clarify its role.

Table 7.1 summarizes the geometrical dimensions of the wires and capillaries for the two processes explored herein.

Wire material	D (±tolerance) [mm]	ID [mm]	OD [mm]	Min. discharge gap [mm]	Cap. wall thickness [mm]
Bismuth	1 (±7.5%)	2	3	0.5	1
Antimony	2 (±10%)	3	4	0.5	1

Table 7.1 - Physical dimensions of capillaries used in function of the wire precursor material used throughout this chapter. These are chosen to keep a constant minimum (min.) discharge gap and constant capillary (cap.) wall thickness irrespective of the wires' diameter.

The reactor in Figure 7.1 is encapsulated in a Perspex frame that gives mechanical support and keeps the vertical and radial position of wires fixed to the frame. Bismuth (American Elements) and Antimony (Goodfellow) wires are 99.99% (N4) purity (metal basis).

7.2.2 Characterization methods

The nanoparticles obtained are characterized using transmission electron microscopy (TEM) with a JEOL JEM-2100F microscope. The TEM analysis includes bright-field imaging to observe the morphology of the nanoparticles and selected area electron diffraction (SAED) to characterize their crystallinity. Additional structural characterization is performed with an X-ray diffractometer (Bruker AXS D8Discover) in a Bragg-Brentano configuration equipped with a z-stage and dedicated optics for grazing-incidence measurements of thin films surface. The source is a Cu K_α (λ= 1.5406 Å) operated at 40 kV and 40 mA at incidence angle below 1° in respect to the sample plane.

The incidence angle is optimized sample by sample to maximize the signal from the sample, the detector spans in an angular region between 20° and 80° with increments of 0.05° for survey spectra and 0.01° for high-resolution of chosen peaks. Chemical analysis is performed using X-ray photoelectron spectroscopy (XPS) core levels measurements. XPS and ultraviolet photoelectron spectroscopy (UPS) measurements were performed using an ESCALAB 250 Xi microprobe spectrometer (Thermo Fisher Scientific, UK), equipped with an X-ray and UV source. XPS analysis was carried out with a focused XR6 monochromatic, micro-focused Al K_α ($h\nu$=1486.6 eV, < 900 μm spot sizes) radiation source with a hemispherical energy analyzer. The binding energy was calibrated against the C 1s peak taken to be located at 284.8 eV with a pass energy of 20 eV. XPS measurements were carried at a pressure 1-5 $\times 10^{-9}$ mbar. Depth profiling is performed with the same instrument, cycling 20 times between sputtering from an Ar^+ beam (<10 μm wide) accelerated at 2 kV for 5 s and measuring the XPS spectra. The films morphology is assessed with a Hitachi SU5000 scanning electron microscope (SEM) with a field emission gun source (10 kV acceleration voltage, ~5 mm working distance) and equipped with an X-ray detector for energy dispersive x-ray (EDX) spectroscopy of characteristic x-rays. Optical absorption is obtained using a Perkin-Elmer 650S ultraviolet-visible (UV-Vis) spectrometer equipped with a 150 mm integrating sphere. Fluorescence spectra are acquired through a spectrophotometer (Agilent Cary Eclipse) capable of emission and excitation wavelengths ranging from 190 nm to 1100 nm. The source is a Xenon flash lamp and the optics system is equipped with monochromators ($\Delta\lambda$ ~1 nm) and a photomultiplier tube as detector.

7.2.3 Experimental procedure

The reactor is held inside a stainless-steel vacuum chamber, which is evacuated and then filled with pure nitrogen to atmospheric pressure in order to reduce the presence of oxygen or moisture in the reactor and prevent external oxidation of products. Precursors wires are rub-cleaned with isopropyl alcohol to remove superficial contamination (e.g. adventitious carbon). Helium gas is flown through the reactor and the ignition of the plasma is accomplished at low power (10-15 W from the power supply) irrespective of the wire's material. The discharge appears to partially cover the body of the wire and tends to develop filamentary structures near the tip of the wire. The power and flow conditions to obtain deposition from this setup depend strongly on the wire's material and

is initially determined by fixing the flow and finding the applied power that result in the melting of the wire. Then, the process conditions are operated at a slightly lower power (1 W to 10 W below the melting conditions previously determined). If the process is controlled, a visible amount of material is deposited within few seconds from setting the power supply. Thermal instabilities and sudden melting of the whole wire is occasionally observed, even when power, flow and other settings are nominally set to values that have, on other occasions, produced stable synthesis. This suggests that the parameter space is relatively narrow and sensitive; while the current set-up has demonstrated the synthetic feasibility, improvements will be required to provide long-term nanoparticles production suitably repeatable for testing out their integration in application devices. For instance, one of the issues encountered was that small variations of the wire position (both radially and vertically) strongly affected the discharge and consequently the outcome of the synthesis. The samples are collected either directly on a vial placed 0.5 cm below the exit nozzle or on a solid substrate placed at 1 cm below. In both cases the process is lasting no more than for 10 minutes. For TEM imaging, the nanoparticles are collected directly in vials containing ethanol, then drop casted onto an ultrathin carbon grid (Agar Scientific) and dried overnight under the illumination of a halogen lamp. For SEM, XPS, UPS and KP analyses, samples are directly deposited on pieces of n-type Si (100) wafers. For optical characterization the colloidal samples are transferred to a high-transparency quartz cuvette and measurements are referenced to a cuvette with only ethanol. The only parameter varied to control the synthesis is the flow of helium input gas for both the materials under study; table 7.2 summarizes the values explored which successfully resulted in the synthesis of nanoparticles.

	Helium Flow settings in standard liters per minute (sLm)			
Bismuth	0.5	1	1.5	2
Antimony	0.25	1	-	-

Table 7.2 - Experimental conditions that resulted in the substantial synthesis of nanoparticles for each process. The experimental parameter varied is the helium input flow through the reactor.

In the reactor used in this work, it was observed that the 1 mm Bi wire melts at a power setting of 55-60 W, hence all the depositions are performed at a value of applied power just below this threshold, i.e. 50 W. The He flow is varied between 0.5 sLm to 2 sLm. The colloids obtained in ethanol are transparent and stable without precipitation or agglomeration at least for one year. The QDs collected on silicon substrates appear mostly whiteish with a darker brown spot in correspondence with the center of the deposition (Figure 7.2).

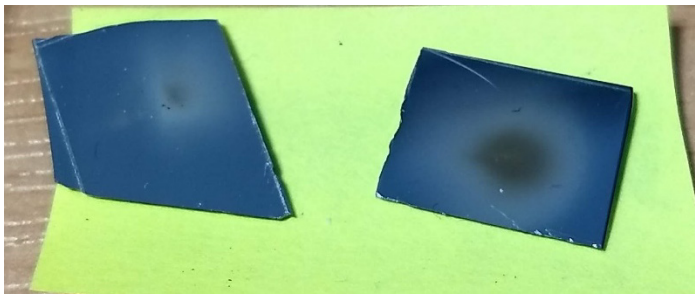

Figure 7.2 - Picture of Bi QDs samples deposited on Si substrates, for different He flows (left 1 sLm, right 2 sLm).

Instead, during the synthesis with the 2 mm diameter sacrificial Sb wire, the applied power is not limited by the wire melting. Instead the process temperature upper limit is determined by the damage of the glass capillary (at 90 W applied power) following the development of a strong filamentary discharge from the wire tip. Synthesis and deposition, without incurring in instabilities and damage, is observed at 80 W applied power. However, it should be noted that the throughput is lower when compared to the process for the synthesis of Bi nanoparticles for the same processing time. Two cases for He flow setting are explored, 0.25 sLm and 1 sLm. Collection directly in ethanol produces colloids that are transparent and do not show any sign of agglomeration or sedimentation.

7.3 Bismuth Quantum Dots (Bi QDs)

7.3.1 Interest in Bi QDs

Bismuth (Bi) in its bulk form is a brittle metal that has been mostly used as an ecofriendly replacement of lead and as admixture for low melting temperature alloys. Bi crystals are characterized by a rhombohedral structure and semi-metallic electronic behavior, which accounts for its poor thermal conductivity and high electrical resistivity. Approaching the nanoscale it has been predicted to show non-trivial electron topologies and peculiar dynamics.[22–26] It has been reported that even at relatively large diameters (~40 nm, exciton Bohr radius), bandgap opening can be observed, thus acquiring a semi-conductive character.[19,20,24,27] Because of its unique electron topologies, Bi has been proven to have potential for thermoelectrics, tunable plasmonics and plasmonic-based catalysis, spin-valve devices and as anode material in Mg- and Na- ion based batteries.[19,28–35]

7.3.2 Structure and morphology of Bi QDs

Bright field TEM analysis shows that abundant and well-separated particles can be found on the sample grids. An example of the outcome of the synthesis with 2 sLm of helium is

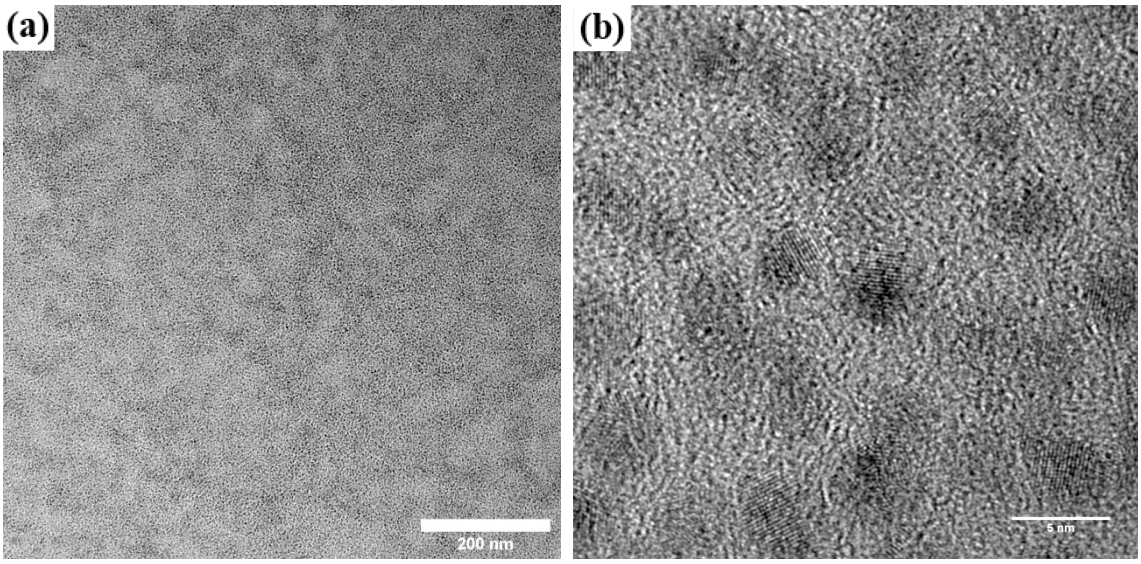

Figure 7.3 - TEM images pertaining to the synthesis process with 2 sLm He directly in ethanol. (**a**) Low magnification bright field TEM image of an area of the grid dense with small particles, no agglomeration can be observed on the 100 nm scale. (**b**) Higher magnification clearly showing the particles are mostly spherical, separated and crystalline, as evidenced by the diffraction fringes due to phase contrast of electrons diffracted by crystalline planes properly oriented with the electron beam.

shown in figure 7.3. A higher magnification image shows that particles are in the nm size range, crystalline and mostly spherical in shape (Figure 7.3b).

The variation of helium flow through the reactor impacted on the size and size dispersion of nanoparticles as well as in spatial dispersion on the grid, as testified by the low magnification TEM images at different experimental conditions (Figure 7.4a-d), while the particles are always non-agglomerated and spherical in shape.

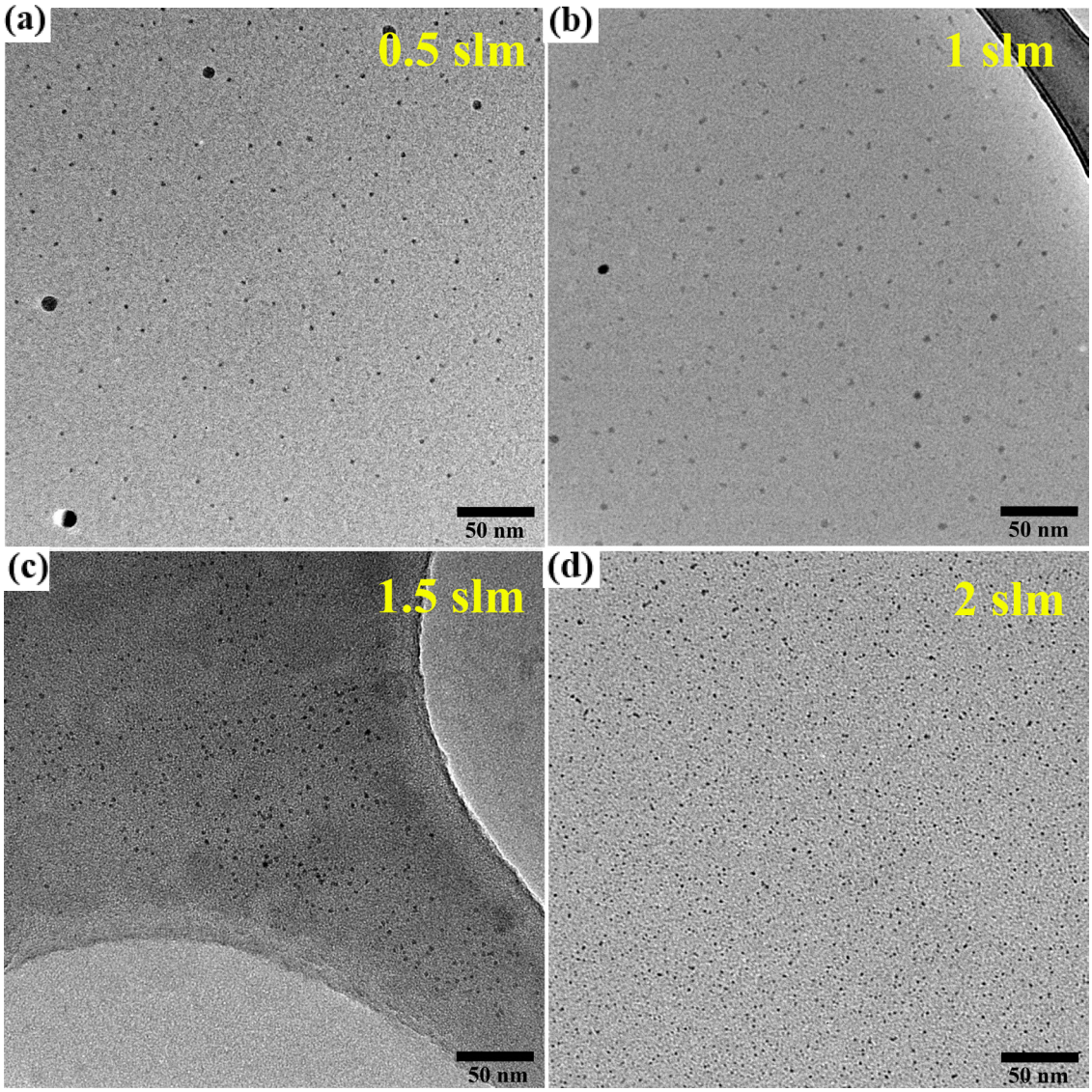

Figure 7.4 - Exemplar low resolution bright field TEM micrographs of the samples produced, showing the variation of particle size and size dispersion with increasing He flow, (**a**) 0.5 sLm (**b**) 1 sLm (**c**) 1.5 sLm (**d**) 2 sLm. No variations in the agglomeration can be observed at this scale.

A collection of low magnification images has been used to characterize the distribution of particles sizes as a function of the carrier gas flow (Figure 7.5a-d). The statistical distribution of particles sizes has been assessed through an image analysis, by measuring the extension of higher contrast areas. Then the diameter is calculated by assuming a spherical shape. The size distribution is better fitted by a Gaussian distribution function at higher flows, while at lower flow conditions resulted in the formation of a higher population of bigger particles and the distributions are better represented by a log-normal function.

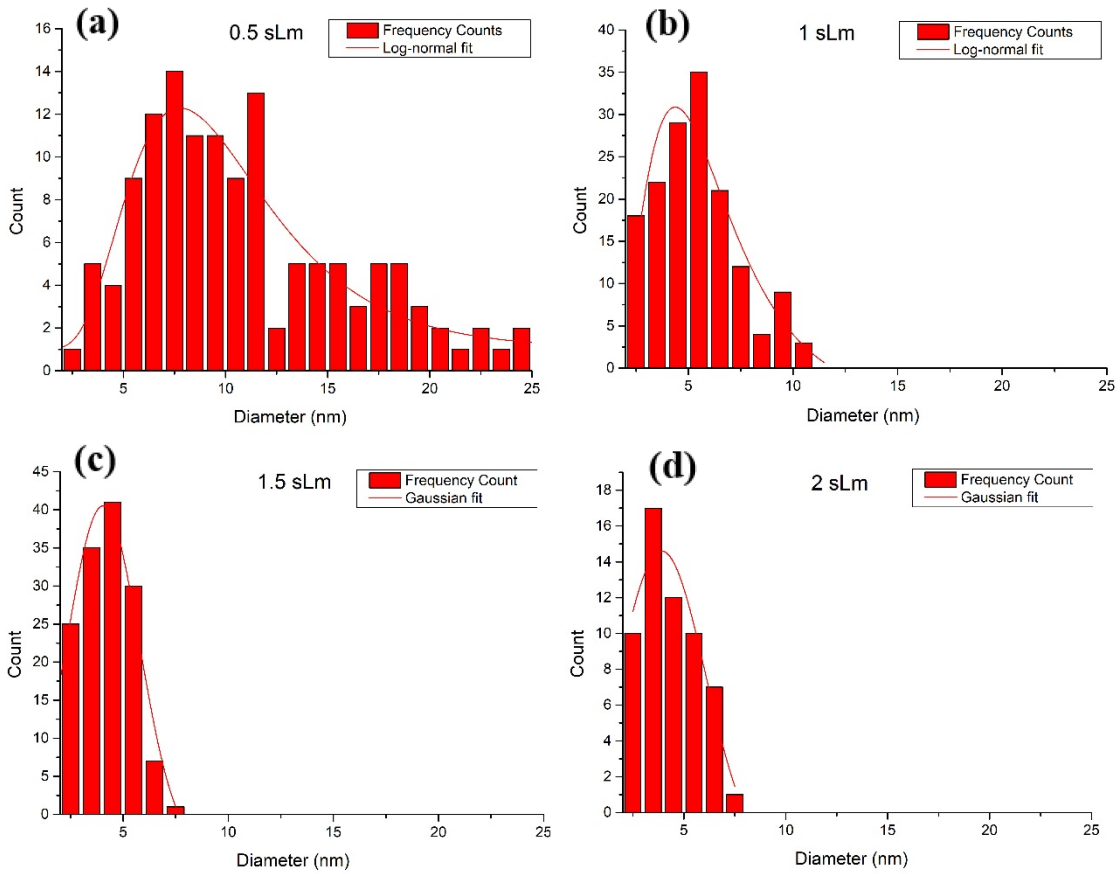

Figure 7.5 - Particle mean diameter obtained from different techniques for different sets of experiments, under nominally equal synthesis condition. Apart from the values obtained by the Scherrer method for the lower flow condition, there is trend for particles to be smaller at higher flows of precursor gas.

It is observed that particle's mean size decreases with increasing gas flow and the size dispersion becomes smaller. The table 7.3 summarizes the results of the fits.

He Flow (sLm)	Mean (nm)	Variance (nm)
0.5	8.6	6.7
1.0	4.9	3.5
1.5	4.0	1.9
2.0	3.9	2.1

Table 7.3 - Values of mean diameter and variance and relative errors extracted from the size distribution fits.

Selective area diffraction (SAED) patterns of areas populated with particles and line profiling of high-resolution TEM (HR-TEM) images of individual particles showing diffraction fringes have been used to characterize the crystalline phase of nanoparticles. The SAED pattern (Figures 7.6a-d) are often composed by scattered spots, and in few cases forming well-defined rings, characteristic of collections of randomly oriented crystalline particles.

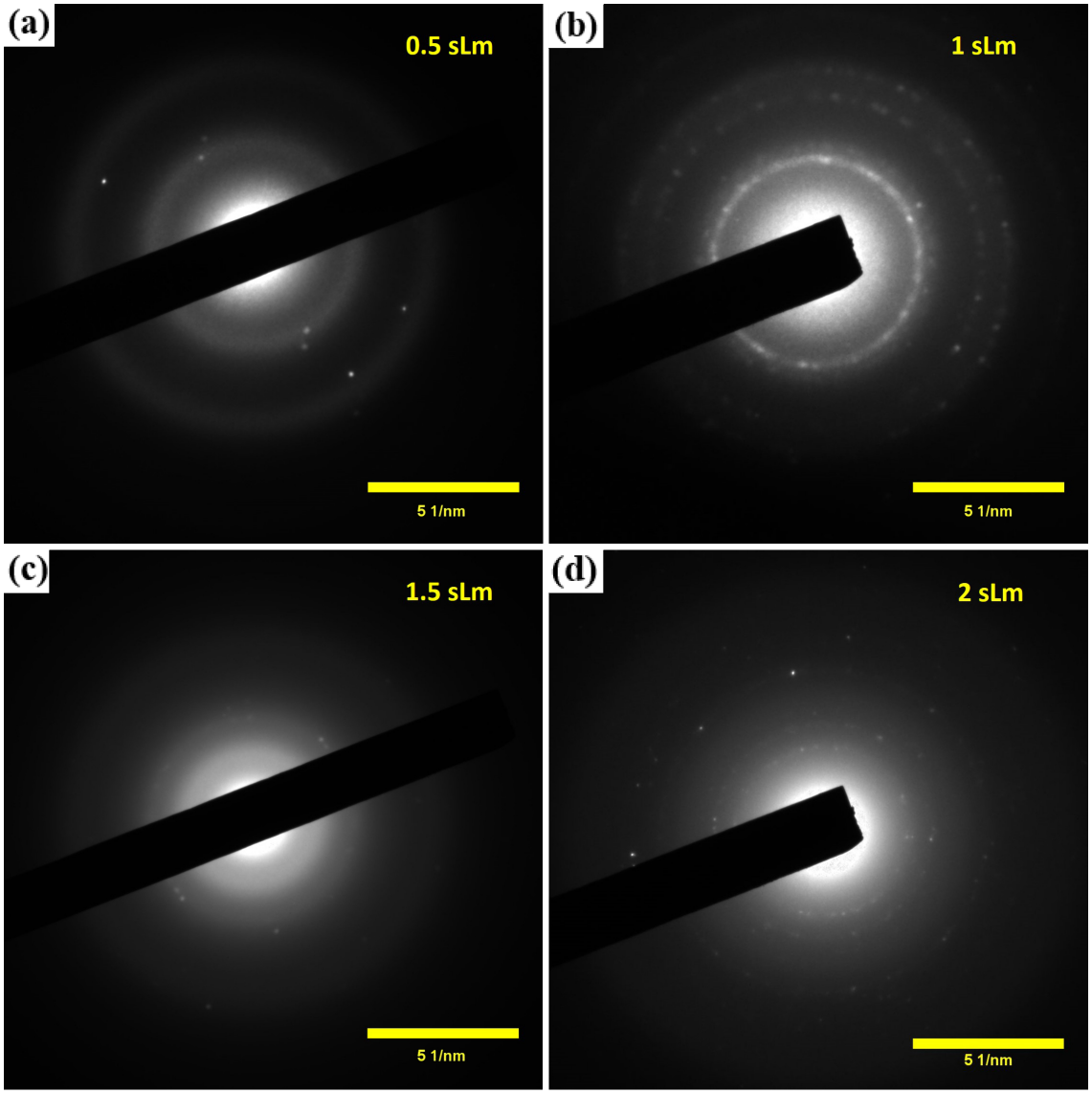

Figure 7.6 - SAED pattern collected in populated areas of the grids, for the different He flows explored (**a**) 0.5 sLm (**b**) 1 sLm (**c**) 1.5 sLm (**d**) 2 sLm. Only the SAEDs relative to 1 sLm and 2 sLm He samples were further analysed for the identification of crystalline phase, as the ones clearly showing a collection of diffraction rings.

The spotty and scattered appearance of some of the SAED patterns is likely linked to a combination of small size and spatially dispersed nanoparticles on the grids. In fact, while the intensity of zero order diffraction maximum is proportional to N^2, with N number of diffracting elements in the probed area, the width of the diffraction peaks is inversely proportional to N. Hence, sparsely populated particles or diffraction from small particles results in more diffused diffraction rings. Nevertheless, the more informative SAED patterns (1 sLm Figure 7.6b and 2 sLm Figure 7.6d) have been used to identify the crystalline phase involved. In figure 7.7a a comparison between the SAED pattern relative to the 2 sLm He sample is shown as an example of analysis. The SAED pattern shows a

good correlation with the theoretical patterns expected for rhombohedral Bi (the common low temperature phase). Moreover, no other ring can be observed which does not fit with the rhombohedral Bi pattern.

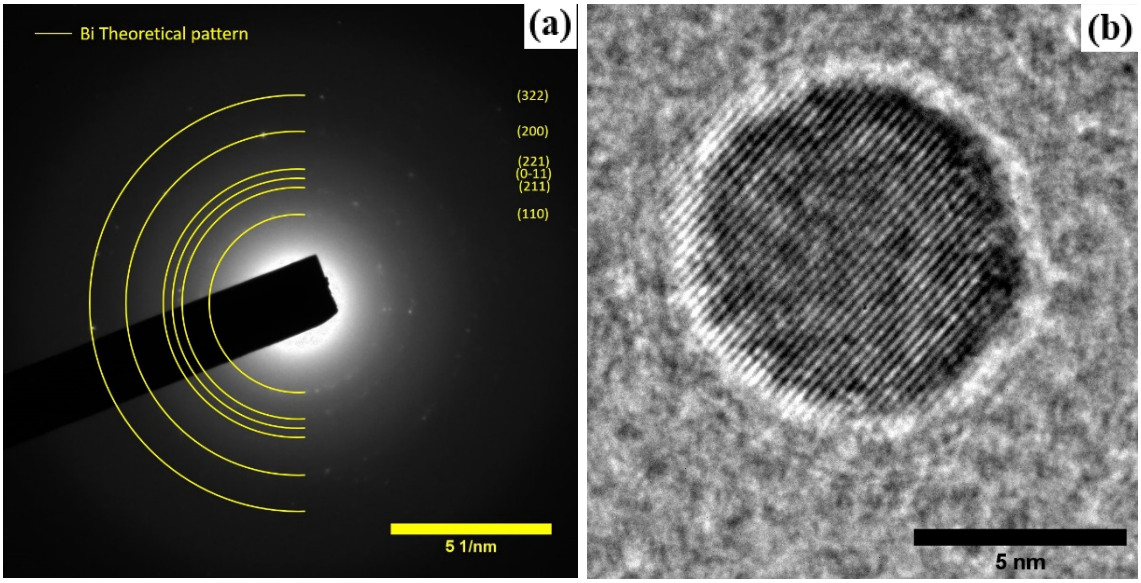

Figure 7.7 - (**a**) Selected area diffraction pattern of the 2 sLm sample, acquired in a fraction of the area shown in Figure 7.3a and (**b**) high resolution close- up of a particle bigger than the average, showing a spacing of 1.88 Å between the fringes as measured by line profiling of the image. This d-spacing can be associated to diffraction from (200) planes of rhombohedral bismuth. The white layer is the result of under-focusing the electron beam to evidence the diffraction fringes.[38]

By measuring the radius of experimentally observable rings in SAED patterns and the analysis of the diffraction fringes of few particles (e.g. Figure 7.7b), d-spacings relative to the diffraction spectra of the samples have been calculated and compared to literature values for bismuth and its most common oxide (α-Bi_2O_3). A summary of the estimated values and their assignments is reported in Table 7.3. The relevant rings are readily associated to rhombohedral bismuth and no diffraction ring can be associated to oxide species.[36]

Measured d-spacing (Å)	Error (nm)	Cryst. Planes	Lit. values
3.35	0.07	Bi (110)	3.28^{++}
2.44	0.05	Bi (211)	2.37^{+}
		Bi (0-11)	2.27^{+}
2.03	0.04	Bi (221)	2.03^{-}
1.88	0.04	Bi (200)	1.87^{-}
1.55	0.03	Bi (322)	1.55^{-}

Table 7.4 - Measured d-spacings obtained from the diameter of rings in the SAED pattern and relative assignment to the strongest diffracting planes of bismuth (R3m space group, a = 4.537 Å, c = 11.838 Å). The symbols on the literature values represent the relative intensity of peaks (++ strongest, +strong, - minor) .[35]

To further understand the structure and chemical composition of the samples, QDs directly deposited on Si substrates were produced and analyzed by XRD (Figure 7.8), XPS (Figure 7.9) and SEM/EDX (Figure 7.10). XRD diffraction spectra are easily assigned to bismuth in the trigonal R3m space group with no apparent variation in peaks position for all the samples, as they correlate very well with literature values in peak position and intensity ratios (Figure 7.8a-d). Only the 1.5 sLm sample (Figure 7.8c), which has the strongest signal among others, shows a minor contribution from peaks unrelated to metallic bismuth which have not been identified.[36]

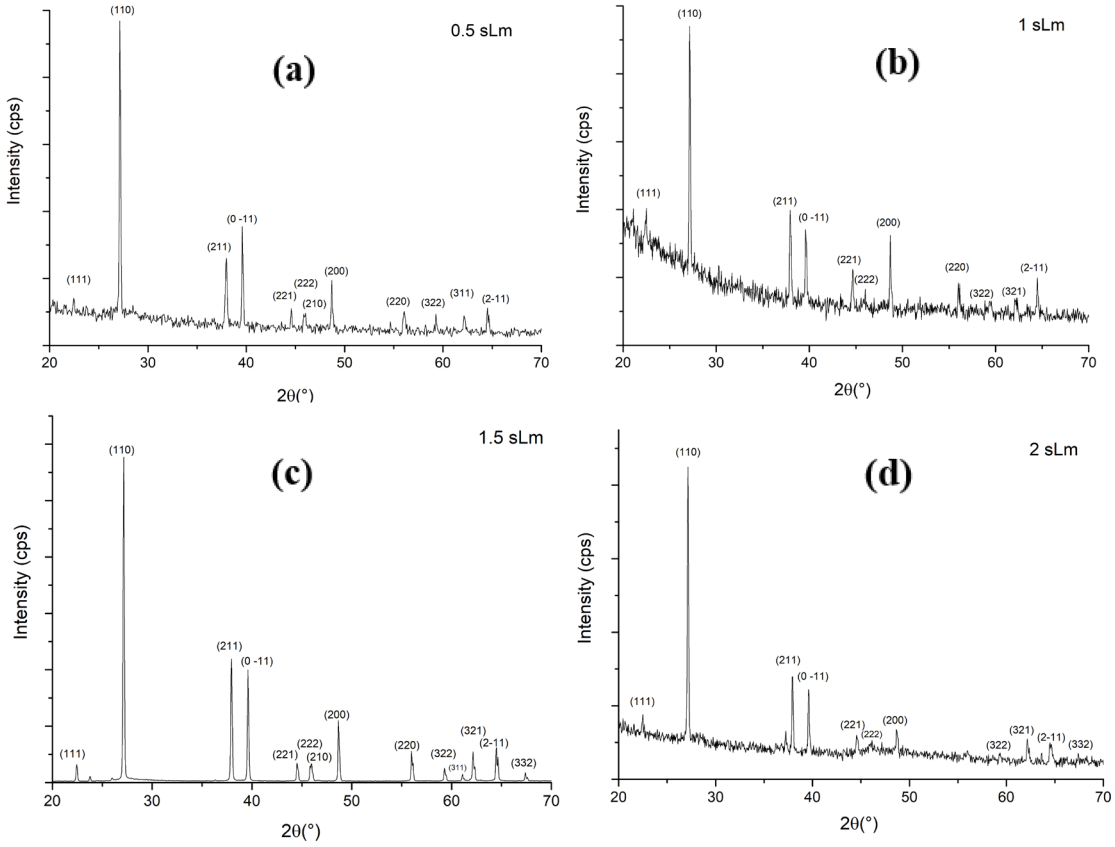

Figure 7.8 - XRD spectra of samples for different helium gas flow: (**a**) 0.5 sLm, (**b**) 1 sLm, (**c**) 1.5 sLm and (**d**) 2 sLm. The peaks have been labelled to bismuth in the trigonal R3m space group, as they are very well correlated with literature values for peak position and intensities.[32]

XPS spectra in the Bi 4f region, instead, show only the spin-orbit components of Bi-O binding in the α-Bi_2O_3 phase (Figure 7.9a-b). Usually the Bi 4f electrons assigned to elemental Bi produce a peak at a binding energy of 157 eV, while for the oxide phase at 159 eV. Both components have spin-orbit contributions separated by $\Delta E_b = 5.3$ eV. These spectra have been calibrated to C 1s peak at a value of 284.8 eV. No apparent variation is observed among the different samples explored.

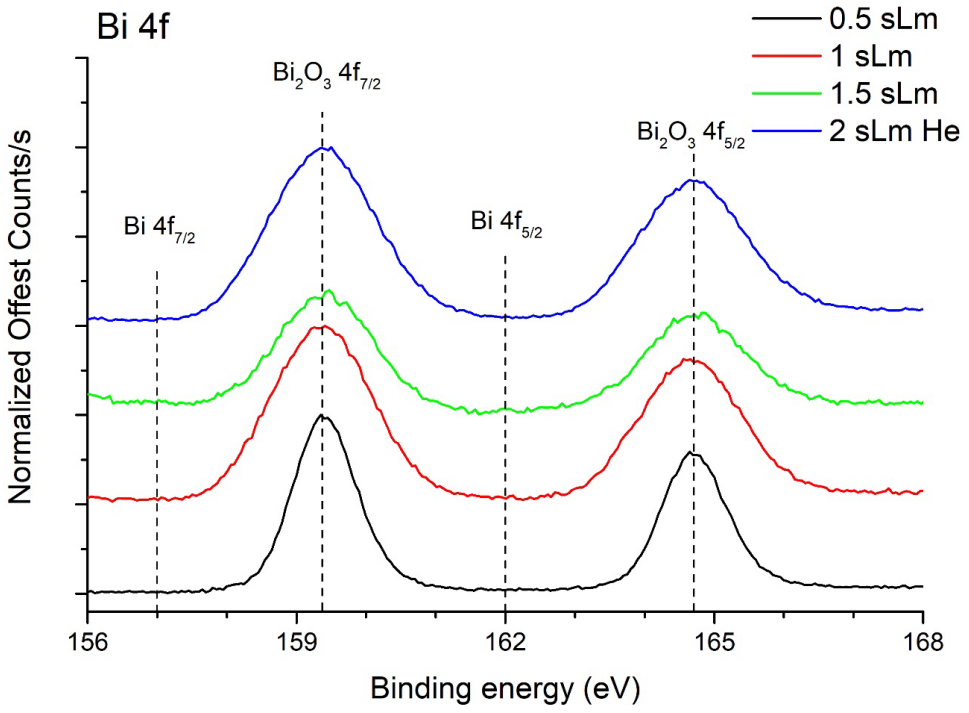

Figure 7.9 - XPS spectra of samples in different experimental conditions in the region pertaining to Bi 4f photoelectrons. The two peaks observed for all the samples are spin-orbit components that fall in the binding energies assigned to Bi in α-Bi_2O_3.

The contrast between the results with XPS and those obtained from XRD and TEM measurements will be discussed further in the text. The SEM micrographs (Figure 7.10a) show that when directly deposited on a Si wafer, particles tend to agglomerate in larger micron-sized assemblies. Along with the secondary electron image, a representative EDX spectrum acquired in a particle abundant area is shown (Figure 7.10c) and the EDX mapping of the whole area (Figure 7.10b). The result of the mapping indicates the overwhelming presence of bismuth and a minor presence of oxygen and carbon. The EDX spectrum in Figure 7.10c further corroborates, for the most part the metallic phase of the particles and shows a surprisingly low amount of oxygen (< 1 wt.%).

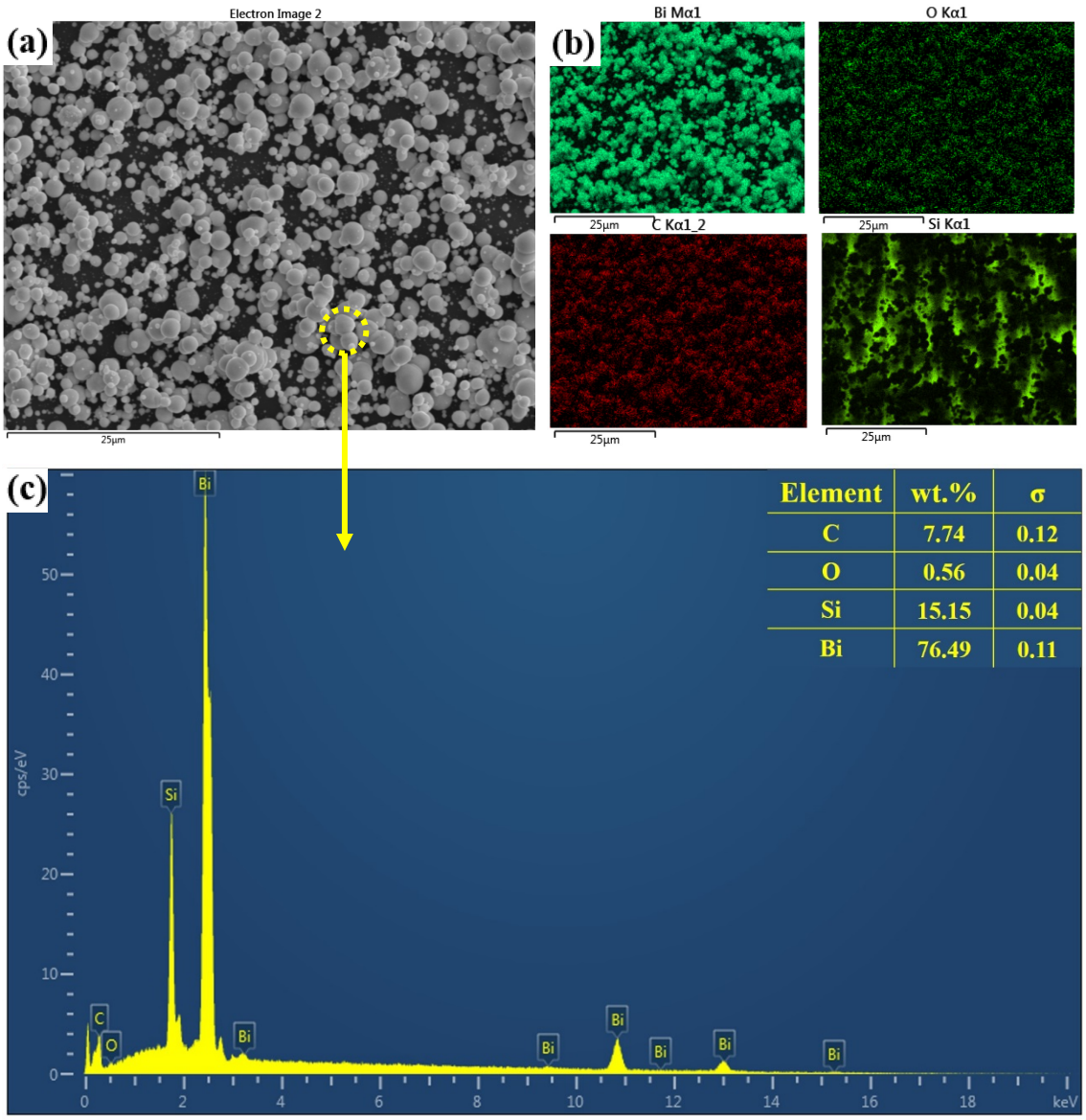

Figure 7.10 - *left* Secondary electron image of the sprayed films, showing micron-size agglomeration of particles, *right* EDX mapping of the same area that shows a dominant contribution from elemental Bi and minor presence of adventitious C and O. Also shown the background from the Si wafer along with beam shadowing effects.

Except for XPS analysis, which indicate the strong presence of a bi-oxide phase, all other characterization methods confirm the phase of the particles to be metallic bismuth with no or very minor Bi-oxides present. As the XPS analysis only probes the top layers (< 10 nm) of deposited nanoparticles we can infer that the synthesis process produces highly crystalline Bi nanoparticles, where those exposed to the atmosphere tend to oxidize completely. We can note that X-rays in XRD are generally penetrating much more (> µm) and characteristic X-rays emitted by the electron beam in the SEM are typically generated from 0.5 to 1 µm below the surface.

The replication of synthesis with the same nominal conditions gave a certain variability of the results, in terms of mean diameter of the nanoparticles. Figure 7.11 shows the results of particle size measurements for different samples, which shows variability due to the process parameter sensitivity. The particles size has been assessed also using the Scherrer method from XRD spectra (red circles in Figure 7.11) assuming a spherical shape. The method consists of fitting high resolution XRD peaks, whose full width at half maximum is related to the lower bound of the particle size in the size distribution as: $L = \frac{K\lambda}{\beta \cos\theta}$, where K is a constant that depends on the shape of crystallites (0.9 for spheres), λ is the wavelength of exciting X-rays, β is the FWMH obtained by a Gaussian fit of the chosen peak at 2θ detection angle (in our case the Bi(110) peak at $2\theta = 27°$, see Figure 4).[37,38] TEM size assessment (black squares in figure 7.11) shows that despite the average particle diameter can vary from sample to sample (± 2 nm), a general trend can be observed as function of the gas flow. The Scherrer method generally is sensitive to the smallest sizes of the distribution,[39] so that smaller values are systematically expected whenever the size distributions have a broader line shape (0.5 sLm and 2 sLm He). Given this variability of particles size with a chosen gas flow, the experimental samples will be distinguished by particle size for further analysis.

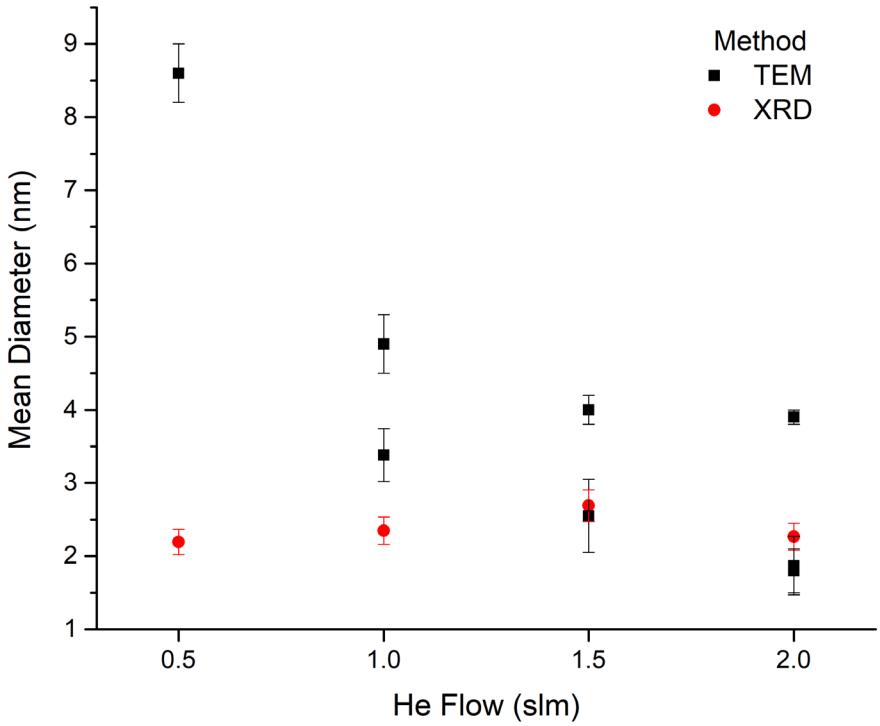

Figure 7.11 - Particle mean diameter obtained from different techniques for different samples. Each data-point corresponds to a sample synthesized at the corresponding flow; error bars represent the variance of the fitted distribution. Apart from the values obtained by the Scherrer method for the lower flow condition, there is trend for particles to be smaller at higher flows of precursor gas. Error bars are uncertainties on the fits.

7.3.3 Optical characterization

UV-Vis spectrophotometry has been performed to study the optical properties of the Bi nanoparticles and the effect of their size. This has been done on colloids obtained by placing a vial with ethanol 0.5 cm below the exit nozzle of the reactor. The contribution of scattering has been evaluated by comparing the spectra acquired at the transmittance port and a measurement at the center of the integrating sphere (see section 5.3.5 for further details). The spectra were identical within 1% of the signal, hence scattering gave a negligible contribution. Consequently, the absorption properties are derived from transmittance spectra measured at the transmittance port of the spectrophotometer, by comparing with the intensity of light transmitted by a cuvette with bare ethanol. Figure 7.12 shows the transmission spectra for selected samples with particularly different particle diameter and referenced to a cuvette with only ethanol. The results show that most of the colloids have a non-negligible absorption in the UV-region, with different thresholds depending on the particle diameter. Also, with the exception of the spectrum for the 4.9 nm diameter particles, the spectra present a shoulder peak whose wavelength decreases as the particles size decreases. The high transmittance and absence of the shoulder peak in the spectrum of the 4.9 nm diameter particles can be attributed to a small concentration of particles in this particular sample.

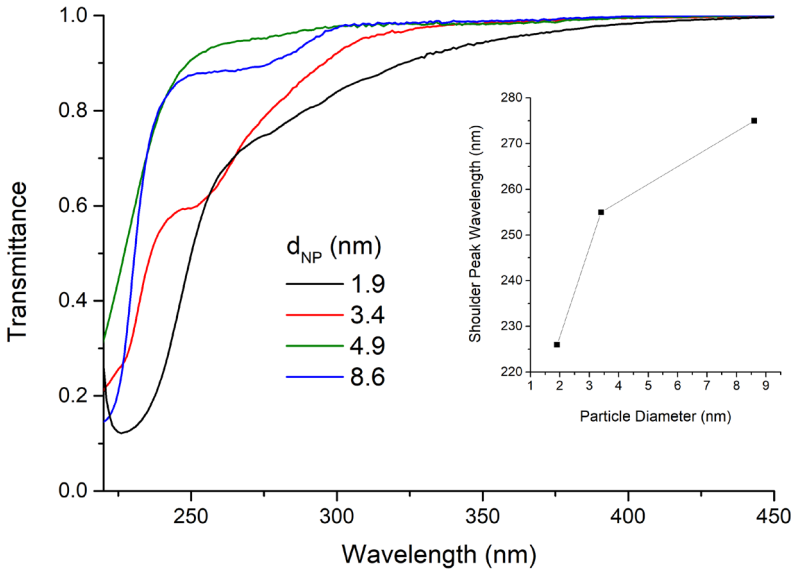

Figure 7.12 - UV-VIS transmittance measurement of colloidal samples with different particle mean diameter. A lower transmission is due to absorption of light from particles. A shoulder is also present, whose peak wavelength shifts as s function of particle's size (*inset*).

Different studies reported similar features in the UV-VIS spectra of small Bi nanoparticles with comparable results for the particles size in this study. [18,29,31,40,41] The origin of the shoulder peak in the absorption spectra (inset in Figure 7.2) is still debated. Some studies assign this to localized surface plasmon resonance,[40,41] others to the presence of Bi(III) species in solution[18] or else to inter-band transitions with large oscillator strength.[29,31] In an attempt to extract a value for a bandgap from UV-VIS data, Tauc plots for indirect and direct transitions were produced (Figure 7.13). From the literature it is not obvious whether to expect one or the other kind of transition, as even if Bi has indirect bandgap in its bulk form (semi-metal), the effects of confinement on the band structure are expected to be complicated and a direct bandgap may appear at a certain size.[42,43] The plots show that smaller particles start to absorb light more efficiently at lower energy. Energy bandgaps from Tauc plots of both indirect (Figure 7.13a) and direct transitions (Figure 7.13b) were estimated only for the spectra that showed linear parts unambiguously (1.9 nm and 3.4 nm).

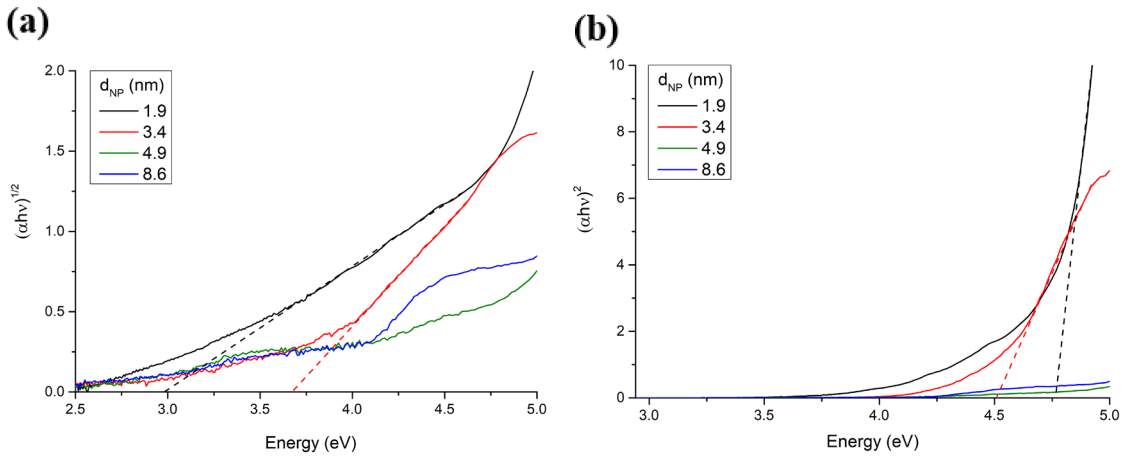

Figure 7.13 - Tauc plots of colloidal samples assuming Indirect transitions (**a**) and Direct transitions (**b**). Smaller nanoparticles start to absorb at lower photon energies, and the energy threshold appears lower when calculated as indirect transitions. In the case of bigger particles, it is not possible to unambiguously identify a linear region to extract a value for the bandgap.

The results of the plot are presented in table 7.5, the sample with smaller mean diameter (1.9 nm) has larger direct bandgap and smaller indirect bandgap than the sample with bigger mean diameter (3.4).

mean d (nm)	Indirect E_g	Std.Error (±)	Direct E_g	Std.Error (±)
1.9	2.99	0.03	4.8	0.2
3.4	3.66	0.01	4.5	0.1

Table 7.5 - Extrapolated values of bandgaps and relative errors from the Tauc plots

In addition, the colloidal samples exhibit photoluminescence (PL) emission when excited with a UV light source (Figure 7.14a). Only the samples with smaller particles (≤ 3.4 nm) show a clear peak structure, while the bigger ones (≥ 4.9 nm) show a much broader (in λ) emission. By comparing the normalized spectra (Figure 7.14b) it is possible to notice that peak wavelengths shift to smaller values for smaller mean particle size.

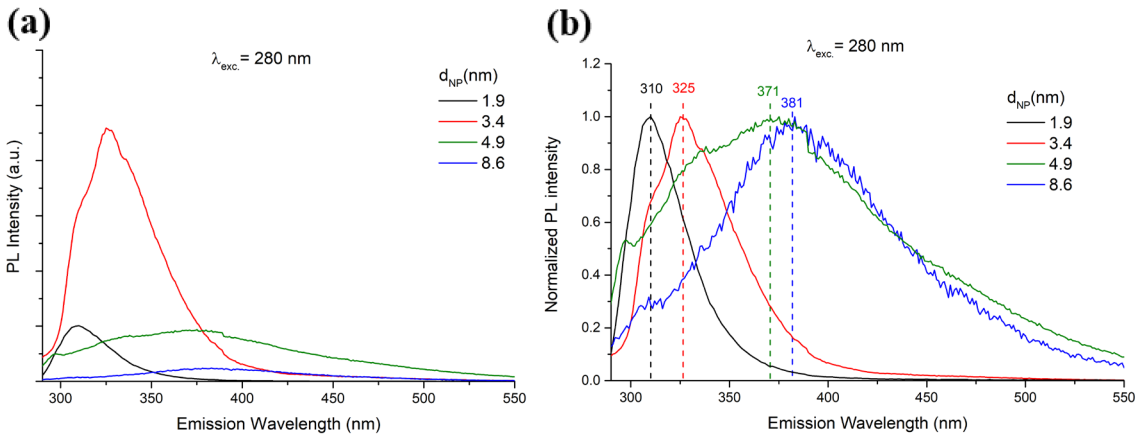

Figure 7.14 - (**a**) PL emission spectra of the samples with different particle mean diameter excited at 280 nm showing weak broad peaks for the particles bigger than 3.4 nm. (**b**) Normalized version of the PL spectra to show the increase of the maximum peak wavelength with increasing particle size.

The emission spectrum of the sample with smaller particles has been studied more in detail as it showed a simpler peak structure, in function of the excitation wavelength (Figure 7.15). The peak wavelength does not change by changing the UV excitation wavelength. The excitation spectrum at 310 nm emission wavelength was also acquired (inset in Figure 7.15). This spectrum is the measurement of the intensity of the PL maximum peak as a function of the wavelength of exciting photons. The excitation

spectrum shows a double peak structure, which combined with the constancy of emission wavelength, is reflecting the structure of the density of states in the valence band.

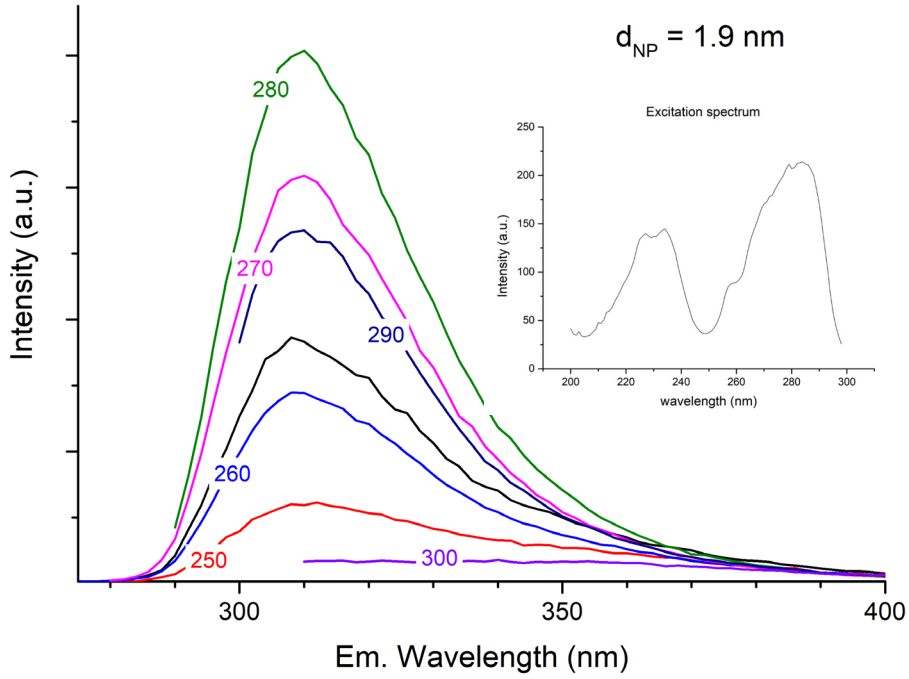

Figure 7.15 - PL emission spectrum of the 1.9 nm mean diameter sample for different UV excitation wavelength. No shift in the peak maximum is observed. The inset shows the maximum intensity of the peak (310 nm) in function of the excitation wavelength.

Also, the PL emission of the 1.9 nm sample shows a remarkable stability over a period of 3 months (minimum), with emission spectra that do not change after three months from the first measurement (Figure 7.16).

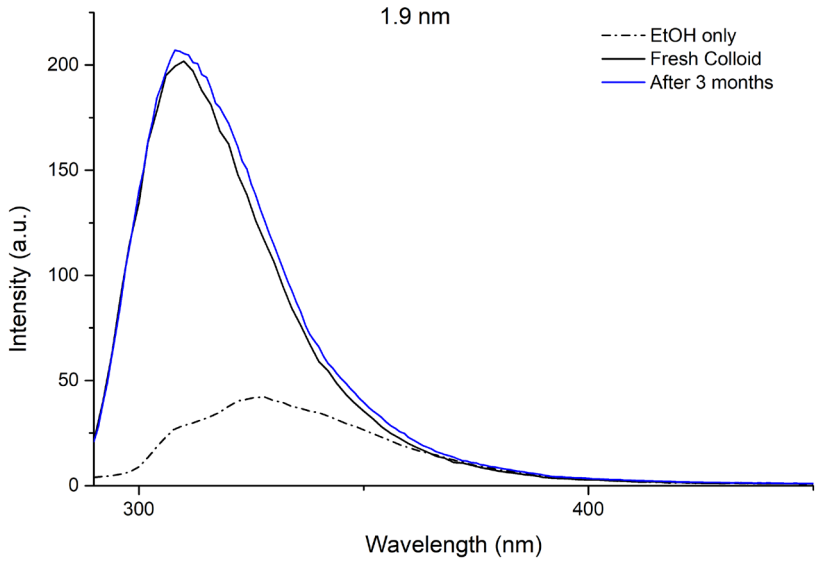

Figure 7.16 - Comparison of PL emission spectra of the 1.9 nm mean diameter sample at different times. "Fresh colloid" refers to the measurement performed right after the synthesis, while the blue spectrum is measured after 3 months have passed, a negligible change in the spectra is observed. The emission spectrum of only ethanol is shown for comparison.

The emission peak wavelength does not change with excitation wavelength, which is a necessary but not sufficient condition for the emission to originate from band-to-band transitions. In fact, PL of nanoparticulate samples can be strongly affected by surface states and impurity states in the middle of the gap, as these are usually preferential recombination centers for electrons and holes, and less importantly affected by changes in the size distribution. Hence, it is not always straightforward to associate the PL emission to an inter-band transition without prior knowledge of the impurity-related states.[44] If it is assumed that the emission of samples comes from an inter-band transition, than the effective bandgap for the samples which show a clear peak structure would be obtained by the maximum peak wavelength λ_{max} as $E_g = hc/\lambda_{max}$, where h is the Planck constant and c is the speed of light ($hc = 1240\ eV/nm$). Thus, the obtained values are 3.8 eV for the 3.4 nm samples and 4.0 eV for the 1.9 nm sample. The table 7.6 show the estimated values of bandgap with UV-Vis absorption and PL. By comparing the values of bandgaps obtained from Tauc plots and PL emission maxima, it is possible to notice that the bandgap estimated with PL is always intermediate between the indirect and direct bandgap calculated from Tauc plots. This fact could be explained considering the PL-derived bandgap as an effective bandgap arising from the combination of both type of transitions contributing to the PL emission. However, it is noticed also that the PL

bandgap decreases with increasing size as the direct bandgap from UV-Vis does, which suggest that these two values may refer to the same interband transition.

Particle diameter (nm)	UV-Vis direct Bandgap (eV)	UV-Vis indirect Bandgap (eV)	PL Bandgap (eV)
1.9	4.8	2.99	4
3.4	4.5	3.66	3.8

Table 7.6 – Values of bandgap estimated through Tauc plots extrapolation from UV-Vis spectra and the PL emission maximum for the two samples characterized by both methods.

7.3.4 Electron levels in Bi QDs

Bulk bismuth is a semi-metal whose Fermi level lies across an almost completely filled valence band and a poorly filled conduction band at different values of the crystal momentum (Figure 7.18b) at the T-point and L-point in the Brillouin zone (Figure 7.17a). The energy band at these points, here approximated by parabolic bands, have particularly different curvatures, hence different effective masses of electrons and holes in the two regions.[22,45] The low free carrier concentration of both sign carriers (electrons and holes) results in poor electrical and thermal conductivity. In the bulk form, the overlap between band structures (E_0 in figure 7.17b) at L- and T-point of the Brillouin zone is of -38 meV, while the energy gaps between valence and conduction bands at the same symmetry point is 13.6 meV at L-point and 40 meV at the T-point (E_{gL} and E_{gT}).

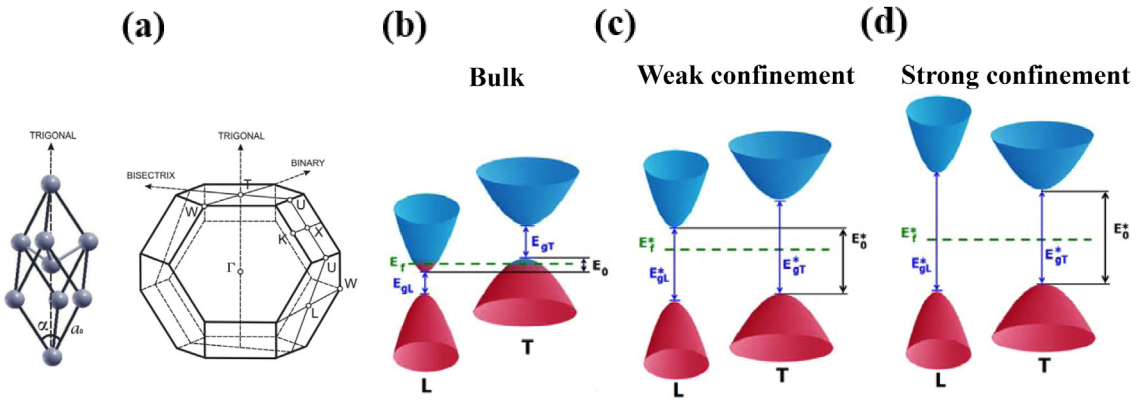

Figure 7.17 - (**a**) Rhombohedral unit cell relative to Bismuth crystal structure and relative Brillouin zone, where the principal symmetry points and symmetry axis are indicated. (b-d) Schematic diagram of the energy bands at symmetry point T and L, approximated to ellispoidal profiles. The different curvature of the ellipsoidal surfaces is related to different mass components of the charge carriers occupying the electron states (higher curvature = higher mass or inertia), in blue empty states, in red occupied ones. (**b**) In the *bulk form* the T valence band and L conduction band overlap by 38 meV and the Fermi levels falls in between, giving semi-metallic behavior. Two confinement regimes are then distinguished (**c**) a *weak confinement regime* were the lowest energy transitions are indirect between the T valence band and L conduction band, and (**d**) *strong confinement regime* that is characterized by direct transitions within the T-point bands. Adapted from[19].

Confinement effects for Bismuth are expected to set in at relatively big particles size because of the low effective masses of carriers in the ground state valence bands (at T point). It has been reported to happen at 30 nm for Bi thin films[27] and 65 nm for Bi nanowires[20,46] through temperature dependent resistivity measurements, 40 nm for embedded nanoparticles[47] via electron energy loss spectroscopy of volume plasmons and 3.3 nm for colloidal particles[18] with IR absorbance.

Butkutè et al.[24] introduced a simple model for the describing the effects of quantum confinement in Bi QDs by assuming the electron energy bands at points T- and L- as ellipsoidal isoenergetic surfaces with different components of the mass tensor for each direction (at T- and L- points). The details of the band structures at points T and L considered are summarized in table 7.7.

Symmetry point	E_g (meV)	E_f (meV)	Mass tensor components	m^*
T	407	11.6	$m_1 = m_2 = 0.059\ m_e$ $m_3 = 0.634\ m_e$	$0.0846\ m_e$
L	15	26.6	$m_1 = 0.00521\ m_e$ $m_2 = 1.21\ m_e$ $m_3 = 0.0136\ m_e$	$0.0113\ m_e$

Table 7.7 - Details of the energetics and mass components of ground state energy bands of bulk Bismuth at points L- and T- of the Brillouin zone assuming elliptical band (parabolas in two dimensions), m_e is the mass of electrons at rest. m^* is the effective mass considered in the model.[25]

They described the effects of quantum confinement as the independent widening of each bandgap (E_{gL} and E_{gT}) of different amounts for electrons and holes at symmetry point *k* (T or L). Assuming a spherical confined particle (quantum dot) the ground state of electrons (holes) in a quantum dot can be approximated by:[24]

$$W = \frac{\pi^2 \hbar^2}{2m^* r_0^2} \qquad \text{Eq. 7.1}$$

where m* is the average effective mass in each band:

$$\frac{1}{m^*} = \frac{1}{3}\left(\frac{1}{m_1} + \frac{1}{m_2} + \frac{1}{m_3}\right) \qquad \text{Eq. 7.2}$$

where m_1, m_2 and $m_3$are the principal effective masses of the ellipsoidal valley. In this approximation, each band *k* (= T or L) effective bandgap (E^*_{gk} in Figures 7.17c-d) can be expressed as the sum of the confinement energy contributions of electrons *e* and holes *h*:

$$E^*_{gk} = E_{gk} + W_e + W_h \qquad \text{Eq. 7.3}$$

The result is that given the initial difference between the bandgaps at each symmetry points ($E_{gL}$and E_{gT} in Figure 7.17b) and the different values of W_e and W_h for the two bands (which originate from differences on the effective masses in the bands) there will be two crossing between band edges by decreasing the size of the QDs. The widening of

the L point bandgap is faster (in respect to the T-point one) due to a lower effective mass of carriers occupying the electron states. The situation is illustrated in the plot in figure 7.18, where the Fermi level is taken as the reference zero energy. The first crossing (border between red-shaded area and green shaded area in Figure 7.18) is happening at r_0=70 nm, the L point conduction band crosses the T-point valence band. The smallest energy bandgap (nearer to the Fermi level) in this region (green shaded area in Figure 7.18) is between L-point valence band and the T-point conduction band, hence the material will behave as an indirect bandgap semiconductor (called weakly confined QD in Figure 7.17c). The maximum value of this indirect bandgap is 0.4 eV, where the second crossing happens (r_0=20 nm). Then, the L- point conduction band edge surpasses the T-point conduction band. At radii smaller than this value (blue shaded area in figure 7.18) the smallest energy bandgap coincides with the effective T-point energy gap (a regime called Strong confinement in Figure 7.17d), which is expected to be direct in nature.

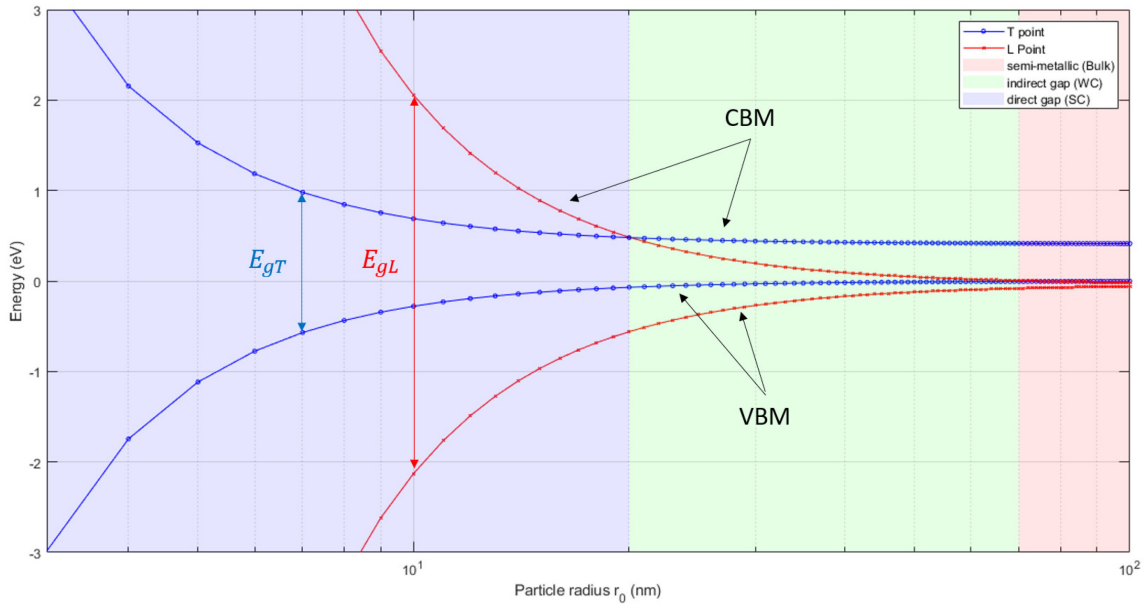

Figure 7.18 - Confined T- and L- points energy band extrema in function of particle radius for Bi QDs following the model presented in the text. The contribution of confinement energy to the bandgap widening is different for the two bands given the different values of effective masses. Colored areas define different regimes for transitions, following the character of the smallest bandgap near the Fermi level. The zero of the energy scale is the Fermi level taken as a reference.

The experimental results obtained in this work agree qualitatively with the prediction of this model by considering the direct bandgaps measured:

1. An increased UV-VIS absorption for smaller particles (< 4.9 nm), which can be determined by the direct transition regime;

2. Both the direct bandgap calculated with UV-Vis and PL peak emission increases with decreasing particle size, which can originate from the widening of the bandgap.

Both conditions can originate from the fact that light absorption and emission cross sections are much larger for direct transitions, hence the higher absorption and the stronger PL signal for small particles (< 4.9 nm). A comparison between measured and theoretical values of bandgaps is presented in table 7.8. While the order of magnitude of measured and predicted values is comparable, the bandgaps predicted by the model are systematically larger. The diameter predicted by model for particles having the bandgaps measured by UV-Vis would be 3.6 nm and 3.9 nm for the 4.8 eV and 4.5 eV bandgaps respectively.

Particle diameter (nm)	UV-Vis Direct Bandgap (eV)	Theoretical Direct Bandgap (eV)
1.9	4.8	8.1
3.4	4.5	5.2

Table 7.8 - Comparison between the different bandgaps obtained from UV-Vis spectroscopy of two samples and the value of the T-point effective bandgap of a quantum dot with an approximate model.

The comparison with the model presented and the experiments in this work evidences that the model may not be suitable to describe the bandgap of quantum dots in this size range. The assumption of ellipsoidal bands is likely a crude approximation since the L-point band dispersion relation is known to be particularly non-parabolic for bismuth [22,45,48], and probably exciton binding energies might play an important role in the energy

balance. Similar dynamics are expected though, in terms of transitions to a semiconducting state and from indirect to direct character. The precise values of bandgap and limiting size might be different with a full theorical treatment.

7.3.5 Summary and discussion

A purely helium plasma at 50 W applied power with a 1-mm diameter Bi wire as grounded electrode resulted in the formation of crystalline Bi nanoparticles with average diameter comprised between 1.9 nm and 8.9 nm. The process is fast and runs right below the conditions needed to melt the wire but can easily develop into thermal instabilities. The particles synthesized are spherical, well-dispersed and do not show signs of oxidation when form a colloid with ethanol. Instead, when directly deposited on a solid substrate and exposed to atmosphere, the exposed ones on the top layer are easily oxidized as testified by XPS measurements. Analysis of low-magnification TEM shows a certain variability of the process in terms of throughput and particle size, with the same nominal synthesis parameters (i.e. power and flow of helium gas). Within this experimental variability, however, the average particles size is observed to get smaller with higher helium flows. Moreover, in high flow conditions the particles size distribution is better described by a Gaussian size distribution, while a lognormal function is more appropriate for lower flow conditions. A Gaussian distribution is expected when the formation mechanism provokes random symmetric fluctuations around a mean value, hence the same number of bigger and smaller particles (with respect to the mean value) are formed. Instead, the log-normal distribution for particle synthesis is the result of a growth mechanism, that unbalances the smaller particles in favour of bigger ones. Hence the distribution will show a higher proportion of particles bigger than the mean value (skewed to large size particles). The potential implication for this is that the reactor used can be made to operate in a way to suppress particle growth completely. The way total gas flow can influence the process is three-fold. It can influence the heat balance of the wire, increasing or decreasing its temperature, or it can accelerate the extraction of species from the plasma region or else it can control the precursor species density in the gas phase. Similarly, particles can be influenced in the same way. If the formation process depends on the temperature of the wire as an evaporation and condensation process, it is expected that higher wire temperatures that result at lower total flow stimulate a faster evaporation rate. This in turns implies a higher condensation rate of the vapours and, consequently, a

bigger size of condensing nuclei. Conversely a higher flow of gas, which result in increased heat loss from the wire and lower temperatures, results in smaller particles. Once the particles are formed (disregarding the detailed formation process) a higher gas flow decreases the particles size by reducing the residence time in the plasma by limiting the chance to grow in flight.

The optical characterization of some samples shows evidence of stronger absorption of light and PL emission for smaller particles (<4.9 nm) and bandgap widening for decreasing size, sign of a transition to a semiconductive state with direct bands. A model that considers the quantum confinement starting from ellipsoidal bands at L an T points in the Brillouin zone agrees qualitatively on the trend with size and in the order of magnitude of calculated gaps.

7.4 Antimony (Sb) QDs

7.4.1 Interest in Sb QDs

In this section we demonstrate the synthesis of Sb nanoparticles with a reactor setup analogous to the one used for the synthesis of bismuth nanoparticles. However, in this case a 2 mm diameter Sb wire is used (the smallest diameter wire available on the market, given the low hardness and brittleness of the material) and the capillary diameter changes accordingly as described in section 7.2.1.

The bulk electronic properties of antimony are very similar to those of bismuth as they belong to the same group in the periodic table (Sb with a lower atomic number); for instance, they both show semi-metallic behaviour and therefore similar quantum confinement regimes are expected. Antimony nanostructures are recently receiving attention due to some interesting applications as high-capacity alloy-based Li- an K- ion batteries,[49,50] for non-linear optical glasses[51] and for the possibility to develop an excitonic insulator.[52] Binary alloys of antimony and bismuth are interesting semiconductors for low temperature superconductors,[53] topological insulators[54] and for thermoelectrics.[55] Oxides of antimony nanoparticles instead are already used for many applications in chemistry. For example as catalysts for the production of PET plastics, as a flame retardant synergist and for optical materials, due to their high refractive index.[56]

After fixing the Sb wire to the Perspex frame, helium gas is flown through the reactor and the ignition of the plasma is accomplished at low power (10-15 W from the power supply). The power and flow conditions are determined by fixing the flow and finding the applied power that result in the melting of the wire or the glass capillary. Then, the process conditions are operated at a slightly lower power (1 W to 10 W below the mentioned conditions). The only parameter varied to control the synthesis is the flow of helium input gas, two cases are explored for the Antimony process, 0.25 sLm and 1 sLm. During the synthesis with the 2 mm diameter sacrificial Sb wire, the applied power is not limited by the wire melting (as in the case of Bismuth), instead the process temperature upper limit is determined by the damage of the glass capillary (at 90 W applied power) following the development of a strong filamentary discharge from the wire tip. Synthesis and deposition, without incurring in instabilities and damage, is practiced at 80 W applied power. However, it should be noted that the throughput is lower when compared to the process for the synthesis of Bi nanoparticles for the same processing time, as visually

witnessed by the deposition on solid substrates. Collection directly in ethanol produces colloids that are transparent and do not show any sign of agglomeration or sedimentation. These colloids are used for TEM imaging, after drop casting it onto an ultrathin carbon grid (Agar Scientific) and drying the grids overnight under the illumination of a halogen lamp. For XPS, samples are directly deposited on pieces of n-type Si (100) wafers.

7.4.2 Material characterization

The outcome of the synthesis process is a collection of small spherical nanoparticles, as testified by low magnification TEM bright field images (Figure 7.19a-b). The nanoparticles are 1-3 nm in diameter, crystalline (see insets in Figures 7.19a-b) and are embedded in an amorphous matrix. The particles seem of a similar size for samples synthesized at different helium flow conditions.

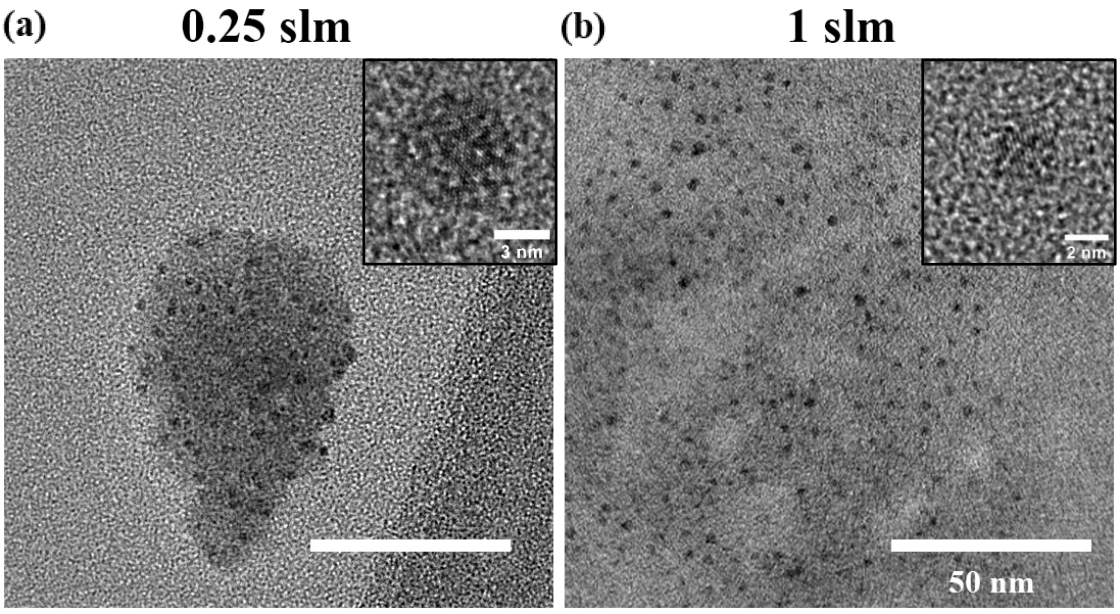

Figure 7.19 - Low magnification bright field images showing the outcome of the synthesis process for different helium flows (**a**) 0.25 sLm and (**b**) 1 sLm He. The insets show high resolution images of isolated particles, displaying phase contrast due to their crystalline nature. Scale bars for low resolution images are of the same length 50 nm.

The particles are unstable under the 200 kV electron beam, a condition that leads to visible coalescence of particles with beam exposure time. In fact, Figure 7.20 shows an example for the 0.25 sLm He flow conditions. The low magnification images are taken 30 seconds after the other in the same area, there are more numerous particles in the first image and

tend to become fewer in number and bigger in size with exposure time. Therefore, precautions have been taken in order to reduce the electron dose on the sample to assess

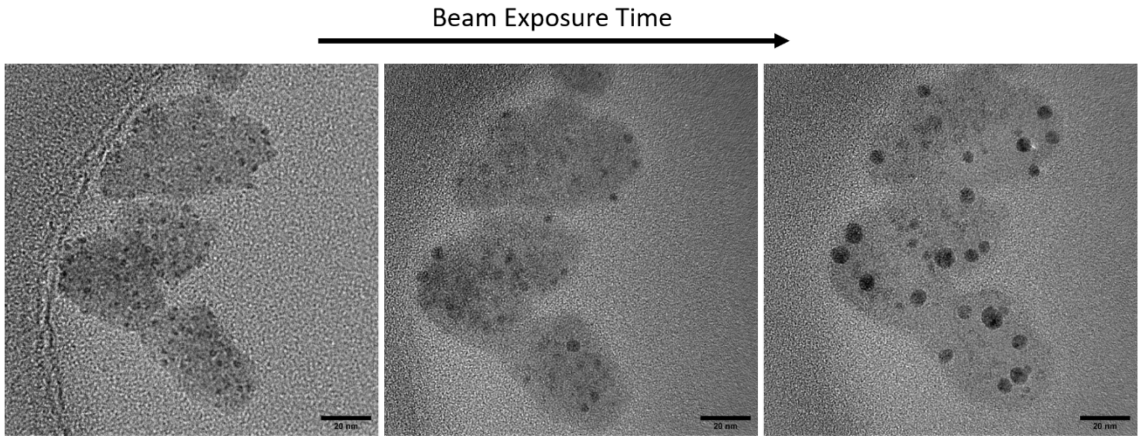

Figure 7.20 - Series of low magnification TEM images of the 0.25 slm He sample in the same area, clearly showing particles coalescence stimulated by the exposure to the electron beam.

the size distribution from bright field images. This has been achieved by spreading the beam until no growth is observed.

The statistical study of particles size distribution from TEM low magnification images highlights a small difference in the average diameter and size dispersion of particles synthesized in different flow conditions (Figure 7.21). Higher flows of helium through the wire reactor result in slightly smaller particles (mean diameter 1.6 nm @ 1 sLm vs 1.7 nm @ 0.25 sLm) and a likewise smaller size dispersion (mean diameter 1.8 nm @ 1 sLm vs 2 nm @ 0.25 sLm). In this case both distributions are well fitted by a log-normal distribution. Even though precautions have been taken to decrease the beam exposure time, it is not possible to exclude that this distribution function might be bi-modal as the result of coalescence between particles.

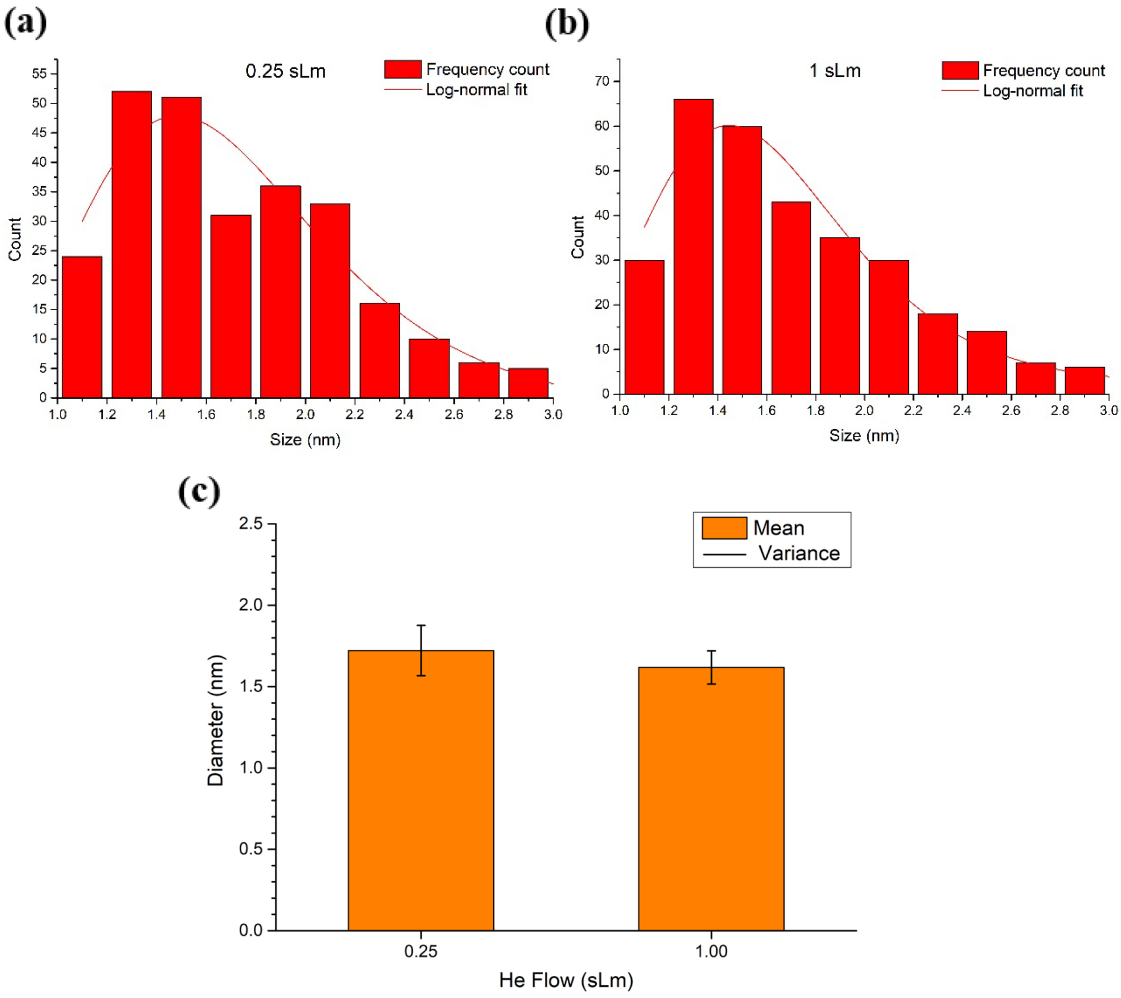

Figure 7.21 - Size distribution estimation from TEM images and relative analysis. Frequency counts histograms and distribution fit for samples produced with different He flows (**a**) 0.25 sLm and (**b**) 1 sLm. (**c**) Fit parameters extracted from the two samples.

To understand the composition and structure of the nanoparticles, we performed analysis of high-resolution TEM images of crystalline particles and selected area diffraction patterns. In high-magnification imaging, a higher fluence of electrons concentrated in a smaller area is necessarily applied and therefore likely leading to particle growth. Hence, particles in high-resolution images are likely to have grown from their original size during the image acquisition time (0.5 s). Nevertheless, we used a procedure to filter HR-TEM images based on their Fourier transform to reduce the noise and distinguish the diffraction fringes and measure the resulting d-spacings. An example of the procedure applied to a 4 nm particle is shown in Figure 7.22.

For each HR-TEM the Fast fourier transform (FFT) is calculated (inset in Figure 7.22a). A circular mask is applied to the spots in the in the FFT, which are related only to the periodic structure in the parent image in Figure 7.22a. The mask cleans the image from all the non-periodic structures when the inverse FFT is calculated (Figure 7.22b). The line intensity profiles of the periodic structures (insets in Figure 7.22b) are then used to calculate the periodicity of the diffraction spots which represent the d-spacings of diffracting planes. If two of them are calculated in two different directions, than a structure is uniquely identified. In the case of Figure 7.22 the calculated d-spacings can be assigned within the uncertainties to the (211) and the (0-11) families of crystal planes of rhombohedral Sb (see table 7.9 for comparison).

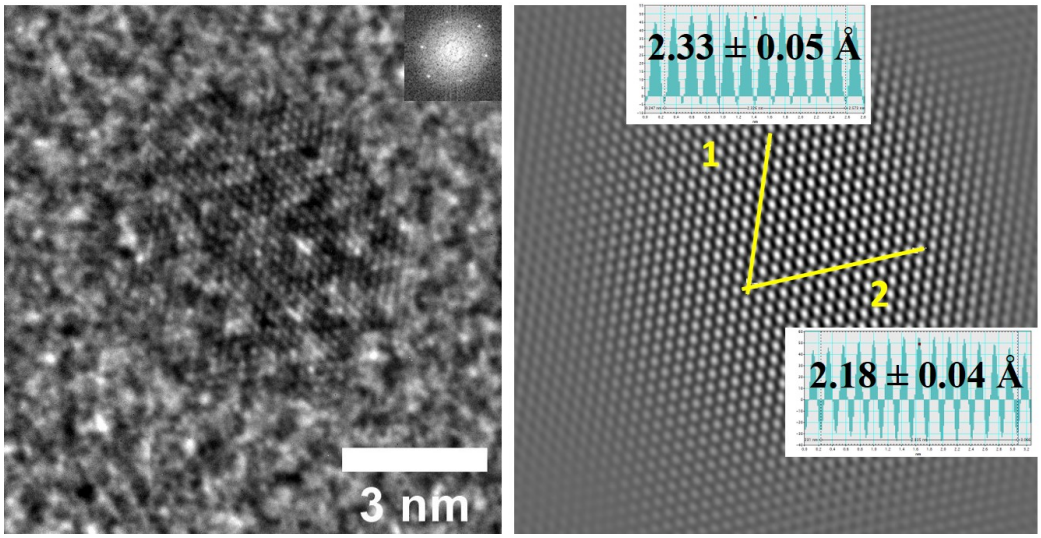

Figure 7.22 - Example of FFT filtering of a high magnification image of a nanoparticle showing phase contrast and assessment of the resulting d-spacings. (*left*) HRTEM of the nanoparticle with its power spectrum (*inset*). (*right*) Inverse FFT of the power spectrum filtered from the continuous background, in the inset the line profiles relative to yellow line used to calculate the d-spacings.

The crystal structure could be confirmed further studying SAED patterns of groups of particles, which could be carried out with lower electron fluence and therefore not affected by changes in the samples (figure 7.23). No significant variation is found between the two samples under study. SAED patterns display few spotty rings, sign of the presence of randomly oriented crystalline particles.

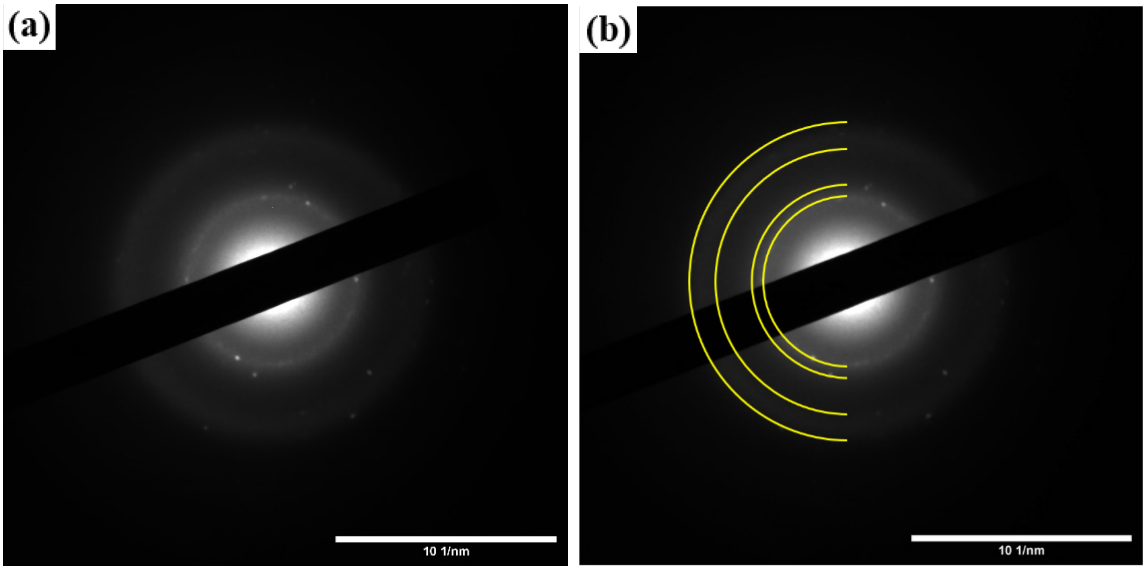

Figure 7.23 - SAED pattern of the sample produced with 1 sLm He, the identification and labeling of the measured rings can be found in table 7.10.

Table 7.9 summarizes the results from structural analysis with HRTEM images and SAED patterns. The comparison with the strongest XRD peaks of common phases of Sb and its oxides indicates that our samples are mixed phases of antimony in its rhombohedral form as well as two allotropes of antimony trioxide, an orthorhombic (o-Sb_2O_3) and a cubic phase (c-Sb_2O_3).

d_{SAED} [Å]	d_{HRTEM} [Å]	Lit. value [Å]	Assignment	Ref.
2.59 (±0.05)		2.64	o-Sb_2O_3 (012)	[57]
	2.44 (±0.05)	2.46	o-Sb_2O_3 (200)	[57]
2.29 (±0.05)	2.33 (±0.05)	2.24	r-Sb (211)	[36]
	2.18 (±0.04)	2.14	r-Sb (0-11)	[36]
	2.01 (±0.04)	1.97	c-Sb_2O_3(440) / o-Sb_2O_3 (240)	[57,58]
	1.84 (±0.04)	1.81	o-Sb_2O_3 (161)	[57]
1.68 (±0.03)		1.68/1.68	c-Sb_2O_3 (622) / o-Sb_2O_3 (113)	[57,58]

1.42 (±0.03)	1.41	r-Sb (321)	[36]

Table 7.9 - Identification and labeling of d-spacings obtained from SAED patterns and analysis of HRTEM images. Assignment to family of planes of Sb and its oxides is based on the strongest XRD peaks of each phase reported in the literature.

XPS has been used to check the composition of samples, but unfortunately the strongest photoemission signal from antimony overlaps the O 1s region; oxygen is likely to be introduced adventitiously, as samples are exposed to atmosphere before loading them in the XPS vacuum chamber. Nevertheless, it was possible to confirm the presence of antimony from a small peak in the Sb 4d region within the survey spectra (Figure 7.24), even though the low resolution does not permit to obtain information about the chemical bonding of Sb in the particles.

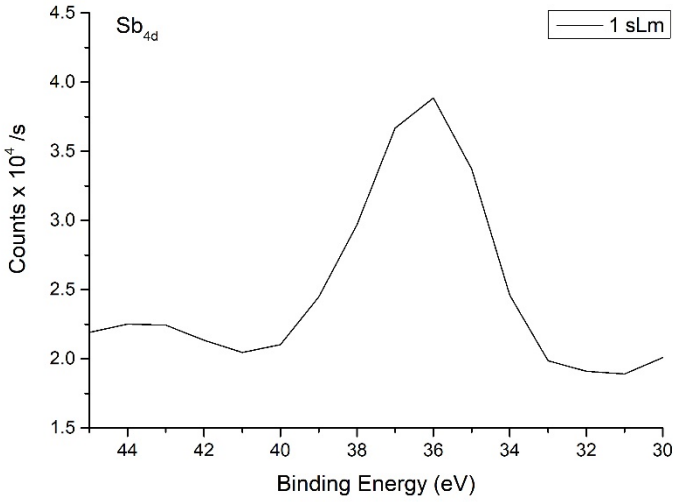

Figure 7.24 - Small peak in the survey spectra used to identify the presence of Sb within our samples. The region is associated to Sb 4d photoemitted electrons.

To summarize, these preliminary experiments proved that an He-only RF plasma process with a 2 mm antimony wire as ground electrode at 80 W resulted in the formation of crystalline 1-3 nm diameter Sb-based particles. While it seems clear from the evidence of SAED patterns and HR-TEM analysis that some particles are in an oxide phase, the presence of individual particles showing the diffraction pattern of elemental Sb (e.g. Figure 7.22) demonstrates that plasma process is able to synthesis antimony quantum dots. It is not clear whether the oxide phases are the result of synthesis or a post process oxidation due to exposure to atmosphere. The control of their phase, size and size

dispersion is limited necessarily require exploring a larger and denser parameter space. However, the process has shown better stability vs. the one used of Bi nanoparticles; hence the thicker wire setup has the potential to improve the repeatability of the synthesis process.

7.5 On the wire plasma process

7.5.1 Rationale

The understanding of the nanoparticle formation process from pure solid precursors at atmospheric pressure would be an important step to control the process and has more fundamental implications of interest to the scientific community. The physical processes happening on the surface of wires have not been understood since most of the reports are incongruent. For example, some studies speculate that ion bombardment processes may be possible if the wire reaches temperatures near the melting point,[59] while some others demonstrated that small amounts of reactive gases are needed in order to obtain particles. [60,61] In this section we study the initial state of the wires used and observe the formation of microstructures on the Bi wire at the end of the process. At the same time, we summarize and attempt to rationalize the experimental observations in order to contribute to the comprehension of the underlying mechanisms involved.

7.5.2 Characterization of wires

XPS analysis as a function of depth for the bare untreated Bi and Sb wires has been performed in order to understand the initial chemical composition. For the present plasma process, wires are only washed with isopropyl alcohol before being used in the reactor, as a preliminary step to clean from adventitious contamination. XPS spectra are acquired in the respective high-resolution regions for Bi and Sb, Bi 4f and Sb 3d respectively. Then, the wires are exposed to a 2 keV Ar^+ gun at multiple cycles lasting 12 s each to sputter the surface and expose the deeper regions of the material. At the end of each cycle a photoemission spectrum is acquired, resulting at the end in a compositional depth profiling. The results are shown in figures 7.25 and 7.26. The estimated sputtering rate for such a beam energy and dose is 1 nm per second of exposure to the ion beam, hence the last sputtering cycle exposes a layer between 100 nm and 120 nm below the top surface of wires. In the Bi 4f region, two peaks separated by 5.3 eV at 157 eV and 162.3 eV binding energies are associated to the 7/2 and 5/2 spin-orbit components of elemental Bi. While at 159 eV and 164.3 eV the 7/2 and 5/2 spin-orbit components are usually associate with Bi bonded with oxygen in the α-Bi_2O_3 oxide phase. In figure 7.25a it is possible to observe two peaks associated with the oxide phase on the topmost surface (black spectrum). Sputtering below the surface provokes the weakening of the oxide-

related peaks and the appearance of the elemental peaks even after the first cycle (~10-12 nm below), that eventually dominate over the oxide-related peaks. A residual signal assignable to the Bi_2O_3 oxide is still present deeper below the surface, as can be seen by a small oxide peak perpetually present in the last probed layer. The atomic percent of elemental Bi and Bi in the oxide phase has been quantified by peak area ratio analysis (Figure 7.25b), and results in the residual presence of 25 at.% of Bi in the oxide phase in the deepest layer probed (100-120 nm).

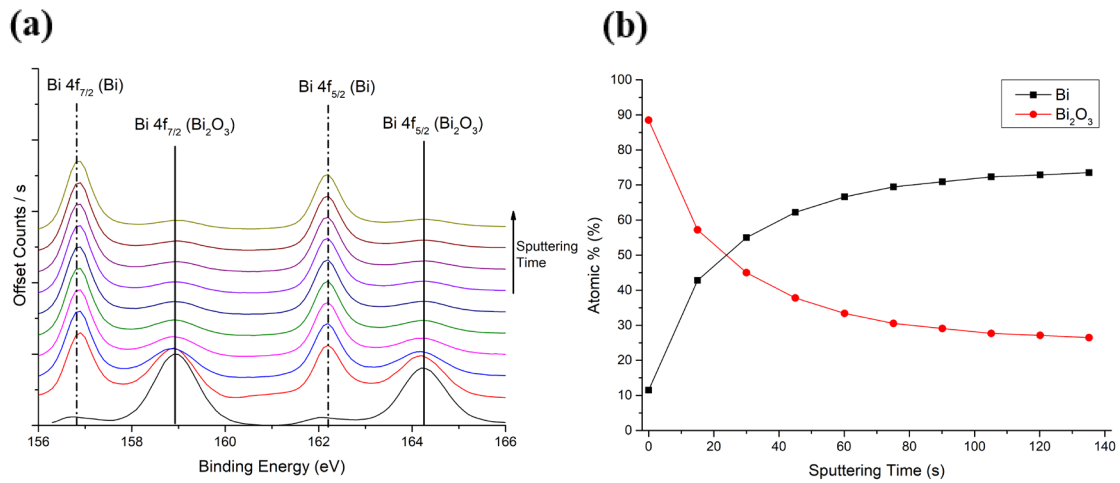

Figure 7.25 - (**a**) Bi 4f photoemission spectrum of the untreated bismuth wire as a function of depth below the surface, showing the heavy presence of bismuth oxide on the surface and a residual amount deeper beneath, (**b**) quantification of the atomic percent through peak area ratio analysis.

For antimony there are two oxides of different stoichiometry which are stable common at room temperature and the main photoemission region is Sb 3d near 530 eV binding energy (BE), region which overlaps with O 1s photoelectrons. Table 7.10 summarizes the probable peaks in this region, pertaining to antimony and oxygen related species.

Species	(spin-orbit comp.) BE (eV)
Sb metal	($4f_{5/2}$) 528.3 ($4f_{3/2}$) 537.7
Sb_2O_3	($4f_{5/2}$) 529.9 ($4f_{3/2}$) 539.3
Sb_2O_5	($4f_{5/2}$) 530.9 ($4f_{3/2}$) 540.3
O in organic C=O	531.5–532

O in organic C-O	~533

Table 7.10 - Components of Sb 3d and O 1s and assignment of relative binding energies.

As wires are exposed to atmospheric, they are expected, at least for the topmost layers, to show oxygen related to organic materials. The high resolution XPS spectra in function of sputtering time for the Sb wire is shown in Figure 7.26a. The topmost layer (black spectrum) shows a broad peak structure at 528 eV and a smaller one at 537.5 eV binding energies. Going below the surface, the broad peak is suppressed leaving small background peaks at 528 eV and 537.5 eV and a second pair of distinct peaks appears at 530.5 eV and 540 eV. Further below the smaller peaks at 528 eV and 537.5 eV grow and the pair of peaks at 530.5 eV and 540 eV are progressively suppressed. The spin-orbit components of Sb and Sb oxide related peaks are at a fixed separation in binding energy (ΔE=9.3 eV), hence if the peaks are associated to such species, the peaks structure between 527 eV and 532 eV are replicated between 536.3 eV and 541.3 eV. This permits to assign easily the peaks in the spectra, except for the topmost layer. From the second layer below (10-12 nm) there is antimony pentoxide (Sb_2O_5) which gradually vanishes with depth to give space to the pure metallic antimony. In the top layer the two peak structures (separated by 9.3 eV) are not similar, this difference is assigned to oxygen in organic species of adventitious origin. However, the presence of a peak at 537.5 eV wider than the metallic peaks deeper below the surface suggests the presence of the trioxide (Sb_2O_3) phase on the topmost layer. Summarizing, the antimony wire shows oxides of different stoichiometry

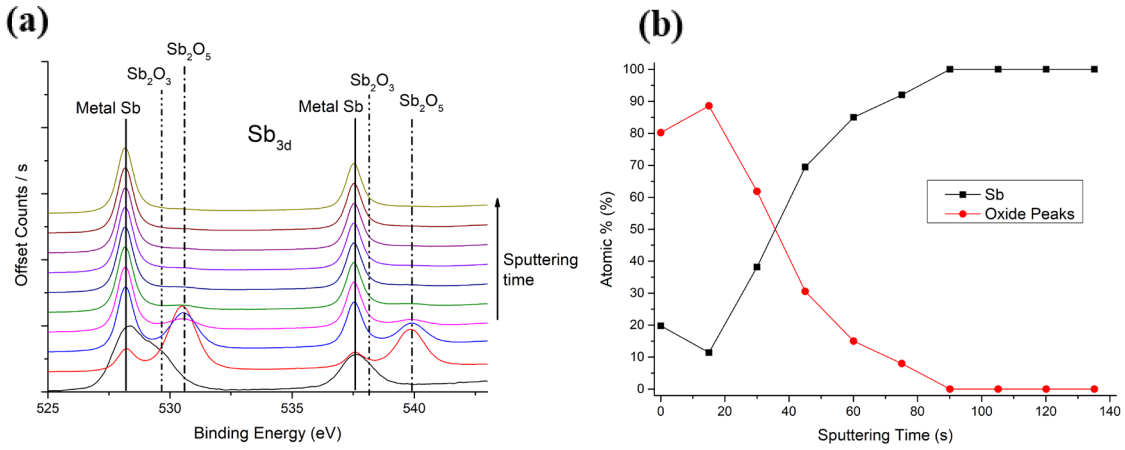

Figure 7.26 - (**a**) Sb 3d photoemission spectrum of the bare antimony wire as a function of depth below the surface showing oxides of different stoichiometries at different depths. Deeper below the surface the oxides are completely depleted. (**b**) Quantification of the atomic percent of elemental Sb with respect to all the oxide species through peak area analysis.

as a function of depth, with the topmost layer composed mostly of the trioxide (Sb_2O_3) and successively by the pentoxide (Sb_2O_5). The spectra in Figure 7.26a have been deconvoluted in the Sb-related peaks detailed in table 7.10, ignoring the contribution of oxygen peaks on the topmost surface. The area of peaks relative to oxide species has been summed and a ratio with the areas relative to metallic Sb, hence the atomic percent of metallic and oxide peaks has been calculated as a function of sputtering time. The result is shown in Figure 7.26b, apart from the anomalous point at the top surface, which is probably due to not considering the contribution of oxygen species, the antimony wire has an 80-90 nm layer composed of a mixture of metal and oxides. Below this layer the oxides are completely depleted.

The discharge during the operation visibly extends few millimeters upwards the wires tip for both materials. In the bismuth case, the treated wire has been characterized morphologically with SEM. The tip contracts during the process and develops a “bulge” (Figure 7.27) due to the partial melting and re-solidification of bismuth, which is known to expand upon solidification.

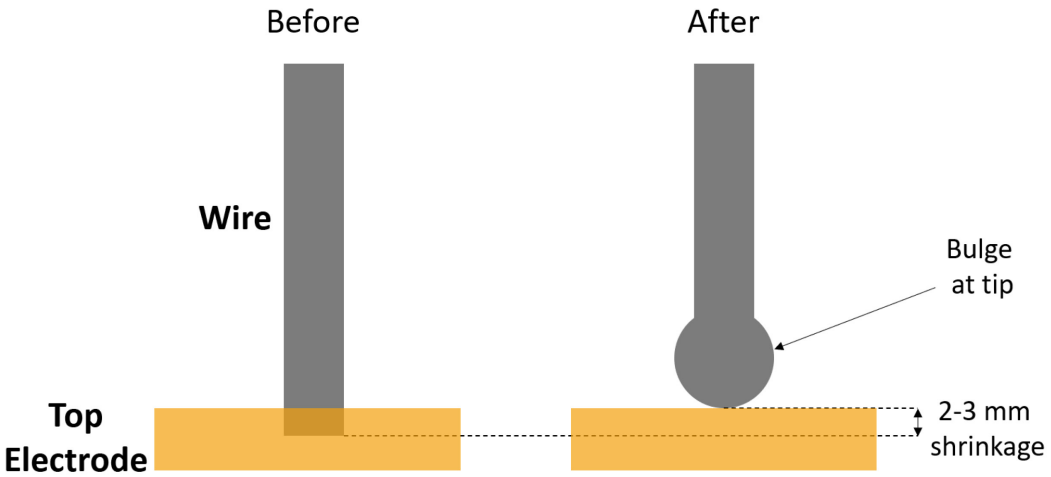

Figure 7.27 - Schematic diagram showing the evolution of the Bi wire during the plasma process. At the end of the plasma process (after) a 2-3 mm contraction in length is noticed and the formation of a bulge at the tip.

After the plasma treatment, a modification of the wire surface morphology is observed, as well as deposition of material on the capillary. An example of comparison for the Bi wire untreated (Figure 7.28a) and treated (Figure 7.28b) at 50 W and 1 sLm of helium is shown in figure 7.28.

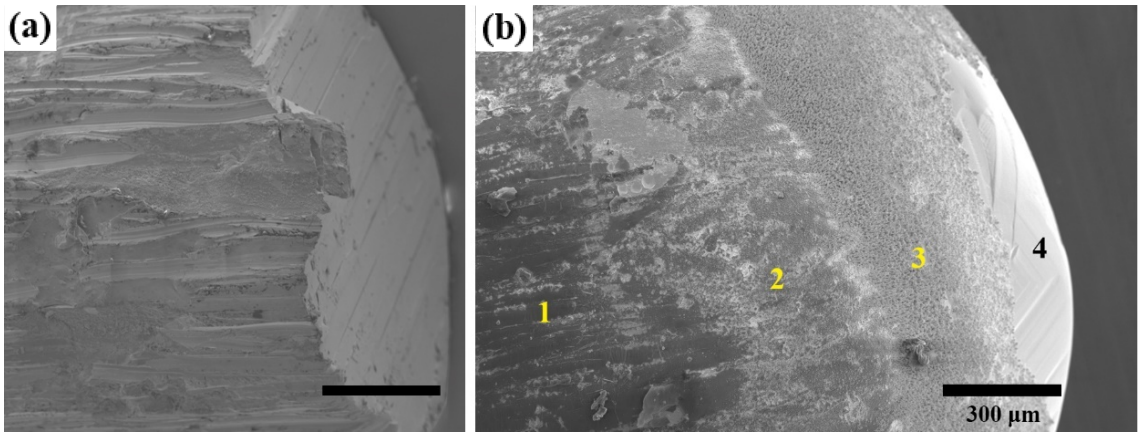

Figure 7.28 - (**a**) Bare untreated wire tip. (**b**) The same tip after a 50 W 1 sLm He plasma treatment that produced particles. The numbers relate to the zones mentioned in the text and relative to figures 7.29 (Zone 1), 7.30 (Zone 2), 7.31 (Zone 3), 7.32 (Zone 4). Scale bars are all 300 µm in length.

Four differently affected zone can be distinguished on the secondary electron image of the processed wire (Figure 7.28). *Zone 1* (Figure 7.29a) has a lower contrast in the SEM with respect to the wire's regions unaffected by the plasma (Figure 7.28a) and shows patches of different contrast and some irregular microstructures resembling molten shapes. The EDX in the same area (Figure 7.29b) finds a considerable concentration of silicon and oxygen.

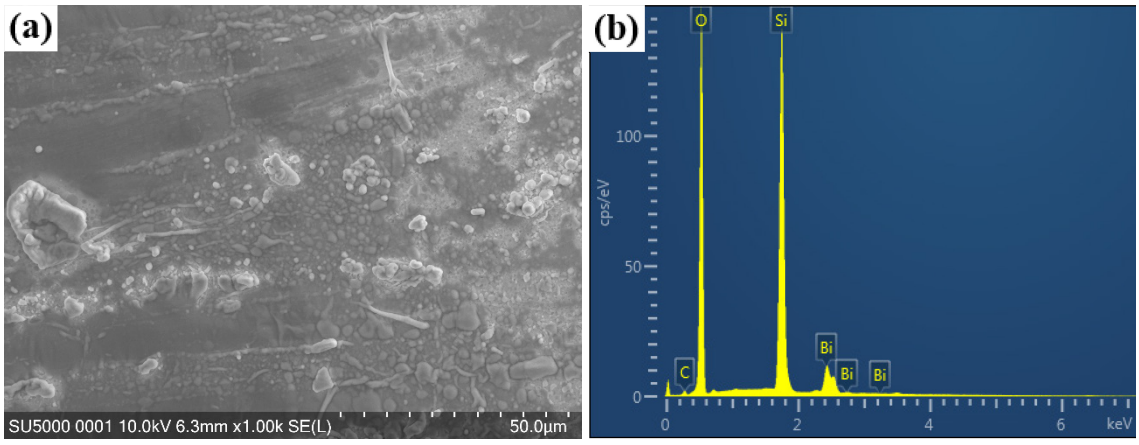

Figure 7.29 - (**a**) Higher magnification of the secondary electron image of the Zone 1 in Figure 7.28b, showing patches of different contrast and microstructures resembling molten material. (**b**) EDX spectrum of the same area showing a consistent abundance of silicon and oxygen.

Zone 2 is populated by spherical micrometer size particles (Figure 7.30a). The EDX spectrum (Figure 7.30b) also detects a significant amount of silicon and oxygen.

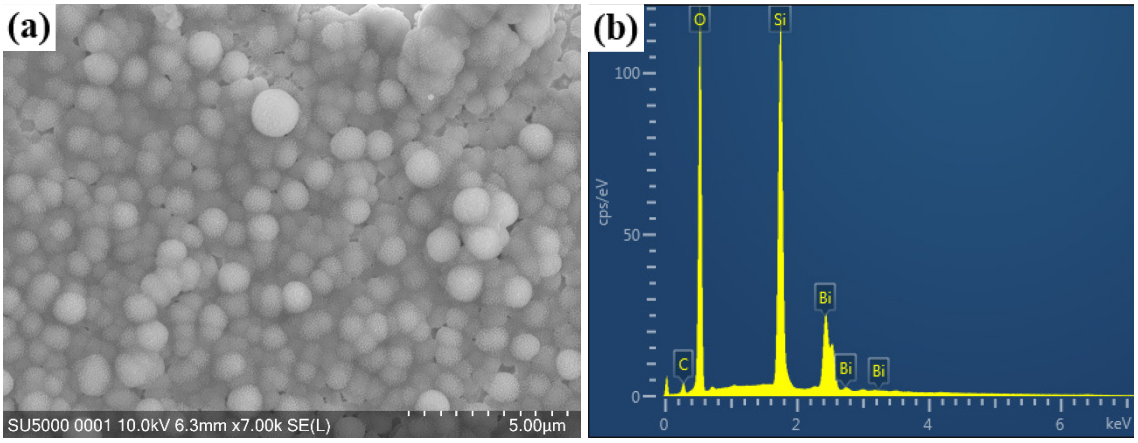

Figure 7.30 - (**a**) Higher magnification of the secondary electron image of the Zone 2 in Figure 7.28b, showing microparticles with spiky surface. (**b**) EDX spectrum of the same area shows a consistent abundance of silicon and oxygen.

Zone 3 (Figure 7.31a) shows vertically elongated structures composed of piles of smaller microparticles on a smooth surface. The EDX spectrum in this area (Figure 7.31b) indicates that they are mainly composed of metallic Bi.

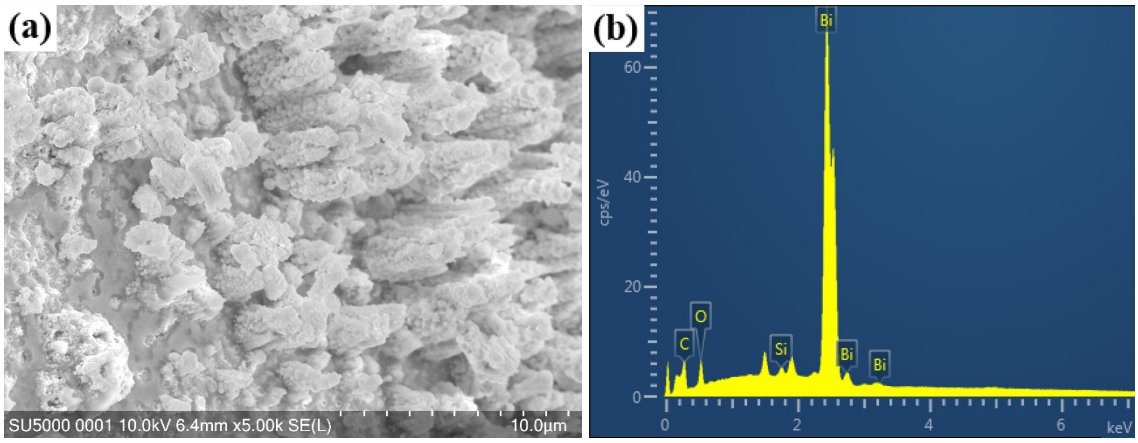

Figure 7.31 - (**a**) Higher magnification of the secondary electron image of the Zone 3 in Figure 7.28b, showing vertically elongated structures on a smooth base. (**b**) EDX spectrum of the same area shows a major contribution by bismuth.

Zone 4 (Figure 7.32a) has the appearance of a smooth polycrystalline surface surrounded by spherical microparticles, probably the result of re-solidification of a molten droplet forming the body of the bulge. Also microparticles are noticed at the edge of this area.

The EDX in zone 4 (Figure 7.32b) shows signal mainly from bismuth (Al and Mg signals are originating from the SEM sample holder).

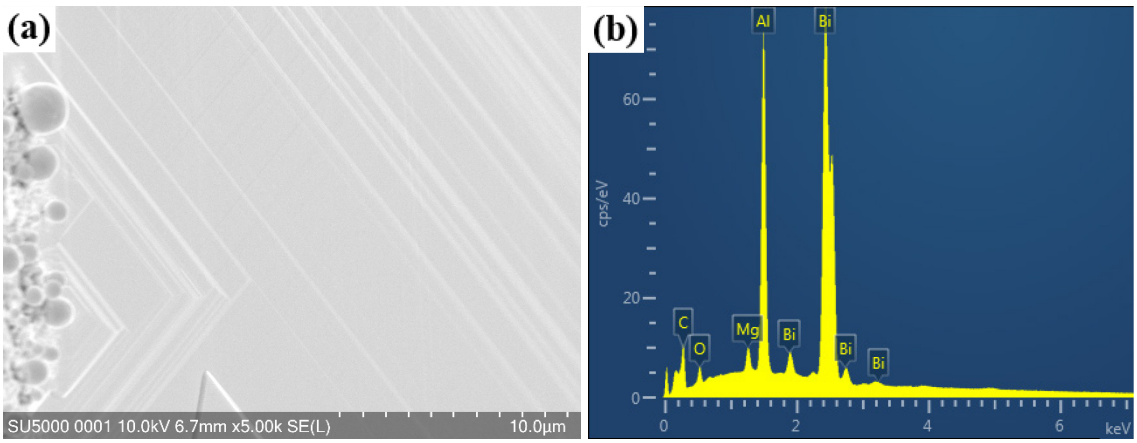

Figure 7.32 - (**a**) Higher magnification of the secondary electron image of the Zone 4 in Figure 7.28b, showing a polycrystalline surface structure surrounded by microparticles. (**b**) EDX spectrum of the same area shows major contribution by bismuth and elements pertaining to the SEM sample holder (Al and Mg).

These SEM micrographs and the relative EDX spectra demonstrate that the Bi wires are affected from the exposure to the plasma even further from the electrodes (Zone 1 is where the top part of the plasma extension, 3-4 millimetres far from the electrodes vertically). Moreover, the only source of silicon and oxygen in abundant quantities is the glass capillary.

Summarizing it is found that the plasma process can form particles starting from wires with a 10-20 nm oxide layer, the plasma affects even the further parts of the wire above the minimum discharge gap and the interactions with the capillary are important, as they determine an exchange of deposited materials to and from the wire. The presence of a bulge at the tip of the treated bismuth wire which has the morphological characteristics of a polycrystalline surface implies that local surface melting is indeed happening in the process, and the consequent re-solidification at the tip.

7.5.3 About the formation mechanism

The formation mechanism of nanoparticles from solid wire sacrificial precursors in non-equilbrium atmospheric pressure plasmas is still unknown and the proposed theories from different groups are inconsistent. The successful formation of metal oxide nanoparticles

with analogous reactors has been reported from Zn, Mo, W, Cu and Fe thin wires of 0.01 to 0.3 mm,[17,59,62–65] while pure metallic particles from Sn, Au and Mo.[15,60,61,66] In this subsection we compare and discuss our results based on the formation mechanisms advanced by other authors, in order to contribute to the understanding of phenomena happening in our and similar plasma reactors.

Shimizu et al. made extensive studies on the characterization of molybdenum and tungsten oxides,[16,64] the characterization of the plasma involved through OES measurements and SEM/EDX of the treated wires. They used an Ar/O_2 microplasma source on a Mo wire and found smaller particles in higher oxidation states at higher flows. Also, they reported the oxidation of the pure metallic wire from atomic oxygen in the discharge. The oxide layer would also lower drastically the sublimation point of molybdenum. They described the process as happening in two different regimes of gas flow where the formed oxide layer has a leading role: lower flows would promote higher gas temperatures which enhance the vaporization of the oxide layer. The vaporized oxides are then dissociated in the gas phase and condense downstream, leaving a rough surface on the wire (Figure 7.33a). This statement is supported by the presence of emission from Mo excited atoms in the OES spectra and a distribution of oxide stoichiometries explainable from the partial pressure of oxygen in the gas phase. At higher gas flows instead, the lower gas temperatures would suppress the vaporization of oxide layers but still be able to eject molten droplets from the melting surface, in analogy to wire arc spraying processes. The surface of the wire in this case is smoother as a product of re-solidification of the molten surface (Figure 7.33b).

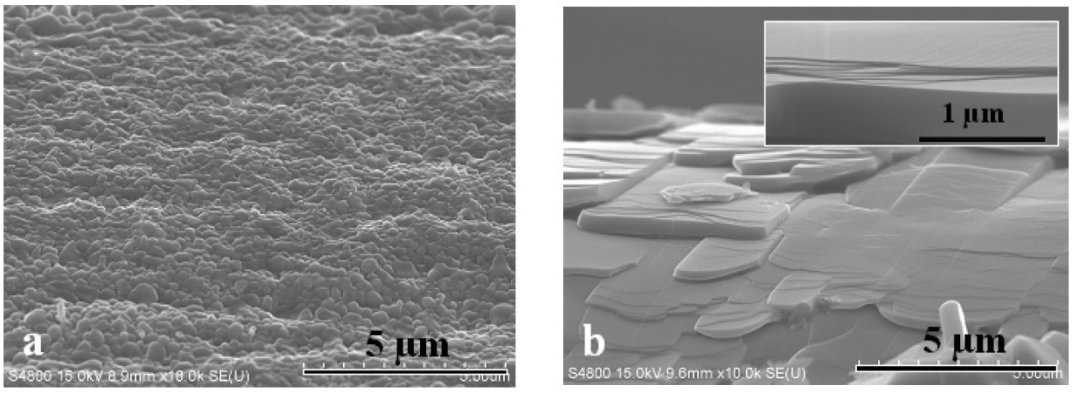

Figure 7.33 - Surface of the treated Mo wires reported in [66], for two different regime of gas flow identifying different formation mechanisms. (**a**) Low flows result in rough surfaces and (**b**) high flow resulting in smoother surface.[66]

The same group reported a different mechanism from the same reactor design using a tungsten wire as precursor [12]. They distinguish two regimes based on the total gas flow. At lower flows particles would nucleate on the surface and then transported to the gas phase, as they observe particles on the wire surface (Figure 7.34a). They speculated a localized vaporization and re-condensation on the surface as the nucleation mechanism. At higher flows instead, the process would proceed as a continuous vaporization of the oxide layer and condensation on the capillary and the substrate surfaces. The apparent contradiction of higher volatilization rate at higher flows (lower gas temperatures) was explained as gas heating due to the gas compression at the pinched zone of the capillary nozzle.

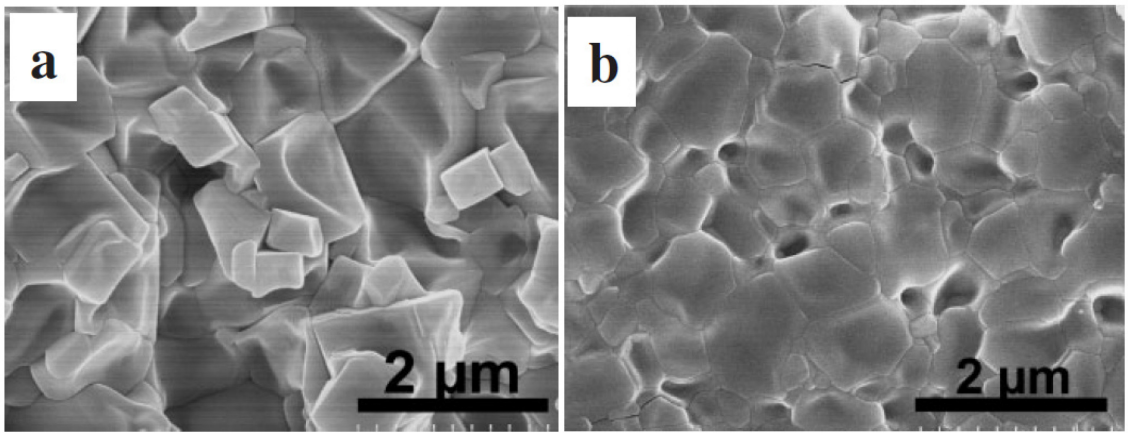

Figure 7.34 - Surface of the treated W wires reported in [12], for two different regime of gas flow identifying different formation mechanisms. (a) Low flows result in particles nucleated on the surface of the wire and then stripped off by the flowing gas and (b) high flow resulting in a continuously vaporized surface of the wire.[12]

The methods reported for obtaining pure metallic particles, instead, typically use a hydrogen admixture to a pulsed Ar plasma.[67] For example, for Au nanoparticles, they explained the formation mechanism as due to the enhanced vaporization of the Au surface by atomic hydrogen in the discharge. The atomic hydrogen would be able to dissolve in the molten surface and transfer heat to the melt via exothermic recombination reactions, thus enhancing the vaporization rate. This was supported by the fact that a higher concentration of hydrogen in the plasma was able to increase the etching rate of the wires surface (figure 7.35) and resulted in bigger condensing particles.

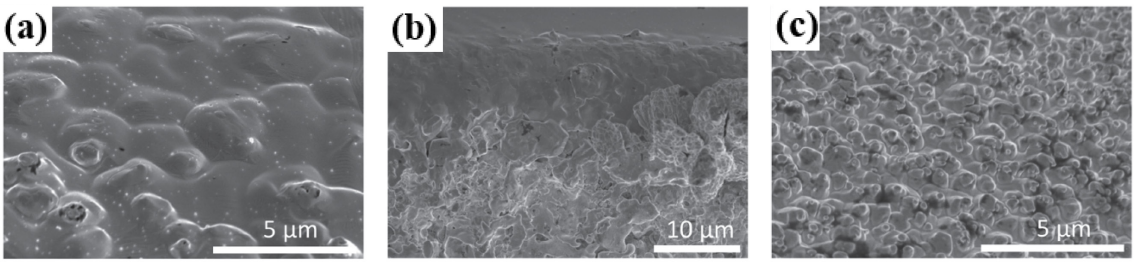

Figure 7.35 - Surface of treated Au wires reported in [54] in function of the concentration of H_2 in the discharge (from left to right, 0.5%, 1% and 2% H_2 in Ar). Higher concentrations result in rougher surfaces.

The experimental work presented here has some points in common and other contrasting with the mechanisms proposed in literature:

1. our process formed *pure metallic Bi particles with only helium*, hence with no intentional admixture of oxygen or hydrogen species. Oxygen may indeed come from the native oxide on the untreated wire surface or the etching of the glass capillary, which resulted in the presence of Si and O on the treated wire surface. In any case, it was pointed out by the experimenters that obtained pure metallic particles that atomic hydrogen in the discharge is fundamental to the formation of particles. In this respect, the work presented herein highlights a difference with previous works. It is possible that the formation mechanism is strongly material dependent.
2. In the present case *the gas temperatures involved are lower* than the estimated ones for the other studies (between 1000 K and 1400 K). In fact, borosilicate glass capillaries can withstand 800 K before melting and 165 K of temperature differential before fracturing. These processes are not happening in particle-forming conditions and with no additional cooling a significant heat dissipation from the reactor is not expected. This does not exclude the possibility of having locally high temperatures on the superficial microstructures and the wire's tip.
3. The *SEM of Bi wire presents the features reported* in other studies in different parts of the wire. Details recalling molten materials in the body of the wire are found in the present work, Bi microparticles and columnar structures near the tip and a re-solidified smooth surface at the tip. The difference with other studies though is the reactor design and the discharge mode that develops therein. In most of the studies the power to the plasma is imposed through a coiled electrode, hence exposing a bigger portion of the wire surface to the plasma. In the present case the configuration of electrodes is such that the smaller gap is in correspondence of the wire tip, and the discharge tends to develop filamentary structures at that point.

The main fundamental mechanisms which may play an important role in the formation of particles from solid precursors in the present plasma reactor will now be discussed.

In low pressure plasmas, physical sputtering is the fundamental mechanism used to erode solid targets for deposition of films. *Physical sputtering* at a solid surface happens when a ions with energy greater than the binding energy of atoms in the solid lattice (10-100 eV/atom, depending on the kind of bonds) impinges on a solid surface.[68,69] It is described as an energy and momentum transfer which initiate chain reactions in the solid lattice, that eventually results in the expulsion of surface atoms of the target with enough recoil momentum. The basic physical sputtering models though, which have been successful in predicting sputtering yield in function of ion energies and heat of sublimation of the targets for low pressure plasmas, consider only binary collisions between projectile and target and a single neighbor atomic potential.[68] A higher temperature of the solid target near its melting point, promotes higher atomic loss rates because of the increased sublimation rate of the solid target. In addition, if projectiles lose energy in a short distance below the surface of the target, surface species as adatoms (which have lower binding energies than atoms in the bulk) play important roles.[70] Also, low energy sputtering phenomena have shown not to be completely explainable in this picture.[9–11]

Chemical sputtering (or reactive sputtering) is defined as the ion bombardment-induced chemical reactions which eventually lead to products loosely bound to the surface of the solid, and easily desorb into the gas phase.[71] These mechanisms need reactive ions in the discharge and change substantially with different combination of projectiles/targets. Hence, these are less important for discharges of noble gases and even though the threshold energies are much lower than in physical sputtering they have a strong temperature dependence well below the melting point of the target material.

In thermal plasmas the mechanism that produces nanoparticles starts from the *vaporization or sublimation* of the target material due to very high gas temperatures, followed by condensation of saturated vapours into nanoparticles. There are also some reports that show the nano-structuring of a tungsten wire with an atmospheric pressure helium-only discharge.[72] The authors of this study found evidence of the formation of He bubbles below the surface, in analogy to walls exposed to fusion plasmas and in a similar mechanism as the one responsible for embrittlement of metals form insertion of hydrogen.

These bubbles may help increasing the vaporization rate at lower temperatures, by influencing the binding energies of surface atoms.

The experimental observations collected during this study suggests that more than one of the reported formation mechanisms may be at work in the present process. In general, non-equilibrium APPs have low ionization densities and the collisions with neutral gas atoms result in limited energy transferred to the plasma ions or the relaxation of their kinetic energy at small distances (ion mean free paths are 10 nm to 100 nm at atmospheric pressure). Ion energy are in the range of 1 eV commonly. For these reasons, it is likely that ionic processes as described for physical and chemical sputtering are not important for substantial erosion of the metal wire, even if sputtering yield should be higher for the melting surface. However, high reduced electric field (E/n where n is the gas density) may induce non-equilibrium effects in the ion energy distributions,[73] and these conditions might be fulfilled in the cathode fall of a metallic tip. In microplasmas also, other species may contribute to the energy transfer from plasma species to a solid surface. For example, helium metastables are expected to be present in significant amounts (in respect to other plasma-born species) in RF-helium discharges with small discharge gaps.[74] The plasma reactor in this study produces substantial amounts of particles in conditions near to the melting of wires, in fact the bulge resulting from melting and re-solidification on the tip of the Bi wire is observed. This observation supports the idea that local melting and vaporization of the metallic surface is at the foundation of the process. In fact, even though the reactors should not reach the melting temperatures of the materials (or melting of the borosilicate glass would be observed), size-dependent changes in melting temperature can allow the melting and vaporization of smaller surface feature of the wires. The arc discharges on the wires tip can supply the necessary high temperatures to sustain the vaporization of metallic wires locally. The different power thresholds needed for Bismuth and Antimony wires may reflect the different heat of sublimation for the two materials (179 kJ/mol and 213.22 kJ/mol respectively), even though the different diameters of wires and heat dissipation in the process should be accounted for. Also, the native oxides (with lower heat of vaporization) and the helium atoms and metastables (via the bubble formation process) could increase the rate of vaporization of the wire's material. In addition, the observation of the deposition of metallic layers on the capillary walls during the deposition process further indicate that particle nucleation happens from the condensation of a metal vapor in the gas phase. Further experiments and modeling are needed though to understand the fundamental mechanisms at play.

7.6 Conclusions

In this chapter we demonstrated the synthesis of bismuth and antimony nanoparticles from solid precursors in the form of pure mm-scale diameters wires through a RF atmospheric pressure helium plasma. The reactor design uses thicker wires than the preexisting concepts (mm vs 10/100 μm) that permits to use wires of more brittle materials. Besides the advantages of the process, the main flaws consist in a limited control over the synthesis process with the present reactor design. The flaws are imputable to a difficult reliable positioning of the wire precursors and the arousal of thermal instabilities, which can either lead to the melting of the wire or melting of the incapsulating glass capillary. In both cases, the limiting factors are technological in nature, while we demonstrated the feasibility of nanoparticle synthesis from thicker wires.

The Bismuth particles obtained are 1.9 nm to 8.6 nm in average diameter with small size dispersions and no oxide phases when a colloid in ethanol is produced. The variation of He flow in the plasma allows to reduce particle size and size dispersion even though the present reactor design shows a certain variability in absolute values. The particles show signs of quantum confinement, which consists in the existence of a semiconducting phase whose direct bandgaps (4.8 eV for the 1.9 nm particles and 4.5 eV for the 3.4 nm particles) and decrease with decreasing particles size. This results in the enhancement of UV-Vis optical absorption for small particles and a photoluminescence emission under UV illumination. A model which explains the quantum confinement for Bi QDs in terms of the simultaneous widening of energy bandgaps at different symmetry points of the Brillouin zone resulted in partial agreement with the experimental observations, as it predicts direct bandgaps increasing with decreasing size but with systematically larger values. This discrepancy highlighted the inadequacy of assuming ellipsoidal band dispersion relations and not considering the exciton binding energies to explain the effect of quantum confinement in Bi QDs.

The synthesis with the 2 mm antimony wire resulted in 1-3 nm Sb particles together with antimony oxide particles. The process shows limited size tunability with the Helium flow settings explored, despite a better thermal stability of the plasma discharge with respect to the 1 mm Bi wire process.

It is found that metal wire precursors used have a native oxide layer which must be involved in the formation process of particles. The SEM and EDX of the Bi wire after the

plasma process showed remnants of local melting of microscopic details of the wire and the exchange of materials from the capillary in addition to the formation of Bi microparticles, columnar structures and a re-solidified surface at the wire's tip.

Collectively, the experimental observations for the synthesis of Bi nanoparticles from a 1 mm Bi wire indicate that the formation process must include the substantial vaporization of local microscopic features of the wires and the condensation of particles from metal vapors in the gas phase.

References

1. Hahn, H. & Averback, R. S. The production of nanocrystalline powders by magnetron sputtering. *J. Appl. Phys.* **67**, 1113–1115 (1990).

2. Vollath, D. Plasma synthesis of nanopowders. *J. Nanoparticle Res.* **10**, 39–57 (2008).

3. Choi, S., Lapitan, L. D. S., Cheng, Y. & Watanabe, T. Synthesis of cobalt boride nanoparticles using RF thermal plasma. *Adv. Powder Technol.* **25**, 365–371 (2014).

4. Chen, J., Lu, G., Zhu, L. & Flagan, R. C. A simple and versatile mini-arc plasma source for nanocrystal synthesis. *J. Nanoparticle Res.* **9**, 203–213 (2007).

5. Yilmaz, F. *et al.* Fabrication of cobalt nano-particles by pulsed wire evaporation method in nitrogen atmosphere. *Powder Technol.* **235**, 1047–1052 (2013).

6. Mandilas, C., Daskalos, E., Karagiannakis, G. & Konstandopoulos, A. G. Synthesis of aluminium nanoparticles by arc plasma spray under atmospheric pressure. *Mater. Sci. Eng. B Solid-State Mater. Adv. Technol.* **178**, 22–30 (2013).

7. Lerner, M. I. *et al.* Structures of binary metallic nanoparticles produced by electrical explosion of two wires from immiscible elements. *Powder Technol.* **288**, 371–378 (2016).

8. Sugunakar Reddy, R., Kamaraj, M., Kamachi Mudali, U., Chakravarthy, S. R. & Sarathi, R. Generation and characterization of zirconium nitride nanoparticles by wire explosion process. *Ceram. Int.* **38**, 5507–5512 (2012).

9. Rosenberg, D. & Wehner, G. K. Sputtering Yields for Low Energy He+-, Kr+-, and Xe+-Ion Bombardment. *J. Appl. Phys.* **33**, 1842–1845 (1962).

10. Laegreid, N. & Wehner, G. K. Sputtering yields of metals for ar+ and ne+ ions with energies from 50 to 600 ev. *J. Appl. Phys.* **32**, 365–369 (1961).

11. Cooper, C. B. Low Energy Sputtering. (1968).

12. Kubo, R. Electronic Properties of Metallic Fine Particles. I. *Journal of the Physical Society of Japan* vol. 17 975–986 (1962).

13. Halperin, B. I. & Rice, T. M. The Excitonic State at the Semiconductor-Semimetal Transition. *Solid State Phys. - Adv. Res. Appl.* **21**, 115–192 (1968).

14. Kappes, M. M., Schär, M., Radi, P. & Schumacher, E. On the manifestation of electronic structure effects in metal clusters. *J. Chem. Phys.* **84**, 1863–1875 (1986).

15. Shimizu, Y., Kawaguchi, K., Sasaki, T. & Koshizaki, N. Generation of room-temperature atmospheric H2/Ar microplasma jet driven with pulse-modulated ultrahigh frequency and its application to gold nanoparticle preparation. *Appl. Phys. Lett.* **94**, 2007–2010 (2009).

16. Shimizu, Y. *et al.* Reactive evaporation of metal wire and microdeposition of metal oxide using atmospheric pressure reactive microplasma jet. *Japanese J. Appl. Physics, Part 1 Regul. Pap. Short Notes Rev. Pap.* **45**, 8228–8234 (2006).

17. Mariotti, D., Lindström, H., Bose, A. C. & Ostrikov, K. Monoclinic β-MoO3 nanosheets produced by atmospheric microplasma: Application to lithium-ion batteries. *Nanotechnology* **19**, (2008).

18. Velasco-Arias, D. *et al.* Stabilization of strong quantum confined colloidal bismuth nanoparticles, one-pot synthesized at room conditions. *J. Phys. Chem. C* **116**, 14717–14727 (2012).

19. Zhou, G., Li, L. & Li, G. H. Semimetal to semiconductor transition and thermoelectric properties of bismuth nanotubes. *J. Appl. Phys.* **109**, (2011).

20. Lee, S., Ham, J., Jeon, K., Noh, J. S. & Lee, W. Direct observation of the semimetal-to-semiconductor transition of individual single-crystal bismuth nanowires grown by on-film formation of nanowires. *Nanotechnology* **21**, (2010).

21. Shick, A. B., Ketterson, J. B., Novikov, D. L. & Freeman, A. J. Electronic structure, phase stability, and semimetal-semiconductor transitions in Bi. *Phys. Rev. B - Condens. Matter Mater. Phys.* **60**, 15484–15487 (1999).

22. Gonze, X., Michenaud, J.-P. & Vigneron, J.-P. First-principles study of As, Sb, and Bi electronic properties. *Phys. Rev. B* **41**, 11827–11836 (1990).

23. Ito, S. *et al.* Proving Nontrivial Topology of Pure Bismuth by Quantum Confinement. *Phys. Rev. Lett.* **117**, 1–6 (2016).

24. Butkutė, R. *et al.* Bismuth Quantum Dots in Annealed GaAsBi/AlAs Quantum Wells. *Nanoscale Res. Lett.* **12**, (2017).

25. You, A., Be, M. A. Y. & In, I. Strong electron-phonon coupling in superconducting bismuth nanoparticles Strong electron-phonon coupling in superconducting bismuth nanoparticles. **031111**, (2019).

26. Enaldiev, V. V. & Volkov, V. A. Quantum confinement and heavy surface states of Dirac fermions in bismuth (111) films: An analytical approach. *Phys. Rev. B* **97**, 1–7 (2018).

27. Hoffman, C. A. *et al.* Semimetal-to-semiconductor transition in bismuth thin films. *Phys. Rev. B* **51**, 5535–5537 (1995).

28. Kravchyk, K. V. *et al.* Colloidal Bismuth Nanocrystals as a Model Anode Material for Rechargeable Mg-Ion Batteries: Atomistic and Mesoscale Insights. *ACS Nano* **12**, acsnano.8b03572 (2018).

29. Toudert, J., Serna, R. & Jiménez De Castro, M. Exploring the optical potential of nano-bismuth: Tunable surface plasmon resonances in the near ultraviolet-to-near infrared range. *J. Phys. Chem. C* **116**, 20530–20539 (2012).

30. Huang, J., Lin, X., Tan, H. & Zhang, B. Bismuth Microparticles as Advanced Anodes for Potassium-Ion Battery. *Adv. Energy Mater.* **8**, 1–7 (2018).

31. Toudert, J. *et al.* Unveiling the Far Infrared-to-Ultraviolet Optical Properties of Bismuth for Applications in Plasmonics and Nanophotonics. *J. Phys. Chem. C* **121**, 3511–3521 (2017).

32. Dong, F. *et al.* A semimetal bismuth element as a direct plasmonic photocatalyst. *Chem. Commun.* **50**, 10386–10389 (2014).

33. Uner, N. B. & Thimsen, E. In-Flight Size Focusing of Aerosols by a Low Temperature Plasma. *J. Phys. Chem. C* **121**, 12936–12944 (2017).

34. Huang, Y. *et al.* Ultrathin Bismuth Nanosheets for Stable Na-Ion Batteries: Clarification of Structure and Phase Transition by in Situ Observation. *Nano Lett.* **19**, 1118–1123 (2019).

35. Yang, F. Y., Liu, K., Chien, C. L. & Searson, P. C. Large magnetoresistance and

finite-size effects in electrodeposited single-crystal bi thin films. *Phys. Rev. Lett.* **82**, 3328–3331 (1999).

36. Wyckoff, R. W. G. *Crystal Structures*. (Interscience Publishers, 1963).

37. Scherrer, P. Bestimmung der inneren Struktur und der Größe von Kolloidteilchen mittels Röntgenstrahlen. in *Kolloidchemie Ein Lehrbuch* 387–409 (Springer Berlin Heidelberg, 1912). doi:10.1007/978-3-662-33915-2_7.

38. Langford, J. & Wilson, A. Seherrer after Sixty Years: A Survey and Some New Results in the Determination of Crystallite Size. *J. Appl. Cryst.* **11**, 102–113 (1978).

39. Singh, A. K. *Advanced x-ray techniques in research and industry*. (IOS press, 2005).

40. Wang, Y. W., Hong, B. H. & Kim, K. S. Size Control of Semimetal Bismuth Nanoparticles and the UV - Visible and IR Absorption Spectra. 7067–7072 (2005) doi:10.1021/jp046423v.

41. Wang, Z., Jiang, C., Huang, R., Peng, H. & Tang, X. The Investigation of Optical and Photocatalytic Properties of Bismuth Nanospheres Prepared by a Facile Thermolysis Method The Investigation of Optical and Photocatalytic Properties of Bismuth Nanospheres Prepared by a Facile Thermolysis Method Key Laborat. (2013).

42. Marchak, D. *et al.* Large anisotropic conductance and band gap fluctuations in nearly round-shape bismuth nanoparticles. *Nano Lett.* **12**, 1087–1091 (2012).

43. Sedov, E. A., Riikonen, K. P. & Arutyunov, K. Y. Quantum size phenomena in single-crystalline bismuth nanostructures. *npj Quantum Mater.* **2**, 1–3 (2017).

44. Fojtik, A. & Henglein, A. Luminescent colloidal silicon particles. *Chem. Phys. Lett.* **221**, 363–367 (1994).

45. Liu, Y. & Allen, R. E. Electronic structure of the semimetals Bi and Sb. **52**, (1995).

46. Zhang, Z., Sun, X., Dresselhaus, M. & Ying, J. Y. Electronic transport properties of single-crystal bismuth nanowire arrays. *Phys. Rev. B - Condens. Matter Mater. Phys.* **61**, 4850–4861 (2000).

47. Wang, Y. W., Kim, J. S., Kim, G. H. & Kim, K. S. Quantum size effects in the volume plasmon excitation of bismuth nanoparticles investigated by electron energy loss spectroscopy. *Appl. Phys. Lett.* **88**, (2006).

48. Levin, A. J., Black, M. R. & Dresselhaus, M. S. Indirect L to T point optical transition in bismuth nanowires. *Phys. Rev. B - Condens. Matter Mater. Phys.* **79**, 1–10 (2009).

49. Feng, P. *et al.* Reversible formation of networked porous Sb nanoparticles during cycling: Sb nanoparticles encapsulated in a nitrogen-doped carbon matrix with nanorod structures for high-performance Li-ion batteries. *J. Mater. Chem. A* **7**, 24292–24300 (2019).

50. Zhang, W. *et al.* High-rate and ultralong-stable potassium-ion batteries based on antimony-nanoparticles encapsulated in nitrogen and phosphorus co-doped mesoporous carbon nanofibers as an anode material. *J. Alloys Compd.* **769**, 141–148 (2018).

51. Zhong, J. *et al.* Preparation and optical properties of sodium borosilicate glasses containing Sb nanoparticles. *J. Alloys Compd.* **607**, 177–182 (2014).

52. Li, Z. *et al.* Possible Excitonic Insulating Phase in Quantum-Confined Sb Nanoflakes. *Nano Lett.* **19**, 4960–4964 (2019).

53. Zally, G. D. & Mochel, J. M. Fluctuation Heat Capacity in Superconducting Thin Films of Amorphous BiSb. *Phys. Rev. Lett.* **27**, 1710–1712 (1971).

54. Hsieh, D. *et al.* A topological Dirac insulator in a quantum spin Hall phase. *Nature* **452**, 970–974 (2008).

55. Smith, G. E. & Wolfe, R. Thermoelectric Properties of Bismuth-Antimony Alloys. *J. Appl. Phys.* **33**, 841–846 (1962).

56. Chin, H. S., Cheong, K. Y. & Razak, K. A. Review on Oxides of antimony nanoparticles: Synthesis, properties, and applications. *J. Mater. Sci.* **45**, 5993–6008 (2010).

57. Svensson, C. The crystal structure of orthorhombic antimony trioxide, Sb2O3. *Acta Crystallogr. Sect. B* **30**, 458–461 (1974).

58. Bozorth, R. M. THE CRYSTAL STRUCTURES OF THE CUBIC FORMS OF ARSENIOUS AND ANTIMONOUS OXIDES. *J. Am. Chem. Soc.* **45**, 1621–1627 (1923).

59. Stauss, S., Imanishi, Y., Miyazoe, H. & Terashima, K. High rate deposition of ZnO thin films by a small-scale inductively coupled argon plasma generated in open air. *J. Phys. D. Appl. Phys.* **43**, (2010).

60. Shimizu, Y. *et al.* Localized deposition of metallic molybdenum particles in ambient air using atmospheric-pressure microplasma. *Dig. Pap. - Microprocess. Nanotechnol. 2007; 20th Int. Microprocess. Nanotechnol. Conf. MNC* **4256**, 174–175 (2007).

61. Shimizu, Y., Koga, K., Sasaki, T. & Koshizaki, N. Dense growth of multiply-twinned star-shaped molybdenum particles by atmospheric H2/Ar microplasma jet. *CrystEngComm* **11**, 1940–1946 (2009).

62. Mariotti, D. & Ostrikov, K. Tailoring microplasma nanofabrication: From nanostructures to nanoarchitectures. *J. Phys. D. Appl. Phys.* **42**, (2009).

63. Mariotti, D., Bose, A. C. & Ostrikov, K. Atmospheric-microplasma-assisted nanofabrication: Metal and metal-oxide nanostructures and nanoarchitectures. *IEEE Trans. Plasma Sci.* **37**, 1027–1033 (2009).

64. Bose, A. C. *et al.* Flow rate effect on the structure and morphology of molybdenum oxide nanoparticles deposited by atmospheric-pressure microplasma processing. *Nanotechnology* **17**, 5976–5982 (2006).

65. Shimizu, Y. *et al.* Cylindrical metal wire surface coating with multiwalled carbon nanotubes by an atmospheric-pressure microplasma CVD technique. *Chem. Vap. Depos.* **11**, 244–249 (2005).

66. Haq, A. U. *et al.* Size-dependent stability of ultra-small α-/β-phase tin nanocrystals synthesized by microplasma. *Nat. Commun.* 1–8 doi:10.1038/s41467-019-08661-9.

67. Shimizu, Y. Diameter control of gold nanoparticles synthesized in gas phase using atmospheric-pressure H2/Ar plasma jet and gold wire as the nanoparticle source: Control by varying the H2/Ar mixture ratio. *AIP Adv.* **7**, (2017).

68. Behrisch, R. SPUTTERING BY PARTICLE BOMBARDMENT. I: PHYSICAL SPUTTERING OF SINGLE-ELEMENT SOLIDS. (1981).

69. Behrisch, R. & Eckstein, W. *Sputtering by particle bombardment: experiments and computer calculations from threshold to MeV energies*. vol. 110 (Springer Science & Business Media, 2007).

70. Doerner, R. P., Krasheninnikov, S. I. & Schmid, K. Particle-induced erosion of materials at elevated temperature. *J. Appl. Phys.* **95**, 4471–4475 (2004).

71. Winters, H. F. & Coburn, J. W. Surface science aspects of etching reactions. *Surf. Sci. Rep.* **14**, 162–269 (1992).

72. Kovach, Y. E., Zhang, F., Gao, F. & Foster, J. E. Study of plasma induced nanostructure formation and surface morphology changes on tungsten and stainless steel at atmospheric pressure. *J. Vac. Sci. Technol. A* **37**, 011301 (2019).

73. Xu, L. & Wang, H. Ion energy distribution in extremely high electric field discharges. (2018) doi:10.1088/1361-6463/aad321.

74. Niemi, K., Waskoenig, J., Sadeghi, N., Gans, T. & O'Connell, D. The role of helium metastable states in radio-frequency driven helium-oxygen atmospheric pressure plasma jets: Measurement and numerical simulation. *Plasma Sources Sci. Technol.* **20**, (2011).

Chapter 8 - Conclusions and outlook

8.1 Conclusions

In this study the versatility of gas-phase microplasmas for the nanomaterial synthesis has been demonstrated, by synthesizing nanoparticles of different elements starting from precursors of various nature, namely a molecular gas, a metalorganic powder, and pure solid wires. In particular, the mentioned versatility has been defined further for small separated nanoparticle synthesis, as all the products of synthesis are not agglomerated and have particles size between 1 nm and 10 nm. However, the technological aspects that relate to repeatability, reproducibility, extended usage, and throughput of the microplasma synthesis methods explored in this work need to be improved for commercial/industrial exploitation.

A combination of optical diagnostics, models about plasma parameters and a particle heating model has been envisioned as an all-optical based method to achieve the understanding of particle formation in microplasmas and the control of forming processes at the same time. In this respect, the generalized model for nanoparticle temperature in a collisional plasma has been improved and applied to some of synthesis processes explored, where it proved useful in understanding some of the features relative to the formation of particles and their post-synthesis evolution. While diagnostics can provide specific details of a synthesis process, a generalized picture of this type of plasma synthesis process is still far from being reached, mainly due to a lack for theoretical framework in the context of synthesis.

An experimental routine based on advanced tools of material science has been developed for the characterization of the main optical and electronic properties of nanomaterials, discussed in light of the specifications of each technique and applied to build the energy band diagrams, which are fundamental for the implementation of nanoparticulate films for applications and devices. While this method has proved operationally useful for the integrability in devices and to understand the main optoelectronic properties of synthesized particles in this work, there is still limited understanding on comparing measurements among the different techniques.

Silicon quantum dots were synthesized from a gaseous molecular precursor, silane, in crystalline, amorphous or mixed phases and varying size depending on the precursor concentration in the plasma process. The particle heating model explained the dynamics of crystallization of particles as a function of their starting size, as an effect of higher temperatures with respect to the background gas temperature. The characterization of the optoelectronic properties of films permitted to estimate the energy band diagrams and used to determine the alignment of energy levels in a solar cell where a film with crystalline quantum dots was implemented. The implication of the mentioned results is that it is possible to tailor size, crystallinity and optoelectronic properties of silicon quantum dot films at the synthesis stage, by carefully choosing the synthesis conditions through the guidance of optical emission spectroscopy-derived plasma parameters and the particle heating model.

The synthesis of nanodiamonds was demonstrated for the first time from ferrocene, a metalorganic precursor in the form of a volatile powder, giving some hints on their formation mechanism. The nanodiamonds are in different crystalline phases and with the co-presence of non-diamond forms of carbon nanoparticles. While optical emission spectroscopy was useful to have some information on the plasma chemistry behind their formation, the particle heating model was useful to understand the thermodynamic conditions of particles forming inside the plasma. This gave a probable explanation of the phase distribution of samples synthesized as a function of the precursor concentrations and a reason of the limited size-control as due to the size-dependent stability of nanocarbon phases. In addition, it was possible to envision a possible formation mechanism based on the species found in optical emission spectra and the particles temperatures inside the plasma, as well as comparing the result of the synthesis with other precursors. However, the phase purity is still limited as requested by applications of nanodiamonds and could not be ameliorated through methods that worked for other studies. From this point of view the presented analysis of parameters derived from optical emission studies and the particle heating model can be used as guidelines to design of a new microplasma reactor working in a different parameter space which would result in phase pure samples.

The synthesis of Bismuth and Antimony quantum dots was demonstrated for the first time from pure solid precursors in the form of wires. While these works are still at the proof of concept stage in terms of controllability and reproducibility of the process, the results showed the great potential of this reactor concept for synthesizing quantum dots of

various metallic elements. The synthesized Bismuth quantum dots show a reasonable tunability in size through the variation of a single synthesis parameter (helium flow) and the determination of optical and electronic properties presented evidence of a semiconductive behaviour, which implies that a size-dependent transition from the bulk semi-metallic behaviour has occurred. Antimony quantum dots instead were found in co-presence of oxide phases and showed less tunability in size as a function of the explored parameters. The technological aspects that relate to integration of the synthesis into application devices fabrication steps and the solid precursor delivery have been explored. In this respect, solid precursor delivery presents a different scenario compared to gas/liquid precursors and yet to be understood even in specific cases. Some observations about the formation of particles from the solid precursors have been made and have been related to the peculiar physics of microplasmas, however it is far from behind understood despite its potential importance for plasma synthesis of metal nanoparticles.

8.2 Outlook and recommendations

The lack of knowledge about the fundamental physics of these complex microplasma sources is impeding the understanding of basic mechanisms underlying particle formation, despite the engineering efforts to make things work. A better characterization of the underlying physics could enable an easier control over the plasma processes and the resulting material properties of synthesized nanoparticles. For this reason, a more important effort from this point of view would imply the use of laser-based diagnostics as higher spatial resolution techniques to measure the plasma parameters and mass spectroscopy techniques to measure the partial products during nanoparticle formation. At the same time, finer diagnostics would be complemented by the development of more generalized theoretical framework describing microplasmas across different reactor designs and for different precursors.

For better understanding of local electronic properties instead, scanning probe microscopies would allow to measure the variations of parameters as work functions and band edges at the nanoscale level. Also, implementing angle-resolved photoemission spectroscopy or inverse photoemission spectroscopy in combination with ultraviolet photoemission spectroscopy would allow to measure electron levels, density of states and bandgaps in a more comprehensive method, without relying on optical spectroscopies for which the interpretation of data in terms of material properties is complicated by scattering events for nanostructured materials and without relying on techniques which are subject to variability due to the exposure of samples to atmosphere, as Kelvin probe-related techniques are.

Future work with respect to the experiments described throughout the thesis will deal with different aspects of plasma characterization and design of improved reactors for the processes studied. To ameliorate the plasma heating model, an assessment of the impact of surface reactions as a function of size would be needed, as some authors with different discharges can explain over-temperatures through these reactions. With respect to the nanodiamonds process, a new reactor working in the parameters of interest to have phase-pure particles would be beneficial, as these have a high impact in different fields of application. Also, the solid precursor reactor design can be ameliorated to improve the thermal stability of the process and to have a more reliable accurate positioning of the wire, hence a better reproducibility of the synthesized particles. In addition, further experiments would be beneficial to understand the formation mechanism, possibly

through the analysis of partial products via mass spectroscopy and the development of models to understand the principia behind the specific erosion mechanism of the solid precursor, as this would have a significant impact both scientifically and technologically.